

THE INFLUENCE OF ANION- π INTERACTIONS BETWEEN MULTI-
ATOMIC ANIONS AND π -ACIDIC RING SYSTEMS ON THE SELF-
ASSEMBLY OF COORDINATION COMPOUNDS

A Dissertation

by

BRANDI LEE SCHOTTEL

Submitted to the Office of Graduate Studies of
Texas A&M University
in partial fulfillment of the requirements for the degree of

DOCTOR OF PHILOSOPHY

May 2007

Major Subject: Chemistry

THE INFLUENCE OF ANION- π INTERACTIONS BETWEEN MULTI-
ATOMIC ANIONS AND π -ACIDIC RING SYSTEMS ON THE SELF-
ASSEMBLY OF COORDINATION COMPOUNDS

A Dissertation

by

BRANDI LEE SCHOTTEL

Submitted to the Office of Graduate Studies of
Texas A&M University
in partial fulfillment of the requirements for the degree of

DOCTOR OF PHILOSOPHY

Approved by:

Chair of Committee, Kim R. Dunbar
Committee Members, Don Darensbourg
François P. Gabbaï
Don Naugle
Head of Department, David H. Russell

May 2007

Major Subject: Chemistry

ABSTRACT

The Influence of Anion- π Interactions Between Multi-Atomic Anions and π -Acidic Ring Systems on the Self-Assembly of Coordination Compounds.

(May 2007)

Brandi Lee Schottel, B.Sc., University of Missouri, Columbia, Missouri

Chair of Advisory Committee: Dr. Kim R. Dunbar

Anion- π interactions, weak attractions between anions and π -acidic ring systems, have become an important topic in supramolecular chemistry within the past five years. Although a variety of computational studies have been undertaken by several groups to investigate the nature of these interactions, no comprehensive experimental investigations had been performed until the completion of the work described herein. The results presented in this dissertation indicate that anion- π interactions involving large complex anions are controlling elements in self-assembly reactions with cations that involve π -acidic ring systems.

Syntheses performed with the ligand 3-6-bis(2'-pyridyl)-1,2,4,5-tetrazine, or bptz, with M(II) first row transition metal salts (M = Mn, Fe, Ni, Cu, and Zn), produced self-assembled complexes that varied in shape and M:ligand ratio based on the presence of particular anions. Through a series of solution and structural studies, it was determined that the cationic polygons are templated by the size and shape of the specific anions during self-assembly. A close inspection of the bptz complexes in the solid state

indicated that the anions were participating in anion- π interactions with the π -acidic central tetrazine ring of the ligand.

To show that these anion- π interactions were indeed important, reactions of bptz ligand as well with 3,6-bis(2'-pyridyl)-1,2-pyridazine (bppn) with Ag(I) salts were performed to compare the effect that specific anions had on self-assembly interactions between similar ligands with different π -acidities. The results indicate that the Ag(I) complexes that included the π -acidic tetrazine ring are strongly influenced by the anion presence, while those complexes that were synthesized with the similarly shaped, but electroneutral bppn ligand only relied on the anions for charge-balance.

To better understand the anion- π interactions in the obtained bptz complexes, a computational study was performed on systems with the polyatomic anions $[\text{BF}_4]^-$ and $[\text{PF}_6]^-$ interacting with simple heteroaromatic rings of varying degrees of π -acidity. Based on the final optimized complex geometries and Atoms in Molecules (AIM) critical point analyses, it was determined that anion- π interactions involving multi-atomic anions interact with π -systems in different orientations based on the symmetry of the ring system in the complex.

To my parents Linda L. Lehde and Lloyd G. Schottel, my step-parents Michael Lehde and Betty Schottel, my brother Matthew L. Schottel, and my only surviving grandparent, Robert Schottel.

“My beard grows to my toes,
I never wears no clothes.
I wraps my hair arounds my bare,
And down the road I goes.” - Shel Silverstein, Where the Sidewalk Ends
--To making the best of any situation, no matter how bizarre it may seem.

ACKNOWLEDGMENTS

This dissertation work could not have been accomplished without the help of many people in my life. First and foremost, I would like to thank Professor Kim Dunbar for her support both professionally and personally these past five years. Her inorganic chemistry expertise and professional poise have truly been an inspiration, and I feel that she is the best possible advisor I could have had for my Ph.D. work. The director of the Laboratory for Molecular Simulation, Dr. Lisa M. Pérez, has also filled an advisory role in my work, particularly in the area of computational chemistry. Through her guidance, collaboration, and friendship, I was able to learn and perform computational chemistry at a professional level.

Although many names come to mind, my coworkers and friends in the Dunbar Laboratories at Texas A&M University stand out as influential in my trials during my Ph. D. work. The guidance and friendships of my coworkers Dr. Eric Shelter, Dr. Curtis Berlinguette, Dr. Jose Ramon Galan-Mascaros, Dr. Jitendra K. Bera, Dr. John Bacsa, Dr. Alfredo Angeles-Boza, and Eric Rheinheimer helped immensely in the beginning of my career at Texas A&M University. Dr. Helen Chifotides and Dr. Mikail Shatruck have been particularly instrumental in my education, and I credit them with teaching me many of my research techniques. More recently, the support of the newer group additions Ferdi Karadas, Dafhne Aguirre, Dr. Andrey Prosvirin, Kristen Chambers, Carolina Avendano, Matthew Hilfiger, Nazario Lopez, Ian Giles, Edward Funk, Dr. Sofi Bin-

Salamon, and Ben Duffuss has helped make my later years in the Dunbar Group enjoyable.

Without the support of my family, however, I would not have even attempted to obtain a PhD. in chemistry. My parents Linda and Lloyd, step-parents Betty and Michael, my uncle Patrick, and my big brother Matthew have never faltered in their support of my academic career. At times their emotional support was all that kept me going.

Thank you.

TABLE OF CONTENTS

	Page
ABSTRACT	iii
DEDICATION	v
ACKNOWLEDGMENTS	vi
TABLE OF CONTENTS	viii
LIST OF FIGURES	xiv
LIST OF TABLES	xxxiii
LIST OF SYMBOLS AND ABBREVIATIONS.....	xxxv
LIST OF COMPOUNDS	xxxvii
CHAPTER	
I INTRODUCTION TO ANION- π INTERACTIONS	1
I. Background and Introduction	1
A. Supramolecular Chemistry of Anions	1
B. Anions as Templates.....	3
C. Anion- π Interactions	4
1. Definition	4
2. Computational Studies on Anion- π Interactions	4
3. Experimental Evidence for Anion- π Interactions.....	25
a. Structural Evidence	25
b. Structural Evidence with Theoretical Support	30
c. Solution Evidence.....	37
D. Previous Work in Our Laboratories	45
E. Systematic Experimental and Theoretical Investigations of Anion- π Interactions.....	46

CHAPTER	Page
II ANION TEMPLATE EFFECT ON THE SELF-ASSEMBLY AND INTERCONVERSION OF METALLACYCLOPHANES	48
I. Introduction.....	48
II. Experimental.....	50
A. Materials.....	50
B. Physical Measurements	51
C. Syntheses	51
1. Preparation of $[\text{Ni}_4(\text{bptz})_4(\text{CH}_3\text{CN})_8][\text{BF}_4]_8$ (1)	51
2. Preparation of $[\text{Ni}_4(\text{bptz})_4(\text{CH}_3\text{CN})_8][\text{ClO}_4]_8$ (2)	52
3. Preparation of $[\text{Zn}_4(\text{bptz})_4(\text{CH}_3\text{CN})_8][\text{BF}_4]_8$ (3)	52
4. Preparation of $[\text{Zn}_4(\text{bptz})_4(\text{CH}_3\text{CN})_8][\text{ClO}_4]_8$ (4).....	52
5. Preparation of $[\text{Ni}_5(\text{bptz})_5(\text{CH}_3\text{CN})_{10}][\text{SbF}_6]_{10}$ (5).....	53
6. Preparation of $[\text{Ni}_3(\text{bptz})_3][\text{NO}_3]_6$ (6)	53
7. Preparation of $[\text{Ni}_4(\text{bptz})_4(\text{CH}_3\text{CN})_8][\text{SbF}_6]_7[\text{I}]$ (7)	53
8. Preparation of $[\text{Ni}_4(\text{bptz})_4(\text{CH}_3\text{CN})_8][\text{BF}_4][\text{PF}_6][\text{SbF}_6]_6$ (8)	54
9. Preparation of $[\text{Ni}_4(\text{bptz})_4(\text{CH}_3\text{CN})_4(\text{H}_2\text{O})_4][\text{ClO}_4][\text{IO}_4]_7$ (9)	54
10. Preparation of $[\text{Ni}_4(\text{bptz})_4\text{Br}_7(\text{CH}_3\text{CN})\text{Br}_3]$ (10).....	54
11. Preparation of $[\text{Ni}_2(\text{bptz})(\text{CH}_3\text{CN})_8][\text{ClO}_4]_4$ (11)	54
12. Preparation of $[\text{Mn}(\text{bptz})(\text{CH}_3\text{CN})_2][\text{BF}_4]_{2\infty}$ (12).....	55
D. X-ray Crystallographic Studies	55
1. $[\{\text{Ni}_4(\text{bptz})_4(\text{CH}_3\text{CN})_8\} \subset \text{BF}_4][\text{BF}_4]_7 \cdot 4\text{CH}_3\text{CN}$, (1) $\cdot 4\text{CH}_3\text{CN}$	55
2. $[\{\text{Ni}_4(\text{bptz})_4(\text{CH}_3\text{CN})_8\} \subset \text{ClO}_4][\text{ClO}_4]_7 \cdot 4\text{CH}_3\text{CN}$ $\cdot \text{C}_4\text{H}_8\text{O}$, (2) $\cdot 4\text{CH}_3\text{CN} \cdot \text{C}_4\text{H}_8\text{O}$	56
3. $[\{\text{Zn}_4(\text{bptz})_4(\text{CH}_3\text{CN})_8\} \subset \text{BF}_4][\text{BF}_4]_7 \cdot 4\text{CH}_3\text{CN}$, (3) $\cdot 4\text{CH}_3\text{CN}$	56
4. $[\{\text{Ni}_5(\text{bptz})_5(\text{CH}_3\text{CN})_{10}\} \subset \text{SbF}_6][\text{SbF}_6]_9 \cdot 2\text{CH}_3\text{CN}$, (5) $\cdot 2\text{CH}_3\text{CN}$	56
5. $[\{\text{Ni}_4(\text{bptz})_4(\text{CH}_3\text{CN})_8\} \subset \text{I}][\text{SbF}_6]_7$, (7)	61
6. $[\{\text{Ni}_4(\text{bptz})_4(\text{CH}_3\text{CN})_8\} \subset \text{BF}_4][\text{PF}_6][\text{SbF}_6]_6$, (8).....	61
7. $[\{\text{Ni}_4(\text{bptz})_4(\text{CH}_3\text{CN})_4(\text{H}_2\text{O})_4\} \subset \text{ClO}_4][\text{IO}_4]_7 \cdot 3\text{CH}_3\text{CN}$, (9) $\cdot 3\text{CH}_3\text{CN}$	62
8. $[\{\text{Ni}_4\text{Br}_7(\text{bptz})_4(\text{CH}_3\text{CN})\} \subset \text{Br}_3] \cdot 2\text{CH}_3\text{CN} \cdot 2.5\text{C}_7\text{H}_8$, (10) $\cdot 2\text{CH}_3\text{CN} \cdot 2.5\text{C}_7\text{H}_8$	63
9. $[\text{Ni}_2(\text{bptz})(\text{CH}_3\text{CN})_8][\text{ClO}_4]_4$ (11)	63

CHAPTER	Page
10. $\{[\text{Mn}(\text{bptz})(\text{CH}_3\text{CN})_2][\text{BF}_4]_2 \cdot 1.5\text{CH}_3\text{CN}\}_\infty$ (12) $\cdot 1.5n\text{CH}_3\text{CN}$	63
III. Results	64
A. Synthesis and Stability Studies of the Cyclic Cations	64
B. Interconversion between the $[\text{Ni}_5]^{10+}$ and $[\text{Ni}_4]$ Cyclic Cations	66
C. Reactions of $[\text{Ni}_4(\text{bptz})_4(\text{CH}_3\text{CN})_8]^{8+}$ with Other Anions	69
D. NMR Spectroscopic Studies	70
E. IR Spectroscopy	75
F. Electrospray Mass Spectroscopic Studies	75
G. X-ray Crystallographic Studies	87
1. $[\{\text{Ni}_4(\text{bptz})_4(\text{CH}_3\text{CN})_8\} \subset \text{BF}_4][\text{BF}_4]_7 \cdot 4\text{CH}_3\text{CN}$, (1) $\cdot 4\text{CH}_3\text{CN}$	87
2. $[\{\text{Ni}_4(\text{bptz})_4(\text{CH}_3\text{CN})_8\} \subset \text{ClO}_4](\text{ClO}_4)_7 \cdot 4\text{CH}_3\text{CN}$ $\cdot \text{C}_4\text{H}_8\text{O}$, (2) $\cdot 4\text{CH}_3\text{CN} \cdot \text{C}_4\text{H}_8\text{O}$	89
3. $[\{\text{Zn}_4(\text{bptz})_4(\text{CH}_3\text{CN})_8\} \subset \text{BF}_4](\text{BF}_4)_7 \cdot 4\text{CH}_3\text{CN}$, (3) $\cdot 4\text{CH}_3\text{CN}$	89
4. $[\{\text{Ni}_5(\text{bptz})_5(\text{CH}_3\text{CN})_{10}\} \subset \text{SbF}_6][\text{SbF}_6]_9 \cdot 2\text{CH}_3\text{CN}$, (5) $\cdot 2\text{CH}_3\text{CN}$	92
5. $[\{\text{Ni}_4(\text{bptz})_4(\text{CH}_3\text{CN})_8\} \subset \text{I}][\text{SbF}_6]_7$ (7)	92
6. $[\{\text{Ni}_4(\text{bptz})_4(\text{CH}_3\text{CN})_8\} \subset \text{BF}_4][\text{PF}_6][\text{SbF}_6]_6$ (8)	95
7. $[\{\text{Ni}_4(\text{bptz})_4(\text{CH}_3\text{CN})_4(\text{H}_2\text{O})_4\} \subset \text{ClO}_4][\text{IO}_4]_7 \cdot 3\text{CH}_3\text{CN}$, (9) $\cdot 3\text{CH}_3\text{CN}$	98
8. $[\{\text{Ni}_4(\text{bptz})_4(\text{CH}_3\text{CN})\text{Br}_7\} \subset \text{Br}_3] \cdot 2\text{CH}_3\text{CN} \cdot 2.5\text{C}_7\text{H}_8$, (10) $\cdot 2\text{CH}_3\text{CN} \cdot 2.5\text{C}_7\text{H}_8$	98
9. $[\text{Ni}_2(\text{bptz})(\text{CH}_3\text{CN})_8][\text{ClO}_4]_4$ (11)	101
10. $\{[\text{Mn}(\text{bptz})(\text{CH}_3\text{CN})_2][\text{BF}_4]_2 \cdot 1.5\text{CH}_3\text{CN}\}_\infty$, (12) $\cdot 1.5n\text{CH}_3\text{CN}$	103
IV. Discussion	103
A. Product Nuclearity Dependence on the Anion Identity	103
B. Anion Selectivity of the Cavity	106
C. Stability of the Molecular Pentagon vs. the Square	107
D. Divalent Transition Metals and Product Identity	109
E. Anion Interactions with the Cyclic Cations	111
V. Conclusions	111

CHAPTER	Page
III ANION- π INTERACTIONS AS CONTROLLING ELEMENTS IN SELF-ASSEMBLY REACTIONS OF Ag(I) COMPLEXES WITH π -ACIDIC AROMATIC RINGS.....	114
I. Introduction.....	114
II. Experimental Section.....	117
A. Starting Materials	117
B. Physical Methods.....	117
C. Synthesis of Ag-bptz and Ag-bppn Compounds	118
1. {[Ag(bptz)][PF ₆]} _∞ (13).....	118
2. [Ag ₂ (bptz) ₂ (CH ₃ CN) ₂][PF ₆] ₂ (14).....	119
3. [Ag ₂ (bptz) ₂ (CH ₃ CN) ₂][AsF ₆] ₂ (15)	119
4. [Ag ₂ (bptz) ₃][AsF ₆] ₂ (16).....	120
5. [Ag ₂ (bptz) ₃][SbF ₆] ₂ (17a and 17b)	120
6. [Ag ₄ (bppn) ₄][PF ₆] ₄ (18).....	121
7. [Ag ₄ (bppn) ₄][AsF ₆] ₄ (19)	121
8. [Ag ₄ (bppn) ₄][SbF ₆] ₄ (20).....	121
9. [Ag ₄ (bppn) ₄][BF ₄] ₄ (21)	122
C. Data Collection and Refinement.....	122
1. {[Ag(bptz)][PF ₆]} _∞ (13).....	123
2. [Ag ₂ (bptz) ₂ (CH ₃ CN) ₂][PF ₆] ₂ (14) and [Ag ₂ (bptz) ₂ (CH ₃ CN) ₂][AsF ₆] ₂ (15)	123
3. [Ag ₂ (bptz) ₃][AsF ₆] ₂ •2CH ₃ CN, (16)•2CH ₃ CN.....	124
4. [Ag ₂ (bptz) ₃][SbF ₆] ₂ •2CH ₃ CN, (17a)•2CH ₃ CN.....	129
5. [Ag ₂ (bptz) ₃][SbF ₆] ₂ (17b)	130
6. Ag ₄ (bppn) ₄][PF ₆] ₄ •4CH ₃ NO ₂ (18)•4CH ₃ NO ₂ , [Ag ₄ (bppn) ₄][AsF ₆] ₄ •4CH ₃ NO ₂ , (19)•4CH ₃ NO ₂ , and [Ag ₄ (bppn) ₄][SbF ₆] ₄ •4CH ₃ NO ₂ , (20)•4CH ₃ NO ₂	130
7. [Ag ₄ (bppn) ₄][BF ₄] ₄ •3CH ₃ NO ₂ •C ₆ H ₆ , (21)•3CH ₃ NO ₂ •C ₆ H ₆	131
D. Theoretical Calculations.....	131
III. Results.....	132
A. X-ray Crystallographic Results	132
1. {[Ag(bptz)][PF ₆]} _∞ (13).....	132
2. [Ag ₂ (bptz) ₂ (CH ₃ CN) ₂][PF ₆] ₂ (14) and [Ag ₂ (bptz) ₂ (CH ₃ CN) ₂][AsF ₆] ₂ (15).....	136
3. [Ag ₂ (bptz) ₃][AsF ₆] ₂ •2CH ₃ CN, (16)•2CH ₃ CN and [Ag ₂ (bptz) ₃][SbF ₆] ₂ •2CH ₃ CN, (17a)•2CH ₃ CN.....	141
4. [Ag ₂ (bptz) ₃][SbF ₆] ₂ , (17b)	146

CHAPTER	Page
5. $[\text{Ag}_4(\text{bppn})_4][\text{PF}_6]_4 \cdot 4\text{CH}_3\text{NO}_2$ (18) $\cdot 4\text{CH}_3\text{NO}_2$, $[\text{Ag}_4(\text{bppn})_4][\text{AsF}_6]_4 \cdot 4\text{CH}_3\text{NO}_2$ (19) $\cdot 4\text{CH}_3\text{NO}_2$, and $[\text{Ag}_4(\text{bppn})_4][\text{SbF}_6]_4 \cdot 4\text{CH}_3\text{NO}_2$ (20) $\cdot 4\text{CH}_3\text{NO}_2$	150
6. $[\text{Ag}_4(\text{bppn})_4][\text{BF}_4]_4 \cdot 3\text{CH}_3\text{NO}_2 \cdot \text{C}_6\text{H}_6$, (21) $\cdot 3\text{CH}_3\text{NO}_2 \cdot \text{C}_6\text{H}_6$	156
B. NMR and Mass Spectrometry Studies.....	158
1. Ag(I)-bptz complexes.....	158
2. Ag(I)-bppn complexes.....	162
C. Bptz and Bppn Ligand Calculations.....	164
D. Silver Complex Calculations.....	167
IV. Discussion.....	178
A. Effect of Anion Identity and Anion- π Interactions on the Products.....	178
B. Solid State Evidence for Anion- π Interactions.....	179
C. Theoretical Evidence of Anion- π Interactions.....	186
V. Conclusions.....	189
 IV COMPUTATIONAL INVESTIGATIONS OF ANION- π INTERACTIONS BETWEEN TETRAHEDRAL AND OCTAHEDRAL ANIONS AND $\text{C}_3\text{N}_3\text{X}_3$, $\text{C}_2\text{N}_4\text{X}_2$, AND $\text{C}_4\text{N}_2\text{X}_4$ (X = Br, Cl, OR CN) RING SYSTEMS.....	191
I. Introduction.....	191
II. Methods and Materials.....	193
III. Results.....	194
A. Π -System Analysis.....	194
B. Computational Analysis of Anion- π Interactions Involving Complex Anions and Ring Systems with Obvious Matching Symmetry.....	197
1. $\text{C}_3\text{X}_3\text{N}_3$ Systems with $[\text{BF}_4]^-$ and $[\text{PF}_6]^-$	197
2. $\text{C}_2\text{N}_4\text{X}_2$ Systems with $[\text{BF}_4]^-$ and $[\text{PF}_6]^-$	208
C. Structural Analysis of $\text{C}_4\text{N}_2\text{X}_4$ with $[\text{BF}_4]^-$ and $[\text{PF}_6]^-$:- No Clear Interaction Symmetry Evident.....	218
1. B3LYP/6-31++G(d',p') geometries of $\text{C}_4\text{N}_2\text{X}_4$ rings with $[\text{BF}_4]^-$	218
2. MP2/6-31++G(d',p') geometries of $\text{C}_4\text{N}_2\text{X}_4$ rings with $[\text{BF}_4]^-$	225
3. MP2/6-31++G(d',p') geometries of $\text{C}_4\text{N}_2\text{X}_4$ rings with $[\text{PF}_6]^-$	233
4. B3LYP/6-31++G(d',p') geometries of $\text{C}_4\text{N}_2\text{X}_4$ rings with $[\text{PF}_6]^-$	236

CHAPTER	Page
IV. Discussion	245
A. The Effect of Ring π -Acidity.....	245
B. The Effect of Symmetry	246
C. Corrections on Previous Results.....	249
V. Conclusions	257
V. CONCLUSIONS.....	258
REFERENCES.....	263
VITA	274

LIST OF FIGURES

FIGURE	Page
1	(a) Line diagram of the original katipinate structure encapsulating [Cl] ⁻ , and (b) the first reported metal-based anion host. Mercury is blue, carbon is gray, boron is pink, hydrogen is white, and chlorine is yellow 3
2	Representation of the AIM-derived critical points found when [Cl] ⁻ complexes with C ₆ F ₆ (top), and when [NO ₃] ⁻ complexes with C ₆ F ₆ (bottom). Both are shown with top and side views. The red circles represent bonding (3,-1) critical points, the yellow circles represent ring (3,+1) critical points, and the light blue circles represent cage (3,+3) critical points. The Figure is adapted from reference 7
3	Diagram representing the angle measured in the structure fragments involving perfluorinated rings and anions for a CSD search..... 9
4	Diagram of the critical points found by AIM analysis of C ₆ H ₆ interacting with both a [F] ⁻ anion and a [Na] ⁺ cation. Red circles = (3,-1) bonding critical points, green circles = (3, +1) ring critical points, and light blue circles = (3,+3) critical points. Figure adapted from reference 21 11
5	Schematic drawings of a halide anion [X] ⁻ interacting with urea, squaramide, and <i>s</i> -tetrazine. Figure is adapted from reference 23 13
6	The π -acidic ring systems used in the topological analysis of anion- π interactions from reference 25. The Q_{zz} values of each ring are listed underneath its line drawing. Figure adapted from reference 25 16
7	The results of a CSD search performed by Deyà and coworkers to find 5-membered ring π -systems that participate in anion- π interactions. Graph A represents the number of fragments (vertical axis) found at specific anion \cdots ring critical point \cdots carbon atom on the ring angle. Graph B represents the distance of the anion (vertical axis) vs. the same angle as graph B. Both show that most anion- π complexes involving 5-membered rings have the defined angle close to 90°. The graphs are reproduced from reference 26..... 17

FIGURE	Page
8	Inductive orbitals of hexafluorobenzene with (a) [Br] ⁻ , (b) [CN] ⁻ , and (c) [NO ₃] ⁻). Figure adapted from reference 27 20
9	π -systems examined (with respective quadrupole moments) in the presence of both anions and cations to study the theoretical differences between anion- π interactions and cation- π interactions. Figure adapted from reference 30 21
10	The anion- π complex models investigated with multiple interactions per anion. Figure adapted from reference 32 23
11	(a) Line drawing of the hexakis(pyridin-2-yl)-[1,3,5]-triazine-2,4,5-triamine ligand (L1). (b) Front (left) and side (right) views of the structure $\{[L_2(CuCl_3)][Cl]\}^{2+}$. Anion to tetrazine centroid contact = 3.11 Å. Figures adapted from reference 35)..... 27
12	(a). Line drawing of N,N'N'',N'''-tetrakis{2,4-bis(di-2-pyridylamino)-1,3,5-triazineyl}-1,4,8,11-tetraazacylotetradecane ligand (L2), and (b) Crystal structure of $[Cu_4(\text{azadendtriz})Cl_4](Cl)_4(H_2O)_{13}$, complex <i>ii</i> from 2 different perspectives. Figures adapted from reference 36 29
13	Several structures from the recent literature that are reported to involve anion- π interactions: (a) $\{[Cu(C_8N_5H_7)_2][CF_3SO_3]\} \cdot C_8N_5H_7\}^+$, (b) $\{[Cu(\text{dppFc}^*)]_2\{HAT-(CN)_6\}_2\}[PF_6]_2$, (c) $\{[Cu(\text{dppFc})]_3\{HAT-(CN)_6\}\}[PF_6]\}^+$, and (d) $(C_{16}H_{13}N_4)[CuCl_4][Cl]$. $\text{dppFc}^* = 1,1'$ -bis(diphenyl-phosphino) octamethylferrocene, and $\text{dppFc} = 1,1'$ -bis(diphenyl-phosphino) ferrocene..... 31
14	Line drawings, labels, and quadrupole moments of the cyanuric acid derivatives studied theoretically in reference 40 32
15	Results of the cyanuric acid study: Line drawings of ligands L4 and L5, and crystal structures of compounds <i>iii</i> and <i>iv</i> . C = grey, O = red, Cl = yellow, N = blue, H = white, and S = orange. Figure adapted from reference 40 34

FIGURE	Page
16	(a) Line drawing of L5, or 2,4,6-tris(di-2-picoylamino)[1,3,5]triazine, (b) crystal structure (v) of $[\text{Cu}_3(\text{L5})(\text{NO}_3)_2(\text{H}_2\text{O})_6](\text{NO}_3)_4$, and (c) theoretical model used for computational studies of complex v . Red = O, dark blue = N, light blue Cu, grey = C, and white = H. Figure reproduced from reference 41 35
17	(a) Line drawing of the (L6) ligand N,N',N'',N'''-tetrakis{2,4-bis(dipyridylamino)-1,3,5-triazine-6-yl}triethyleneteramine, (b) crystal structure of $\{[\text{Cu}_2(\text{L6})(\text{NO}_3)_2][\text{NO}_3]\}^+$, and (c) the model used for the BLYP optimization and AIM evaluation for the theoretical part of the study. Red = O, dark blue = N, light blue = Cu, grey = C, and white =H. All figures are adapted from reference 42 37
18	Line drawing of how an <i>N</i> -confused porphyrin (L8) will bind to a halide anion $[\text{X}]^-$ in solution through both an H-bond from the peripheral N atom on the <i>N</i> -confused pyridine as well as through an anion- π interaction with the nearest C_6F_5 ring. Drawing adapted from reference 43 38
19	(a) Line drawings of the ring systems examined in the UV/Vis study of Kochi and coworkers, (b) UV/Vis spectra of a 5 mM tetracyanopyrazine (TCP) ring in acetonitrile with increasing concentrations of $[(n\text{-But})_4\text{N}][\text{Br}]$ added. The peak at 400 nm slowly increases because of charge-transfer from the anion to the TCP ring. Concentrations: 1 = 0 mM, 2 = 4.9 mM, 3 = 19 mM, 4 = 46 mM, 5 = 83 mM, and 6 = 208 mM of $[\text{Br}]^-$. Inset is the Mulliken dependence of the energy absorption band (ν_{CT}), which equals 400 nm for TCP with $[\text{Br}]^-$, with the reduction potential of the π -acceptor ring from 22a. (c) Crystal structure of TCP with $[\text{Cl}]^-$ (vii). The $[(n\text{-But})_4\text{N}]^+$ cation is omitted for the sake of clarity. Blue = N, grey = C, and yellow = Cl. Figures adapted from reference 44 40
20	Synthesis of $(+/-)\text{-}\{\text{Cp}^*\text{Ru}\}_6(\mathbf{E})^{6+}$ from $(+/-)\text{-cryptophane E}$, $(+/-)\text{-E}$ and $[\text{Cp}^*\text{Ru}][\text{X}]$, where $\text{X} = [\text{CF}_3\text{SO}_3]^-$ or $[\text{PF}_6]^-$, (b) $\{[(+/-)\text{-2}][\text{CF}_3\text{SO}_3]\}^{5+}$ (viii) and $\{[(+/-)\text{-2}][\text{SbF}_6]\}^{5+}$ (ix). Red = O, Yellow = S, dark blue = N, light blue = Ru, green = F, grey = C, and white = H. (c) Left: ^1H NMR spectrum of viii in CD_3NO_2 at equilibrium, and right: ^{19}F NMR spectrum of viii in CD_3NO_2 at equilibrium. Figures are taken from reference 46 42

FIGURE	Page
21 (a) Line drawings of the ligands L8 and L9, and (b) HF/6-31+G* geometry optimization results of L8 and L9 in the presence of [Cl] ⁻ . Figures adapted from reference 47	44
22 (a) Line drawing of the bptz ligand in the trans-orientation, (b) crystal structure diagram of [Ni ₄ (bptz) ₄ (CH ₃ CN) ₈ ⊂BF ₄] ⁷⁺ , and (c) crystal structure diagram of [Ni ₅ (bptz) ₅ (CH ₃ CN) ₁₀ ⊂SbF ₆] ⁹⁺ . Figures are taken from references 48 and 49	46
23 Line drawing of 3,6-bis(2'-pyridyl)-1,2,4,5-tetrazine with appropriate ¹ H NMR labels	50
24 Aromatic region of the ¹ H NMR spectrum of (a) [Zn ₄ (bptz) ₄ (CH ₃ CN) ₈][BF ₄] ₈ and (b) bptz, in CD ₃ CN at room Temperature	71
25 ¹⁹ F NMR spectra of [Zn ₄ (bptz) ₄ (CH ₃ CN) ₈][BF ₄] ₈ in CD ₃ CN at 22°C. Due to coupling of ¹¹ B and ¹⁰ B to the ¹⁹ F nuclei, the ¹⁹ F NMR resonance of [Zn ₄ (bptz) ₄ (CH ₃ CN) ₈][BF ₄] ₈ at room temperature is split into two with a relative ratio ~ 4:1 (inset) corresponding to the natural abundance of ¹¹ B to ¹⁰ B. The two distinct maxima of the ¹⁹ F NMR resonance for the free [BF ₄] ⁻ ions collapse at temperatures below 5°C.....	73
26 Electrospray mass spectrum of [Ni ₄ (bptz) ₄ (CH ₃ CN) ₈ ⊂ClO ₄][ClO ₄] ₇ (2) in acetonitrile. The ion signals displayed correspond to [Ni ₄ (bptz) ₄ (ClO ₄) ₇ + 2H] ³⁺ (I) at <i>m/z</i> 625.9, [Ni ₄ (bptz) ₄ (ClO ₄) ₆] ²⁺ (II) at <i>m/z</i> 888.2, and (C) [Ni ₄ (bptz) ₄ (ClO ₄) ₇] ⁺ (III) at <i>m/z</i> 1875.8 (parent ion peak). The experimental and theoretical isotopic distribution patterns of III are shown in the inset.....	76
27 Theoretical and experimental isotopic distribution patterns of the ES-MS parent ion peak of [Zn ₄ (bptz) ₄ (ClO ₄) ₇] ⁺ at <i>m/z</i> 1902.6.....	77

FIGURE	Page
28	Electrospray mass spectrum of $[\text{Ni}_5(\text{bptz})_5(\text{CH}_3\text{CN})_{10}\text{C}\text{SbF}_6][\text{SbF}_6]_9$ (5) in acetonitrile. The ion signals displayed correspond to $[\text{Ni}_2(\text{bptz})(\text{SbF}_6)_3]^+$ (I) at m/z 1060.8, $[\text{Ni}_2(\text{bptz})(\text{SbF}_6)_4]$ (II) at m/z 1296.6, and $[\text{Ni}_5(\text{bptz})_5(\text{SbF}_6)_9]^+$ (III) at m/z 3596.3 (parent ion peak). The experimental and theoretical isotopic distribution patterns of III are shown in the inset 79
29	Electrospray mass spectrum of $[\text{Ni}_3(\text{bptz})_3][\text{NO}_3]_6$ (6) in acetonitrile. Parent ion peak for $[\text{Ni}_3(\text{bptz})_3(\text{NO}_3)_5]^+$ at m/z 1194.7. (A) Theoretical and (B) experimental isotopic distribution patterns of the parent ion peak 80
30	Electrospray mass spectrum of (A) original $[\text{Ni}_4(\text{bptz})_4(\text{CH}_3\text{CN})_8\text{C}\text{ClO}_4][\text{ClO}_4]_7$ square sample; (B) $[\text{Ni}_4(\text{bptz})_4((\text{CH}_3\text{CN})_8(\text{ClO}_4)_7)]^+$ sample that has been refluxed with excess $[n\text{-Bu}_4\text{N}][\text{SbF}_6]$ for 2 days; partial conversion of the square to the pentagon has taken place. Ion signals at m/z 2829.9, 3122.8, 3359.5 and 3596.3 correspond to the species $[\text{Ni}_4(\text{bptz})_4(\text{SbF}_6)_7]^+$ (IV), $[\text{Ni}_5(\text{bptz})_5(\text{SbF}_6)_{7-2\text{H}}]^+$ (V), $[\text{Ni}_5(\text{bptz})_5(\text{SbF}_6)_8 - \text{H}]^+$ (VI) and $[\text{Ni}_5(\text{bptz})_5(\text{SbF}_6)_9]^+$ (VII), respectively 81
31	ES-MS spectrum of $[\text{Mn}_4(\text{bptz})_4(\text{CH}_3\text{CN})_8][\text{ClO}_4]_8$. Ion signals at m/z 620.9, 880.7, 1126.7, 1134.5 and 1860.8 (parent ion peak) correspond to $[\text{Mn}_4(\text{bptz})_4(\text{ClO}_4)_7 + 2\text{H}]^{3+}$ (I), $[\text{Mn}_4(\text{bptz})_4(\text{ClO}_4)_6]^{2+}$ (II), $[\text{Mn}_2(\text{bptz})_3(\text{ClO}_4)_3]^+$ (III), $[\text{Mn}_3(\text{bptz})_2(\text{ClO}_4)_5]^+$ (IV), and $[\text{Mn}_4(\text{bptz})_4(\text{ClO}_4)_7]^+$ (V), respectively. Ion signals due to the progressive loss of bptz molecules are also observed for $[\text{Mn}_4(\text{bptz})_4(\text{ClO}_4)_7 - (\text{bptz})]^+$ and $[\text{Mn}_4(\text{bptz})_4(\text{ClO}_4)_7 - 2(\text{bptz})]^+$ at m/z 1624.6 and 1388.3, respectively. The theoretical and experimental isotopic distribution patterns of the parent ion peak V have been expanded in the inset 83
32	ES-MS spectrum of $[\text{Fe}_4(\text{bptz})_4(\text{CH}_3\text{CN})_8][\text{ClO}_4]_8$. Ion signals at m/z 522.3, 622.1, 882.5, 1864.5 correspond to $[\text{Fe}_4(\text{bptz})_4(\text{ClO}_4)_4 + \text{H}]^{3+}$ (I), $[\text{Fe}_4(\text{bptz})_4(\text{ClO}_4)_7 + 2\text{H}]^{3+}$ (II), $[\text{Fe}_4(\text{bptz})_4(\text{ClO}_4)_6]^{2+}$ (III), $[\text{Fe}_4(\text{bptz})_4(\text{ClO}_4)_7]^+$ (IV) (parent ion peak), respectively. Ion signals due to the progressive loss of bptz molecules are also observed for $[\text{Fe}_4(\text{bptz})_4(\text{ClO}_4)_7 - (\text{bptz})]^+$ and $[\text{Fe}_4(\text{bptz})_4(\text{ClO}_4)_7 - 2(\text{bptz})]^+$ at m/z 1628.3 and 1392.0, respectively. The theoretical and experimental isotopic distribution patterns of the parent ion peak IV have been expanded in the inset 84

FIGURE	Page
33	ES-MS spectrum of $[\text{Cu}_4(\text{bptz})_4(\text{CH}_3\text{CN})_8][\text{ClO}_4]_8$. Ion signals at m/z 632.4, 897.9, 1895.2 correspond to $[\text{Cu}_4(\text{bptz})_4(\text{ClO}_4)_7 + 2\text{H}]^{3+}$ (I), $[\text{Cu}_4(\text{bptz})_4(\text{ClO}_4)_6]^{2+}$ (II), and $[\text{Cu}_4(\text{bptz})_4(\text{ClO}_4)_7]^+$ (III) (parent ion peak), respectively. An ion signal due to the loss of a bptz molecule is also observed for $[\text{Cu}_4(\text{bptz})_4(\text{ClO}_4)_7 - 2(\text{bptz})]^+$ at m/z 1422.7. The theoretical and experimental isotopic distribution patterns of the parent ion peak III have been expanded in the inset..... 85
34	ES-MS spectra of the products from the reaction between $\text{Ni}(\text{ClO}_4)_2 \cdot 6\text{H}_2\text{O}$ and bptz in acetonitrile, acetone, nitromethane, and ethanol. Parent ion peak for $[\text{Ni}_4(\text{bptz})_4(\text{ClO}_4)_7]^+$ at m/z 1875.8. The highly polar solvent ethanol does not favor formation of the $[\text{Ni}_4(\text{bptz})_4(\text{ClO}_4)_7]^+$ square 86
35	Thermal ellipsoid plot of the cationic unit $[\{\text{Ni}_4(\text{bptz})_4(\text{CH}_3\text{CN})_8\} \subset \text{BF}_4]^{7+}$ in 1 •4 CH_3CN . Thermal ellipsoids are represented at the 50% probability level. Selected bond distances (Å) and angles (°): Ni1-N5 2.031(7), Ni1-N6 2.043(7), Ni1-N5B 2.097(6), Ni4-N1 2.038(8), Ni4-N2 2.041(7), Ni4-N2A 2.067(7), Ni3-N7 2.041(7), N5C-N6C 1.327(8), N5-Ni1-N6 89.4(3), N2C-Ni2-N3 98.3(3), N5-Ni1-N5B 173.7(3) 88
36	Thermal ellipsoid plot of the cationic unit $[\{\text{Ni}_4(\text{bptz})_4(\text{CH}_3\text{CN})_8\} \subset \text{ClO}_4]^{7+}$ in 2 •4 $\text{CH}_3\text{CN} \cdot \text{C}_4\text{H}_8\text{O}$. Thermal ellipsoids are represented at the 50% probability level. Selected bond distances (Å) and angles (°): Ni4-N7D 2.035(5), Ni4-N3C 2.099(4), Ni4-N8D 2.038 (5), Ni1-N2A 2.081(4), Ni1-N5D 2.073(5), Ni4-N5C 2.062(4), N2D-N3D 1.334(6), N2A-Ni1-N8A 90.10(18), N8A-Ni1-N7A 90.59(19), N7A-Ni1-N5D 87.29(18), N2A-Ni1-N7A 174.57(18), N7C-Ni3-N8C 88.21(19), N5B-Ni3-N2C 91.69(16), N2C-Ni3-N6B 87.89(17), N7C-Ni3-N2C 175.43(18) 90

FIGURE	Page
<p>37 Thermal ellipsoid plot of the cationic unit $[\{\text{Zn}_4(\text{bptz})_4(\text{CH}_3\text{CN})_8\}\text{C}\text{BF}_4]^{7+}$ in 3•4CH₃CN. Thermal ellipsoids are represented at the 50% probability level. Selected bond distances (Å) and angles (°): Zn1-N8A 2.074(4), Zn1-N7A 2.080(4), Zn1-N5D 2.260(4), Zn1-N2A 2.293(4), Zn4-N7D 2.070(4), Zn4-N8D 2.074(4), Zn4-N1D 2.095(4), Zn4-N6C 2.129(4), Zn4-N5C 2.246(4), Zn4-N2D 2.273(4), N8A-Zn1-N7A 92.62(17), N8A-Zn1-N5D 170.65(16), N7A-Zn1-N5D 92.98(16), N6B-Zn3-N5B 75.096(16), N8A-Zn1-N2A 89.79(16), N7A-Zn1-N2A 170.11(17), N5D-Zn1-N2A 85.95(14).....</p>	91
<p>38 Thermal ellipsoid plot of the cationic unit $[\{\text{Ni}_5(\text{bptz})_5(\text{CH}_3\text{CN})_{10}\}\text{C}\text{SbF}_6]^{9+}$ in 5•2CH₃CN. Thermal ellipsoids are represented at the 50% probability level. Selected bond distances (Å) and angles (°) are: Ni1-N7 2.078(7), Ni1-N3 2.085(7), Ni1-N16 2.039(7), Ni1-N17 2.058(9), Ni1-N4 2.067(6), Ni2-N19 2.026(9), Ni2-N18 2.057(7), Ni2-N13 2.068(7), Ni2-N6 2.055(6), N4-Ni1-N7 91.8(3), N3-Ni1-N7 89.1(3), N17-Ni1-N7 176.8(3), N4-Ni1-N3 78.8(3), N18-Ni2-N19 92.4(3), N6-Ni2-N18 98.5(3), N19-Ni2-N13 177.4(3), N6-Ni2-N13 86.4(3), N18-Ni2-N13 86.4(3).....</p>	93
<p>39 Ball and stick plot of the cationic unit $[\{\text{Ni}_4(\text{bptz})_4(\text{CH}_3\text{CN})_8\}\text{C}\text{I}]^{7+}$ in 7. Thermal ellipsoids are represented at the 50% probability level except for the C and N atoms of the bptz ligands, which are circles of arbitrary radii. Selected bond distances (Å) and angles (°): Ni-N8 2.021(7), Ni-N7 2.045(8), Ni-N6 2.067(7), Ni-N1 2.076(6), Ni-N3 2.105(7), Ni-N4 2.103(8), N8-Ni-N7 89.5(3), N8-Ni-N6 97.6(3), N7-Ni-N6 95.2(3), N8-Ni-N1 174.1(3), N7-Ni-N1 88.73(3), N6-Ni-N1 88.1(3), N8-Ni-N3 95.4(3), N7-Ni-N3 91.9(3), N6-Ni-N3 165.2(3), N1-Ni-N3 79.6(3), N8-Ni-N4 92.2(3), N7-Ni-N4 173.1(3), N6-Ni-N4 77.9(3), N1-Ni-N4 90.2(2), N3-Ni-N4 94.6(2).....</p>	94
<p>40 Packing diagram viewed along the <i>a</i>-axis of (A) $[\{\text{Ni}_4(\text{bptz})_4(\text{CH}_3\text{CN})_8\}\text{C}\text{I}]^{7+}$ cations and $[\text{SbF}_6]^-$ anions in compound 7 and (B) $[\{\text{Ni}_4(\text{bptz})_4(\text{CH}_3\text{CN})_8\}\text{C}\text{ClO}_4]^{7+}$ cations and $[\text{ClO}_4]^-$ anions in compound 2</p>	96

FIGURE

Page

- 41 Thermal ellipsoid plot of the cationic unit
 $\{[\{\text{Ni}_4(\text{bptz})_4(\text{CH}_3\text{CN})_8\}\subset\text{BF}_4][\text{PF}_6]\}^{6+}$ in **8**. Thermal ellipsoids are drawn at the 50% probability level. Selected bond distances (Å) and angles (°): Ni1-N8 2.008(15), Ni1-N1 2.055(11), Ni1-N7 2.068(13), Ni1-N4 2.095(10), Ni1-N6 2.088(11), Ni1-N3 2.096(11), P1-F2A 1.625(13), B1-F1 1.422(13), N8-Ni1-N1 173.2(4), N8-Ni1-N7 91.0(5), N1-Ni1-N7 86.9(5), N8-Ni1-N4 89.5(5), N1-Ni1-N4 93.3(5), N7-Ni1-N4 173.3(4), N1-Ni1-N6 87.8(5), N7-Ni1-N6 95.6(5), N4-Ni1-N6 77.8(4), N8-Ni1-N3 96.5(5), N1-Ni1-N3 77.1(5), N7-Ni1-N3 90.7(5), N4-Ni1-N3 95.8(4)..... 97
- 42 Thermal ellipsoid plot of the cationic unit
 $\{[\{\text{Ni}_4(\text{bptz})_4(\text{CH}_3\text{CN})_4(\text{H}_2\text{O})_4\}\subset\text{ClO}_4][\text{IO}_4]\}^{6+}$ in **9**•3CH₃CN. Thermal ellipsoids are represented at the 50% probability level. Selected bond distances (Å) and angles (°): Ni1-O2 2.035(13), Ni1-O1 2.031(12), Ni1-N1A 2.072(14), Ni1-N2A 2.067(14), Ni2-N1B 2.053(17), Ni2-N7A 2.08(2), Ni2-N2B 2.056(14), Ni2-N8A 2.067(16), Ni2-N6A 2.077(16), Ni2-N5A 2.103(13), O2-Ni1-O1 86.6(5), O2-Ni1-N1A 93.5(6), O1-Ni1-N1A 92.9(5), O2-Ni1-N2A 87.4(5), O1-Ni1-N2A 169.4(6), N1A-Ni1-N2A 78.7(5), N1B-Ni2-N7A 95.8(6), N1B-Ni2-N2B 78.6(6), N7A-Ni2-N2B 173.7(6), N1B-Ni2-N6A 163.6(6) 99
- 43 Thermal ellipsoid plot of the unit $[\{\text{Ni}_4(\text{bptz})_4(\text{CH}_3\text{CN})\text{Br}_7\}\subset\text{Br}_3]$ in **10**•2CH₃CN•2.5C₆H₅CH₃. Thermal ellipsoids are represented at the 50% probability level. Selected bond distances (Å) and angles (°): Br1-Br2 2.525(2), Br2-Br3 2.566(2), Ni1-N1A 2.097(10), Ni1-N6D 2.079(10), Ni1-N2A 2.092(10), Ni1-N5D 2.128(9), Ni1-Br1A 2.479(2), Ni1-Br2A 2.537(2), Br1-Br2-Br3 179.17(7), N1B-Ni2-N6A 161.1(4), N1A-Ni1-N2A 78.0(4), N6D-Ni1-N2A 89.1(4), N1A-Ni1-N5D 89.7(4), N6D-Ni1-N5D 77.6(4), N2A-Ni1-N5D 87.7(3), N1A-Ni1-Br1A 96.8(3), N6D-Ni1-Br1A 96.1(3), N2A-Ni1-Br1A 174.8(3), N1A-Ni1-Br2A 94.9(3), N6D-Ni1-Br2A 95.4(3), N2A-Ni1-Br2A 82.5(2), N5D-Ni1-Br2A 168.1(3), Br1A-Ni1-Br2A 97.59(7) 100

FIGURE	Page
44 Thermal ellipsoid plot of the cationic unit $[\text{Ni}_2(\text{bptz})(\text{CH}_3\text{CN})_8]^{4+}$ in 11 . Thermal ellipsoids are drawn at a 50% probability level. Selected bond distances (Å) and angles (°): Ni1-N1 2.067(7), Ni1-N2 2.078(6), Ni1-N4 2.072(6), Ni1-N5 2.078(7), Ni1-N6 2.075(7), Ni1-N7 2.045(7), N4-C7 1.131(8), N6-C11 1.145(9), N5-C9 1.153(9), N2-C6 1.294(9), C6-C5 1.497(10), C1-C2 1.375(10), C2-C3 1.335(11), C3-C4 1.384(11), N7-Ni1-N4 177.8(3), N1-Ni1-N5 171.7(2), C13-N7-Ni1 177.5(7), N4-Ni1-N5 86.1(2), N6-Ni1-N5 94.8(2), N2-Ni1-N5 95.0(2), N1-Ni1-N4 89.8(2), N7-Ni1-N6 90.2(2), N1-Ni1-N6 92.4(2), N4-Ni1-N6 88.6(2), N7-Ni1-N2 90.9(2), N1-Ni1-N2 77.8(2), N4-Ni1-N2 90.6(2).....	102
45 Thermal ellipsoid plot of the cationic repeat unit $[\text{Mn}_2(\text{bptz})_2(\text{CH}_3\text{CN})_4]^{4+}$ in the polymer 12 •1.5 <i>n</i> CH ₃ CN. Thermal ellipsoids are represented at the 50% probability level. Selected bond distances (Å) and angles (°): Mn1-N8 2.143(4), Mn1-N7 2.166(4), Mn1-N4 2.225(4), Mn1-N1 2.231(4), Mn1-N5 2.313(4), Mn1-N2 2.318(4), N4-C11 1.333(5), N4-C7 1.351(5), N3-N2 1.328(5), Mn1···Mn1' 7.327(1), N7-Mn1-N5 172.45(14), N4-Mn1-N5 71.18(13), N1-Mn1-N2 71.32(13), N5-Mn1-N2 94.54(12), N8-Mn1-N1 97.32(14), N7-Mn1-N1 99.20(14), N8-Mn1-N7 93.81(14), N8-Mn1-N4 108.67(14)	104
46 Space-filling representations of the cationic units $[\{\text{Ni}_5(\text{bptz})_5(\text{CH}_3\text{CN})_{10}\} \subset \text{SbF}_6]^{9+}$, $[\{\text{Ni}_4(\text{bptz})_4(\text{CH}_3\text{CN})_8\} \subset \text{ClO}_4]^{9+}$ or $[\{\text{Ni}_4(\text{bptz})_4(\text{CH}_3\text{CN})_8\} \subset \text{BF}_4]^{9+}$ and their scheme of interconversion	108
47 Schematic Diagram of how several compounds that can be synthesized starting with $[\text{Ni}_5(\text{bptz})_5(\text{CH}_3\text{CN})_{10} \subset \text{SbF}_6][\text{SbF}_6]_9$	113
48 Schematic drawing of 3,6-bis(2'-pyridyl)-1,2,4,5-tetrazine, or bppn	117
49 Thermal ellipsoid plot of a fragment of $\{[\text{Ag}(\text{bptz})][\text{PF}_6]\}_\infty$, (13), at the 50% probability level. Selected bond distances (Å) and angles (°): Ag1-N1 2.218(5), Ag1-N2 2.564(5), N2-Ag1-N1 69.9(2), N1-Ag1-N1' 180.0(2), N2-Ag1-N1', 110.1(2), N2-Ag1-N2' 180.0(2).....	133
50 Packing diagram of $\{[\text{Ag}(\text{bptz})][\text{PF}_6]\}_\infty$ along the bc plane with alternating chains in red and blue. The anions (shown in yellow) are clearly in close proximity to the central tetrazine rings of bptz	134

FIGURE	Page
51	(a) Packing diagram of $\{[\text{Ag}(\text{bptz})][\text{PF}_6]\}_\infty$ (1) depicting the shortest contacts between the $[\text{PF}_6]^-$ anions and the tetrazine rings. Shortest F \cdots centroid distance 2.840(5) Å; F \cdots tetrazine plane distances in the range 2.785-2.968 Å. (b) Tetrazine ring with two $[\text{PF}_6]^-$ anions in 1 , displaying the three F atoms involved in each anion- π interaction (dotted lines drawn to the ring centroid)..... 135
52	Thermal ellipsoid plot of $[\text{Ag}_2(\text{bptz})_2(\text{CH}_3\text{CN})_2][\text{PF}_6]_2$ (14) at the 50% probability level (one $[\text{PF}_6]^-$ ion has been omitted for clarity). The methyl carbon atom ellipsoids (C14) are depicted at the 25% probability level for the sake of clarity. Selected bond distances (Å) and angles (°): Ag1-N1 2.376(6), Ag1-N2 2.517(6), Ag1-N7 2.256(6), Ag1'-N6 2.342(6), Ag1-N3 2.580(6), N1-Ag1-N2 68.3(2), N7-Ag1-N1 108.3(2), N7-Ag1-N2 94.7(2), N6-Ag1'-N3 67.0(3)..... 137
53	Thermal ellipsoid plot of $[\text{Ag}_2(\text{bptz})_2(\text{CH}_3\text{CN})_2][\text{AsF}_6]_2$ (15) at the 50% probability level. The methyl carbon ellipsoids are shown at the 25% probability level for the sake of clarity. Selected bond distances (Å) and angles (°): Ag1-N2 2.524(4), Ag1-N3 2.376(4), Ag1-N4 2.341(4), Ag1-N5 2.567(4), Ag1-N7, 2.268(4), N7-Ag1-N4 118.4(1), N7-Ag1-N3 105.4(2), N7-Ag1-N2 95.3(1), N4-Ag1-N5 67.31(13), N4-Ag1-N2 143.53(1), N3-Ag1-N2 68.4(4), N7-Ag1-N5 99.4(1), N2-Ag1-N5 95.2(1)..... 138
54	Packing diagram of $[\text{Ag}_2(\text{bptz})_2(\text{CH}_3\text{CN})_2][\text{PF}_6]_2$ (14) in the <i>bc</i> plane 139
55	(a) Fragment of the cation/anion arrangements in $[\text{Ag}_2(\text{bptz})_2(\text{CH}_3\text{CN})_2][\text{PF}_6]_2$ (14) depicting the shortest contacts between the $[\text{PF}_6]^-$ anions and the tetrazine rings. Shortest F \cdots tetrazine centroid distances (Å): centroid 1-F2 2.806(7), centroid 2-F5 2.835(7); F \cdots tetrazine plane distances in the range 2.791-3.045 Å. (b) Fragment of the structure of $[\text{Ag}_2(\text{bptz})_2(\text{CH}_3\text{CN})_2][\text{AsF}_6]_2$ (15) depicting the shortest contacts between the $[\text{AsF}_6]^-$ anions and the tetrazine rings. Shortest F \cdots tetrazine centroid distances (Å): centroid 1-F3A 2.838(6), centroid 2-F6A 2.784(6) Å; F \cdots tetrazine ring plane distances in the range 2.758-3.142 Å..... 140

FIGURE	Page
56	Thermal ellipsoid plot of the cationic unit $[\text{Ag}_2(\text{bptz})_3]^{2+}$ in 16 at the 50% probability level. Selected bond distances (Å) and angles (°): Ag1-N1 2.426(3), Ag1-N2 2.516(3), Ag1-N7 2.418(3), Ag1-N8 2.571(3), Ag1-N13 2.500(3), Ag2-N9 2.439(3), Ag2-N12 2.561(3), Ag2-N16 2.391(3), Ag2-N6 2.420(3), Ag2-N3 2.500(3), N1-Ag1-N2 66.77(10), N1-Ag1-N7 95.60(10), N8-Ag1-N7 66.92(9), N13-Ag1-N2 130.43(9), N9-Ag2-N12 66.67(9), N12-Ag2-N16 93.57(9), N3-Ag2-N16 140.14(9), N6-Ag2-N16 105.07(10) 142
57	Thermal ellipsoid plot of $[\text{Ag}_2(\text{bptz})_3][\text{SbF}_6]_2$ (17a) at the 50% probability level (one $[\text{SbF}_6]^-$ ion has been omitted for clarity). Selected bond distances (Å) and angles (°): Ag1-N1 2.451(9), Ag1-N2 2.487(9), Ag1-N4 2.491(9), Ag1-N5 2.509(8), Ag1-N7 2.41(1), Ag1-N8 2.543(9), N1-Ag1-N2 68.9(3), N2-Ag1-N8 88.5(3), N7-Ag1-N8 66.5(3), N5-Ag1-N7 118.1(3), N4-Ag1-N7 95.2(3), N1-Ag1-N4 93.7(3), N4-Ag1-N5 66.3(3) 143
58	(a) Packing diagram of $[\text{Ag}_2(\text{bptz})_3][\text{AsF}_6]_2$ (16) in the <i>ab</i> plane. (b) Packing diagram of $[\text{Ag}_2(\text{bptz})_3][\text{SbF}_6]_2$ (17a) depicting the π - π intermolecular interactions between pyridyl rings of bptz ligands from different propeller-type units 144
59	(a) Fragment of the $[\text{Ag}_2(\text{bptz})_3][\text{AsF}_6]_2$ (16) structure depicting the shortest contacts between the $[\text{AsF}_6]^-$ anions and the tetrazine rings. Shortest F...tetrazine centroid distances (Å): centroid 1-F12 2.948(2), centroid 2-F5 2.941(3), centroid 3-F5 2.965(3), centroid 3-F12 2.913(2), centroid 4-F8 3.029(2), centroid 5-F6 3.038(3) Å; F...tetrazine ring plane distances in the range 2.783-3.116 Å. (b) Fragment of the $[\text{Ag}_2(\text{bptz})_3][\text{SbF}_6]_2$ (17a) structure depicting the shortest contacts between the $[\text{SbF}_6]^-$ anions and the tetrazine rings. Shortest F...tetrazine centroid distances (Å): centroid 1-F4 2.927(9), centroid 2-F4 2.913(6), centroids 2 and 3-F3 2.952(6); F...tetrazine plane distances in the range 2.743-3.004 Å. (c) Tetrazine ring with two $[\text{SbF}_6]^-$ anions in 17a , displaying the three F atoms involved in each anion- π interaction (dotted lines drawn to the ring centroid) 145

FIGURE	Page
60	Thermal ellipsoid plot of $[\text{Ag}_2(\text{bptz})_3][\text{SbF}_6]_2$ (17b) at the 50% probability level. Selected bond distances (Å) and angles (°): Ag1-N1 2.438(3), Ag1-N2 2.554(3), Ag2-N3 2.575(3), Ag2-N6 2.434(3), N1-Ag1-N2 67.41(9), N3-Ag2-N6 66.19(9) 147
61	(a) Packing diagram of $[\text{Ag}_2(\text{bptz})_3][\text{SbF}_6]_2$ (17b) along the <i>c</i> axis; and (b), view perpendicular to the <i>c</i> axis 148
62	Anion- π interactions between a $[\text{SbF}_6]^-$ anion and six tetrazine rings in $[\text{Ag}_2(\text{bptz})_3][\text{SbF}_6]_2$ (17b). The F-centroid distance is 3.265(3) Å (red dash lines); F-tetrazine plane distance 2.844 Å. The π - π contacts (3.36 Å) are indicated with purple dash lines 149
63	Thermal ellipsoid plot of the cationic unit $[\text{Ag}_4(\text{bppn})_4]^{4+}$ in 18 at the 50% probability level. Selected bond distances (Å) and angles (°): Ag1-N1 2.319(5), Ag1-N2 2.222(4); Ag2-N3 2.369(4), Ag2-N4 2.272(4), Ag2-N5 2.288(5), Ag2-N6, 2.338(4), Ag3-N7 2.284(4), Ag3-N8 2.305(4), N1-Ag1-N2 72.5(2), N3-Ag2-N4 70.7(2), N4-Ag2-N6 129.1(1), N6-Ag2-N5 71.2(2), N5-Ag2-N3 117.7(1), N7-Ag3-N8 72.2(2) 151
64	Thermal ellipsoid plot of the cationic unit $\{[\text{Ag}_4(\text{bppn})_4][\text{AsF}_6]_2\}^{2+}$ in 19 at the 50% probability level. Selected bond distances (Å) and angles (°): N1-Ag1 2.331(3), N2-Ag1 2.225(3), N5-Ag2 2.295(3), N6-Ag1 2.338(3), N4-Ag2 2.273(3), N3-Ag2 2.370(3), N7-Ag3 2.293(3), N8-Ag3 2.303(3), N8-Ag3-N7 70.7(1), N6-Ag2-N5 71.3(1), N1-Ag1-N2 72.2(1), N3-Ag2-N4 70.6(1) 152
65	Thermal ellipsoid plot of the cation $\{[\text{Ag}_4(\text{bppn})_4][\text{SbF}_6]_2\}^{2+}$ in 20 at the 50% probability level. Selected bond distances (Å) and angles (°): N1-Ag1 2.298(4), N2-Ag1 2.325(4), N5-Ag1 2.281(4), N6-Ag1 2.364(4), N3-Ag2 2.294(4), N4-Ag2 2.308(4), N8-Ag3 2.334(4), N7-Ag3 2.230(4), N8-Ag3-N7 72.0(2), N5-Ag1-N6 70.8(1), N1-Ag1-N2 71.1(2), N2-Ag1-N5 130.3(2), N3-Ag2-N4 71.7(2) 153

FIGURE	Page	
66	(a) Grid-type structure of $[\text{Ag}_4(\text{bppn})_4][\text{PF}_6]_4$ (18) depicting the π - π (3.38 Å; purple dashed lines) and anion- π interactions (red dashed lines); the F \cdots pyridazine ring plane distances are in the range 2.902-3.181 Å; shortest F \cdots tetrazine ring centroid distances (Å): centroids 1 and 4-F8A 3.095(6) and centroids 2 and 3-F4A 3.336(4). (b) Space-filling representation of 18 . (c) Pyridazine ring with one $[\text{PF}_6]^-$ anion in 18 , displaying the three F atoms involved in each anion- π interaction (dotted lines drawn to the ring centroid).....	154
67	Packing diagram of 6 in the <i>ab</i> plane. Solvent molecules have been omitted for the purpose of clarity.....	155
68	Thermal ellipsoid plot of $[\text{Ag}_4(\text{bppn})_4][\text{BF}_4]_4$ (21) at the 50% probability level. Selected bond distances (Å) and angles (°): Ag2-N3 2.284(5), Ag2-N6 2.290(5), Ag2-N4 2.355(5), Ag2-N5 2.360(5), N3-Ag2-N4 70.9(2), N6-Ag2-N5 70.5(2), N3-Ag2-N6 138.4(2), N6-Ag2-N4 138.9(2), N3-Ag2-N5 141.0(2), N4-Ag2-N5 104.4(2).....	157
69	Aromatic region of the ^1H NMR spectrum of $[\text{Ag}_2(\text{bptz})_3][\text{AsF}_6]_2$ (16) in $\text{CD}_3\text{CN}-d_3$	159
70	ESI-MS spectrum of $\text{Ag}_2(\text{bptz})_3[\text{AsF}_6]_2$ (16).....	160
71	Aromatic region of the ^1H NMR spectrum of (a) <i>bppn</i> , and (b) $[\text{Ag}_4(\text{bppn})_4][\text{AsF}_6]_4$ (20) in $\text{CD}_3\text{NO}_2-d_3$	163
72	B3LYP/6-311+G(d,p) geometry optimization and electrostatic potential maps for (a) <i>bptz</i> in the <i>anti</i> orientation, (b) <i>bppn</i> in the <i>anti</i> orientation, (c) <i>bptz</i> in the <i>syn</i> orientation, and (d) <i>bppn</i> in the <i>syn</i> orientation (the dihedral angle defined by the atoms labeled with red numbers is -85.9°). The maps were generated with Cerius ² 4.8 (Accelrys, Inc.) at a 0.02 isodensity value and a color scale of 126 (blue) to -63 (red) kcal/mol.....	165

FIGURE	Page
73	BP86/TZP geometry optimization and electrostatic potential maps for (a) bptz in the <i>anti</i> orientation, (b) bppn in the <i>anti</i> orientation, (c) bptz in the <i>syn</i> orientation, and (d) bppn in the <i>syn</i> orientation (the dihedral angle defined by the atoms labeled with red numbers is -84.6°). The maps were generated with the ADFView interface at a 0.02 isodensity value and a color scale of 126 (blue) to -63 (red) kcal/mol 166
74	Electrostatic potential map from the BP86/TZP SPE calculations of 3 for (a) doubly charged cation $[\text{Ag}_2(\text{bptz})_2(\text{CH}_3\text{CN})_2]^{2+}$ with a color scale of 220 (blue) to -31 (red) kcal/mol, and (b) neutral complex $[\text{Ag}_2(\text{bptz})_2(\text{CH}_3\text{CN})_2][\text{AsF}_6]_2$ with a color scale of 126 (blue) to -126 (red) kcal/mol. The maps were generated with ADFView at a 0.02 isodensity value 168
75	Electrostatic potential map from the BP86/TZP SPE calculations for the singly charged cation $\{[\text{Ag}_2(\text{bptz})_2(\text{CH}_3\text{CN})_2][\text{AsF}_6]\}^+$ of 15 with a color scale of 188 (blue) to -31 (red) kcal/mol. The maps were generated with ADFView at a 0.02 isodensity value 171
76	Electrostatic potential map from the BP86/TZP SPE for 17b (a) doubly charged $[\text{Ag}_2(\text{bptz})_3]^{2+}$ with a color scale of 220 (blue) to -31 (red) kcal/mol, and (b) singly charged cation $\{[\text{Ag}_2(\text{bptz})_3][\text{SbF}_6]\}^+$ with a color scale of 188 (blue) to -31 (red) kcal/mol. The maps were generated with ADFView at a 0.02 isodensity value 173
77	Electrostatic potential map from the BP86/TZP SPE calculations for 16 (a) doubly charged cation $[\text{Ag}_2(\text{bptz})_3]^{2+}$ with a color scale of 200 (blue) to -31 (red) kcal/mol, and (b) neutral complex $[\text{Ag}_2(\text{bptz})_3][\text{AsF}_6]_2$ with a color scale of 126 (blue) to -94 (red) kcal/mol. The maps were generated with ADFView at a 0.02 isodensity value 174
78	Electrostatic potential map from the BP86/TZP SPE calculations of 19 for (a) cationic unit $[\text{Ag}_4(\text{bppn})_4]^{4+}$ with a color scale of 314 (blue) to -126 (red) kcal/mol, and (b) neutral complex $[\text{Ag}_4(\text{bppn})_4][\text{AsF}_6]_4$ with a color scale of 157 (blue) to -63 (red) kcal/mol. The maps were generated with ADFView at a 0.02 isodensity value 177

FIGURE	Page	
79	Geometry-optimized MP2/6-31++G(d',p') results of the C ₄ N ₂ X ₄ , C ₃ N ₃ X ₃ , and C ₂ N ₄ X ₂ systems along with each rings' ESP map. The ESP maps are shown at an isodensity value of 0.02 with a color range of -40.66 kcal/mol (red) – 133.46 kcal/mol (blue). Atom colors are as follows: Carbon =gray, hydrodgen = white, nitrogen = blue, fluorine = green, chlorine = yellow, and bromine = red. Theoretical bond distances (Å) and angles (°) are shown in black and red, respectively.....	195
80	Geometry-optimized B3LYP/6-31++G(d',p') results of the C ₄ N ₂ X ₄ , C ₃ N ₃ X ₃ , and C ₂ N ₄ X ₂ systems along with each rings' ESP map. The ESP maps are shown at an isodensity value of 0.02 with a color range of -40.66 kcal/mol (red) – 133.46 kcal/mol (blue). Atom colors are as follows: Carbon =gray, hydrogen = white, nitrogen = blue, fluorine = green, chlorine = yellow, and bromine = red. Theoretical bond distances (Å) and angles (°) are shown in black and red, respectively .	196
81	Geometry optimization results of the C ₃ N ₃ X ₃ ring systems with [BF ₄] ⁻ computed by the 6-31++G(d',p') basis set at both the MP2 and B3LYP levels of theory. Colors: C = grey, N = blue, B = pink, F = green, Cl = yellow, and Br = red.....	198
82	Geometry optimization results of the C ₃ N ₃ X ₃ ring systems with [PF ₆] ⁻ computed by the 6-31++G(d',p') basis set at both the MP2 and B3LYP levels of theory. Colors: C = grey, N = blue, P = purple, F = green, Cl = yellow, and Br = red.....	199
83	Line diagrams of generic C ₃ N ₃ X ₃ rings with [BF ₄] ⁻ and [PF ₆] ⁻ that assign labels to the values given in Tables 9 and 10. Bond labels are red, and atom labels are blue.....	200
84	Examples of the AIM critical point analyses of C ₃ N ₃ X ₃ systems for both the MP2 and B3LYP/6-31++G(d',p') wavefunctions. The top row displays entire complexes from the side, the middle row shows these same complexes from the top, and the bottom row has the same view with the anion removed. The numbers assigned to the critical points are labels for the values used in Table 11. Atom colors: C = grey, N = blue, B = pink, P = purple, F = green. Critical point colors: (3,-1) = red, (3,+1) = yellow, (3,+3) = orange.....	206

FIGURE	Page
85	Geometry optimization results of the $C_2N_4X_2$ ring systems with $[BF_4]^-$ computed by the 6-31++G(d',p') basis set at both the MP2 and B3LYP levels of theory. Colors: C = grey, N = blue, P = purple, F = green, Cl = yellow, and Br = red..... 209
86	Geometry optimization results of the $C_2N_4X_2$ ring systems with $[PF_6]^-$ computed by the 6-31++G(d',d') basis set at both the MP2 and B3LYP levels of theory. Colors: C = grey, N = blue, P = purple, F = green, Cl = yellow, and Br = red..... 210
87	Line drawings of generic $[BF_4]^-$ and $[PF_6]^-$ anion + $C_2N_4X_2$ ring systems. The atom numbers are labeled in blue, and the bonds are labeled in red. These designations correspond to the values in Tables 12 and 13..... 211
88	Examples of the AIM critical point analyses of $C_2N_4F_2$ systems for both the MP2 and B3LYP/6-31++G(d',d') wavefunctions. The top row displays entire complexes from the side, the middle row shows these same complexes from the top, and the bottom row has the same view with the anion removed. The numbers assigned to the critical points are labels for the values used in Table 14. Atom colors: C = grey, N = blue, B = pink, P = purple, F = green. Critical point colors: (3,-1) = red, (3,+1) = yellow, (3,+3) = orange. The numerical label for the orange (3,+3) cage point is orange 215
89	Geometry optimization results of the $C_4N_2X_4$ ring systems with $[BF_4]^-$ computed by the 6-31++G(d',d') basis set at both the MP2 and B3LYP levels of theory. Colors: C = grey, N = blue, P = purple, F = green, Cl = yellow, and Br = red 220
90	Geometry optimization results of the $C_4N_2X_4$ ring systems with $[PF_6]^-$ computed by the 6-31++G(d',d') basis set at both the MP2 and B3LYP levels of theory. Colors: C = grey, N = blue, P = purple, F = green, Cl = yellow, and Br = red..... 221
91	Generic line drawing of $[BF_4]^-$ paired with a $C_4N_2X_4$ ring. The bond labels (red) and atom labels (blue) correspond to the values listed in Tables 15 and 17 222
92	AIM calculated bond paths for complexes of $C_4N_2X_4$ (X = F or CN) from the B3LYP/6-31++G(d',p') computation results. Colors: Gray = C, blue = N, gold = F, pink = B, and (3,-1) CPs are red 226

FIGURE	Page
93	Example of the AIM critical point analysis results of $C_4N_2F_4 + [BF_4]^-$ systems for the B3LYP/6-31++G(d',p') wavefunction. The top row displays the entire complex from the side, the middle row shows the same complex from the top, and the bottom row depicts the same view with the anion removed. The numbers assigned to the critical points are labels for the values used in Table 16. Atom colors: C = grey, N = blue, B = pink, , F = green. Critical point colors: (3,-1) = red, (3,+1) = yellow, (3,+3) = orange 227
94	AIM calculated ring bond paths for the MP2/6-31++G(d',p') geometry optimization results of $[BF_4]^-$ complexed with (a) $C_4N_2F_4$ and (b) $C_4N_2(CN)_4$. Colors: C = grey, N = blue, F = gold, B = light blue, and the (3,-1) CPs are red..... 230
95	Examples of the AIM critical point analysis results of $C_4N_2F_4 + [BF_4]^-$ systems for the MP2/6-31++G(d',p') wavefunction. The top row displays the entire complex from the side, the middle row shows the same complex from the top, and the bottom row depicts the same view with the anion removed. The numbers assigned to the critical points are labels for the values used in Table 18. Atom colors: C = grey, N = dark blue, B = light blue, F = green. Critical point colors: (3,-1) = red, (3,+1) = yellow, (3,+3) = orange 231
96	Generic line drawing of $[PF_6]^-$ paired with a $C_4N_2X_4$ ring. The bond labels (red) and atom labels (blue) correspond to the values listed in Tables 19 and 21 235
97	AIM calculated bond paths for the MP2/6-31++G(d',p') optimized geometries of $[PF_6]^-$ interacting with (a) $C_4N_2F_4$ and (b) $C_4N_2(CN)_4$. Colors: Grey = c, dark blue = N, gold = F, dark red = P, and red = (3,+1) critical points 236
98	Example of the AIM critical point analysis results of the $C_4N_2F_4 + [PF_6]^-$ system the MP2/6-31++G(d',p') wavefunction. The top row displays the complex from the side, the middle row shows the same complex from the top, and the bottom row depicts the same view with the anion removed. The numbers assigned to the critical points are labels for the values used in Table 20. Atom colors: C = grey, N = blue, P = purple, F = green. Critical point colors: (3,-1) = red, (3,+1) = yellow, (3,+3) = orange..... 239

FIGURE	Page
99	AIM calculated bond paths for the B3LYP/6-31++G(d',p') optimized geometries of [PF ₆] ⁻ interacting with (a) C ₄ N ₂ F ₄ and (b) C ₄ N ₂ (CN) ₄ . Colors: Grey = C, dark blue = N, gold = F, dark red = P, and red = (3,+1) critical points 241
100	Examples of the AIM critical point analysis results of C ₄ N ₂ X ₄ + [PF ₆] ⁻ systems (X = F or CN) for the B3LYP/6-31++G(d',p') wavefunctions. The top row displays the complexes from the side, the middle row shows the same complexes from the top, and the bottom row depicts the same view with the anion removed. The numbers assigned to the critical points are labels for the values used in Table 22. Atom colors: C = grey, N = blue, P = purple, F = green. Critical point colors: (3,-1) = red, (3,+1) = yellow, (3,+3) = orange 243
101	(a) Compound 1 with both encapsulated [BF ₄] ⁻ disorder positions shown, (b) Compound 1 with one [BF ₄] ⁻ disorder position shown with the anion- π contacts between the anion and the tetrazine ring diagrammed with red dashed lines, (anion- π contacts = 2.709-2.971 Å), and (c) Compound 1 with the second [BF ₄] ⁻ disorder position shown with the anion- π contacts between the anion and the tetrazine ring diagrammed with yellow dashed lines, (anion- π contacts = 2.799-3.017 Å) 251
102	(a) Truncated packing diagram of compound 16 , (b) close-up view of two bptz tetrazine rings interaction with one anion (anion- π contacts shown with red dashed lines) drawn from the F anion atoms to the centroids of the tetrazine rings (F- centroid distances = 3.656, 4.280, 2.785, 2.840, 3.956, and 4.121 Å), and (b) a corrected version of the anion- π contacts between the same two rings (F-C distances = 3.138, 2.976, 3.122, and 3.553 Å) 252

FIGURE	Page
103	(a) Packing diagram of compound 17b with anion- π contacts (red dashed lines) drawn from the F anion atoms to the centroids of the tetrazine rings (distance = 3.269 Å), and (b) corrected packing diagram of compound 17b with the anion- π contacts drawn from the anion F atoms to a carbon atom on the bptz tetrazine rings (distance = 3.249 Å). The carbon atoms that are in participating in anion- π contact are shown at a larger scale, and the centroids of the tetrazine rings are indicated with orange spheres..... 254
104	(a) Truncated packing diagram of compound 18 showing the corrected anion- π contacts (red dashed lines) and the multiple hydrogen bond interactions (yellow dashed lines) between the [PF ₆] ⁻ anions and the bppn ligands as well as the hydrogen bond interactions between the anions and nitromethane molecules (yellow dashed lines) in the crystal interstices. (b) Original (incorrect) anion- π contacts speculated in Chapter III for compound 17 from the [PF ₆] ⁻ fluorine atoms to the ring centroid (distances = 2.902-3.181 Å), and (c) corrected F-ring anion- π contacts from compound 17 (anion- π distances = 2.991 and 3.161 Å and 3.124 and 3.240 Å for the two unique [PF ₆] ⁻ anions, respectively)..... 255

LIST OF TABLES

TABLE	Page
1	The accepted supramolecular interactions and their relative strengths..... 2
2	MIPp numerical breakdown of the total interaction energy (E_t) into its constituent components (kcal/mol)..... 8
3	MIPp numerical breakdown of the total interaction energy (E_t) into its constituent components (kcal/mol) for the $[\text{Na}]^+$ -benzene complex interacting with $[\text{F}]^-$ at selected distances 11
4	Binding energies (kcal/mol) with (E_{cp}) and without (E) the (BSSE) correction and equilibrium Distances (R_e , Å) at several levels of theory for Complexes 1-12 24
5	Interaction energies (E), all in kcal/mol with and without the basis set superposition error (BSSE) and zero point energy (ZPE) corrections and equilibrium distances (R_e , Å) at the MP2/6-311++G** level of theory 33
6	Crystal and structural refinement data for 1 •4CH ₃ CN, 2 •4CH ₃ CN•C ₄ H ₈ O, 3 •4CH ₃ CN, 5 •2CH ₃ CN, 7 , 8 , 9 •3CH ₃ CN, 10 •2CH ₃ CN•2.5C ₆ H ₅ CH ₃ , 11 , and 12 •1.5 <i>n</i> CH ₃ CN..... 57
7	Crystal and structural refinement data for 13 , 14 , 15 , 16 •2CH ₃ CN, 17a •2CH ₃ CN, 17b , 18 •4CH ₃ NO ₂ , 19 •4CH ₃ NO ₂ , 20 •4CH ₃ NO ₂ and 21 •3CH ₃ NO ₂ •C ₆ H ₆ 125
8	Anion- π and π - π Distances for the Central Rings in Compounds 13-21 185
9	MP26-31++G(d') bond distances and binding energies (E_t) for the C ₃ N ₃ F ₃ complexes with $[\text{BF}_4]^-$ and $[\text{PF}_6]^-$ 201
10	B3LYP/6-31++G(d',p') bond distances and binding energies (E_t) for the C ₃ N ₃ F ₃ complexes with $[\text{BF}_4]^-$ and $[\text{PF}_6]^-$ 202
11	Critical point ρ values ($e^-/\text{a.u.}^3$) recorded for the C ₃ N ₃ X ₃ (X= F or CN) systems at both the MP2 and B3LYP Levels of Theory 207

TABLE	Page
12	MP2/6-31++G(d',p') geometry optimization results of C ₂ N ₄ X ₂ ring systems with the [BF ₄] ⁻ and [PF ₆] ⁻ anions, and the interaction energies (<i>E_t</i>) resulting from these geometries 212
13	B3LYP/6-31++G(d') geometry optimization results of C ₂ N ₄ X ₂ ring systems with the [BF ₄] ⁻ and [PF ₆] ⁻ anions, and the interaction energies (<i>E_t</i>) resulting from these geometries..... 213
14	Critical point ρ values (<i>e⁻/α_s³</i>) recorded for the C ₂ N ₄ X ₂ (X = F or CN) systems at both the MP2 and B3LYP Levels of Theory 216
15	Bond distances, anion-π contact distances and binding energies (<i>E_t</i>) for the B3LYP/6-31+G(d',p') geometry results of C ₄ N ₂ X ₄ with [BF ₄] ⁻ 223
16	AIM critical point ρ values (<i>e⁻/α_s³</i>) obtained from the B3LYP/6-31++G(d',p') geometry optimization results of the C ₄ N ₂ X ₄ rings with [BF ₄] ⁻ (X = F or CN)..... 228
17	Bond distances and anion-π contact distances and binding energies (<i>E_t</i>) for the MP2/6-31++G(d',p) geometry results of C ₄ N ₂ X ₄ with [BF ₄] ⁻ 229
18	AIM critical point ρ values (<i>e⁻/α_s³</i>) obtained from the MP2/6-31++G(d',p') geometry optimization results of the C ₄ N ₂ X ₄ rings with [BF ₄] ⁻ (X = F or CN)..... 232
19	Bond distances and anion-π contact distances and binding energies (<i>E_t</i>) for the MP2/6-31++G(d',p') geometry results of C ₄ N ₂ X ₄ with [PF ₆] ⁻ 238
20	AIM critical point ρ values (<i>e⁻/α_s³</i>) obtained from the MP2/6-31++G(d',p') geometry optimization results of the C ₄ N ₂ X ₄ rings with [PF ₆] ⁻ (X = F or CN) 240
21	Bond distances and anion-π contact distances and binding energies (<i>E_t</i>) for the B3LYP/6-31+G(d') geometry results of C ₄ N ₂ X ₄ with [PF ₆] ⁻ 242
22	AIM determined important critical point ρ values (<i>e⁻/α_s³</i>) for the C ₄ N ₂ X ₄ + [PF ₆] ⁻ (X = F or CN) complexes from the B3LYP/6-31++G(d',p') geometry optimizations..... 244

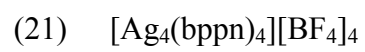
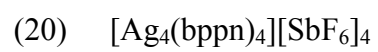
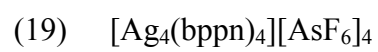
LIST OF SYMBOLS AND ABBREVIATIONS

ADF	Amsterdam density functional theory
AIM	Atoms in Molecules
Å	angstrom
(α_0)	Bohr radius
bppn	3,6-bis(2'-pyridyl)-1,2-pyridazine
bptz	3,6-bis(2'-pyridyl)-1,2,4,5-tetrazine
BSSE	basis set superposition error
cal	calorie
CP	critical point
°	degree
DFT	density functional theory
e ⁻	electron
g	gram
K	Kelvin
k	kilo
m/z	mass to charge ratio
mg	milligram
mL	milliliter
mmol	millimole
mol	mole

MP2	Møllar-Plessant 2
ρ	density
UV	ultraviolet
vis	visible
ZPE	zero point energy correction

LIST OF COMPOUNDS

- (1) $[\{\text{Ni}_4(\text{bptz})_4(\text{CH}_3\text{CN})_8\} \subset \text{BF}_4][\text{BF}_4]_7 \cdot 4\text{CH}_3\text{CN}$
- (2) $[\{\text{Ni}_4(\text{bptz})_4(\text{CH}_3\text{CN})_8\} \subset \text{ClO}_4][\text{ClO}_4]_7 \cdot$
- (3) $[\{\text{Zn}_4(\text{bptz})_4(\text{CH}_3\text{CN})_8\} \subset \text{BF}_4][\text{BF}_4]_7$
- (4) $[\{\text{Zn}_4(\text{bptz})_4(\text{CH}_3\text{CN})_8\} \subset \text{ClO}_4][\text{ClO}_4]_7$
- (5) $[\{\text{Ni}_5(\text{bptz})_5(\text{CH}_3\text{CN})_{10}\} \subset \text{SbF}_6][\text{SbF}_6]_9$
- (6) $[\text{Ni}_3(\text{bptz})_3][\text{NO}_3]_6$
- (7) $[\text{Ni}_4(\text{bptz})_4(\text{CH}_3\text{CN})_8][\text{SbF}_6]_7[\text{I}]$
- (8) $[\text{Ni}_4(\text{bptz})_4(\text{CH}_3\text{CN})_8][\text{BF}_4][\text{PF}_6][\text{SbF}_6]_6$
- (9) $[\text{Ni}_4(\text{bptz})_4(\text{CH}_3\text{CN})_4(\text{H}_2\text{O})_4][\text{ClO}_4][\text{IO}_4]_7$
- (10) $[\text{Ni}_4(\text{bptz})_4\text{Br}_7(\text{CH}_3\text{CN})\text{Br}_3]$
- (11) $[\text{Ni}_2(\text{bptz})(\text{CH}_3\text{CN})_8][\text{ClO}_4]_4$
- (12) $\{[\text{Mn}(\text{bptz})(\text{CH}_3\text{CN})_2][\text{BF}_4]_2\}_\infty$
- (13) $\{[\text{Ag}(\text{bptz})][\text{PF}_6]\}_\infty$
- (14) $[\text{Ag}_2(\text{bptz})_2(\text{CH}_3\text{CN})_2][\text{PF}_6]_2$
- (15) $[\text{Ag}_2(\text{bptz})_2(\text{CH}_3\text{CN})_2][\text{AsF}_6]_2$
- (16) $[\text{Ag}_2(\text{bptz})_3][\text{AsF}_6]_2$ (16).
- (17a) $[\text{Ag}_2(\text{bptz})_3][\text{SbF}_6]_2$
- (17b) $[\text{Ag}_2(\text{bptz})_3][\text{SbF}_6]_2$
- (18) $[\text{Ag}_4(\text{bppn})_4][\text{PF}_6]_4$



CHAPTER I

INTRODUCTION TO ANION- π INTERACTIONS

I. Background and Introduction

Supramolecular chemistry, the chemistry of the non-covalent bond, is an important interdisciplinary topic of relevance to research in biology, physics, and engineering. The field is constantly evolving as new concepts are being developed and accepted as part of the spectrum of supramolecular self-assembly processes. In this dissertation, a new type of supramolecular interaction, namely the anion- π interaction, is investigated, and the existence of such an interaction is probed by structural and computational methods.

The classifications and strength ranges of accepted supramolecular interactions are listed in Table 1 (for comparison, a carbon-carbon covalent bond is 346 kJ/mol). Those on the weaker end of the range (weak coordination bonds, hydrogen bonds, etc.) are more representative of supramolecular interactions.

A. Supramolecular Chemistry of Anions

Due to the relatively infant nature of this topic, a brief introduction into the supramolecular chemistry of anions is followed by a thorough literature review of anion- π research from the last five years. Of the commonly recognized supramolecular interactions listed in Table 1, one omission is an interaction specifically involving anions.

Table 1: The accepted supramolecular interactions and their relative strengths.¹

Interaction	Strength Range	Example
Ion-ion	100-350 kJ/mol	NaCl
Ion-dipole	20-200 kJ/mol	Coordination Bonds
Dipole-dipole	5-50 kJ/mol	SO ₂ + SO ₂
Hydrogen bonding	4-120 kJ/mol	Water
Cation- π interactions	5-80 kJ/mol	Na ⁺ channels
π - π stacking	0-50 kJ/mol	benzene crystal structure
van der Waals forces	< 5 kJ/mol	crystal close packing/charge balance
Hydrophobic Effects	No measurement	oil and water

Secondary interactions including anions have been much less investigated (until recently) than cations despite the fact that the first example of such interactions was reported at the nascence of supramolecular chemistry.² In 1967, a report by C. H. Park and H. E. Simmons involving supramolecular interactions with anions introduced a new halide-encapsulating molecule dubbed a katapinand.³ The first of these was the diammonium katapinand shown in Figure 1a. The authors postulated that hydrogen bonds held the chloride in place, a hypothesis that was confirmed in the mid 1970's by an X-ray crystallographic study.⁴ Later, Hawthorne and coworkers published the first example of an anion template based on the incorporation of [Cl]⁻ anions in the cavity of a mercurocarborand with ion-ion interactions (Figure 1b).⁵ More recently, studies reporting how specific anions are involved in structure formation have become quite common. For example, the independent works of Kristen Bowman James⁶ and Jonathan Steed⁷ stand out in the recent literature as excellent examples of research in this area. Also, a thorough description of this topic is given in the recent review by Ramon Vilar on anion template chemistry.⁸

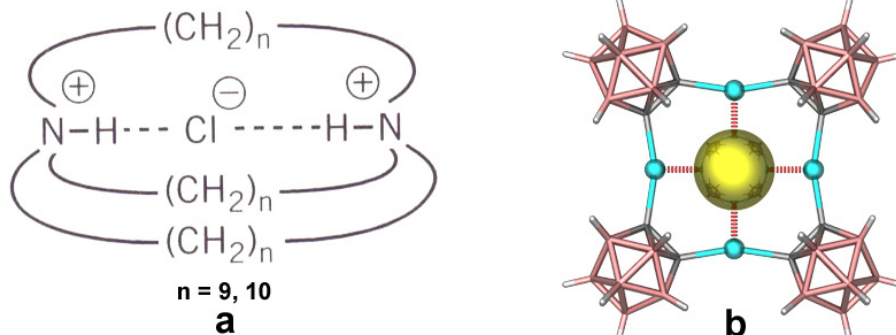


Figure 1: (a) Line diagram of the original katipinate structure encapsulating $[\text{Cl}]^-$, and (b) the first reported metal-based anion host. Mercury is blue, carbon is gray, boron is pink, hydrogen is white, and chlorine is yellow.

Several key factors that relate to the inherent nature of anions explain why they have been less commonly explored in supramolecular chemistry.⁸ Anions have high energies of solvation ($\Delta G_{\text{hydration}}$: $[\text{F}]^- = -465 \text{ kJ/mol}$ vs. $[\text{K}]^+ = -295 \text{ kJ/mol}$)¹ which means that the energy cost for a host to remove an anion from its solvated shell is much greater, particularly in protic solvents.⁹ The larger size of anions and the fact that they are “electronically saturated” also contributes to their lower probability for becoming directly involved in self-assembly processes. The wide range of geometrical shapes that anions exhibit, including spherical, linear, tetrahedral, octahedral, *etc.*, while originally regarded as another problematic trait, is now considered to be a distinct advantage when using anions in the context of supramolecular chemistry. By exploiting both size and shape, it is feasible to design anion hosts and specific interactions by using directionality and size to select one anion over another.¹⁰

B. Anions as Templates

Although many types of anion interactions with hosts are possible, most can be loosely categorized as template interactions. This term refers to the “rank” or

importance of these interactions in a self-assembly reaction. In many cases, the anion acts as a controlling element that favors one major product over other possibilities, ultimately dictating which structure will be formed, or the template of the process. The most encompassing definition of the template process is the one of Jean-Marie Lehn who dubbed it a “procedure involving the use of temporary or permanent ‘helper’ species, of organic or inorganic nature, for the stepwise assembly of molecular or supramolecular structures of high complexity.”¹¹

The research in this dissertation is based on the hypothesis that anion- π interactions are viable templates for self-assembled coordination compounds. Since this topic is relatively new, a fairly comprehensive description of the literature involving this topic is presented herein. The following literature review, while lengthy, provides an in-depth narrative of each study relevant to the topic. Each subsequent chapter will refer the reader back to these descriptions for clarification.

C. Anion- π Interactions

1. Definition - Anion- π interactions, defined as electrostatic attractions between an anion and a π -acidic ring system, have only been recognized in the last 5 years.¹² Although it was demonstrated as early as 1992¹³ that an anion can induce a weak dipole in an aromatic system, only three research groups originally focused on the possible existence of this interaction. In 2002, the independent computational studies of Alkorta *et al.*, Mascali *et al.*, and Deyá *et al.*, set the stage for experimental investigations into this new type of weak supramolecular interaction.

2. Computational Studies on Anion- π interactions - As stated above, anion- π interactions have been documented since 1992.¹³ Using an incremental approach to studying noncovalent interactions, Zimmermann and coworkers investigated the

equilibria of ion pairs with aromatic units in water with UV/vis, NMR, and conductivity measurements. They concluded that there is a stabilization energy of $\Delta G_v \approx 2$ kJ/mol for the interaction of either a cation or an anion with a phenyl ring when this ring is located in close proximity to an opposing charge. This proximity induced a favorable dipole in the π -systems for binding to either the cation or the anion, an effect that served as an inspiration for the work of the research groups who followed up on these observations.

While Alkorta's studies were the first to thoroughly examine this interaction by theoretical methods, no specific name was given to describe the interaction.^{12a} By using several different ring systems (hexafluorobenzene, octafluoronaphthalene, and pentafluoropyridine), this group concluded that interactions between π -acidic ring systems and the anions $[\text{H}]^-$, $[\text{F}]^-$, $[\text{Cl}]^-$, $[\text{Br}]^-$, $[\text{CN}]^-$, and $[\text{CNO}]^-$ were favorable. The use of both *ab initio* and DFT methods indicated that, while DFT could predict qualitatively that these interactions could occur in a specific system, *ab initio* methods were more appropriate for assigning quantitative values to describe anion- π interactions (anion to ring distances, binding energies, etc.) As a result of these findings, many of the following studies only include *ab initio* computational examinations of anion- π interactions.

Mascal and coworkers began their studies by examining the π -acidic *s*-triazine and its perfluorinated derivative in the presence of halide anions and azide.^{12a} Depending on the nature of the ring system studied, they obtained three different theoretical positions for the anion in relation to the π -system at the MP2¹⁴/6-31+G*¹⁵ level of theory: (1) Centered over the centroid of the ring, (2) nucleophilic attack at a carbon atom (in the case of $[\text{F}]^-$), and (3) hydrogen bonding. They further showed

that the energy of these systems increased overall when the complexes were surrounded by progressively more polar solvents introduced to the calculations. These authors concluded that triazine derivatives are viable resources as anion-traps, but the term anion- π interaction was not coined until Deyà's essentially simultaneous study described in the following section.

Deyà's initial study was similar in many ways, but involved hexafluorobenzene instead of the triazines.^{12b} The study probed the electrostatic interactions of halides, hydride, $[\text{CN}]^-$, $[\text{NO}_3]^-$, and $[\text{CO}_3]^{2-}$ with hexafluorobenzene. The computations used Hartree-Fock (HF)¹⁶ and (MP2)¹⁴ geometry optimization analysis with the basis set 6-31++G**¹⁷, the conclusion of which was that electron-deficient aromatic rings are capable of electrostatic interactions with anions. The Hartree-Fock results were subjected to an AIM (Atoms in Molecules)¹⁸ theoretical evaluation to reveal bond (3,-1) critical points connecting the anions (halides in particular) to the carbon atoms of the ring. Distinguished by their specific classes, cage (3,+3) critical points between the anion and the (3,+1) critical point at the centroid of the ring (its area of lowest electron density), indicated that there is an electrostatic interaction between the two species (see Figure 2).

To analyze the binding properties of the aromatic rings and the overall physical nature of the binding energies of these interactions, an MIPp breakdown was employed. MIP¹⁹ (Molecular Interaction Potential) analysis begins with 2D Molecular Electrostatic Potential Maps (MEPs). A repulsion-dispersion term is then added with the addition of point charge (giving an MIP map). MIPp²⁰ (Molecular Interaction Potential with polarization) includes an electrostatic term identical to that in MEPs, and, along with a classical dispersion-repulsion term, it also incorporates a

desired polarization term derived through perturbation theory. This method allows for assignation of numerical values to the important components of the total interaction energy between two species at the HF¹⁶ level of theory and thus, permits an assessment of their overall importance to the binding process (with the components being polarization, electrostatic, and van der Waals contributions). The computed values are shown in Table 2.

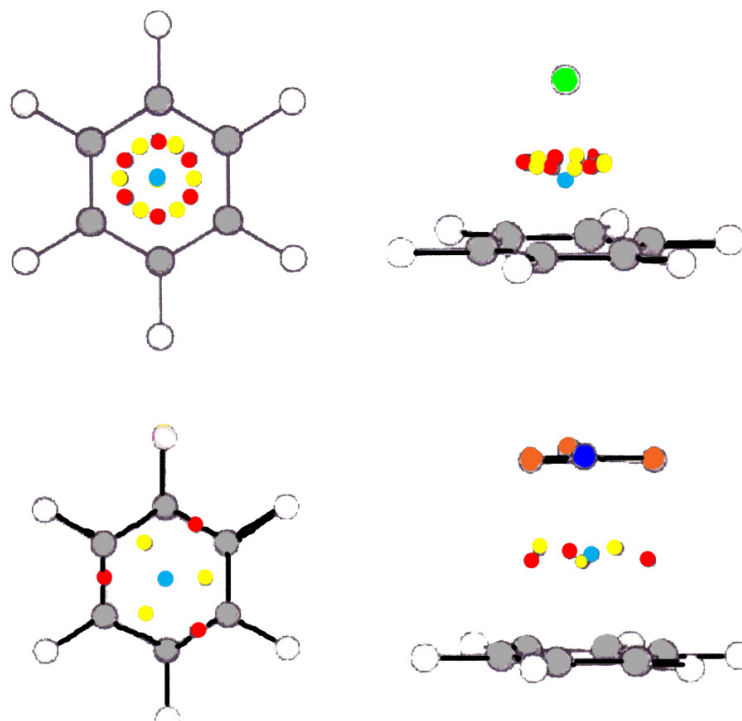


Figure 2: Representation of the AIM-derived critical points found when [Cl]⁻ interacts with C₆F₆ (top), and when [NO₃]⁻ interacts with C₆F₆ (bottom). Both are shown with top and side views. The red circles represent bonding (3,-1) critical points, the yellow circles represent ring (3,+1) critical points, and the light blue circles represent cage (3,+3) critical points. The Figure is adapted from reference 12c.

Table 2: MIPp numerical breakdown of the total interaction energy (E_t) into its constituent components (kcal/mol). The representative portions are electrostatic (E_e), polarization (E_p), and van der Waals (E_{vw}). The table is adapted from reference 12c.

Distance (Å)	E_e	E_p	E_{vw}	E_t
1.5	-36.59	-43.8	1048	967.38
2.0	-22.44	-24.9	119.1	71.72
2.5	-16.39	-13.9	13.44	-16.89
3.0	-12.66	-7.96	-0.50	-20.12
3.5	-9.90	-4.74	-0.83	-15.48

These results indicated that, in the case of hexafluorobenzene in the presence of [F]⁻, the polarization and electrostatic constituents are numerically similar when the anion- π distance is in the most favorable range between 2-5 and 3.0 Å, and both should be considered as relevant forces that contribute to anion- π interactions.

To further support the existence of anion- π binding, Deyà and coworkers searched the Cambridge Crystal Database (CSD) for possible interactions of this type in previously reported structures. Explicit search parameters were employed:“(1) the interacting atom with any pentafluorobenzene derivative was either S, N, O, F, Cl, Br, or I; (2) the type of nonbonding contact was either intramolecular or intermolecular; (3) the nonbonding contact was defined by distance criteria, i.e. less than the sum of van der Waals radii; (4) a hit was stored when a nonbonding contact existed between the interacting atom and all six carbon atoms of the aromatic ring; and (5) for the search of the anion- π interactions, a negative charge was defined explicitly on the interacting atom.” The search for perfluorobenzene derivatives with electronegative atoms resulted in 1944 fragment hits, a large number of which contained an angle of $\sim 90^\circ$ defined by an intersection of two lines; one from the

anion to the centroid, and the other from the centroid of the ring to any atom on the ring (Figure 3). If the anion was complex, this situation was further defined by drawing the line from the central anion atom to the ring centroid. The results of this portion of the study led Deyà and coworkers to report that, for an anion- π interaction to be present, the anion should align with the central axis of the ring in question, and that other positions, such as those slipped off this central axis, represented a weaker attraction (equal van der Waals contact of all ring atoms with the anion is not feasible in these cases).

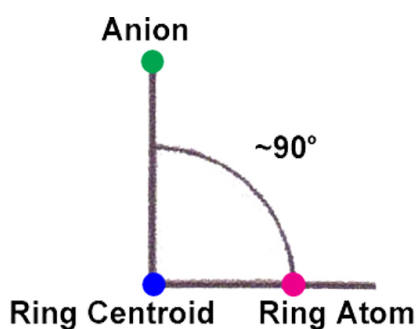


Figure 3: Diagram representing the angle measured in the structure fragments involving perfluorinated rings and anions in a CSD search.

Although all three independent groups of Deyà and Mascali, and Alkorta contributed to the development of the topic of anion- π interactions, only Deyà's group continued to explore the subject in an in-depth fashion. In one of these studies, Deyà and coworkers examined aromatic ring systems that are electron-rich.²¹ The benzene molecule C_6H_6 , a ring system with a tendency to participate in *cation- π* interactions, was chosen to investigate the possibility for π -basic systems to participate in anion- π interactions. An analysis was conducted on two model systems with the anions $[F]^-$, $[Cl]^-$, and $[Br]^-$: Benzene interacting with $[Na]^+$ and

hexafluorobenzene interacting with $[\text{Na}]^+$. Along with geometry optimizations performed at the HF¹⁶ and MP2¹⁴ levels of theory with the basis set 6-31++G**,¹⁷ critical point analyses of the compounds were conducted using the AIM¹⁹ method. In general, the calculated geometries of the systems revealed the trend of $[\text{F}]^-$ being closer to the centroid of either type of ring, with $[\text{Cl}]^-$ being the next closest, and $[\text{Br}]^-$ being the furthest from the centroid. Overall, the distances measured that included the C_6F_6 ring were shorter than those that included the C_6H_6 ring, indicating that the anion- π interaction with C_6F_6 was more favorable.

The critical point analysis performed on the MP2¹⁴ wavefunctions assigned matching patterns of ring and cage critical points on both sides of the rings in all systems (Figure 4). These results reveal that the rings are participating in both anion and cation- π interactions simultaneously on opposite sides of the phenyl rings, an expected result considering the outcomes of the geometry optimizations. The more interesting results, however, were obtained from the MIP¹⁹ analysis. Examination of the 2D MIP maps revealed that C_6H_6 coupled with $[\text{Na}]^+$ and a $\frac{1}{2}[\text{O}]^-$ point charge had negative isopotential contour lines close to both the $[\text{Na}]^+$ (expected) and the opposite face of the ring from the cation. A similar map of C_6F_6 coupled with $[\text{H}]^-$ and a $\frac{1}{2}[\text{H}]^+$ point charge revealed the same, but oppositely charged results. These results support the conclusion that both rings can participate in cation- π and anion- π interactions. The additional perturbational polarization term was included (MIPp)²⁰ to obtain a numerical value for the contribution of this component to the total interaction energy between $[\text{F}]^-$ and the ring/ $[\text{Na}]^+$ cation complex. The numerical breakdown of the results obtained at the optimal interaction distances between 2.0-2.5 Å (Table 3) indicated a large polarization contribution to the anion- π interaction

energy when an electron-rich ring is participating in an anion- π interaction. In comparison, the magnitude of the polarization component of C_6F_6 (electron poor) with only an anion in the same 2.5-2.5 Å anion-ring range is much less (Table 2).^{12b}

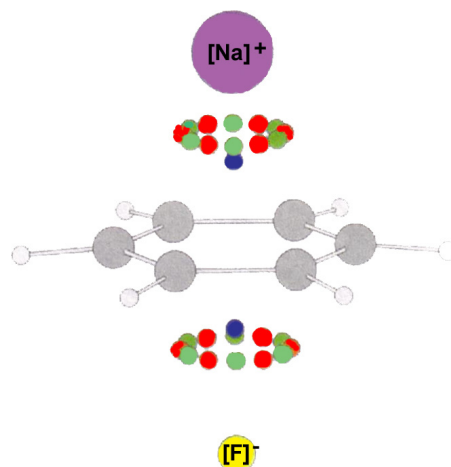


Figure 4: Diagram of the critical points found by AIM analysis of C_6H_6 interacting with both a $[F]^-$ anion and a $[Na]^+$ cation. Red circles = (3,-1) bonding critical points, green circles = (3,+1) ring critical points, and light blue circles = (3,+3) critical points. Figure adapted from reference 21.

Table 3: MIPp numerical breakdown of the total interaction energy (E_t) into its constituent components (kcal/mol) for the $[Na]^+$ -benzene complex interacting with $[F]^-$ at selected distances. The representative portions are electrostatic (E_e), polarization (E_p), and van der Waals (E_{vw}). The table is adapted from reference 21.

Distance (Å)	E_e	E_p	E_{vw}	E_t
1.5	-105.03	-64.38	99.68	-69.73
2.0	-90.74	-40.68	8.13	-123.28
2.5	-82.46	-25.90	-0.46	-108.83
3.0	-75.95	-17.15	-0.77	-93.87
3.5	-70.23	-11.93	-0.47	-82.63

One last possible component that may have been hidden in the previously described results is the charge transfer effect in these systems. To evaluate this contribution, the atomic charges of the complexes were determined using the Merz-Kollman²² method. In all 6 cases, (both rings, all three anions), the electronic flow of charge is mainly from the anion to the cation, and there is very little alteration of the charge in the ring. This final calculation, which eliminated charge transfer as important in the case of a ring participating in both an anion- and cation- π interaction, backed up the previous definition of an anion- π interaction being a purely electrostatic interaction.^{12c}

Another theoretical study was conducted by Deyà and coworkers to examine the ability of *s*-tetrazine to participate in anion- π interactions.²³ For comparison, urea and squaramine, two known neutral anion receptors, were examined in the same manner to study the difference between hydrogen bonds to anions versus electrostatic interactions between an anion and the electron-deficient tetrazine ring (see Figure 5). All three compounds were optimized in the presence of [F]⁻, [Cl]⁻, and [Br]⁻ at the MP2¹⁴ level of theory using the basis set 6-311+G**.^{24,17k-m} In the case of the complexes of urea and squaramide, the anion is hydrogen bonded to two hydrogen atoms from different amine nitrogen atoms, while in the case of *s*-tetrazine, the anion approaches the centroid of the ring. The carbon atoms of the *s*-tetrazine became non-planar to be closer to the approaching anion (and possibly to bring the hydrogen atoms attached to these carbon atoms closer to the anion). The binding energies calculated for urea and squaramide were much more favorable than that found for the tetrazine anion- π interaction, which is not unexpected since hydrogen bonds are much stronger than weak electrostatic forces.

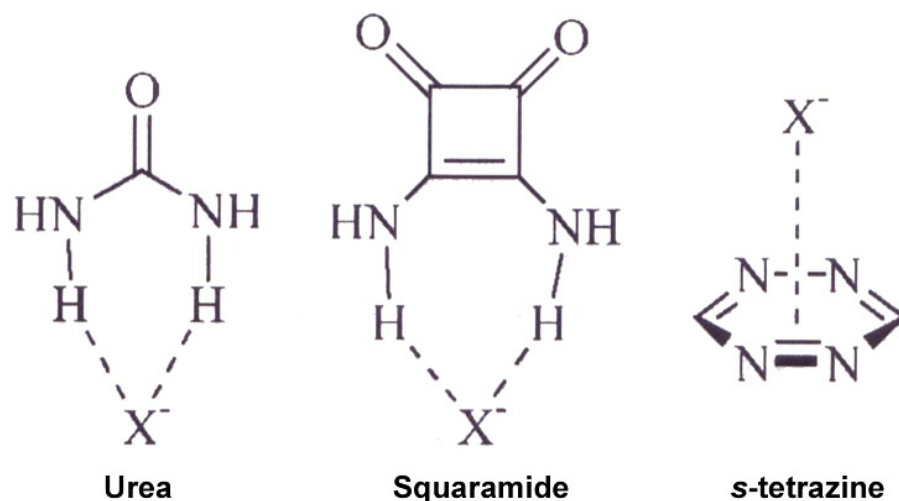


Figure 5: Schematic drawings of a halide anion $[X]^-$ interacting with urea, squaramide, and *s*-tetrazine. Figure is adapted from reference 23.

As before, MIP¹⁹ with polarization²⁰ was employed (only on the receptor molecules interacting with $[F]^-$). As expected, the electrostatic component of the total binding energy of the anions to squaramide and urea dominated. The previous study revealed that, in the case of anion- π interactions involving electron rich rings, the polarization component increases in magnitude while still being outweighed by the electrostatic component. In this instance, however, with the highly π -acidic tetrazine ring, the terms are equal (-20.56 and -20.51 kcal/mol for the polarization and electrostatic components, respectively at an interaction distance of 2.40 Å). According to a Merz-Kollman²² analysis of the atomic charges in the optimized structures, the charge transfer from the anion to the tetrazine is greater than the charge transfer of the anion to the urea or the squaramide upon hydrogen-bond formation, which could be expected in these purely gas-phase calculations with a π system and an anion not paired with a cation. The conclusion of these results was that anion- π interactions with highly electron deficient rings, while relying equally on

electrostatic and polarization components (as seen in Deyà's first study),^{12b} on the stronger end of the binding spectrum, may actually participate in charge transfer.

The next study concerned a topological analysis of the electron density in anion- π interactions to probe whether the quadrupole moment of an aromatic ring has an impact on interaction strength.²⁵ For this study, Deyà and coworkers utilized six phenyl ring derivatives (Figure 6), all of which have varying quadrupole moments (Q_{zz} , listed on Figure 6). In all cases, Q_{zz} is positive, indicating that the rings are more likely to interact with negatively charged species. For comparison, benzene, which prefers cation- π interactions to anion- π interactions, has a Q_{zz} of -8.48 Buckingham (1B = 3.336×10^{-4} Cm²). All six rings were optimized in the presence of [Cl]⁻ with the MP2¹⁴ /6-311++G**²⁴ level of theory/basis set, subjected to wavefunction critical point analysis using the AIM¹⁸ method, and examined using MIP¹⁹ with polarization.²⁰

The structural results correlate well with the critical point analysis results, namely the interaction distance of the anion to the centroid of the aromatic ring was proportional to the value of the density of the (3,+3) cage critical point. As the density value increases (more density at this point when the electrostatic interaction is stronger) the distance shortened. The authors suggested that the "bond order" of anion- π interactions can be measured by the value of the density at the cage critical point. The terminology is flawed since bond order is a designation normally reserved to describe covalent bonds, but the idea that the density at the cage critical point can be used to measure the strength of the interaction is solid, especially since the interaction energies become more favorable (more negative) with increasing (3,+3) density values.

The MIPp^{19,20} analysis revealed other correlations, one of which is the trend of increasing quadrupole moment (more positive) leading to a decrease (more favorable/negative) in the total binding energy. Thus, ring systems with larger positive quadrupole values are most likely to participate in stronger anion- π interactions than those with smaller positive quadrupole moments. The final correlation was drawn from the data between the polarization component of the total interaction energy and the polarizability of the ring system. The more polarizable the phenyl ring derivative (those rings with smaller magnitudes, positive or negative, of their Q_{zz} value), the larger the influence the polarization component has on the total energy. This final observation led the authors to conclude that, although quadrupole moments are a good measure of whether or not a ring system will participate in an anion- π interaction, the polarizability of the rings should also be taken into consideration. Both play a part in determining if an anion- π interaction can form with only slightly electron-deficient (modest positive Q_{zz} values) aromatic rings.

An analogous study was conducted with 5-membered aromatic ring systems.²⁶ Before they began, Deyà's group examined data in the CSD to look for contacts between anions and the π -clouds of 5-membered rings using the following criteria: "(1) The type of nonbonding interaction was either intra or intermolecular; (2) the nonbonded contact was defined by distance criteria, i. e.; less than the sum of the van der Waals radii; (3) a hit was stored when a nonbonded contact existed between the anion and all 5 carbon atoms of the aromatic ring; and (4) a negative charge was defined explicitly on the interacting atom." The results of the search produced 126 fragments of 111 structures all involving cyclopentadienyl (Cp) rings. Most of these structures included the complex anions $[\text{BF}_4]^-$ and $[\text{PF}_6]^-$, so the

authors defined the ring centroid to anion distance to the central B or P atoms of these anions. To further analyze these results, the complex anion- π angles (see Figure 3) were measured for comparison. The results (see Figure 7), reveal that most anions reside directly over the centroid of the Cp ring (90°).

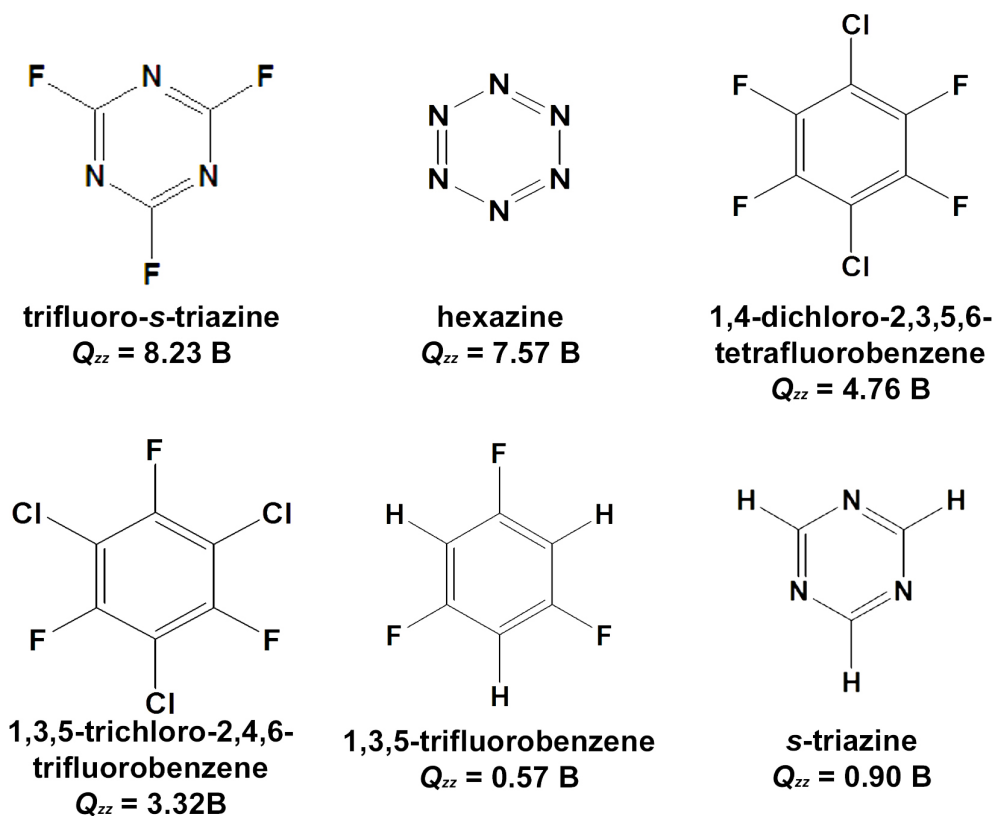


Figure 6: The π -acidic ring systems used in the topological analysis of anion- π interactions from reference 25. The Q_{zz} values of each ring are listed underneath its line drawing. Figure adapted from reference 25.

The model used in the computational study involved a beryllium cation positioned on the C5 axis of a Cp ring with an anion on the opposite face of the ring (anions: $[\text{H}]^-$, $[\text{F}]^-$, $[\text{Cl}]^-$, $[\text{Br}]^-$, and $[\text{CN}]^-$). Using both AIM¹⁸ and MIPp^{19,20} analyses

gleaned from the optimized geometries of the complexes at the HF16 and MP2¹⁴/6-31++G**¹⁷ levels of theory, it was found that the structures bind to anions preferentially on the side of the Cp rings opposite the [Be]⁺ cation (as judged from the presence of both cage and bond critical points between the anion and the ring), and that these particular anion- π interactions are primarily electrostatic in nature. The MIPp^{19,20} analysis, however, did reveal that polarization caused by proximity of the anion to the ring is not negligible and cannot be ignored.

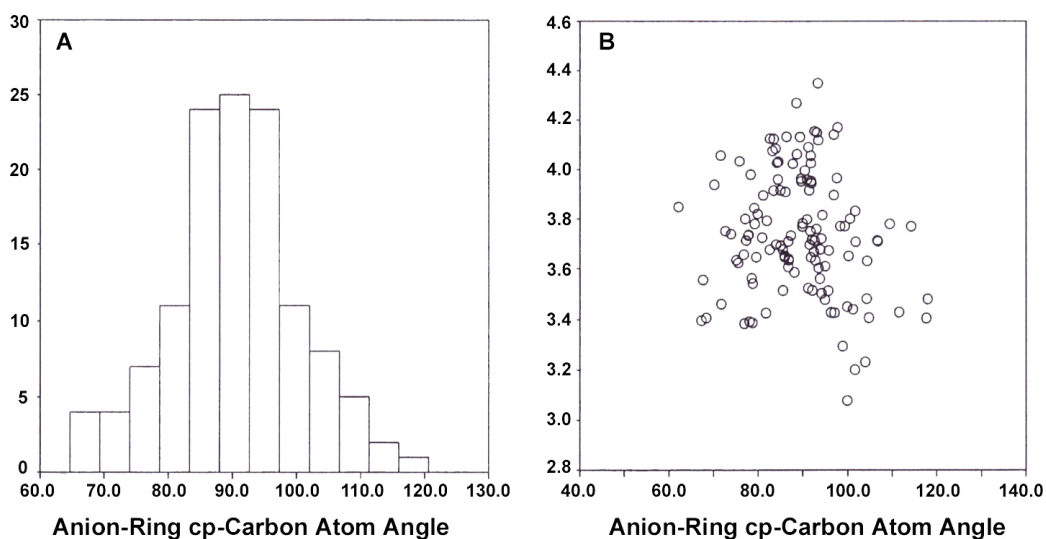


Figure 7: The results of a CSD search performed by Deyà and coworkers to find 5-membered ring π -systems that participate in anion- π interactions. Graph A represents the number of fragments (vertical axis) found at specific anion \cdots ring critical point \cdots carbon atom on the ring angle. Graph B represents the distance of the anion (vertical axis) vs. the same angle as graph B. Both show that most anion- π complexes involving 5-membered rings have the defined angle close to 90°. The graphs are reproduced from reference 26.

After these initial studies, the theoretical investigation of anion- π interactions began to attract the attention of other research groups. Kim and coworkers published a theoretical study aimed at investigating the role of the anion and the π -system

involved in these interactions as separate components to understand where their contributions lie.²⁷ To study the influence of the π -system on this interaction, the authors chose three different molecules for this study: Tetrafluoroethene (olefinic), hexafluorobenzene (aromatic), and 1,3,5-triazine (heteroaromatic). The anions examined were the halides ($[F]^-$, $[Cl]^-$, and $[Br]^-$), $[CN]^-$ (both directions of approach to the π -systems), and the trigonal-planar $[NO_3]^-$ and $[CO_3]^{2-}$ anions. The goal was to compare equilibrium geometries of the π -systems in the presence of these anions, the interaction energies of the complexes, and the vibrational frequencies of the complexes with an emphasis on a quantitative estimation of the individual components of the interaction. In all cases, only geometries in which the anion is centered over the major axis of symmetry of the π -system were investigated.

The theoretical methods used in this study to determine the components of total interaction energies were quite different from those previously employed by Deyà and coworkers. Instead of using MIPp,^{19,20} Kim and coworkers exploited supramolecular (SM) variational²⁸ and symmetry adapted perturbation theory (SAPT)²⁹ to calculate the separate forces that compose the total interaction energies of the anion- π complexes. While SM does not provide a clear picture of the interaction forces, it is computationally less-demanding than SAPT, which “computes the interaction energy directly as a sum of electrostatic, exchange repulsion, induction, and dispersion contributions.”²⁷ The SM calculations were computed from MP2¹⁴/6-311++G**²⁴ and aug-cc-pVDZ/6-311++G** geometry optimized wavefunctions. The SAPT values were obtained from the optimized geometries of the SM calculations from the MP2/aug-cc-pVDZ results.

The first result of these calculations indicated that interaction energies of anion- π complexes are comparable to those of cation- π complexes. For instance, the calculated interaction enthalpies (ΔH_{298}) for $[\text{K}]^+$ with ethene and benzene at the MP2¹⁴/-6-31++G**²⁴ level of theory are -7.05 and -14.79 kcal/mol, respectively, while the values for fluorinated ethene and hexafluorobenzene with $[\text{Cl}]^-$ are -6.16 and -11.42 kcal/mol, respectively. SAPT²⁹ analysis revealed that the total interaction energy of anion- π interactions is largely composed of the electrostatic and induction energies, the inductive molecular orbitals (Figure 8) being the main facilitators of charge transfer from the anions (HOMO) to the π -system LUMOs. Also, unlike the findings for cation- π interactions, anion- π interactions rely heavily on dispersion forces, according to SAPT.²⁹ Furthermore, although the electrostatic term dominates overall, in the case of larger anions, the polarization term becomes more important to the anion- π interaction. Kim and coworkers concluded that, although the total interaction energies of anion- π and cation- π interactions are very similar in strength, they depend on different components.

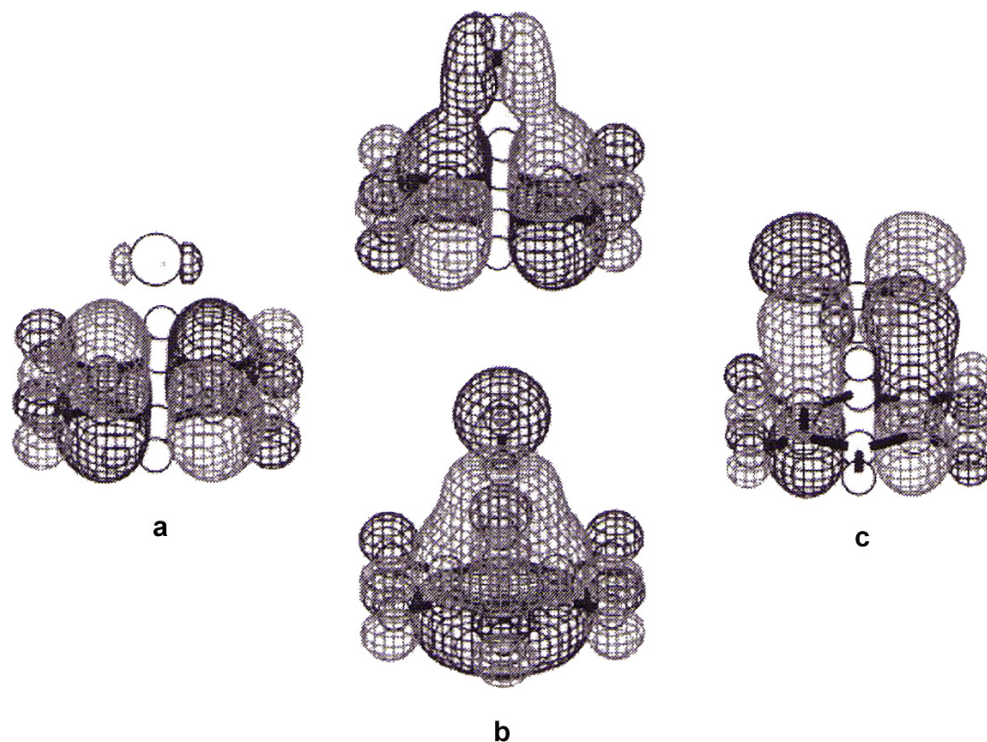


Figure 8: Inductive orbitals of hexafluorobenzene with (a) $[\text{Br}]^-$, (b) $[\text{CN}]^-$, and (c) $[\text{NO}_3]^-$). Figure adapted from reference 27.

In an effort to better define some of the findings of this previous report, Deyà and coworkers published a study aimed at comparing the differences between cation- π and anion- π interactions in the trifluorobenzene, *s*-triazine, and dichloropyrazine systems (Figure 9) in the presence of both $[\text{Na}]^+$ and $[\text{F}]^-$ ions.³⁰ The choice of $[\text{Na}]^+$ and $[\text{F}]^-$ as interacting ions was made because they are isoelectronic. The authors stated that, since hexafluorobenzene and benzene were different rings, the results that Kim *et al.*²⁷ reported could not be generalized for both cation- and anion- π interactions. It was argued that, since the rings in this study were the same for both the anion- π and cation- π interactions, and the ions were isoelectronic, the results could be generalized.

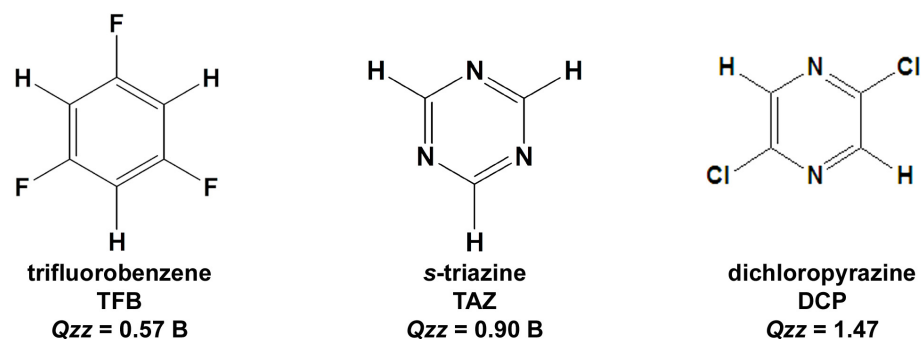


Figure 9: π -systems examined (with respective quadrupole moments) in the presence of both anions and cations to study the theoretical differences between anion- π interactions and cation- π interactions. Figure adapted from reference 30.

As expected from the quadrupole moments of the rings, trifluorobenzene (with the smallest Q_{zz} value of 0.57 B) exhibits the closest cation- π contact. It was also found through MP2¹⁴ optimization that dispersion forces (similar to Kim's results)²⁷ and correlation forces are more important for anion- π interactions than for cation- π interactions. Beyond this observation, it is noted that the cation-ring contact is closer than the $[\text{F}]^-$ ring contact (most likely due to the smaller van der Waals radius of $[\text{Na}]^+$ compared to $[\text{F}]^-$). This closer proximity of the cation to the ring results in a larger polarization contribution to the overall energy as computed by MIPp.^{19,20}

An examination of the rings alone with MIPp^{20,20} also correlated that those rings which are more polarizable tend to have more negative (more favorable) polarization terms associated with the total interaction energy. An NICS³¹ (Nucleus Independent Chemical Shift Criterion) examination of the rings indicated that, after association with a cation, all three aromatic rings decreased in aromaticity, while

association with the $[F]^-$ anions increased their aromaticity. The bond critical points (3,-1) between the carbon atoms of the rings support this finding. The differences in the density computed at these critical points ($\Delta\rho$) using AIM¹⁸ theory show that, when any one of the three rings studied is in contact with an anion, the value increases (greater density/more aromaticity). The opposite is true for when the rings are in contact with a cation.

Armed with much less costly basis sets, Deyà and coworkers set out to study the additivity of anion- π interactions.³² The focus of this inquiry was to demonstrate that, although anion- π interactions are considered to be weak, especially as compared to other neutral anion receptors that utilize hydrogen bonding, they should make excellent anion receptors when they work in concert. For this study, the only anions examined were $[Br]^-$ and $[Cl]^-$ ($[F]^-$ was not examined since it often favors nucleophilic attack at one of the π -system carbon atoms). The two rings examined were *s*-triazine and trifluorotriazine, both of which were optimized at the HF¹⁶/6-31++G**¹⁷ level of theory with each anion in a 1:1 (ring:anion), 2:1 and 3:1 ratios (Figure 10). From these geometry optimizations, a single point energy calculation was performed at the RI-MP2/6-31++G**^{33,17} and the MP2/6-31++G**^{14,17} levels of theory for binding energy comparisons. While the results were corrected for Basis Set Superposition Error (BSSE), none were corrected for Zero Point Energy (ZPE) since frequency calculations are not an option when using Resolution of the Identity (RI).³³ Charge-transfer was monitored by Mulliken Population Analysis,³⁴ the Merz-Kollman Scheme,²² and AIM.¹⁸ With the AIM program, the values of the (3,+3) cage critical points between the anions and the centroid of the π -systems were also evaluated in order to determine the strength of each anion- π interaction.

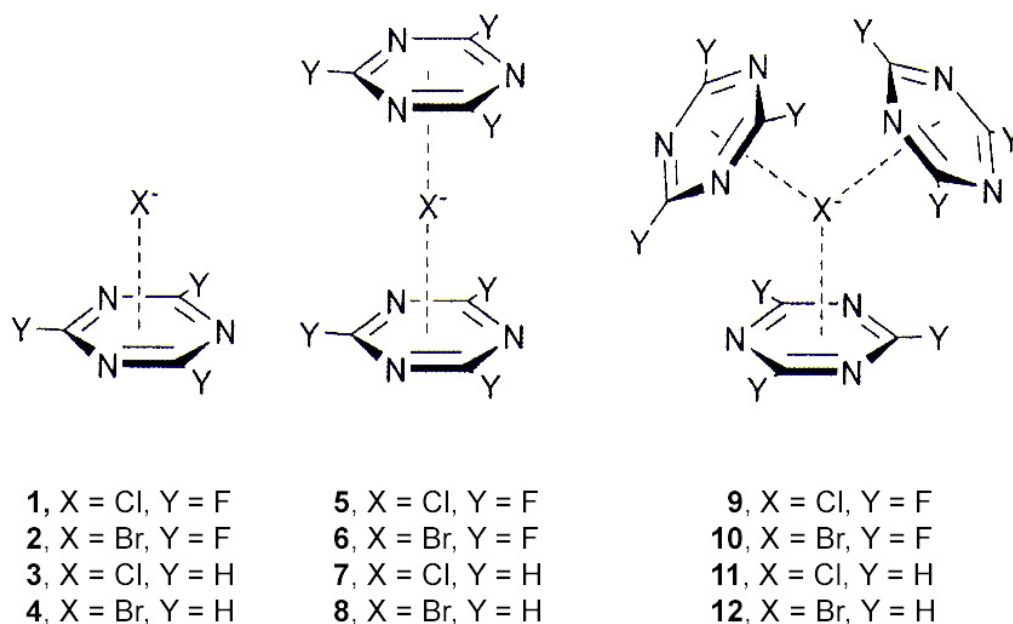


Figure 10: The anion- π complex models investigated with multiple interactions per anion. Figure adapted from reference 32.

The most interesting data that emerged from this study (shown in Table 4) indicate that the interaction energies are additive. Generally, the interaction energies double and triple moving from the 1:1, to the 1:2, to the 1:3 anion to ring ratio. In some cases, the energy is somewhat higher in the 1:3 final structure than the mentioned trend for the *s*-triazine version. The rationale for this observation is that the rings are also weakly hydrogen-bonded between their hydrogen and nitrogen atoms. A similar optimization without the anion present allowed for this contribution to be subtracted and confirmed that the trend was intact for these special cases.

Table 4: Binding energies (kcal/mol) with (E_{cp}) and without (E) the (BSSE) correction and equilibrium Distances (R_e , Å) at several levels of theory for Complexes 1-12. Also included are the atomic charges of [Cl]⁻ and [Br]⁻ and the values of the electron charge density (ρ , au) and its Laplacian ($\Delta^2\rho$, au) at the cage critical point formed upon complexation. Table is adapted from reference 32.

Complex	E	E_{CP}	R_e	E	E_{CP}	q_{AIM}	$q_{M.K}$	q_{Mull}	$10^2\rho$	$10(\Delta^2r)$
1 (TFZ-[Cl] ⁻)	-20.3	-15.1	3.008	-20.3	15.0	-1.006	-0.871	-0.856	0.853	0.323
2 (TFZ-[Br] ⁻)	-18.8	-14.2	3.176	-21.8	-14.2	-1.050	-0.882	-0.839	0.801	0.282
3 (TAZ-[Cl] ⁻)	-9.0	-5.3	3.220	-9.0	-5.2	-1.021	-0.902	-0.956	0.595	0.223
4 (TAZ-[Br] ⁻)	-8.4	-5.0	3.338	-10.7	-5.1	-1.106	-0.917	-0.959	0.599	0.216
5 (TFZ ₂ [Cl] ⁻)	-38.2	-28.6	3.006	-38.5	-28.5	-0.943	-0.692	-0.790	0.832	0.326
6 (TFZ ₂ [Br] ⁻)	-36.4	-26.8	3.170	-41.7	-26.8	-1.103	-0.762	-0.448	0.789	0.284
7 (TFZ ₂ [C] ⁻)	-17.3	-10.4	3.213	-17.4	-10.4	-1.065	-0.724	-0.989	0.594	0.227
8 (TAZ ₂ [Br] ⁻)	-16.8	-10.2	3.370	-20.6	-10.0	-1.125	-0.748	-1.099	0.568	0.205
9 (TAZ ₃ [Cl] ⁻)	-64.2	-41.0	3.019 ^a	-65.6	-41.0	-0.769	-0.653	-0.773	0.838	0.324
10 (TFZ ₃ [Br] ⁻)	-60.7	-38.6	3.172 ^a	-75.3	-38.6	-1.135	-0.734	-0.964	0.794	0.286
11 (TFZ ₃ [Cl] ⁻)	-39.2	-22.2	3.015 ^a	-39.6	-22.2	-1.015	-0.692	-0.939	0.599	0.220
12 (TFZ ₃ [Br] ⁻)	-37.6	-21.7	3.372 ^a	-49.2	-21.7	-1.113	-0.686	-0.660	0.573	0.203

The charge-transfer calculations proved to be somewhat confusing; the AIM¹⁸ and Mulliken³⁴ results both show in most cases that the charge, while small, is flowing from the ring to the anion. These counter-intuitive results are refuted, however, by the Merz-Kollman²¹ results which display charge moving from the anion to the ring systems as expected. No explanation for these discrepancies was provided. Throughout all of the calculations, the distances of the anion from the ring centroid (whether it be one, two, or three rings) and the value of the cage critical points that lie along the axis of this distance do not vary. These results suggest that once the appropriate distance between the anion and a π -system is achieved, the energy of the system can be lowered by adding another anion- π interaction, a result that bodes well for the use of anion- π interactions as neutral anion receptors.

In summary, several key observations about the theoretical nature of anion- π interactions have been determined. The definition of anion- π interactions as an electrostatic attraction of an anion to a π -acidic ring system holds mostly true. In all studies, the electrostatic component of these interactions with π -acidic ring systems was very large. The polarization component, however, was almost equal in all cases involving π -acidic systems. The π -systems that exhibit the greatest π -acidity depend on the electrostatic component of the total binding energy the greatest. The theory falls short, however, in the case of π -basic electron-rich rings, which can also participate in anion- π interactions. These situations rely on the polarizability of the rings in question, and the breakdown of their interaction energies disclose that, while the polarization component becomes a more important portion of the total binding energies, it nevertheless does not overcome the electrostatic contribution. In all cases, as the anion approaches the π -system in question, the aromaticity of the system increases, thus indicating a donation of electron density from the anion to the ring system. The final observation is that the most stable anion- π interactions are encountered when the anion resides over the centroid of the π -system in question, and that the angle defined by a line drawn from the anion to the centroid and a line from the centroid to any atom of the π -system should be $\sim 90^\circ$.

3. Experimental Evidence for Anion- π Interactions -

a. Structural Evidence

Shortly after the previously discussed theoretical studies were published, two papers appeared in which the first structures involving recognized anion- π interactions were reported. The first, published by Meyer and coworkers, detailed the large ligand hexakis(pyridine-2-yl)-[1,3,5]-triazine (L1), complexed with Cu(II)

(Figure 11a).³⁵ The crystal structure consists of two L1 ligands ligated to three Cu(II) ions to give the complex $[L_1_2(CuCl_3)][CuCl_4][Cl]$ displayed in Figure 11b (compound *i*). The two ligands are arranged such that the triazine rings are in a nearly perfect overlapping position (roughly 3.78 Å measured plane-to-plane). The most startling feature of this structure, however, is that one of the $[Cl]^-$ counter ions is within close contact to a triazine ring of one of the ligands (the contact to the ring centroid listed as 3.11 Å, close to the calculated distance of 3.2 Å predicted by Mascali and coworkers).^{12a} The angle of this contact, defined by Deyà and coworkers (Figure 3), is 88°, very close to the 90° angle that was predicted by Deyà to be the most ideal for anion- π interactions.^{12b} These two measurements led the authors to claim the first experimentally documented anion- π interaction.

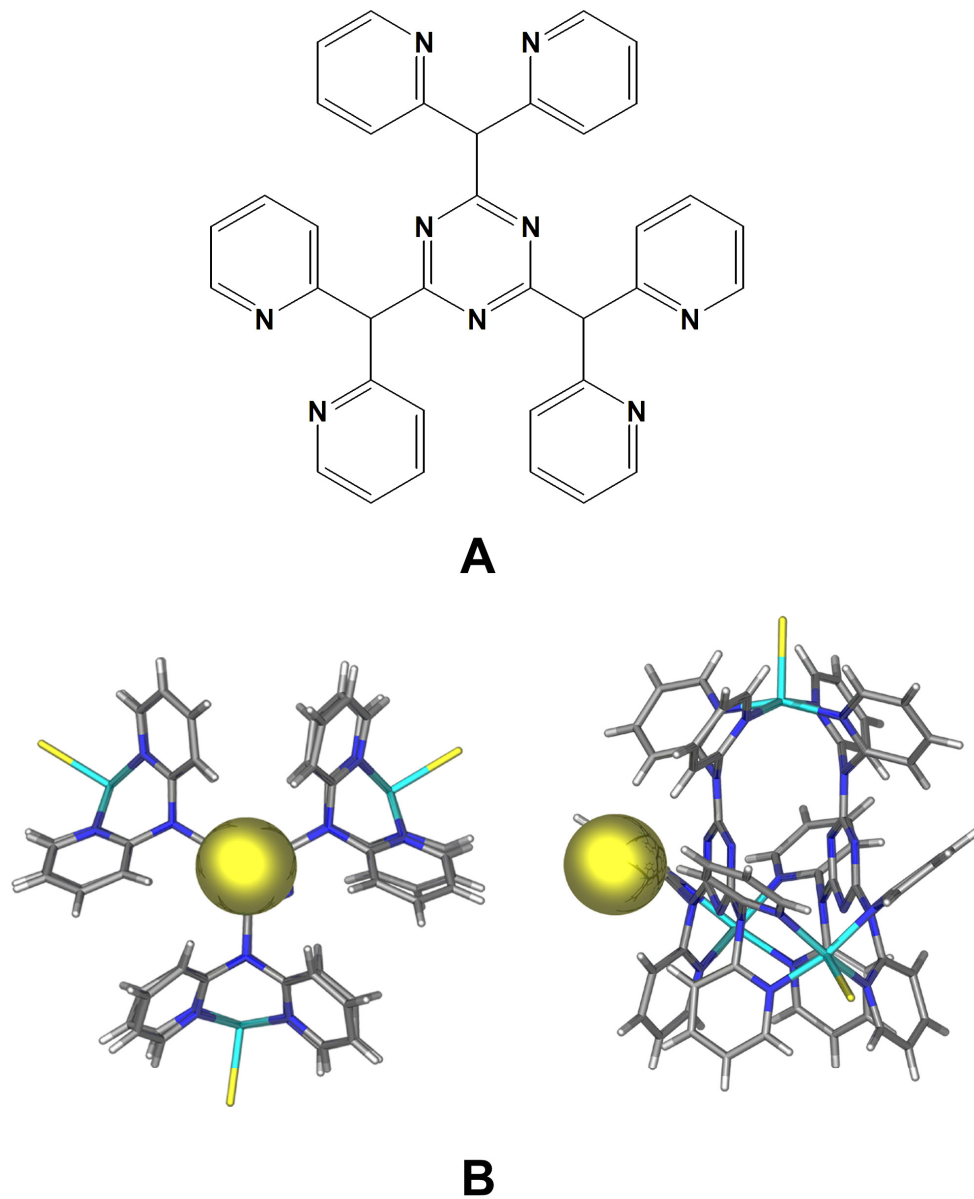


Figure 11: (a) Line drawing of the hexakis(pyridin-2-yl)-[1,3,5]-triazine-2,4,5-triamine ligand (L1). (b) Front (left) and side (right) views of the structure $\{[L_2(CuCl_3)][Cl]\}^{2+}$. Anion to tetrazine centroid contact = 3.11 Å. Figures adapted from reference 35.

Later that same year, Reedijk and coworkers published a similar structure involving the more complicated ligand N,N',N'',N''' -tetrakis{2,4-bis(di-2-pyridylamino)-1,3,5-triazineyl}-1,4,8,11-tetraazacylotetradecane (L2) with Cu(II) to give $[Cu_4(L2)Cl_4](Cl)_4(H_2O)_{13}$ (see Figure 12a).³⁶ In this example (Figure 12b), one ligand is complexed with four different Cu(II) ions, and two $[Cl]^-$ anions are trapped in proximity to four pyridyl rings (compound **ii**, shortest distance = 3.60 Å to the centroid), as well as in close contact to a triazine ring (3.013 Å being the shortest distance). The angle of binding (see Figure 3) of the anions with the pyridyl rings is commented upon as being far from those predicted by Deyà and coworkers (82° the steepest), a difference which is attributed to the nature of the pyridyl rings.^{12c} No theoretical studies involving anion- π interactions with pyridyl rings accompanied this work, and no comment was made on the angle of binding between the $[Cl]^-$ anion and the tetrazine rings.

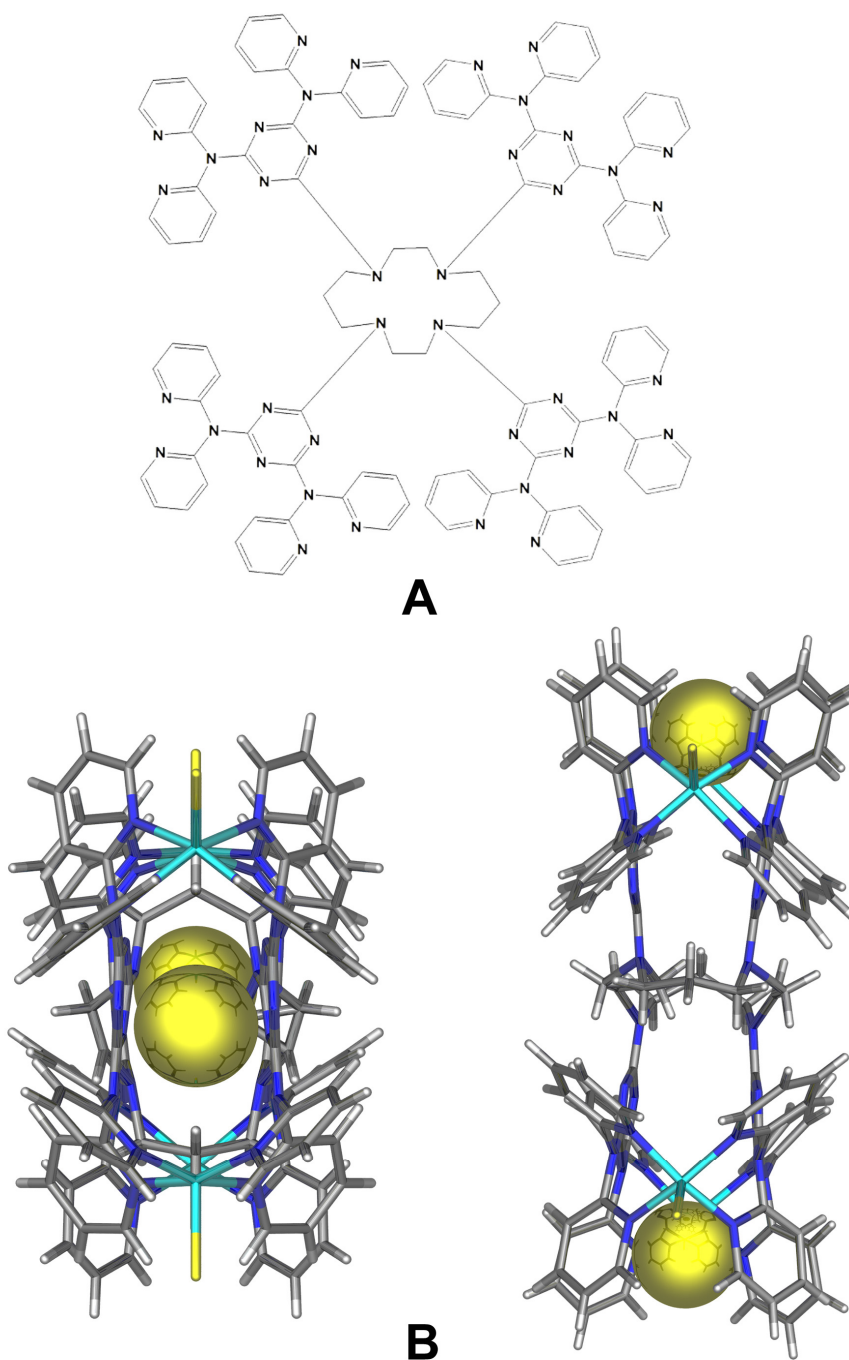


Figure 12: (a). Line drawing of $N,N'N'',N'''$ -tetrakis{2,4-bis(di-2-pyridylamino)-1,3,5-triazineyl}-1,4,8,11-tetraazacyclotetradecane ligand (L2), and (b) Crystal structure of $[Cu_4(L2)Cl_4](Cl)_4(H_2O)_{13}$, complex *ii* from 2 different perspectives. Figures adapted from reference 36.

After these first two structures were communicated, other research groups began to take note of anion- π interactions in their structures. Several studies investigating other properties made note of these interactions and mentioned that they may have an impact on the resulting structure. These studies, however, did not include any type of theoretical evidence as a back-up for their claims. Instead, they relied upon the distance criteria defined by the works of Deyà and Mascà, an indication that the community had accepted these basic guidelines.^{12b,c} The structures recently reported in this vein are shown in Figure 13.^{37,38,39}

b. Structural Evidence with Theoretical Support

As other researchers began recognizing anion- π interactions, Deyà and coworkers collaborated with the synthetic group of Saczewski to produce a combined crystallographic and computational study on anion- π interactions involving cyanuric acid derivatives.⁴⁰ The computational portion of the work involved the study of cyanuric, thiocyanuric, dithiocyanuric and trithiocyanuric acid (ICA, TIA, DIA, and TTA, respectively), four derivatives that differ only in the number of exocyclic sulfur atoms (Figure 14). As each oxygen atom is replaced by a sulfur atom, the ring is expected to become less π -acidic since sulfur is less electronegative than oxygen. The results (given in Table 5) of the MP2¹⁴/6-31++G**¹⁷ calculations (with both basis set superposition error (BSSE) and ZPE corrections), reveal several different trends. The most intriguing observation is that the number of sulfur atoms versus oxygen atoms on the rings of these cyanuric acid derivatives does not seem to affect the overall binding energy of the complexes (i. e. all the complexes with [Br]⁻ have similar calculated binding energies). The second finding is that the strength in the order of binding is [F]⁻ > [Cl]⁻ > [Br]⁻.

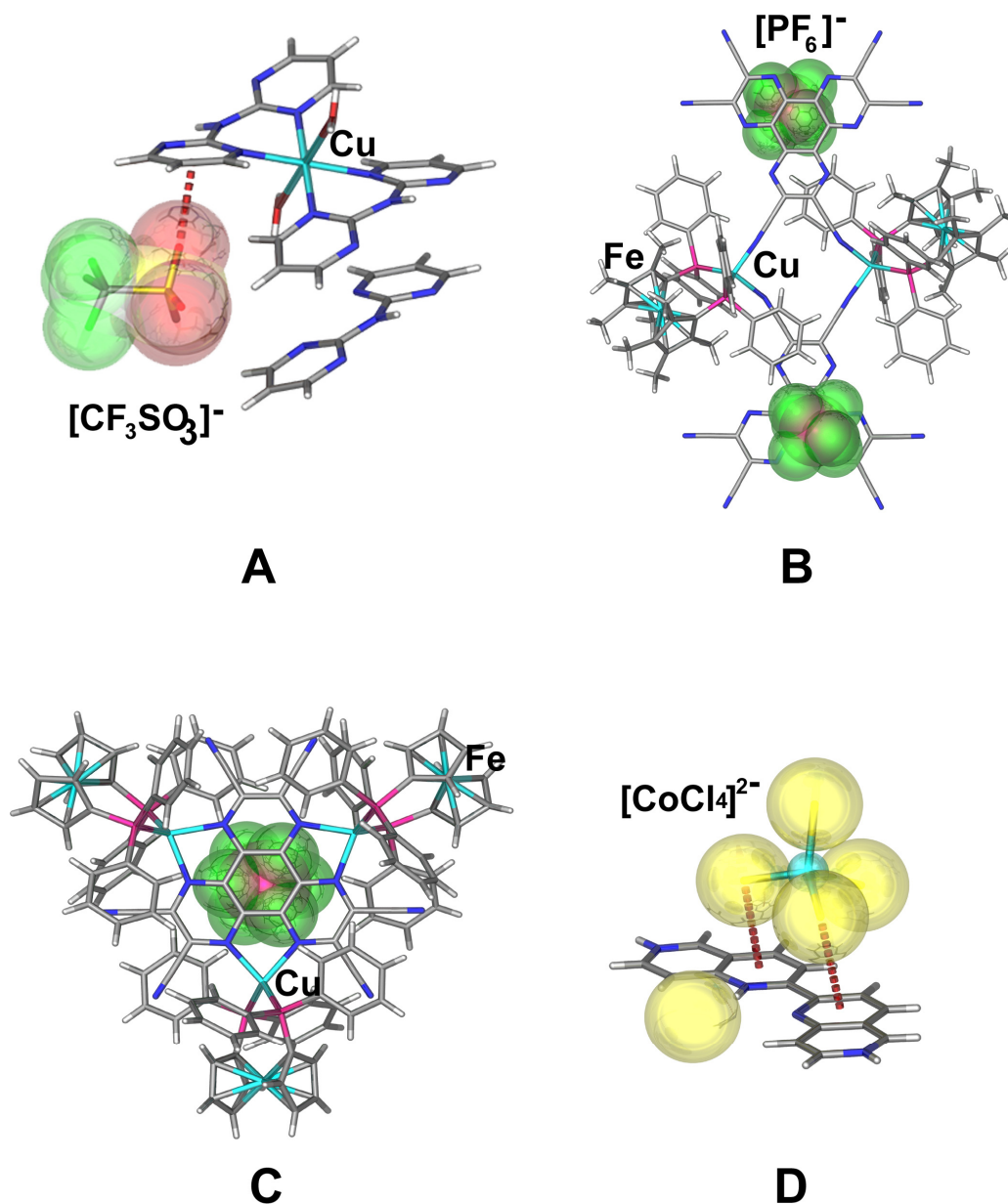


Figure 13: Several structures from the recent literature that are reported to involve anion- π interactions: (a) $\{[\text{Cu}(\text{C}_8\text{N}_5\text{H}_7)_2][\text{CF}_3\text{SO}_3]\} \cdot \text{C}_8\text{N}_5\text{H}_7^+$, (b) $\{[\text{Cu}(\text{dppFc}^*)]_2\{\text{HAT}(\text{CN})_6\}_2\}[\text{PF}_6]_2$, (c) $\{[\{\text{Cu}(\text{dppFc})\}_3\{\text{HAT}(\text{CN})_6\}][\text{PF}_6]\}^+$, and (d) $(\text{C}_{16}\text{H}_{13}\text{N}_4)[\text{CuCl}_4][\text{Cl}]$. $\text{dppFc}^* = 1,1'$ -bis(diphenyl-phosphino) octamethylferrocene, and $\text{dppFc} = 1,1'$ -bis(diphenyl-phosphino) ferrocene.^{37,38,39}

The AIM¹⁸ analysis also yielded the same trend when the cage (3,+3) critical point is considered; the larger value means a stronger interaction (see Table 5). MIPp²⁰ results with the [Cl]⁻ complexes showed, as expected from previous studies, that the compounds rely mostly on electrostatic and polarization contributions to the total binding energy, with the electrostatic term dominating. As more oxygen atoms are replaced by sulfur atoms, however, the polarization term becomes more important. This trend is common in the breakdown of anion- π interactions involving less π -acidic rings.

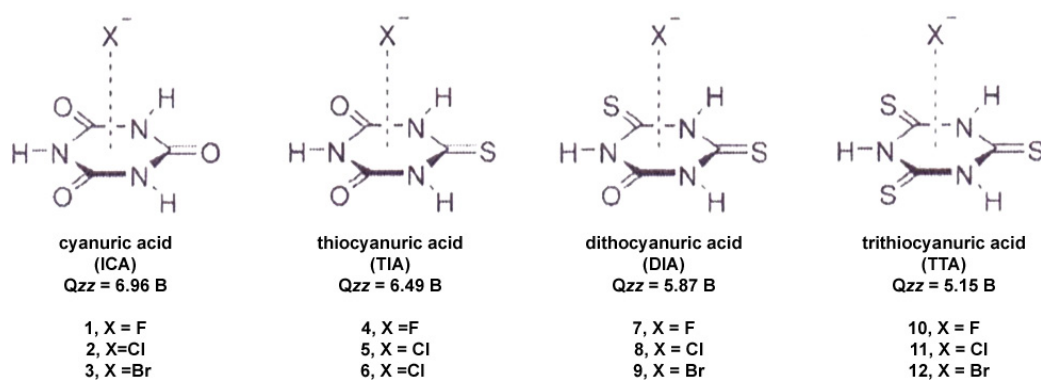


Figure 14: Line drawings, labels, and quadrupole moments of the cyanuric acid derivatives studied theoretically in reference 40.

To experimentally study these cyanuric acid derivatives with halides, the two ligands (L3 and L4) shown in Figure 15a were synthesized, differing only in the number of sulfur atoms on the ring. When these molecules were reacted with HCl, two similar structures formed (See Figure 15b). The NH₃ group of both ligands participate in a hydrogen bond with the [Cl]⁻ anion, allowing the anion the freedom to reside over the central portion of the cyanuric acid ring (3.18 Å and 3.28 Å for compounds *iii* and *iv*, respectively).

Table 5: Interaction energies (E), all in kcal/mol with and without the basis set superposition error (BSSE) and zero point energy (ZPE) corrections and equilibrium distances (R_e , Å) at the MP2/6-311++G** level of theory. The last column is the value of the (3,+3) cage critical point which indicates an electrostatic interaction between the anion and the ring. The table is adapted from reference 40.

Compound	E	E_{BSSE}	$E_{BSSE+ZPE}$	R_e	$10^2\rho(+3,+3)$
1	-32.28	-27.95	-26.85	2.190	1.2834
2	-22.81	-16.45	-15.50	2.848	0.8919
3	-25.18	-15.04	-14.27	2.979	0.8746
4	-33.09	-28.28	-27.27	2.197	1.2626
5	-23.16	-16.45	-15.63	2.852	0.8871
6	-25.81	-15.13	-14.40	2.981	0.8763
7	-32.90	-27.67	symmetry constraints	2.168	1.2446
8	-23.18	-16.33	-15.39	2.865	0.8729
9	-26.15	-15.00	-14.27	2.988	0.8714
10	-31.35	-26.34	-25.13	2.255	1.2068
11	-22.83	-15.81	-14.69	2.887	0.8530
12	-26.25	-14.61	-13.73	2.999	0.8602

The ring in complex *iii*, which was predicted to be more favorable (closer to the anion) by the calculations, contains one more highly electronegative oxygen atom than the ring in complex *iv* (See Figure 15).

The last two studies which are much more recent, have appeared in the literature after the aforementioned studies. The first one, performed by Reedijk and coworkers, involves the ligand (L5) 2,4,6-tris(di-2-picolylamino)[1,3,5]triazine (Figure 16a).⁴¹ The ligand L5 was reacted with both $Zn(NO_3)\cdot 6H_2O$ and $Cu(NO_3)\cdot 6H_2O$ to yield two different structures of the formula $[M_3(L5)(NO_3)_2(H_2O)_6](NO_3)_4$ ($M = Zn(III)$ and $Cu(III)$) that participate in anion- π interactions between a triazine ring from the ligand and an oxygen atom from the nitrate (see structure *v* with distances in Figure 16b).

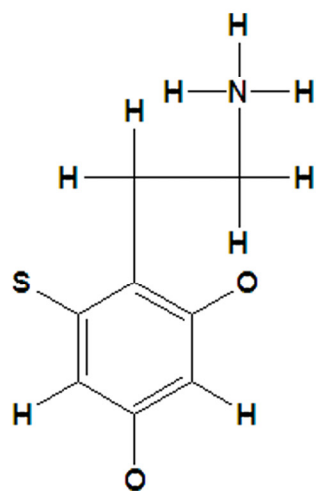
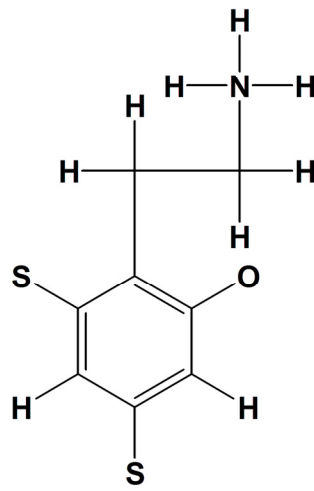
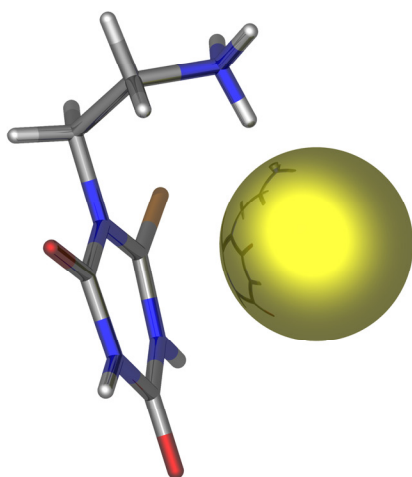
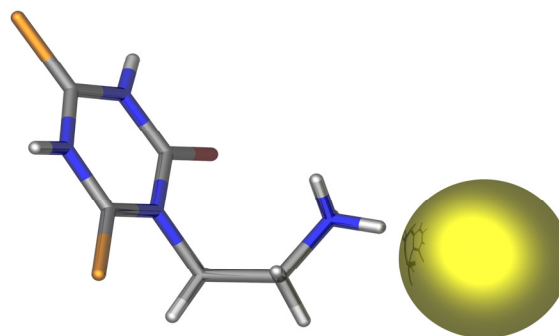
**L3****L4*****iii******iv***

Figure 15: Results of the cyanuric acid study: Line drawings of ligands L3 and L4, and crystal structures of compounds *iii* and *iv*. C = grey, O = red, Cl = yellow, N = blue, H = white, and S = orange. Figure adapted from reference 40.

The most intriguing part, however, is that in structure **v**, the triazine ring of the ligand seems to be participating in two different anion- π interactions at the same time, one over each face of the ring. To study this result theoretically, Reedijk and coworkers started by conducting a SPE calculation on the “triazine ring + 2 anions” fragment from these structures at the MP2¹⁴/6-311++G(3df,p) level of theory. The two anions were separated from the ring at different distances R and R' (see Figure 16c), the results indicating that the binding energy was most favorable (-22.38 kJ/mol) at R = R' = 3.2 Å distances (very different from the ~ 0.3 -0.4 Å difference found in the actual structure). Although they report the angles of interaction (see Figure 3) in the experimental structure to be much smaller than the predicted favorable 90° (largest angle being 68.0(2)°), no comment is made on the discrepancy.

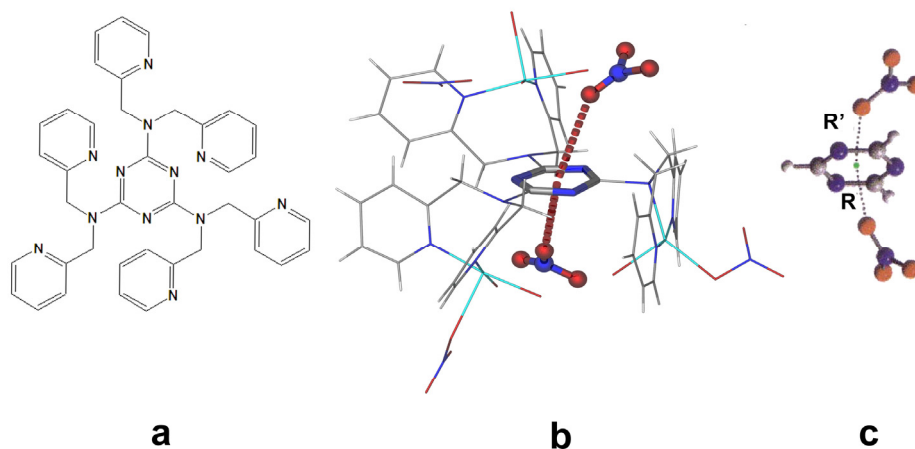


Figure 16: (a) Line drawing of L5, or 2,4,6-tris(di-2-picoylamino)[1,3,5]triazine, (b) crystal structure (**v**) of $[\text{Cu}_3(\text{L5})(\text{NO}_3)_2(\text{H}_2\text{O})_6](\text{NO}_3)_4$ and (c) theoretical model used for computational studies of complex **v**. Red = O, dark blue = N, light blue Cu, grey = C, and white = H. Figure reproduced from reference 41.

When the authors attempted to optimize the geometry of this anion-ring-anion system, the anions moved far apart from each other, most likely due to the repulsive features of the calculation.

The final study to fall under this category, also performed by Reedijk and coworkers, involved the highly complicated ligand *N,N',N'',N'''*-tetrakis{2,4-bis(di-2-pyridylamion)-1,3,5-triazin-6-yl}trihylenetetramine (L6, Figure 17a) and $\text{Cu}(\text{NO}_3)_2 \cdot 3\text{H}_2\text{O}$.⁴² The structure obtained, $[\text{Cu}_4(\text{L6})(\text{NO}_3)_4][\text{NO}_3]_4 \cdot 12\text{H}_2\text{O}$ (*vi*), shown in Figure 17b, has the unusual feature of a triazine ring participating in a π - π stacking interaction on one side, and an anion- π interaction with $[\text{NO}_3]^-$ anion oxygen atom on the other side. When these two rings and anions participating in the interaction in the structure were subjected to theoretical AIM¹⁸ optimization calculations, two issues became evident (Figure 17c). The first one was that two different interactions on either side of the triazine ring are favorable. The second observation was that the theoretically obtained distances were much different than those observed in the crystal structure (i.e., 3.42(7) Å and 3.051 Å, actual and theoretical anion- π distances, respectively, and 3.45(9) Å and 4.16 Å actual and theoretical π - π distances, respectively). These discrepancies were attributed to the calculation being in the gas phase, and therefore more favorable for the anion- π interaction. Also, the calculation did not take into the effect the entire structure which is highly influenced by crystal close packing. This is likely to be the reason for the discrepancy in the π - π distances between the theoretical model and the experimental structure.

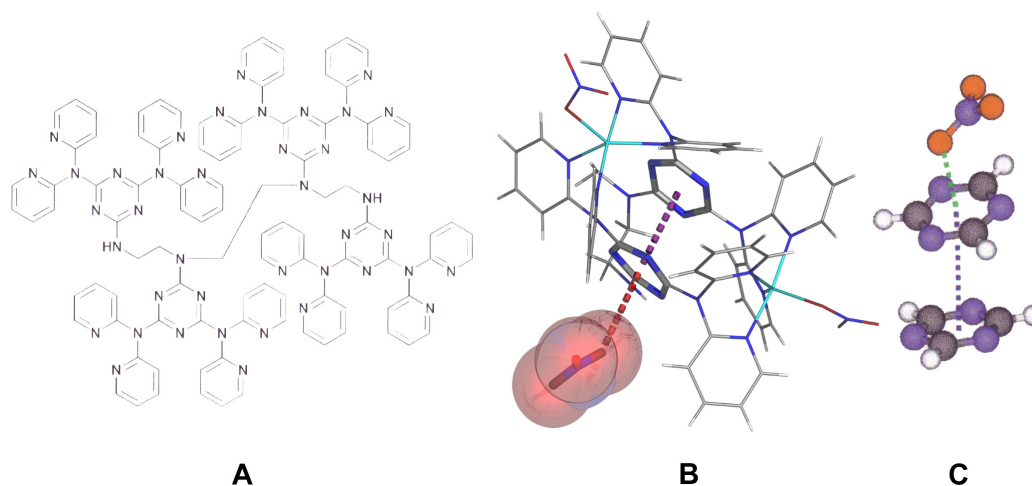


Figure 17: (a) Line drawing of the (L6) ligand N,N',N'',N''' -tetrakis{2,4-bis(dipyridylamino)-1,3,5-triazine-6-yl}triethyleneteramine, (b) crystal structure of $\{[Cu_2(L6)(NO_3)_2][NO_3]\}^+$, and (c) the model used for the BLYP optimization and AIM evaluation for the theoretical part of the study. Red = O, dark blue = N, light blue = Cu, grey = C, and white = H. All figures are adapted from reference 42.

c. Solution Evidence

Despite the increasingly large number of reports touting solid-state evidence of anion- π interactions, very few studies have emerged that investigate this phenomenon in solution. The first conclusive solution evidence to recognize anion- π interactions (although not officially named), was provided by Zimmermann and coworkers in 1991 and 1992 which went only so far as to assume remaining association energies to anion-aromatic interactions.¹³ The first study that focused primarily on investigating these interactions in solution was performed on an *N*-confused Porphyrin Ni(II) complex. Maeda and coworkers altered a *N*-confused porphyrin (a porphyrin ring that has a α - β' linked pyrrole ring, and thus possesses a reactive inner carbon and a peripheral nitrogen) by adding both plain phenyl groups and fluorinated phenyl groups to its periphery (L7, See Figure 18).⁴³ Normally, at the peripheral nitrogen atom, binding can occur with several different transition

metal cations. In this study, the square planar metals Ni(II), Pd(II) and Cu(II) were employed for complexing with these altered N-confused porphyrins. Much to the authors' surprise, the counter ion participated not only in an expected hydrogen bond at the confused ring, but also showed evidence of attracting the closest fluorinated phenyl ring as well (See Figure 18).

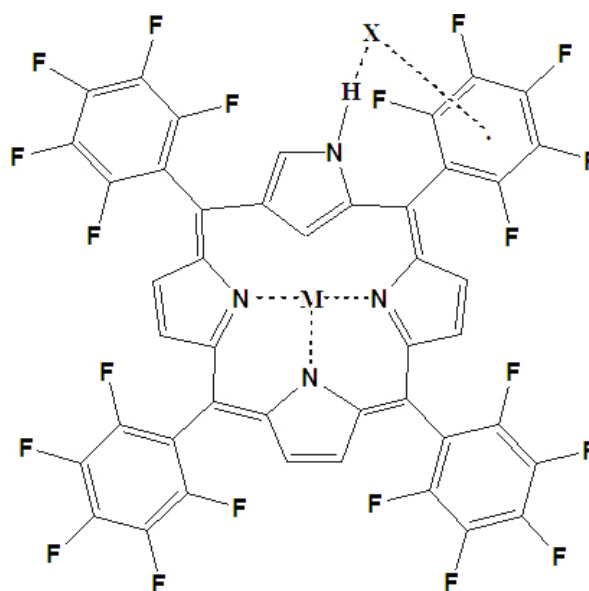


Figure 18: Line drawing of how an *N*-confused porphyrin (L8) will bind to a halide anion $[X]^-$ in solution through both an H-bond from the peripheral N atom on the *N*-confused pyridine as well as through an anion- π interaction with the nearest C_6F_5 ring. Drawing adapted from reference 43.

The evidence for this unlikely attraction was derived from both ^{19}F NMR and from ^1H -NMR experiments. The ^{19}F NMR of the Ni(II) complex of both porphyrin species—the ortho, para, and meta F signals of the C_6F_5 shifted to a higher field (became more aromatic), while the ^1H -NMR spectrum for porphyrin rings without

fluorinated phenyl groups only contained a shift in the proton that corresponded to hydrogen-bonding with the peripheral N-H group of the porphyrin with ^1H NMR.

Kochi and coworkers examined solution interactions by UV/Vis spectroscopy.⁴⁴ Beginning with a solution of one of the π -acidic ring molecules shown in Figure 19a, equivalents of $[\text{Cl}]^-$, $[\text{Br}]^-$, or $[\text{I}]^-$ were slowly added. This addition caused a new peak to appear in the spectrum, indicative of charge transfer from the anion to the π -system. Figure 19b shows the spectrum result of tetracyanopyrazine with $[\text{Br}]^-$ as an example. A ring of this type would normally have a strong absorption at $\lambda = 220\text{-}300$ nm. The new peak that arises at $\lambda_{\text{max}} = 400$ nm upon addition of the halide indicates a 1:1 stoichiometry of the anion/ring complex after treatment of the data.

The authors were also able to grow crystals of TCP with all three halides, an example of which (structure *vi*) is shown in Figure 19c. In all cases, notwithstanding the anion-ring ratio, close contacts exist between the halide anion and one or more neighboring rings, indicative of anion- π interactions. Although such structures most likely do not exist in solution, the authors state that these structures are further evidence that these ring/anion mixtures are participating in anion- π interactions. One conflicting observation, however, from previous theoretical work, is that in all structures, the anion does not seem to prefer to reside over the central point of the ring. Instead, it is slipped toward the carbon atoms at the edge of the ring.

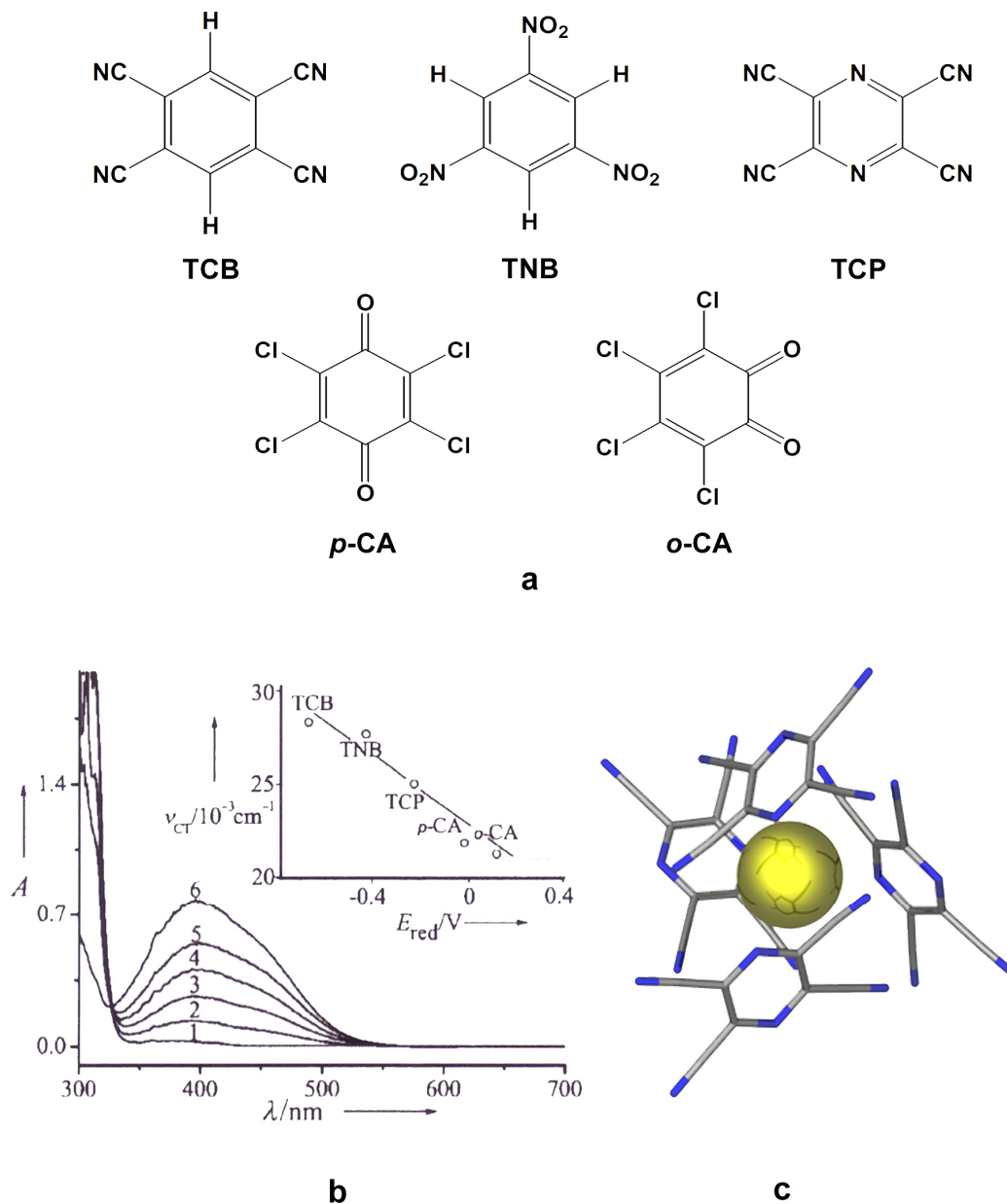


Figure 19: (a) Line drawings of the ring systems examined in the UV/Vis study of Kochi and coworkers, (b) UV/Vis spectra of a 5 mM tetracyanopyrazine (TCP) ring in acetonitrile with increasing concentrations of [(*n*-But)₄N][Br] added. The peak at 400 nm slowly increases because of charge-transfer from the anion to the TCP ring. Concentrations: 1 = 0 mM, 2 = 4.9 mM, 3 = 19 mM, 4 = 46 mM, 5 = 83 mM, and 6 = 208 mM of [Br⁻]. Inset is the Mulliken dependence of the energy absorption band (ν_{CT}), which equals 400 nm for TCP with [Br⁻], with the reduction potential of the π -acceptor ring from 22a. (c) Crystal structure of TCP with [Cl⁻] (*vii*). The [(*n*-But)₄N]⁺ cation is omitted for the sake of clarity. Blue = N, grey = C, and yellow = Cl. Figures adapted from reference 44.

Arguably the most convincing structural evidence for anion- π interactions has been reported by Fairchild et al. These researchers functionalized Collet's cryptophane $-E[(+)-\mathbf{E}]^{45}$ with $[\text{Cp}^*\text{Ru}]^+$ to make a capsule with a π -acidic interior (see Figure 20a).⁴⁶ Within this capsule resided the counter ion used in the synthesis, captured in the solid state as either a $[\text{CF}_3\text{SO}_3]^-$ (**viii**) or $[\text{SbF}_6]^-$ (**ix**) salt (see Figure 20b). Both of these anions are in close contact with the phenyl rings on the inner surface of this $[(+)-\mathbf{2}]^{6+}$ cryptophane. In the case of the triflate salt **viii**, the disorder was too severe to obtain accurate F-ring distances. The $[\text{SbF}_6]^-$ structure **ix**, however, revealed the close F-centroid contact of 3.08 Å and the extremely close anion F atom-phenyl C atom contact of 2.97(1) Å.

In solution, these structures were shown to retain specific interactions with the anion and indicate preference for specific shapes and sizes. The triflate salt **viii** was dissolved in CD_2Cl_2 to give a 1:5 triflate ratio (5 peripheral anion signals, one encapsulated) as can be seen in Figure 20c. When this same structure is dissolved in CD_3CN and subjected to 6 equivalents of $[\text{PF}_6]^-$, the triflate is exchanged for this smaller anion. No exchange was observed with smaller anions such as $[\text{BF}_4]^-$, leading to the speculation that the smaller anions cannot make proper anion- π contacts with the inner surfaces of the π -acidic cryptophane rings.

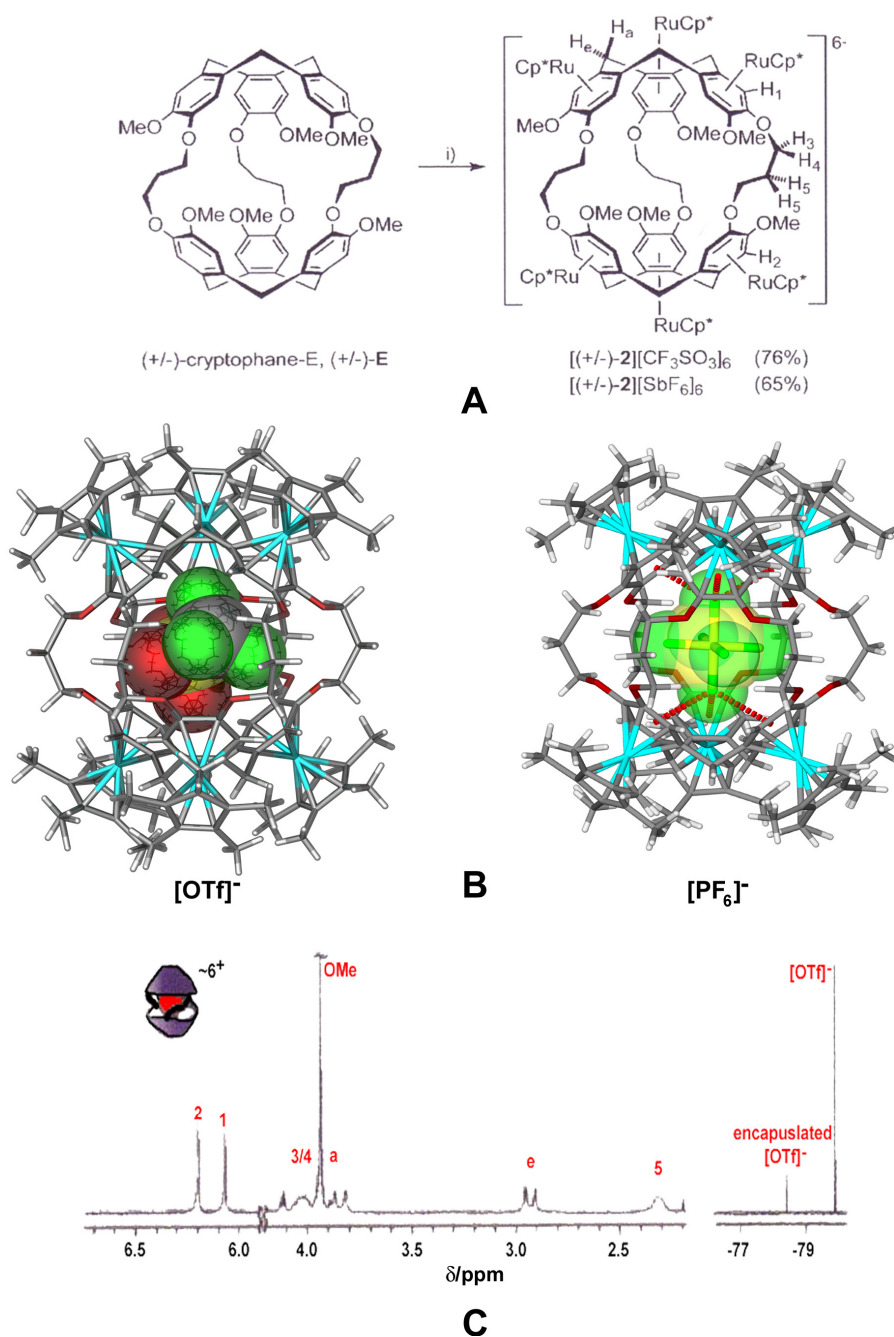


Figure 20: Synthesis of $(+/-)\text{-}\{\text{Cp}^*\text{Ru}\}_6(\text{E})^{6+}$ from $(+/-)$ -cryptophane E, $(+/-)$ -E and $[\text{Cp}^*\text{Ru}][\text{X}]$, where $\text{X} = [\text{CF}_3\text{SO}_3]^-$ or $[\text{PF}_6]^-$, (b) $\{[(+/-)\text{-}2][\text{CF}_3\text{SO}_3]\}^{5+}$ (**viii**) and $\{[(+/-)\text{-}2][\text{SbF}_6]\}^{5+}$ (**ix**). Red = O, Yellow = S, dark blue = N, light blue = Ru, green = F, grey = C, and white = H. (c) Left: ^1H NMR spectrum of **viii** in CD_3NO_2 at equilibrium, and right: ^{19}F NMR spectrum of **viii** in CD_3NO_2 at equilibrium. Figures are taken from reference 46.

The final study thus far that provides experimental evidence for anion- π interactions was communicated by Berryman and coworkers in 2006.⁴⁷ The anion-trapping ligands L8 and L9, shown in Figure 21a, were synthesized in order to form a hydrogen-bond with a halide at the amine hydrogen to position a halide over the phenyl derivative. The fluorinated derivative L8 was expected to participate in anion- π interactions while L9 was not.

¹H NMR titration experiments in CDCl₃ gave the binding constants of both ligands in the presence of NEt₄⁺ salts of [Cl]⁻, [Br]⁻ and [I]⁻. In the case of the fluorinated ligand, the binding constants are large (K_a (M⁻¹) = 30, 20, and 34 for [Cl]⁻, [Br]⁻, and [I]⁻, respectively). The benzene derivative has such small binding constants in comparison that they cannot even be measured appropriately (< 1 in all cases). The most convincing proof of an anion- π interaction is that, with the fluorinated ligand, the [I]⁻ experiment gave the most favorable binding constant. Normally, it would be expected that the [Cl]⁻ complex would be more favorable because of the presence of a hydrogen-bonding opportunity. The authors speculated that the larger, more polarizable [I]⁻ anion was able to participate in a stronger interaction with the C₆F₅ ring and thus, further stabilize the interaction.

For more support of their conclusions, Berryman and coworkers optimized the ligands in the presence of [Cl]⁻ at the HF¹⁶ level of theory with the 6-31+G*¹⁷ basis set (see Figure 21b).

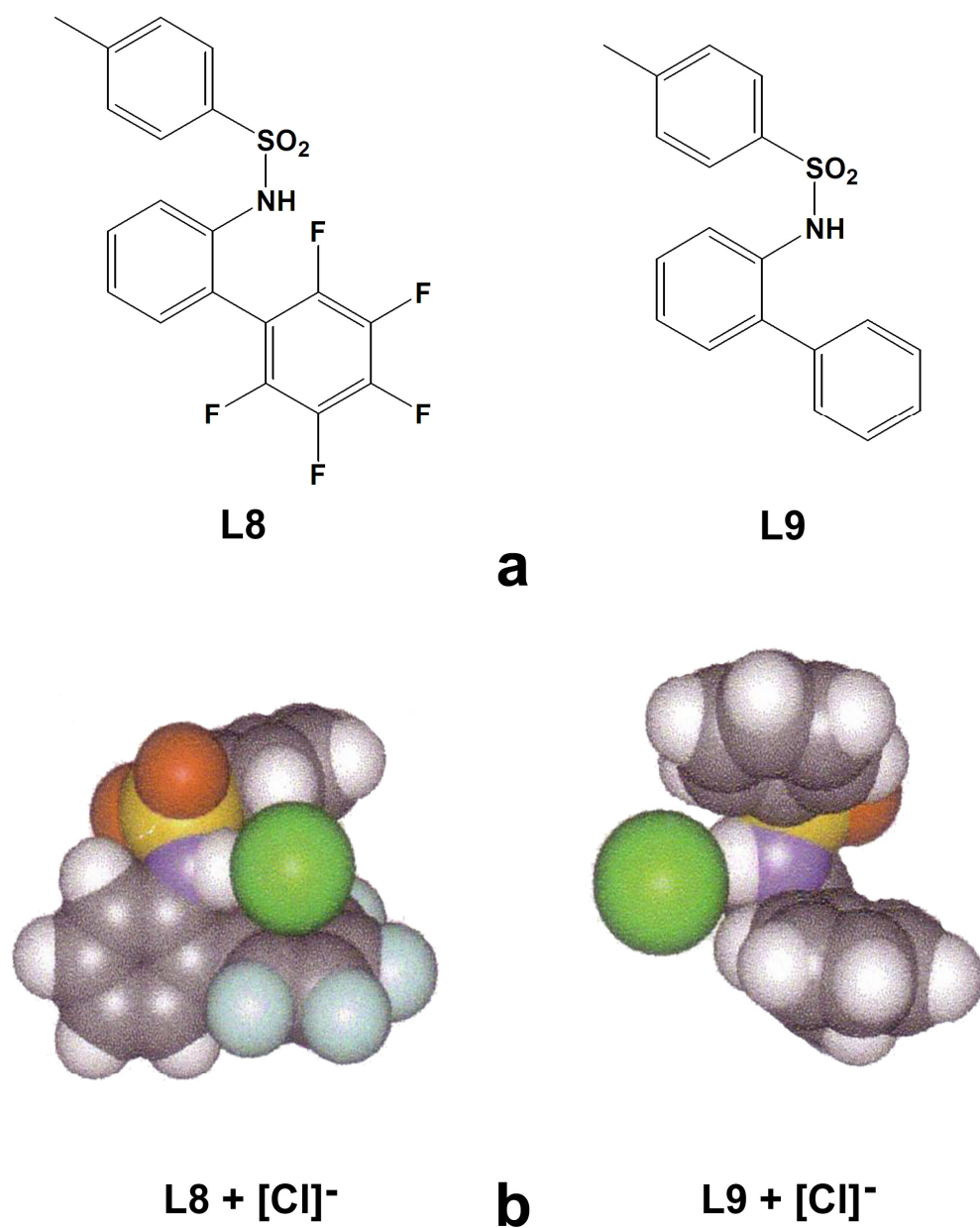


Figure 21: (a) Line drawings of the ligands L8 and L9, and (b) HF/6-31+G* geometry optimization results of L8 and L9 in the presence of [Cl]⁻. Figures adapted from reference 47.

The fluorinated derivative clearly shows both a hydrogen-bonding and anion- π interaction with the anion, while the benzene version of the ligand shows only a hydrogen bond between the anion and the amine nitrogen. This study, along with many of the previously discussed investigations, has set the stage for the research presented in this dissertation.

D. Previous Work in Our Laboratories

At the beginning of the project that is highlighted herein, the groundwork was already laid for the study of anion- π interactions. A former student, Cristian Campos-Fernández, reacted Ni(II) salts with the ligand 3,6-(2'-bispyridyl)-1,2,4,5-tetrazine (bptz) in acetonitrile (Figure 22a). The resulting complex, $[\text{Ni}_4(\text{bptz})_4(\text{CH}_3\text{CN})_8\subset\text{BF}_4][\text{BF}_4]_7$, formed from a 1:1 ligand-to-metal ratio (see Figure 22b).⁴⁸ The presence of an encapsulated $[\text{BF}_4]^-$ anion presented the possibility that the structure was anion-templated. When the larger $[\text{SbF}_6]^-$ counter-ion was used in place of $[\text{BF}_4]^-$, the $[\text{Ni}_5(\text{bptz})_5(\text{CH}_3\text{CN})_{10}\subset\text{SbF}_6][\text{SbF}_6]_9$, a Ni pentagon, was formed (Figure 22c).⁴⁹ In the course of these studies, a square with Ni(II) ions and $[\text{ClO}_4]^-$ was prepared as well as Zn(II) analogues of the square structures. It was hypothesized that, if these structures were templated by the anion present, then the final controlling effects of assembly, based on the observation of a close proximity of the encapsulated anions to the tetrazine rings of the bptz ligands, could be due to anion- π interactions. These studies represented a starting point for the in-depth investigation of anion- π interactions in the structures presented in this thesis.

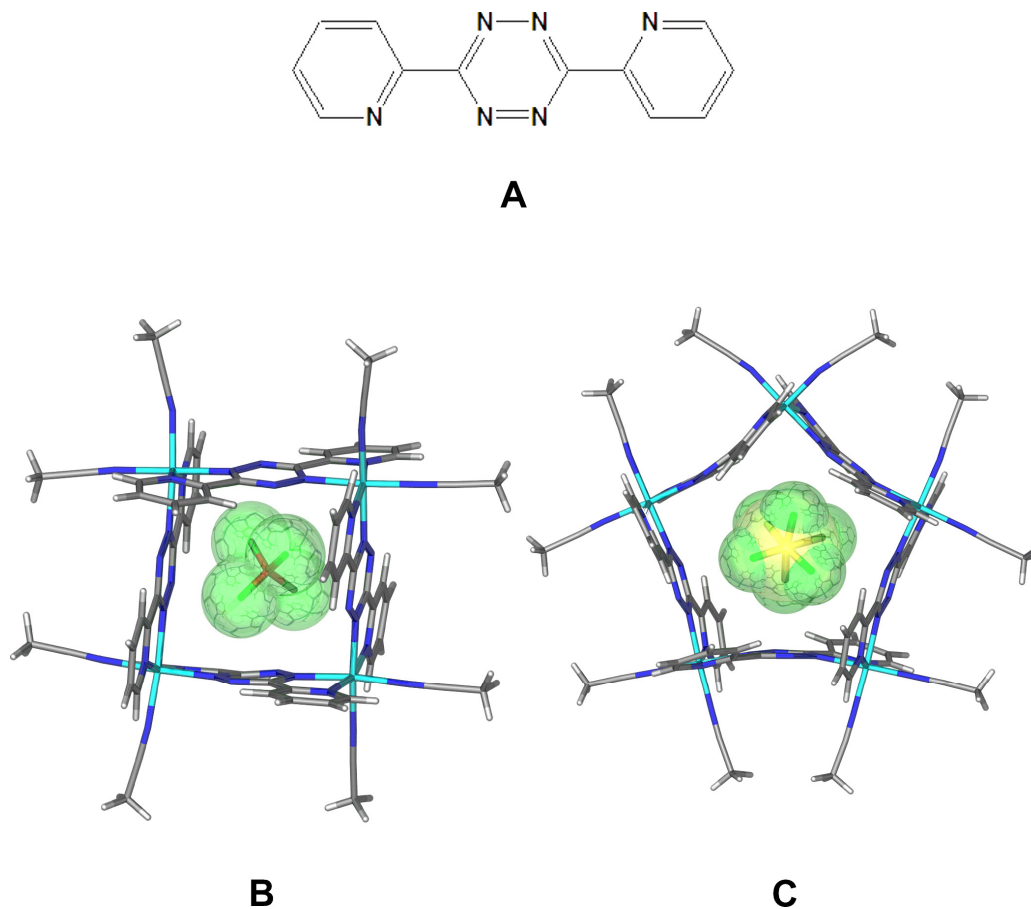


Figure 22: (a) Line drawing of the bptz ligand in the trans-orientation, (b) crystal structure diagram of $[\text{Ni}_4(\text{bptz})_4(\text{CH}_3\text{CN})_8]\cdot\text{BF}_4^{7+}$, and (c) crystal structure diagram of $[\text{Ni}_5(\text{bptz})_5(\text{CH}_3\text{CN})_{10}]\cdot\text{SbF}_6^{9+}$. Figures are taken from references 48 and 49.

E. Systematic Experimental and Theoretical Investigations of Anion- π Interactions

The results in this dissertation are aimed at a detailed investigation of anion- π interactions. Beginning with a study to demonstrate that anions are the main controlling element in self-assembled coordination compounds, it is shown that large and complex anions can indeed have a templating influence. Taking this one step further, we then set out to prove that these anions act as templates through anion- π interactions. By using Ag(I) salts and ligands containing phenyl rings of differing π -

acidity, we were able to compare structures, by both theoretical and experimental means, that were controlled by anion- π interactions with those that were dictated by crystal close-packing effects. As an offshoot of these studies, a theoretical and experimental study examining complex anions in the presence of simple, electron-deficient ring systems was undertaken. Throughout these studies, we were able to establish the parameters to determine the presence of anion- π interactions and to help define a proper description of these interactions when they involve complex anions.

CHAPTER II

ANION TEMPLATE EFFECT ON THE SELF-ASSEMBLY AND INTERCONVERSION OF METALLACYCLOPHANES*

I. Introduction

Traditional synthetic chemistry involves the design of molecules by the stepwise formation of covalent bonds in a prearranged fashion. Such an approach is not feasible, however, for the high-yield syntheses of large, complex molecules from multiple building blocks. Instead, one must turn to self-assembly reactions that facilitate the connection of individual building blocks via non-covalent interactions, which permit the integration of desired functional groups into the resulting supramolecules. In order to achieve the formation of a single product in high yield, the precursors of the self-assembled structures must be stable and relatively rigid, whereas the bonds that join the components should be sufficiently labile so that the organization of the supramolecular assembly is ultimately under thermodynamic control. The final product represents a minimum in the energy profile of the system based on a combination of enthalpic and entropic factors.⁵⁰

Transition metal coordination bonds satisfy the aforementioned criteria and have been exploited for the synthesis of numerous metal-based supramolecular architectures in recent years.⁵¹

*Reprinted with permission from “Anion Template Effect on the Self-Assembly and Interconversion of Metallacyclophanes” by Cristian Saul Campos-Fernández, Brandi L. Schottel, Helen T. Chifotides, John Bacsa, Jitendra K. Bera, John M. Koomen, David H. Russell, and Kim Dunbar, *J. Am. Chem. Soc.* 2005, 127, 12909-12923.

Metal ion complexation by multidentate ligands generates equilibrium mixtures of cyclic and open-frame oligomeric structures depending on the number and geometry of the individual building blocks. The factors that influence the size and shape of these structures are complex and include the number, relative strength, and directionality of weak interactions between the building blocks.⁵² The product distribution of a particular reaction under thermodynamic control is dictated by the relative free energies of the products,⁵³ whereas the stability of a given cyclic product is determined, to some extent, by the ring strain of the molecule as well as by the concentration of the starting materials.⁵⁴ Dilute solutions favor ring closure whereas concentrated solutions result in the isolation of infinite polymers. Self-assembly reactions may also depend on a variety of other parameters such as temperature, pressure and identity of the solvent.

Armed with increasing knowledge of non-covalent interactions,⁵⁵ chemists have applied the tools of molecular recognition to favor a desired supramolecular entity. A useful approach in this direction is the use of a chemical species that selectively recognizes and stabilizes the desired product in a mixture via supramolecular interactions. Herein, we report a comprehensive investigation of an anion-templated self-assembly reaction, namely that of solvated first-row transition metal ions M(II) (M= Ni, Zn, Mn, Fe, Cu) with the divergent bis-bipyridine ligand 3,6-bis(2-pyridyl)-1,2,4,5-tetrazine (bptz; Figure 23). Reports on the synthesis of the molecular polygons $[\text{Ni}_4(\text{bptz})_4(\text{CH}_3\text{CN})_8\text{C}\text{BF}_4][\text{BF}_4]_7$ ⁴⁸ and $[\text{Ni}_5(\text{bptz})_5(\text{CH}_3\text{CN})_{10}\text{C}\text{SbF}_6][\text{SbF}_6]_9$,⁴⁹ in the presence of the appropriate anions, have appeared in preliminary communication form. The combined results of X-ray

crystallography, mass spectrometry and NMR studies provide compelling evidence that the anions play a decisive role in the formation of a particular cyclic structure both in the solid state and in solution.

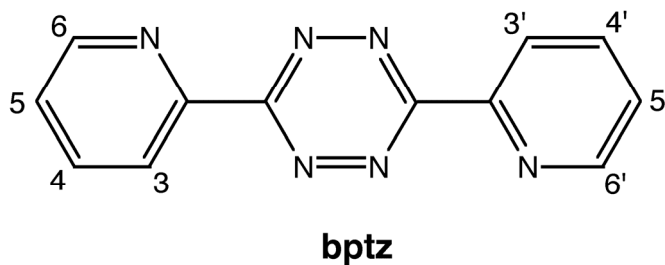


Figure 23: Line drawing of 3,6-bis(2'-pyridyl)-1,2,4,5-tetrazine with appropriate ^1H NMR labels.

II. Experimental

A. Materials

All manipulations were carried out under an inert atmosphere of N_2 gas with the use of dry-box and Schlenk-line techniques. Acetonitrile, methanol, dichloromethane, tetrahydrofuran (THF), benzene and toluene were dried by conventional methods, distilled over nitrogen and deoxygenated prior to use. The compounds $[\text{Ni}(\text{CH}_3\text{CN})_6][\text{X}]_2$, ($\text{X} = [\text{BF}_4]^-$, $[\text{SbF}_6]^-$ or $[\text{CF}_3\text{SO}_3]^-$), $[\text{Zn}(\text{CH}_3\text{CN})_4][\text{BF}_4]_2$, and $[\text{Mn}(\text{CH}_3\text{CN})_6][\text{BF}_4]_2$ were synthesized by literature procedures.⁵⁶ The salts $\text{M}(\text{ClO}_4)_2 \cdot x\text{H}_2\text{O}$ ($\text{M} = \text{Ni}(\text{II})$, $\text{Zn}(\text{II})$, $\text{Mn}(\text{II})$, $\text{Fe}(\text{II})$, $\text{Cu}(\text{II})$) were purchased from Aldrich and used without further purification. **(Caution! Perchlorate salts of metal complexes with organic ligands are potential explosives. While we have encountered no incidents in the preparation and reactivity studies of the salts, it is advisable to use only small amounts and to handle the compounds with caution in the presence of wet solvents).** The bptz ligand was prepared by a literature

method and recrystallized from benzene.⁵⁷ The tetra-*n*-butylammonium salts of iodide, nitrate, periodate, tetrafluoroborate, hexafluorophosphate and tribromide were purchased from Aldrich and used without further purification.

B. Physical Measurements

Infrared spectra were recorded in the range 4000-400 cm^{-1} using a Nicolet 470 FT-IR spectrometer on Nujol mull samples suspended between KBr plates. The ^1H NMR spectra were recorded on a 500 MHz Inova spectrometer with a 5-mm switchable probehead. The ^{19}F and ^{11}B NMR spectra were recorded on a 400 MHz Unity Inova spectrometer with a 5-mm autoswitchable probe operating at 375.99 and 128.22 MHz, respectively. The ^1H NMR spectra were referenced relative to the residual proton impurities of the deuterated solvent ($\text{CD}_3\text{CN}-d_3$). The ^{19}F NMR spectra were referenced relative to CFCl_3 (0 ppm), whereas the ^{11}B NMR spectra were referenced relative to BF_3 in CHCl_3 at 0 ppm. Electrospray mass spectra were obtained with a Sciex Qstar Pulsar and a Protana Nanospray ion source. Data were acquired with a TOFMA 2.0RC3 and analyzed with BioiMultiView 1.5RC3. Solutions of the metal complexes were diluted to approximately 10 μM , and 7.0 μL aliquots were loaded into the Au/Pd coated silica spray needle. Ionspray voltages were set between 900 and 1200 V. Theoretical isotope ratio calculations were performed using the program ISOPRO3.0.⁵⁸

C. Syntheses

1. Preparation of $[\text{Ni}_4(\text{bptz})_4(\text{CH}_3\text{CN})_8][\text{BF}_4]_8$ (1) - Compound **1** was synthesized using a previously reported procedure.⁴⁸ IR (KBr mull) cm^{-1} : 2321, 2325 (w, $\nu(\text{C}\equiv\text{N})$), 1064 (s, $\nu(\text{B-F})$). UV-Vis: λ , nm (ϵ , $\text{M}^{-1}\text{cm}^{-1}$): 510 (530), 680 (266). ES-MS: m/z 1787.3 $[\text{Ni}_4(\text{bptz})_4(\text{BF}_4)_7]^+$. Yield: 97 mg (84%). Anal. Calcd for

Ni₄C₆₄N₃₂H₅₆B₈F₃₂: C, 34.90; N, 20.35; H, 2.56. Found: C, 35.21; N 19.83; H, 2.52.

2. Preparation of [Ni₄(bptz)₄(CH₃CN)₈][ClO₄]₈ (2) - Compound **2** was synthesized using a previously reported procedure.⁴⁸ IR (KBr mull), cm⁻¹: 2321, 2325 (w, sh, ν(C≡N)), 1098 (s, br, ν(Cl-O)). UV-Vis: λ, nm (ε, M⁻¹cm⁻¹): 510 (530), 680 (266). ES-MS: *m/z* 1875.8 [Ni₄(bptz)₄(ClO₄)₇]⁺. Yield: 111 mg (92%). Anal. Calcd for Ni₄C₆₄N₃₂H₅₆Cl₈O₃₂: C, 33.37; N, 19.46; H, 2.45. Found: C, 33.34; N 18.93; H, 2.48.

3. Preparation of [Zn₄(bptz)₄(CH₃CN)₈][BF₄]₈ (3) - Compound **3** was synthesized using a previously reported procedure.⁴⁸ ¹H NMR in CD₃CN (δ, ppm): 8.10 (d, 8H, 3,3'-H), 8.31 (ddd, 8H, 5,5'-H), 8.52 (ddd, 8H, 4,4'-H), 9.25 (dd, 8H, 6,6'-H), 2.49 (s, CH₃CN). ¹⁹F NMR in CD₃CN at 22° C (δ, ppm): -151 ([BF₄]⁻ free ions); ¹⁹F NMR in CD₃CN at -15° C (δ, ppm): -151 ([BF₄]⁻ free ions), -144 ([BF₄]⁻ encapsulated ions). ¹¹B NMR in CD₃CN-*d*₃, δ, ppm: 3.6 ([BF₄]⁻), IR (KBr mull), cm⁻¹: 1054 (s, ν(B-F)). UV-Vis: λ, nm (ε, M⁻¹cm⁻¹): 540 (270). ES-MS: *m/z* 1814.1 [Zn₄(bptz)₄(BF₄)₇]⁺. Yield: 84 mg (72%). Anal. Calcd for Zn₄C₆₄N₃₂H₅₆B₈F₃₂: C, 34.48; N, 20.11; H, 2.53. Found: C, 34.11; N, 19.69; H, 2.48.

4. Preparation of [Zn₄(bptz)₄(CH₃CN)₈][ClO₄]₈ (4) - Compound **4** was synthesized according to a previously reported procedure.⁴⁸ ¹H NMR in CD₃CN (δ, ppm): 8.13 (d, 8H, 3,3'-H), 8.32 (ddd, 8H, 5,5'-H), 8.50 (ddd, 8H, 4,4'-H), 9.24 (dd, 8H, 6,6'-H), 2.50 (s, CH₃CN). IR (KBr mull), cm⁻¹: 1098 (s, br, ν(Cl-O)). UV-Vis: λ, nm (ε, M⁻¹cm⁻¹): 540 (270). ES-MS: *m/z* 1902.6 [Zn₄(bptz)₄(ClO₄)₇]⁺. Yield: 105 mg (86%). Anal. Calcd for Zn₄C₆₄N₃₂H₅₆Cl₈O₃₂: C, 32.98; N, 19.23; H, 2.42. Found: C, 33.13; N 18.74; H, 2.43.

5. Preparation of $[\text{Ni}_5(\text{bptz})_5(\text{CH}_3\text{CN})_{10}][\text{SbF}_6]_{10}$ (5**)** - Compound **5** was synthesized according to a previously reported procedure.⁴⁹ IR (KBr mull), cm^{-1} : 2320, 2318 (ν , $\nu(\text{C}\equiv\text{N})$). UV-Vis: λ , nm (ϵ , $\text{M}^{-1}\text{cm}^{-1}$): 510 (540), 690 (260). ES-MS: m/z 3596.3 $[\text{Ni}_5(\text{bptz})_5(\text{SbF}_6)_9]^+$. Yield: 160 mg (90%). Anal. Calcd for $\text{Ni}_5\text{C}_{80}\text{H}_{70}\text{N}_{40}\text{Sb}_{10}\text{F}_{60}$: C, 22.65; N, 13.21; H, 1.66. Found: C, 22.70; N 12.81; H, 1.61.

6. Preparation of $[\text{Ni}_3(\text{bptz})_3][\text{NO}_3]_6$ (6**)** - A solution of $[n\text{-Bu}_4\text{N}][\text{NO}_3]$ (32 mg, 0.10 mmol) in acetonitrile (10 mL) was added to 42.4 mg of **5** (0.01 mmol) dissolved in 10 mL of acetonitrile. An instantaneous precipitation of a yellow solid was observed. The reaction mixture was stirred for an additional 2 h; the solid was collected by filtration, washed with acetonitrile (3×5 mL) followed by dichloromethane (3×5 mL), and dried *in vacuo*. IR (KBr mull), cm^{-1} : 1475 ($\nu(\text{N}=\text{O})$), 1293 ($\nu(\text{NO}_2)$). ES-MS: m/z 1194.7 $[\text{Ni}_3(\text{bptz})_3(\text{NO}_3)_5]^+$. Yield: 19.5 mg (93%). Anal. Calcd for $\text{Ni}_3\text{C}_{36}\text{N}_{24}\text{H}_{24}\text{O}_{18}$: C, 34.40; N, 26.75; H, 1.93. Found: C, 34.36; N 26.33; H, 1.91.

An alternative synthetic route consists in treating an acetonitrile solution (10 mL) of bptz (50 mg, 0.21 mmol) with $[\text{Ni}(\text{CH}_3\text{CN})_6][\text{NO}_3]_2$ (90 mg, 0.21 mmol) in acetonitrile (10 mL). After 2 h, a yellow-brown solid was collected by filtration, washed with benzene (3×5 mL), and dried *in vacuo*. Yield: 60 mg (68%).

7. Preparation of $[\text{Ni}_4(\text{bptz})_4(\text{CH}_3\text{CN})_8][\text{SbF}_6]_7[\text{I}]$ (7**)** - An acetonitrile solution (10 mL) of $[n\text{-Bu}_4\text{N}][\text{I}]$ (7.4 mg, 0.02 mmol) was added to a stirring solution of **5** (42.4 mg, 0.01 mmol) in acetonitrile and the mixture was stirred for 2 h. The resulting brown solution was filtered, concentrated and layered over benzene (20 mL). The brown solid that appeared after several days was collected by filtration, washed with benzene (3×5 mL), and dried *in vacuo*. Yield: 30 g (73%). Anal.

Calcd for $\text{Ni}_4\text{C}_{64}\text{N}_{32}\text{H}_{56}\text{Sb}_7\text{F}_{42}\text{I}$: C, 23.40; N, 13.64; H, 1.72. Found: C, 23.63; N 13.68; H, 1.81.

8. Preparation of $[\text{Ni}_4(\text{bptz})_4(\text{CH}_3\text{CN})_8][\text{BF}_4][\text{PF}_6][\text{SbF}_6]_6$ (8) - An acetonitrile solution (10 mL) of **5** (25.4 mg, 0.006 mmol) was layered over an equimolar mixture of $[\text{n-Bu}_4\text{N}][\text{BF}_4]$ (8.9 mg, 0.027 mmol) and $[\text{n-Bu}_4\text{N}][\text{PF}_6]$ (10.1 mg, 0.026 mmol) in dichloromethane. The yellow-brown solid that appeared after several days was collected by filtration, washed with benzene (3×5 mL), and dried *in vacuo*. Yield: 9 mg (46%).

9. Preparation of $[\text{Ni}_4(\text{bptz})_4(\text{CH}_3\text{CN})_4(\text{H}_2\text{O})_4][\text{ClO}_4][\text{IO}_4]_7$ (9) - A procedure similar to that described for the synthesis of **8** was carried out with **2** (23 mg, 0.01 mmol) dissolved in acetonitrile and a methanol solution of $[\text{n-Bu}_4\text{N}][\text{IO}_4]$ (69.2 mg, 0.16 mmol). The crop of brown crystals that grew at the interface of the two solvents was filtered, washed with benzene (3×5 mL), and dried *in vacuo*. Yield: 16 mg (56%).

10. Preparation of $[\text{Ni}_4(\text{bptz})_4\text{Br}_7(\text{CH}_3\text{CN})\text{Br}_3]$ (10) - An acetonitrile solution (10 mL) of **2** (23 mg, 0.01 mmol) was diffused into a 1:2 dichloromethane/toluene solution of $[\text{n-Bu}_4\text{N}][\text{Br}_3]$ (29 mg, 0.06 mmol). Crystals grew at the interface of the two solvents over two weeks and were filtered, washed with dichloromethane (3×5 mL), and dried *in vacuo*. Yield: 15 mg (74%). Anal. Calcd for $\text{Ni}_4\text{C}_{50}\text{N}_{25}\text{H}_{35}\text{Br}_{10}$: C, 29.73; N, 17.34; H, 1.75. Found: C, 29.69; N 16.91; H, 1.80.

11. Preparation of $[\text{Ni}_2(\text{bptz})(\text{CH}_3\text{CN})_8][\text{ClO}_4]_4$ (11) - A crop of single crystals was obtained by layering diethyl ether on the filtrate obtained after harvesting the bulk sample of **2**. The approximate yield of crystals was less than 5%.

12. Preparation of $\{[\text{Mn}(\text{bptz})(\text{CH}_3\text{CN})_2][\text{BF}_4]_2\}_\infty$ (12) - An acetonitrile solution (10 mL) of $[\text{Mn}(\text{CH}_3\text{CN})_6][\text{BF}_4]_2$ (52.2 mg, 0.11 mmol) was layered over a dichloromethane solution (10 mL) of bptz (26 mg, 0.11 mmol) in a Schlenk tube. After one month, light-orange crystals of **12** intimately mixed with an unidentified green amorphous solid were obtained. Yield: 18 mg (30%).

D. X-ray Crystallographic Studies

Single crystal X-ray data were collected on a Bruker SMART CCD based X-ray diffractometer with 1.5 kW graphite monochromated Mo- K_α radiation ($\lambda = 0.71073$ Å) at T=110(2) K. Data reduction, cell-refinements, and corrections for Lorentz and polarization effects were carried out with the SAINT program.⁵⁹ An empirical absorption correction was carried out by the SADABS program.⁶⁰ The structures were solved and refined using X-SEED,⁶¹ a graphical interface to SHELX.⁶² Additional crystallographic calculations were performed with the PLATON⁶³ and PARST programs.⁶⁴ In many cases the diffraction intensities were weak (even after prolonged exposures) which is attributed to disorder and loss of interstitial solvent molecules. Disordered solvent molecules with fractional site occupancies were observed in several of the structures. A summary of experimental details and pertinent crystallographic data for complexes **1–3**, **5** and **7–13** is provided in Table 6.

1. $\{[\text{Ni}_4(\text{bptz})_4(\text{CH}_3\text{CN})_8]\text{c}[\text{BF}_4][\text{BF}_4]_7 \cdot 4\text{CH}_3\text{CN}$, (1**) $\cdot 4\text{CH}_3\text{CN}$** - Single crystals were grown by diffusion of toluene into a solution of compound **1** in acetonitrile. A dark green rectangle was selected for the X-ray analysis. Compound **1** crystallizes in the triclinic system, space group $P\bar{1}$. Five of the eight $[\text{BF}_4]^-$ ions were found to be disordered and were modeled in two orientations with restraints on the B-F and F \cdots F distances. The $[\text{BF}_4]^-$ anion inside the cavity of the square is disordered with the two

major components being situated in a direction perpendicular to the plane of the square. The site occupancies were determined to be 0.757(8) and 0.243(8).

2. $[\{\text{Ni}_4(\text{bptz})_4(\text{CH}_3\text{CN})_8\}\text{C}\text{ClO}_4][\text{ClO}_4]_7 \cdot 4\text{CH}_3\text{CN} \cdot \text{C}_4\text{H}_8\text{O}$, (2) $\cdot 4\text{CH}_3\text{CN} \cdot \text{C}_4\text{H}_8\text{O}$

- Crystals were grown by layering an acetonitrile solution of compound **2** over THF. A dark brown platelet was selected for the X-ray analysis. Compound **2** crystallizes in the monoclinic system, space group $P2_1/n$. Partially occupied THF and acetonitrile molecules were refined with individual site occupancies equal to 0.5. All non-hydrogen atoms belonging to non-disordered groups were refined anisotropically. Two of the seven perchlorate ions located outside the square are disordered and were modeled appropriately. The $[\text{ClO}_4]^-$ anion residing in the cavity of the square revealed no signs of disorder.

3. $[\{\text{Zn}_4(\text{bptz})_4(\text{CH}_3\text{CN})_8\}\text{C}\text{BF}_4][\text{BF}_4]_7 \cdot 4\text{CH}_3\text{CN}$, (3) $\cdot 4\text{CH}_3\text{CN}$ - Crystals were

grown by slow diffusion of benzene into an acetonitrile solution of **3**. Compound **3** crystallizes in the triclinic system, space group $P\bar{1}$. The $[\text{BF}_4]^-$ anion residing in the cavity of the square is disordered over two positions. Geometric restraints were applied to one of the bptz ligands and to the disordered $[\text{BF}_4]^-$ anions. In the final stages of refinement, all non-hydrogen atoms were refined anisotropically.

4. $[\{\text{Ni}_5(\text{bptz})_5(\text{CH}_3\text{CN})_{10}\}\text{C}\text{SbF}_6][\text{SbF}_6]_9 \cdot 2\text{CH}_3\text{CN}$, (5) $\cdot 2\text{CH}_3\text{CN}$ - Crystals were

grown by layering an acetonitrile solution of compound **5** over toluene. A dark brown platelet was selected for the X-ray analysis. Compound **5** crystallizes in the monoclinic system, space group $C2/c$. All the $[\text{SbF}_6]^-$ ions are severely disordered, which accounts for the higher than usual R factors. The encapsulated $[\text{SbF}_6]^-$ is also disordered, with two closely-spaced ($\text{Sb} \cdots \text{Sb}$ 0.744(2)Å) components in different orientations.

Table 6. Crystal and structural refinement data for **1**•4CH₃CN, **2**•4CH₃CN•C₄H₈O, **3**•4CH₃CN, **5**•2CH₃CN, **7**, **8**, **9**•3CH₃CN, **10**•2CH₃CN•2.5C₆H₅CH₃, **11**, and **12**•1.5*n*CH₃CN.

Compound	1 •4CH ₃ CN	2 •4CH ₃ CN•C ₄ H ₈ O	3 •4CH ₃ CN
Formula	C ₆₄ H ₅₆ N ₃₂ Ni ₄ , 8(BF ₄), 4(C ₂ H ₃ N)	C ₆₄ H ₅₆ N ₃₂ Ni ₄ , 8(ClO ₄), 4(C ₂ H ₃ N), C ₄ H ₈ O	C ₆₄ H ₅₆ N ₃₂ Zn ₄ , 8(BF ₄), 4(C ₂ H ₃ N)
Formula weight	2366.94	2540.17	2393.58
Temperature/ K	110(2)	110(2)	110(2)
Crystal system	Triclinic	Monoclinic	Triclinic
Space group	<i>P</i> -1	<i>P</i> 2 ₁ / <i>n</i>	<i>P</i> -1
<i>a</i> , <i>b</i> , <i>c</i> / Å	14.118(3), 17.090(3), 21.774(4)	15.082(3), 31.922(6), 22.305(5)	13.924(1), 17.071(1), 21.940(1)
<i>α</i> , <i>β</i> , <i>γ</i> °	94.87(3), 91.43(3), 97.47(3)	90, 104.11(3), 90	94.46(1), 92.51(1), 97.79(1)
<i>V</i> / Å ³	5187(2)	10415(4)	5143.5(5)
Crystal description, color	Block, green	Plate, brown	Plate, orange
Crystal size/ mm ³	0.5 x 0.2 x 0.1	0.9 x 0.7 x 0.1	0.3 x 0.1 x 0.05
<i>Z</i>	2	4	2
<i>D</i> _{calc.} / g/cm ³	1.516	1.620	1.545
<i>μ</i> / mm ⁻¹	0.831	1.014	1.039
<i>F</i> (000)	2384	5184	2400
Theta range for data collection/°	1.46 to 24.71	1.97 to 28.36	1.21 to 28.33
Diffraction limits (<i>h</i> , <i>k</i> , <i>l</i>)	-15 < <i>h</i> < 16, -20 < <i>k</i> < 19, -25 < <i>l</i> < 12	-19 < <i>h</i> < 17, -42 < <i>k</i> < 42, - 27 < <i>l</i> < 29	-18 < <i>h</i> < 18, -22 < <i>k</i> < 22, -28 < <i>l</i> < 28
Reflections measured	24784	79349	62932
Independent reflections	16454 [<i>R</i> (int) = 0.0434]	25377 [<i>R</i> (int) = 0.1143]	24556 [<i>R</i> (int) = 0.0545]
Completeness to <i>θ</i> max/ %	92.9	97.5	95.7
Data / restraints / parameters	16454 / 92 / 1365	25377 / 128 / 1430	24556 / 77 / 1361
Goodness-of-fit parameter (all data)	1.03	0.86	1.048
Residual factors [<i>I</i> > 2 σ (<i>I</i>)]	<i>R</i> = 0.087, <i>wR</i> = 0.206	<i>R</i> = 0.058, <i>wR</i> = 0.126	<i>R</i> = 0.070, <i>wR</i> = 0.191
Residual factors (all data)	<i>R</i> = 0.154, <i>wR</i> = 0.243	<i>R</i> = 0.194, <i>wR</i> = 0.161	<i>R</i> = 0.134, <i>wR</i> = 0.237
Largest diff. peak and hole/ e.Å ⁻³	1.18 and -0.95	1.40 and -1.15	1.97 and -2.57

Table 6 (continued). Crystal and structural refinement data for **1**•4CH₃CN, **2**•4CH₃CN•C₄H₈O, **3**•4CH₃CN, **5**•2CH₃CN, **7**, **8**, **9**•3CH₃CN, **10**•2CH₃CN•2.5C₆H₅CH₃, **11**, and **12**•1.5*n*CH₃CN.

Compound	5 •2CH ₃ CN	7	8
Formula	C ₈₀ H ₇₀ N ₄₀ Ni ₅ , 10(SbF ₆), 2(C ₂ H ₃ N)	C ₆₄ H ₅₆ N ₃₂ Ni ₄ , 7(SbF ₆), I	C ₆₄ H ₅₆ N ₃₂ Ni ₄ , BF ₄ , 6(SbF ₆), PF ₆
Formula weight	4324.92	3285.4	3154.53
Temperature/ K	110(2)	110(2)	110(2)
Crystal system	Monoclinic	Orthorhombic	Orthorhombic
Space group	<i>C2/c</i>	<i>I222</i>	<i>I222</i>
<i>a, b, c</i> / Å	17.933(4), 28.314(6), 29.459(6)	18.145(4), 14.925(3), 22.529(4)	17.869(4), 14.762(3), 22.326(4)
α, β, γ °	90, 104.82(3), 90	90	90
<i>V</i> / Å ³	14460(5)	6101(2)	5889(2)
Crystal description, color	Prism, green	Block, brown	Plate, brown
Crystal size/ mm ³	0.20 x 0.13 x 0.05	0.88 x 0.68 x 0.31	0.73x 0.41 x 0.28
<i>Z</i>	4	2	2
<i>D</i> _{calc.} / g/cm ³	1.987	1.788	1.779
μ / mm ⁻¹	2.600	2.488	2.112
<i>F</i> (000)	8256	3128	3032
Theta range for data collection/°	1.38 to 24.71	1.77 to 27.13	1.46 to 24.71
Diffraction limits (<i>h, k, l</i>)	-21 < <i>h</i> < 19, -30 < <i>k</i> < 33, -29 < <i>l</i> < 34	-22 < <i>h</i> < 23, -19 < <i>k</i> < 19, -24 < <i>l</i> < 28	-16 < <i>h</i> < 21, -17 < <i>k</i> < 17, -26 < <i>l</i> < 26
Reflections measured	36480	22697	17435
Independent reflections	12303 [<i>R</i> (int) = 0.0372]	6678 [<i>R</i> (int) = 0.0554]	5005 [<i>R</i> (int) = 0.0829]
Completeness to θ max/ %	99.7	98.9	99.4
Data / restraints / parameters	12303 / 169 / 1179	6678 / 32 / 331	5005 / 49 / 358
Goodness-of-fit parameter (all data)	1.303	0.909	1.040
Residual factors [<i>I</i> >2 σ (<i>I</i>)]	<i>R</i> = 0.108, <i>wR</i> = 0.316	<i>R</i> = 0.066, <i>wR</i> = 0.163	<i>R</i> = 0.081, <i>wR</i> = 0.209
Residual factors (all data)	<i>R</i> = 0.143, <i>wR</i> = 0.343	<i>R</i> = 0.076, <i>wR</i> = 0.169	<i>R</i> = 0.111, <i>wR</i> = 0.231
Largest diff. peak and hole/ e.Å ⁻³	6.3 and -2.9	2.1 and -2.6	1.7 and -0.8

Table 6 (continued). Crystal and structural refinement data for **1**•4CH₃CN, **2**•4CH₃CN•C₄H₈O, **3**•4CH₃CN, **5**•2CH₃CN, **7**, **8**, **9**•3CH₃CN, **10**•2CH₃CN•2.5C₆H₅CH₃, **11**, and **12**•1.5*n*CH₃CN.

Compound	9 •3CH ₃ CN	10 •2CH ₃ CN•2.5C ₆ H ₅ CH ₃
Formula	C ₅₆ H ₅₂ N ₂₈ Ni ₄ O ₄ , ClO ₄ , 7(IO ₄), 3(C ₂ H ₃ N)	C ₅₀ H ₃₅ N ₂₅ Ni ₄ Br ₇ , Br ₃ , 2.5(C ₇ H ₈), 2(C ₂ H ₃ N)
Formula weight	2975.01	2332.41
Temperature/ K	110(2)	110(2)
Crystal system	Monoclinic	Monoclinic
Space group	<i>C2/c</i>	<i>P2₁/n</i>
<i>a</i> , <i>b</i> , <i>c</i> / Å	20.358(4), 17.493(4), 28.123(6)	13.197(3), 27.700(6), 23.557(5)
α , β , γ °	90, 98.53(3), 90	90, 100.45(3), 90
<i>V</i> / Å ³	9904(3)	8469(3)
Crystal description, color	Rectangular plate, brown	Plate, brown
Crystal size/ mm ³	0.20 x 0.10 x 0.06	0.44 x 0.26 x 0.05
<i>Z</i>	4	4
<i>D</i> _{calc.} / g/cm ³	1.995	1.829
μ / mm ⁻¹	3.053	5.652
<i>F</i> (000)	5752	4564
Theta range for data collection/°	1.64 to 24.71	1.15 to 25.72
Diffraction limits (<i>h</i> , <i>k</i> , <i>l</i>)	-16 < <i>h</i> < 23, -20 < <i>k</i> < 20, -33 < <i>l</i> < 33	-12 < <i>h</i> < 16, -33 < <i>k</i> < 26, -28 < <i>l</i> < 28
Reflections measured	34889	43302
Independent reflections	8369 [<i>R</i> (int) = 0.0923]	15992 [<i>R</i> (int) = 0.1422]
Completeness to θ max/ %	99.2	99.0
Data / restraints / parameters	8369 / 73 / 654	15992 / 17 / 859
Goodness-of-fit parameter (all data)	1.06	0.956
Residual factors [<i>I</i> > 2 σ (<i>I</i>)]	<i>R</i> = 0.109, <i>wR</i> = 0.280	<i>R</i> = 0.065, <i>wR</i> = 0.147
Residual factors (all data)	<i>R</i> = 0.192, <i>wR</i> = 0.345	<i>R</i> = 0.209, <i>wR</i> = 0.205
Largest diff. peak and hole/ e.Å ⁻³	2.9 and -2.5	1.4 and -1.0

Table 6 (continued). Crystal and structural refinement data for **1**•4CH₃CN, **2**•4CH₃CN•C₄H₈O, **3**•4CH₃CN, **5**•2CH₃CN, **7**, **8**, **9**•3CH₃CN, **10**•2CH₃CN•2.5C₆H₅CH₃, **11**, and **12**•1.5*n*CH₃CN.

Compound	11	12 •1.5 <i>n</i> CH ₃ CN
Formula	C ₂₈ H ₃₂ N ₁₄ Ni ₂ , 4(ClO ₄)	C ₁₆ H ₁₄ N ₈ Mn 2(BF ₄), 1.5(C ₂ H ₅ N)
Formula weight	1079.90	608.49
Temperature/ K	110(2)	110(2)
Crystal system	Triclinic	Triclinic
Space group	<i>P</i> -1	<i>P</i> -1
<i>a</i> , <i>b</i> , <i>c</i> / Å	8.639(5), 10.856(5), 12.362(5)	9.135(2), 10.859(2), 14.631(3)
α , β , γ °	98.355(5), 104.675(5), 97.317(5)	99.48(3), 107.53(3), 102.27(3)
<i>V</i> / Å ³	1093.2(9)	1311(1)
Crystal description, color	Needle, green	Orange, plate
Crystal size/ mm ³	0.41 x 0.23 x 0.10	0.30 x 0.18 x 0.15
<i>Z</i>	1	2
<i>D</i> _{calc.} / g/cm ³	1.640	1.541
μ / mm ⁻¹	1.188	0.589
<i>F</i> (000)	550	612
Theta range for data collection/°	4.21 to 25.49	2.37 to 24.71
Diffraction limits (<i>h</i> , <i>k</i> , <i>l</i>)	-10 < <i>h</i> < 7, -10 < <i>k</i> < 12, - 14 < <i>l</i> < 14	-10 < <i>h</i> < 10, -12 < <i>k</i> < 12, - 17 < <i>l</i> < 17
Reflections measured	4421	12767
Independent reflections	3362 [<i>R</i> (int) = 0.0349]	4445 [<i>R</i> (int) = 0.0802]
Completeness to θ max/ %	82.6	99.2
Data / restraints / parameters	3362 / 15 / 310	4445 / 41 / 382
Goodness-of-fit parameter (all data)	0.965	0.907
Residual factors [<i>I</i> > 2 σ (<i>I</i>)]	<i>R</i> = 0.061, <i>wR</i> = 0.142	<i>R</i> = 0.053, <i>wR</i> = 0.113
Residual factors (all data)	<i>R</i> = 0.128, <i>wR</i> = 0.181	<i>R</i> = 0.123, <i>wR</i> = 0.139
Largest diff. peak and hole/ e.Å ⁻³	0.7 and -0.6	0.3 and -0.5

5. $[\{\text{Ni}_4(\text{bptz})_4(\text{CH}_3\text{CN})_8\}\text{C}\text{I}][\text{SbF}_6]_7$, (**7**) - Crystals were grown by diffusion of an acetonitrile solution of **7** into toluene (20 ml). Indexing of the diffraction patterns gave an approximate cell and established that the crystals belong to the orthorhombic system and one of the following space groups: $I222$, $Imm2$, $Immm$, or $I2_12_12_1$. These space groups were tested and the structure was ultimately solved and refined in the chiral space group $I222$, in spite of the fact that the absolute structure parameter is 0.5(1).⁶⁵ The low standard deviation for this parameter indicated that twinning rather than a centrosymmetric structure was responsible for the Flack parameter. No additional crystallographic symmetry was detected from the atomic coordinates, thereby confirming merohedral twinning by inversion. The inversion twin law is: -1 0 0, 0 -1 0, 0 0 -1, and the twin populations refined to 50(5):50(5)% (with a Flack parameter of 0). The cation $[\{\text{Ni}_4(\text{bptz})_4(\text{CH}_3\text{CN})_8\}\text{C}\text{I}]^{7+}$ resides on a 222 symmetry element with the iodide ion positioned at the center of $[\text{Ni}_4(\text{bptz})_4(\text{CH}_3\text{CN})_8]^{8+}$. The $[\text{SbF}_6]^-$ ion located on a general position, is slightly disordered. In the final cycles of refinement all non-hydrogen and non-disordered atoms were refined anisotropically.

6. $[\{\text{Ni}_4(\text{bptz})_4(\text{CH}_3\text{CN})_8\}\text{C}\text{BF}_4][\text{PF}_6][\text{SbF}_6]_6$, (**8**) - Crystals were obtained by layering an acetonitrile solution of **8** with toluene. The crystals belong to the orthorhombic system, space group $I222$. As in the case of **7**, $[\text{Ni}_4(\text{bptz})_4(\text{CH}_3\text{CN})_8\text{C}\text{BF}_4]^{7+}$ has point symmetry 222 but with a $[\text{BF}_4]^-$ ion located at the special position where the three 2-fold rotation axes coincide. The combination of these symmetry elements results in two $[\text{BF}_4]^-$ disorder components. The $[\text{PF}_6]^-$ ion is also located at a special position and is disordered. The asymmetric

unit contains the fragment PF_3 and the 2-fold rotation axes at this special position resulted in two $[\text{PF}_6]^-$ disorder components. The four B-F bond distances and the four $\angle\text{F-B-F}$ angles of each $[\text{BF}_4]^-$ component and the P-F bond distances and the angles F-P-F of each $[\text{PF}_6]^-$ component were restrained to similar values. Similarity restraints rather than distance restraints were used to confirm the identity of the anions from the refined distances. The $[\text{BF}_4]^-$ and $[\text{PF}_6]^-$ disorder components exhibited tetrahedral and octahedral geometry, respectively, after least-squares refinement. The refined B-F and P-F distances (1.424(13) and 1.640(13) Å) were found to be slightly longer than those typically observed in $[\text{BF}_4]^-$ and $[\text{PF}_6]^-$ ions, presumably due to disorder.

7. $[\{\text{Ni}_4(\text{bptz})_4(\text{CH}_3\text{CN})_4(\text{H}_2\text{O})_4\}\text{ClO}_4](\text{IO}_4)_7 \cdot 3\text{CH}_3\text{CN}$, (**9**) $\cdot 3\text{CH}_3\text{CN}$ - Crystals were obtained by layering an acetonitrile solution of **2** over a methanol solution of $[n\text{-Bu}_4\text{N}][\text{IO}_4]$. These crystals belong to the monoclinic system, space group $C2/c$. All seven $[\text{IO}_4]^-$ anions were found to be disordered. For each anion, two components were defined with 50% site occupancies; the I-O distances and $\angle\text{O-I-O}$ angles distances were constrained to have similar values. The $[\text{ClO}_4]^-$ inside the cavity of the square is also disordered and was modeled using two components and restraints on the Cl-O and $\text{O}\cdots\text{O}$ distances. The site occupancies of each component derived from the final refinement are 0.325(2) and 0.675(2). As previously done, constraints were used so that the two residues of each disorder component would have the same displacement parameters. Due to the complexity of the disorder model, several atoms that belong to disordered groups were refined isotropically during the final cycles of refinement.

8. $\{[\text{Ni}_4\text{Br}_7(\text{bptz})_4(\text{CH}_3\text{CN})]\text{c-Br}_3\} \cdot 2\text{CH}_3\text{CN} \cdot 2.5\text{C}_7\text{H}_8$, (10) $\cdot 2\text{CH}_3\text{CN} \cdot 2.5\text{C}_7\text{H}_8$ -

Crystals were grown by diffusing a 1:2 dichloromethane/toluene solution of [*n*-Bu₄N][Br₃] into an acetonitrile solution of **2** in a 0.5 mm sealed glass tube. Disordered interstitial toluene molecules were located, but it was difficult to establish their exact site occupancies from the X-ray data. The structure was solved and refined in the space group *P2₁/n*. One toluene molecule resides on an inversion center, which leads to a phenyl ring that appears to be substituted at both positions 1 and 4. The C-C 1,2 and 1,3-distances of the molecule were restrained. Due to the complexity of the disorder model, the strong scattering of X-rays by heavier atoms, and the diffuse nature of the peaks in the interstices of the crystal, all atoms of the solvent molecules were refined isotropically during the final cycles of refinement.

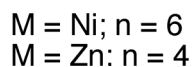
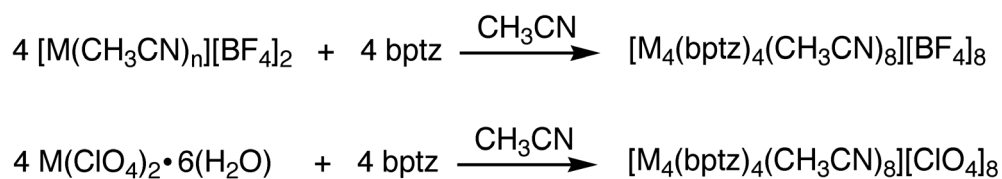
9. $[\text{Ni}_2(\text{bptz})(\text{CH}_3\text{CN})_8][\text{ClO}_4]_4$ (11) - Crystals of **11** were obtained by layering the reaction filtrate obtained after isolation of compound **2** with diethyl ether. The structure was solved and refined in the space group *P* $\bar{1}$. Two of the [ClO₄]⁻ anions were disordered and appropriately modeled. 1 non-hydrogen atoms were refined anisotropically. The maximum and minimum peaks in the final difference Fourier map corresponded to 0.69 and -0.60 e⁻/Å³, respectively.

10. $\{[\text{Mn}(\text{bptz})(\text{CH}_3\text{CN})_2][\text{BF}_4]_2 \cdot 1.5\text{CH}_3\text{CN}\}_\infty$ (12) $\cdot 1.5n\text{CH}_3\text{CN}$ - This structure was solved and refined in the space group *P* $\bar{1}$. One [BF₄]⁻ anion and one acetonitrile molecule were disordered and appropriately modeled. The disordered CH₃CN is located on an inversion center. The bond distances and angles of the components used to describe the disorder were restrained to chemically reasonable values. In the final cycles of refinement, all non-hydrogen and non-disordered atoms were refined anisotropically.

III. Results

A. Synthesis and Stability Studies of the Cyclic Cations

The cation Ni(II) reacts with bptz in CH₃CN to form products of nuclearity five, four or three depending on the anions present in solution. In accord with the structural similarity of the products to polygons, they are referred to as molecular triangles, squares and pentagons. Reactions of [Ni(CH₃CN)₆][BF₄]₂ or Ni(ClO₄)₂•6H₂O with bptz in a 1:1 molar ratio in acetonitrile afford high yields of the partially solvated [Ni₄] molecular squares of the type [$\{Ni_4(bptz)_4(CH_3CN)_8\}cX\}^{7+}$ X = [BF₄]⁻ (**1**), [ClO₄]⁻ (**2**), respectively (Scheme 1). The structure of **1** with a [BF₄]⁻ anion located inside the cavity has already been reported.⁴⁸ Analogous results are obtained with the Zn(II) ion; reactions of [Zn(CH₃CN)₄][BF₄]₂ or Zn(ClO₄)₂•6H₂O with bptz in a 1:1 molar ratio afford molecular squares of the type [$\{Zn_4(bptz)_4(CH_3CN)_8\}cX\}^{7+}$ X = [BF₄]⁻ (**3**), [ClO₄]⁻ (**4**), respectively (Scheme 1).⁶⁶ In both cases, the X-ray crystal structural determinations revealed that the anions are encapsulated in the tetranuclear cation cavities, similar to their Ni(II) analogs.

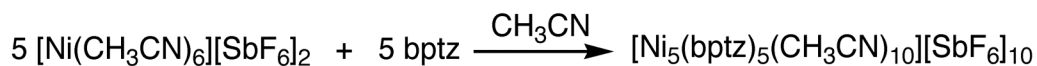


Scheme 1

The [Ni₄]⁸⁺ cations are stable under a variety of conditions as evidenced by the fact that, regardless of the ratio of bptz to Ni(II) salts (up to 10:1), the reactions

proceed in acetonitrile at room temperature to afford molecular squares. If the reactions are performed under reflux for one week, the same products are obtained in nearly quantitative yields. Identical reactions performed in acetone or nitromethane, in the presence of the same anions, also yield the cyclic $[\text{Ni}_4(\text{bptz})_4(\text{ClO}_4)_7]^+$ cation, as evidenced by mass spectrometric data (*vide infra*), but alcohols and water hinder the formation of the square.

The reaction of $[\text{Ni}(\text{CH}_3\text{CN})_6][\text{SbF}_6]_2$ with bptz in 1:1 ratio in acetonitrile affords the pentagon $[\text{Ni}_5(\text{bptz})_5(\text{CH}_3\text{CN})_{10}][\text{SbF}_6]_{10}$, **5** (Scheme 2) with one $[\text{SbF}_6]^-$ ion encapsulated in the cation cavity, as evidenced by the single crystal X-ray structural determination of the product.⁴⁹ As in the case of the squares **1-4**, $[\{\text{Ni}_5(\text{bptz})_5(\text{CH}_3\text{CN})_{10}\} \subset \text{SbF}_6]^{9+}$ is stable in solution; the compound persists in solution in high yields even after one week of reflux, as confirmed by mass spectrometric and X-ray crystallographic studies (*vide infra*). The use of different ratios of bptz to $[\text{Ni}(\text{CH}_3\text{CN})_6][\text{SbF}_6]_2$ does not affect the identity of the product, but results in lower yields.



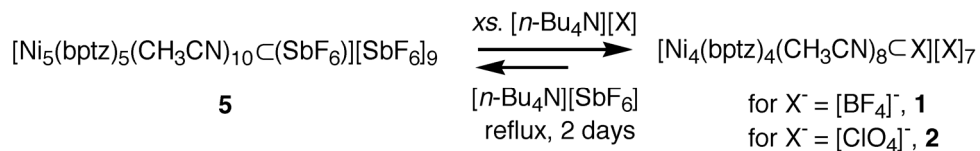
Scheme 2

Alternatively, the reaction of $[\text{Ni}(\text{CH}_3\text{CN})_6][\text{NO}_3]_2$ with bptz in a 1:1 ratio produces an insoluble yellow solid **6**. IR spectroscopic data of **6** confirmed the presence of bptz and nitrate anions and no evidence of coordinated acetonitrile molecules. The same product is obtained by treating **5** with $[n\text{-Bu}_4\text{N}][\text{NO}_3]$ in

acetonitrile. Electrospray mass spectrometric studies indicate that compound **6** is trinuclear, the only instance in which this nuclearity is observed in solution (*vide infra*). Despite numerous efforts, structural information for this species could not be obtained in the solid state due to lack of suitable single crystals. Likewise, efforts to obtain single crystals from the reaction of $[\text{Ni}(\text{CH}_3\text{CN})_6][\text{CF}_3\text{SO}_3]_2$ with bptz were unsuccessful, which may be attributed to the size and shape of $[\text{CF}_3\text{SO}_3]^-$ which make it an unsuitable template for cyclic oligomers.

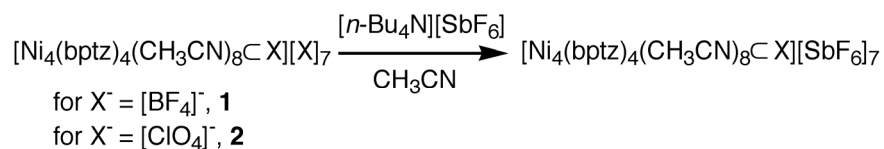
B. Interconversion between the $[\text{Ni}_5]^{10+}$ and $[\text{Ni}_4]^{8+}$ Cyclic Cations

The role of the anion in determining the preferred metallacyclophane of the bptz/metal reactions is evident. Small anions with similar shapes⁶⁷ such as $[\text{BF}_4]^-$ and $[\text{ClO}_4]^-$ yield the squares **1–4**, whereas the larger anion $[\text{SbF}_6]^-$ favors the pentagon **5**. The possibility of transforming the $[\text{Ni}_5]^{10+}$ core into $[\text{Ni}_4]^{8+}$ was tested by treating a pure sample of **5** with an excess of $[\text{BF}_4]^-$ anions (Scheme 3). Crystals were obtained from an acetonitrile solution of **5**, which had been layered over a saturated benzene solution of $[n\text{-Bu}_4\text{N}][\text{BF}_4]$. Indexing of the X-ray data confirmed that the crystal exhibits the same unit-cell dimensions as **1**.⁴⁸ Accordingly, addition of excess $[n\text{-Bu}_4\text{N}][\text{ClO}_4]$ to a sample of **5** and subsequent recording of the mass spectrum leads to the conclusion that complete conversion of the pentagon to the square takes place (Scheme 3; *vide infra*).



Scheme 3

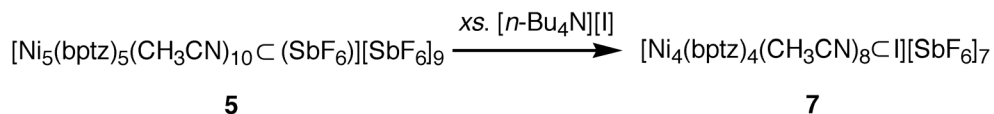
It was found, however, that the transformation of the molecular squares to the pentagon is not as facile as the reverse transformation. A solution of **1** or **2** dissolved in acetonitrile and layered on a saturated solution of $[n\text{-Bu}_4\text{N}][\text{SbF}_6]$ in toluene affords crystals of the molecular square only, with either encapsulated $[\text{BF}_4]^-$ or $[\text{ClO}_4]^-$ anions and $[\text{SbF}_6]^-$ located in the interstices (Scheme 4). Under more harsh conditions, *i.e.*, addition of large excess of $[n\text{-Bu}_4\text{N}][\text{SbF}_6]$ to a solution of **1** in acetonitrile (ratio > 50:1) with reflux for two days, a partial transformation of the square to the pentagon takes place (Scheme 3), as evidenced by mass spectrometric studies of the resulting solution (*vide infra*). The fact that the reverse transformation of the pentagon into the square (Scheme 3) takes place under milder conditions provides convincing evidence that the square is more stable than its pentagon counterpart.



Scheme 4

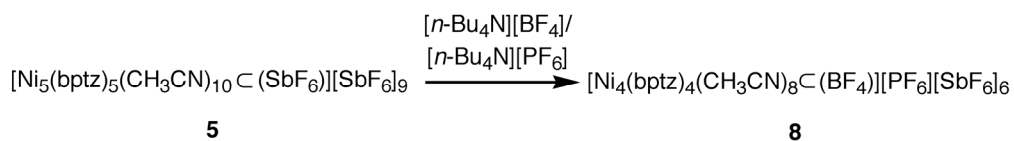
The relative instability of the pentagon **5** was capitalized upon for the synthesis of other square derivatives with the aim of probing the template effects of various anions. In one reaction, a solution of **5** was treated with excess $[n\text{-Bu}_4\text{N}][\text{I}]$, which resulted in the instantaneous precipitation of a brown solid. After the initial insoluble solid was removed by filtration, the remaining light brown solution was

treated with toluene to yield crystals of $[\{\text{Ni}_4(\text{bptz})_4(\text{CH}_3\text{CN})_8\}\text{C}]\text{I}[\text{SbF}_6]_7$ (**7**) (Scheme 5), which were found to contain an iodide anion in the cavity of the square. Attempts to synthesize this compound by using NiI_2 as the source of Ni(II) led to an insoluble, presumably polymeric material.



Scheme 5

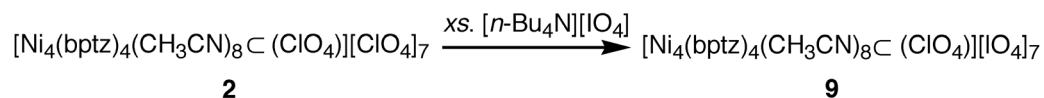
The effect of size, shape and geometry of the anion on the formation of a particular cyclic product was further probed by layering a solution of **5** with an equimolar mixture of $[n\text{-Bu}_4\text{N}][\text{BF}_4]$ and $[n\text{-Bu}_4\text{N}][\text{PF}_6]$, which resulted in the isolation of **8** (Scheme 6). In crystals of **8**, a $[\text{BF}_4]^-$ ion is located inside the square, presumably because $[\text{SbF}_6]^-$ and $[\text{PF}_6]^-$ anions lack the appropriate size (they are too large) and shape⁶⁷ to occupy the square cavity. Microanalytical data collected on independent batches of the product indicated that different amounts of $[\text{PF}_6]^-$ and $[\text{SbF}_6]^-$ were incorporated in the crystals.



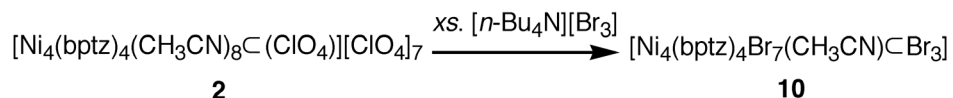
Scheme 6

C. Reactions of $[\text{Ni}_4(\text{bptz})_4(\text{CH}_3\text{CN})_8]^{8+}$ with Other Anions

From the aforementioned results, it is obvious that anions such as $[\text{BF}_4]^-$ and $[\text{ClO}_4]^-$ assist in the formation of stable molecular squares (Scheme 3). A natural question that arises is how important are both the encapsulated and outer-sphere anions to the overall stability of the cyclic cations. Addition of a large excess of $[n\text{-Bu}_4\text{N}][\text{IO}_4]$ to a solution of $[\{\text{Ni}_4(\text{bptz})_4(\text{CH}_3\text{CN})_8\}\text{C}(\text{ClO}_4)]_7$ (**2**) resulted in the isolation of crystals of $[\{\text{Ni}_4(\text{bptz})_4(\text{CH}_3\text{CN})_4(\text{H}_2\text{O})_4\}\text{C}(\text{ClO}_4)]_7$ (**9**) (Scheme 7). Although the solution was saturated with $[\text{IO}_4]^-$, the isolated compound contains a $[\text{ClO}_4]^-$ anion inside the cavity and only the outer-sphere anions have been exchanged. Analogous reactions with $[\text{Br}^-]$ ions proceed with rapid formation of an insoluble product rather than crystals. Slow diffusion of an acetonitrile solution of **2** into a dichloromethane/toluene solution of $[n\text{-Bu}_4\text{N}][\text{Br}_3]$, however, yields crystals of the formally neutral molecule $[\{\text{Ni}_4(\text{bptz})_4\text{Br}_7(\text{CH}_3\text{CN})\}\text{C}(\text{Br}_3)]$ (**10**) with a $[\text{Br}_3]^-$ ion encapsulated in the cavity (Scheme 8).



Scheme 7



Scheme 8

D. NMR Spectroscopic Studies

The aromatic region of the ^1H NMR spectrum of $[\text{Zn}_4(\text{bptz})_4(\text{CH}_3\text{CN})_8][\text{BF}_4]_8$ in CD_3CN (Figure 24a) exhibits four sets of resonances, which indicates that each bptz ligand is bridging two metal centers in a symmetric fashion. The resonances at δ 8.10, 8.31, 8.52, 9.25 ppm are ascribed to the 3,3', 5,5', 4,4' and 6,6' protons of the pyridyl rings, respectively (Figure 23). Unbound bptz exhibits resonances at δ 8.64 (3,3'), 7.65 (5,5'), 8.10 (4,4') and 8.93 (6,6') ppm for the corresponding protons (Figure 24b). The resonance (doublet) for protons 6,6'-H of $[\text{Zn}_4(\text{bptz})_4(\text{CH}_3\text{CN})_8][\text{BF}_4]_8$, which are adjacent to the metal binding sites, is shifted downfield by $\Delta\delta$ 0.33 ppm with respect to the corresponding free bptz protons due to the inductive effect of the metal.⁶⁸ Likewise, the resonances for protons 5,5'-H and 4,4'-H shift downfield by $\Delta\delta$ 0.66 and 0.42 ppm, respectively, and show multiplet splitting due to three-bond coupling to neighboring protons on the same ring. Conversely, the resonance (doublet) for 3,3'-H is shifted upfield by $\Delta\delta$ 0.54 ppm with respect to 3,3'-H of free bptz; this upfield shift is ascribed to the shielding of 3,3'-H due to their close proximity to the pyridyl ring of the neighboring bptz unit.⁶⁹

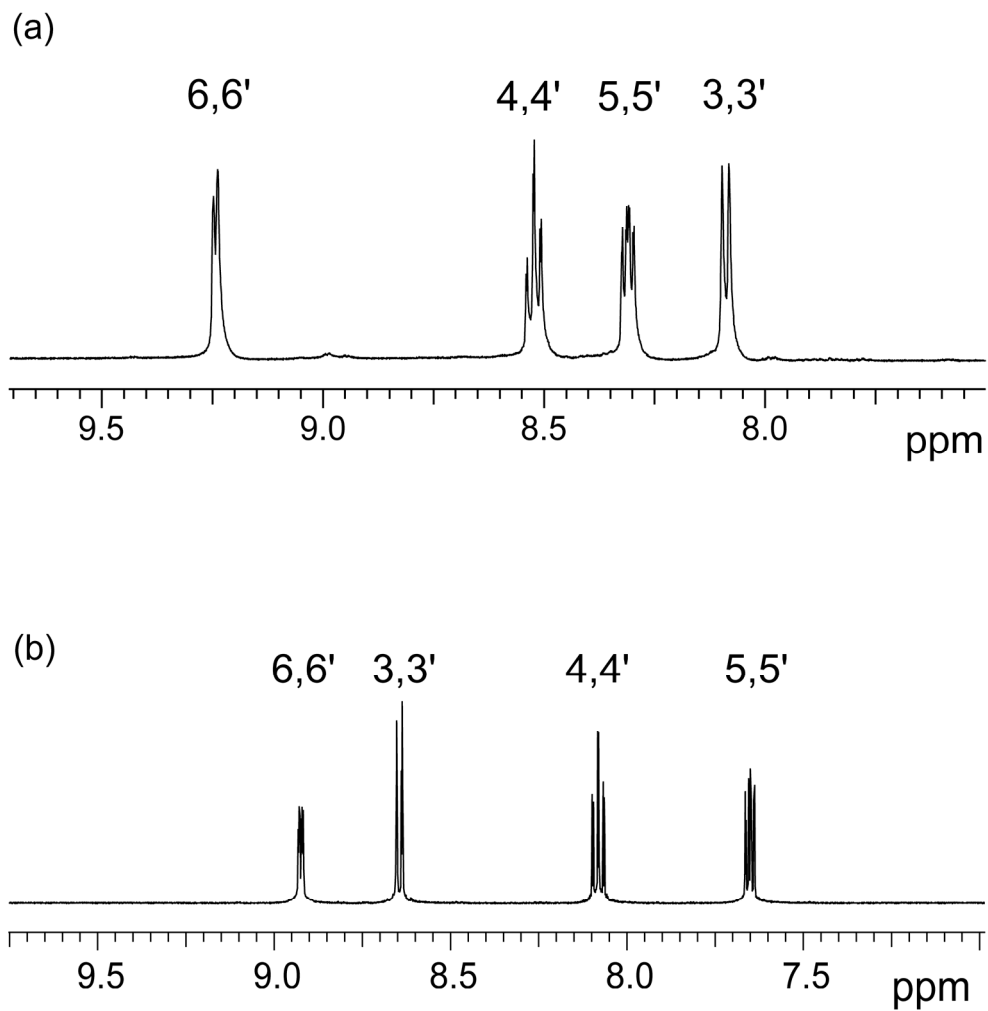


Figure 24: Aromatic region of the ^1H NMR spectrum of (a) $[\text{Zn}_4(\text{bptz})_4(\text{CH}_3\text{CN})_8][\text{BF}_4]_8$ and (b) bptz, in CD_3CN at room temperature.

Consideration of the relative positions of these protons in **3** indicates that, the distances from 3,3'-H to the centroid of the shielding pyridyl rings are 3.913 and 4.338 Å, respectively (for comparison, 4,4'-H are at 5.819 and 6.262 Å from the pyridyl ring centroid of the neighboring bptz unit).

Gradual addition of a $[\text{Zn}(\text{CH}_3\text{CN})_4][\text{BF}_4]_2$ solution in CD_3CN to a bptz solution in CD_3CN at room temperature leads to shifting and broadening of all the proton bptz resonances (no resonances of the free ligand remain which suggests rapid chemical exchange⁷⁸), but resonances identical in chemical shift to those of $[\text{Zn}_4(\text{bptz})_4(\text{CH}_3\text{CN})_8][\text{BF}_4]_8$ in the same solvent, do not appear until the molar ratio $\text{Zn(II)}:\text{bptz}$ is 3:4. In the presence of excess $[\text{Zn}(\text{CH}_3\text{CN})_4]^{2+}$ ions, however, the acquired ^1H NMR spectrum is identical to that of the isolated complex $[\text{Zn}_4(\text{bptz})_4(\text{CH}_3\text{CN})_8][\text{BF}_4]_8$ in CD_3CN . The ^1H NMR spectrum in CD_3CN of the product from the reaction between $[\text{Zn}(\text{CH}_3\text{CN})_4](\text{SbF}_6)_2$ and bptz in 1:1 ratio does not have any resonances that indicate the presence of the square $[\text{Zn}_4(\text{bptz})_4(\text{CH}_3\text{CN})_8][\text{BF}_4]_8$ in solution.

The ^{19}F NMR spectrum of $[\text{Zn}_4(\text{bptz})_4(\text{CH}_3\text{CN})_8][\text{BF}_4]_8$ in CD_3CN at + 22° C, exhibits one resonance at $\delta -151$ ppm (Figure 25), which is ascribed to the free $[\text{BF}_4]^-$ ions.^{70,71} The ^{19}F NMR spectrum of $[\text{Zn}(\text{CH}_3\text{CN})_4][\text{BF}_4]_2$ in CD_3CN also exhibits a resonance at $\delta -151$ ppm, due to the free $[\text{BF}_4]^-$ ions. Due to coupling of ^{11}B and ^{10}B to the ^{19}F nuclei, the ^{19}F resonance of $[\text{Zn}_4(\text{bptz})_4(\text{CH}_3\text{CN})_8][\text{BF}_4]_8$ at room temperature is split in two with a relative ratio $\sim 4:1$ (Figure 25, inset) corresponding to the natural abundance of ^{11}B to ^{10}B ;⁷² the two distinct maxima of the ^{19}F NMR resonance for the $[\text{BF}_4]^-$ ions collapse at temperatures below -5°C .⁷²

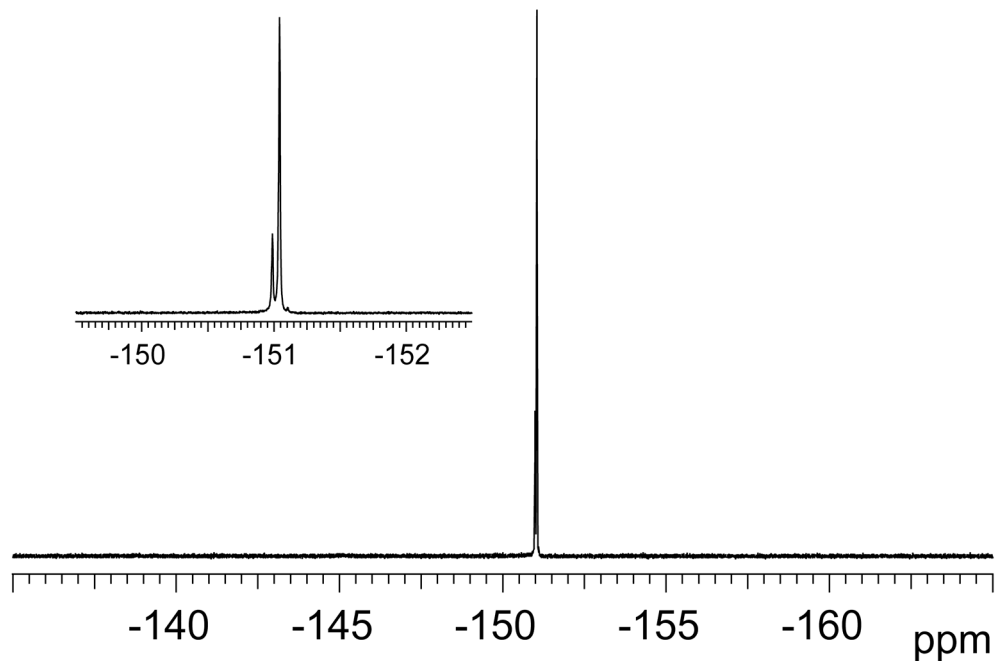


Figure 25: ^{19}F NMR spectra of $[\text{Zn}_4(\text{bptz})_4(\text{CH}_3\text{CN})_8][\text{BF}_4]_8$ in CD_3CN at $22\text{ }^\circ\text{C}$. Due to coupling of ^{11}B and ^{10}B to the ^{19}F nuclei, the ^{19}F NMR resonance of $[\text{Zn}_4(\text{bptz})_4(\text{CH}_3\text{CN})_8][\text{BF}_4]_8$ at room temperature is split in two with a relative ratio $\sim 4:1$ (inset) corresponding to the natural abundance of ^{11}B to ^{10}B . The two distinct maxima of the ^{19}F NMR resonance for the free $[\text{BF}_4]^-$ ions collapse at temperatures below -5°C .

The ^{19}F NMR spectrum of $[\text{Zn}_4(\text{bptz})_4(\text{CH}_3\text{CN})_8][\text{BF}_4]_8$ in CD_3CN exhibits a single resonance at -151 ppm in the temperature range -10 to $+70^\circ\text{C}$ (the collapse of the ^{10}B - ^{11}B isotope shift at high temperatures in the ^{19}F NMR spectra of **3** in CD_3CN is attributed to the exchange of fluorine among boron atoms⁷²), but at -10°C , a second ^{19}F resonance of lower intensity appears at -144 ppm. The latter resonance is ascribed to the encapsulated $[\text{BF}_4]^-$ ions in the cavity of the square, exchanging slowly with the free $[\text{BF}_4]^-$ ions on the NMR timescale at this temperature. The identity of this peak is also supported by its consistent appearance in the ^{19}F NMR spectra of dissolved crystals of $[\text{Zn}_4(\text{bptz})_4(\text{CH}_3\text{CN})_8][\text{BF}_4]_8$ in CD_3CN , its downfield position relative to free $[\text{BF}_4]^-$ ions (the magnetically shielded zone of the cavity shifts the ^{19}F NMR resonances of the encapsulated ions to lower field⁷³),^{70,71,74} as well as its $\Delta\delta(^{19}\text{F}) \sim 7$ ppm with respect to the free $[\text{BF}_4]^-$ ions, which is comparable to the $\Delta\delta(^{19}\text{F})$ of other systems with free and encapsulated $[\text{BF}_4]^-$ ions.⁷⁴ The presence of the resonance at -144 ppm persists at lower temperatures, but spectra at temperatures below -42°C could not be acquired due to the limitation from the freezing point of CD_3CN . The fact that the ratio of the ^{19}F NMR resonances for the free to the encapsulated $[\text{BF}_4]^-$ ions is not 7:1 may be attributed to the limited resolution and integration accuracy of the spectra at lower temperatures as well as the inherent difficulty in acquiring spectra at temperatures below -42°C to completely stop the exchange of the $[\text{BF}_4]^-$ ions.

E. IR Spectroscopy

Notable features of the IR spectra of **1**, **2** and **5** include two $\nu(\text{C}\equiv\text{N})$ bands at $\sim 2318\text{-}2325\text{ cm}^{-1}$ corresponding to the stretching modes of the coordinated acetonitrile ligands. Sharp bands at 1064 and 1054 cm^{-1} in the IR spectra of **1** and **3**, respectively, are attributed to the $\nu(\text{B-F})$ stretching mode of the tetrafluoroborate anions.⁷⁵ Analogous $\nu(\text{Cl-O})$ stretches of the perchlorate ions⁷⁵ are observed at 1098 cm^{-1} for compounds **2** and **4**. The expected $\nu(\text{C}\equiv\text{N})$ stretches for the coordinated acetonitrile molecules in **3** and **4** were not observed, however, which may be due to prolonged pumping of the samples leading to the loss of the ligands in the solid-state. An alternative explanation is that these stretching modes may be too weak to be observed.⁷⁶ IR spectroscopic data of **6** did not reveal any $\nu(\text{C}\equiv\text{N})$ modes for coordinated CH_3CN ligands. It is inferred, however, due to bands in the range $1000\text{-}1500\text{ cm}^{-1}$,⁷⁵ that the nitrate groups are chelating to the Ni(II) ions in addition to acting as outer-sphere anions.

F. Electrospray Mass Spectroscopic Studies

For compound **2**, the ion signal at m/z 1875.8 is ascribed to the parent ion $[\text{Ni}_4(\text{bptz})_4(\text{ClO}_4)_7]^+$ (Figure 26). The experimental and theoretical isotopic distribution patterns are identical. Ion signals were also observed for $[\text{Ni}_4(\text{bptz})_4(\text{ClO}_4)_6]^{2+}$ and $[\text{Ni}_4(\text{bptz})_4(\text{ClO}_4)_7 + 2\text{H}]^{3+}$ at m/z 888.2 and 625.9, respectively. The mass spectrum of **2** remains unchanged when the solution is left to stand for over a week, which indicates that the $[\text{Ni}_4]$ square is stable in solution and supports the conclusion that the other lower nuclearity species result from fragmentation in the gas phase.

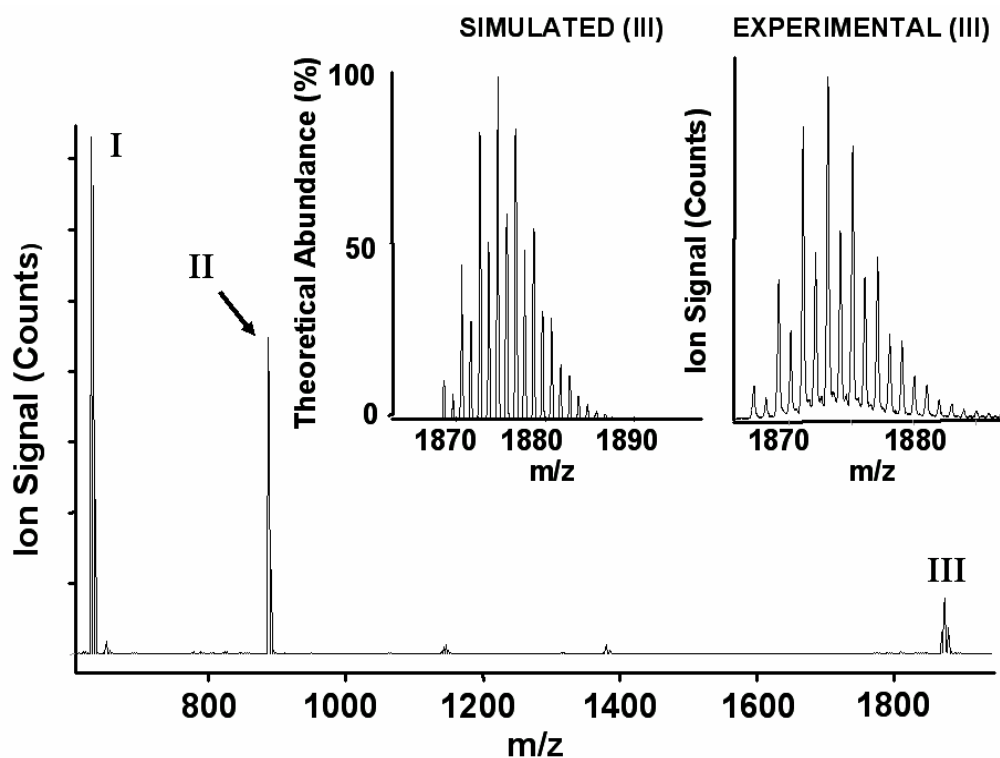


Figure 26: Electrospray mass spectrum of $[\text{Ni}_4(\text{bptz})_4(\text{CH}_3\text{CN})_8 \cdot \text{ClO}_4][\text{ClO}_4]_7$ (**2**) in acetonitrile. The ion signals displayed correspond to $[\text{Ni}_4(\text{bptz})_4(\text{ClO}_4)_7 + 2\text{H}]^{3+}$ (**I**) at m/z 625.9, $[\text{Ni}_4(\text{bptz})_4(\text{ClO}_4)_6]^{2+}$ (**II**) at m/z 888.2, and (C) $[\text{Ni}_4(\text{bptz})_4(\text{ClO}_4)_7]^+$ (**III**) at m/z 1875.8 (parent ion peak). The experimental and theoretical isotopic distribution patterns of **III** are shown in the inset.

Parent Ion Peak is $[\text{Zn}_4(\text{bptz})_4(\text{ClO}_4)_7]^+$

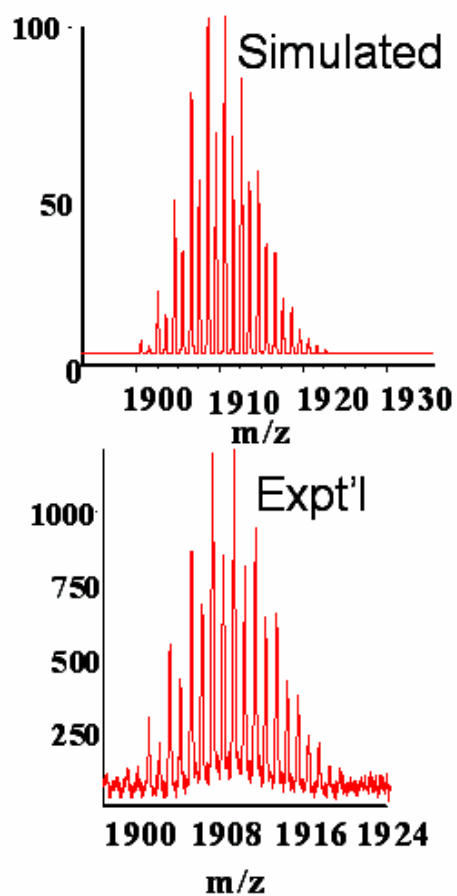


Figure 27: Theoretical and experimental isotopic distribution patterns of the ES-MS parent ion peak of $[\text{Zn}_4(\text{bptz})_4(\text{ClO}_4)_7]^+$ at m/z 1902.6.

Compound **4** exhibits an ion signal for $[\text{Zn}_4(\text{bptz})_4(\text{ClO}_4)_7]^+$ at m/z 1902.6 (Figure 27), which is indicative of the presence of the molecular square in solution. The ESI-MS spectra of complexes **1** and **3**, *i.e.* the tetrafluoroborate counterparts of **2** and **4**, show similar results, but the spectra were complicated by reactions with the anion to give fluoride-containing species.⁷⁷ The mass spectrum of the pentagon **5** exhibits the highest m/z ion signal at 3596.3 (Figure 28), ascribed to $[\text{Ni}_5(\text{bptz})_5(\text{SbF}_6)_9]^+$, with no evidence of a $[\text{Ni}_4]$ species in equilibrium with the pentagon, thus confirming the presence of the intact pentagon cage.⁴⁹ Ion signals at m/z 1060.8 and 1296.6 correspond to $[\text{Ni}_2(\text{bptz})(\text{SbF}_6)_3]^+$ and $[\text{Ni}_2(\text{bptz})(\text{SbF}_6)_4]$, respectively. Moreover, the nuclearity of complex **5** in the presence of $[\text{NO}_3]^-$ anions was probed by mass spectrometry. Addition of excess $[n\text{-Bu}_4\text{N}][\text{NO}_3]$ to **5** led to the instantaneous precipitation of a yellow solid. After sonication in acetonitrile for 1 h, the sample was subjected to ESI-MS, which revealed an ion signal that corresponds to $[\text{Ni}_3(\text{bptz})_3(\text{NO}_3)_5]^+$ at m/z 1194.7 (Figure 29).

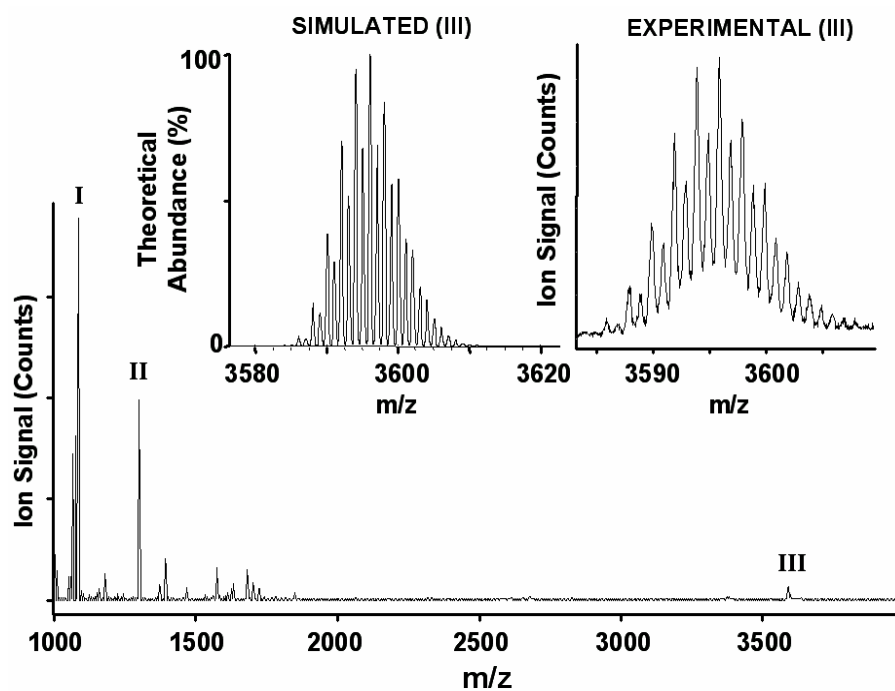


Figure 28: Electrospray mass spectrum of $[\text{Ni}_5(\text{bptz})_5(\text{CH}_3\text{CN})_{10}\text{C}(\text{SbF}_6)[\text{SbF}_6]_9$ (**5**) in acetonitrile. The ion signals displayed correspond to $[\text{Ni}_2(\text{bptz})(\text{SbF}_6)_3]^+$ (**I**) at m/z 1060.8, $[\text{Ni}_2(\text{bptz})(\text{SbF}_6)_4]^+$ (**II**) at m/z 1296.6, and $[\text{Ni}_5(\text{bptz})_5(\text{SbF}_6)_9]^+$ (**III**) at m/z 3596.3 (parent ion peak). The experimental and theoretical isotopic distribution patterns of **III** are shown in the inset.

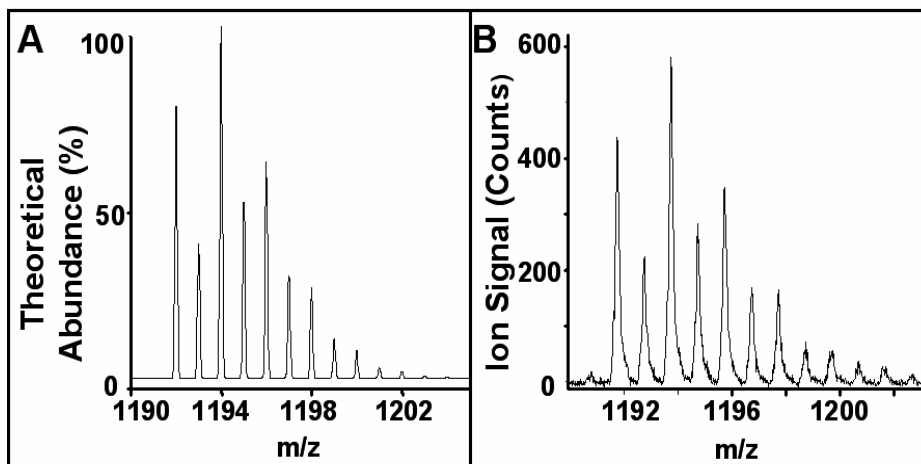


Figure 29: Electrospray mass spectrum of $[\text{Ni}_3(\text{bptz})_3][\text{NO}_3]_6$ (**6**) in acetonitrile. Parent ion peak for $[\text{Ni}_3(\text{bptz})_3(\text{NO}_3)_5]^+$ at m/z 1194.7. (A) Theoretical and (B) experimental isotopic distribution patterns of the parent ion peak.

The conversion of the $[\text{Ni}_5]^{10+}$ species to $[\text{Ni}_4]^{8+}$, by adding an excess of $[\text{ClO}_4]^-$ ions, and the reverse reaction of converting $[\text{Ni}_4]^{8+}$ to $[\text{Ni}_5]^{10+}$, by addition of $[\text{SbF}_6]^-$ ions, was monitored by mass spectrometry and the results were compared to the ESI spectra for isolated crystals of **5** and **2**. Addition of excess $[n\text{-Bu}_4\text{N}][\text{ClO}_4]$ to complex **5** and subsequent recording of the mass spectrum leads to the conclusion that complete conversion of the pentagon to the square takes place (Scheme 3).

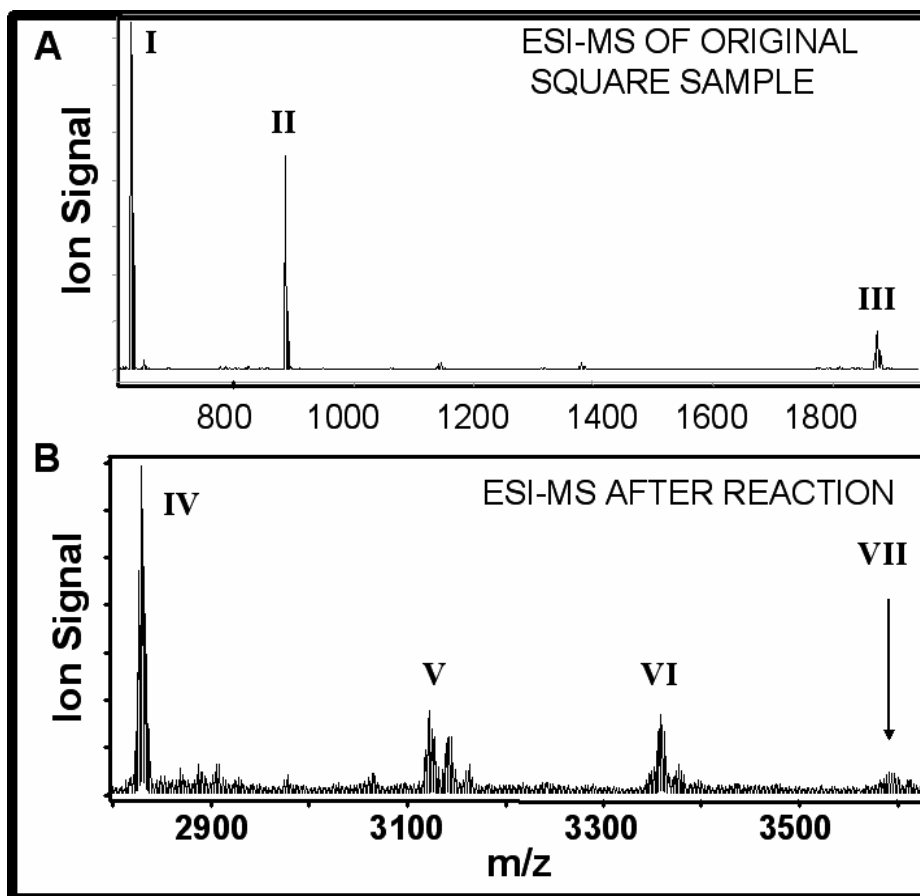


Figure 30: Electrospray mass spectrum of (A) original $[\text{Ni}_4(\text{bptz})_4(\text{CH}_3\text{CN})_8\text{C}(\text{ClO}_4)][\text{ClO}_4]_7$ square sample; (B) $[\text{Ni}_4(\text{bptz})_4((\text{CH}_3\text{CN})_8(\text{ClO}_4)_7)^+]$ sample that has been refluxed with excess $[n\text{-Bu}_4\text{N}][\text{SbF}_6]$ for 2 days; partial conversion of the square to the pentagon has taken place. Ion signals at m/z 2829.9, 3122.8, 3359.5 and 3596.3 correspond to the species $[\text{Ni}_4(\text{bptz})_4(\text{SbF}_6)_7]^+$ (IV), $[\text{Ni}_5(\text{bptz})_5(\text{SbF}_6)_7 - 2\text{H}]^+$ (V), $[\text{Ni}_5(\text{bptz})_5(\text{SbF}_6)_8 - \text{H}]^+$ (VI) and $[\text{Ni}_5(\text{bptz})_5(\text{SbF}_6)_9]^+$ (VII), respectively.

The reverse reaction, *viz.*, the transformation of the square to pentagon, does not occur at room temperature. Addition of a large excess of [*n*-Bu₄N][SbF₆] to a solution of **2** with subsequent refluxing eventually leads to detectable quantities of [Ni₅] cores, but the conversion is not complete even after heating for 5 days (Schemes 3 and 4). In the mass spectrum of the solution after refluxing for 2 days, ion signals for the species [Ni₅(bptz)₅(SbF₆)₇ - 2H]⁺, [Ni₅(bptz)₅(SbF₆)₈ - H]⁺ and [Ni₅(bptz)₅(SbF₆)₉]⁺ at *m/z* 3122.8, 3359.5 and 3596.3, respectively (Figure 30) are observed; these corroborate the formation of the pentagon.

Acetonitrile solutions of M(ClO₄)₂·*x*H₂O (M = Mn, Fe, Cu) and bptz in a 1:1 ratio were mixed and their ESI-MS spectra were recorded after 10 min. In all cases, parent ion signals that correspond to [M₄(bptz)₄(ClO₄)₇]⁺ for Mn(II), Fe(II) and Cu(II) at *m/z* 1860.8 (Figure 31), 1864.4 (Figure 32) and 1895.2 (Figure 33), respectively, were observed. Ion signals corresponding to the loss of one or two bptz ligands from the [M₄(bptz)₄(ClO₄)₇]⁺ are apparent. It is important to note the parent [M₄] species for these particular metal ions are short-lived and their ion signals were observed only when the MS spectrum of a fresh sample was recorded; after 1 hour, only lower nuclearity species were detected.

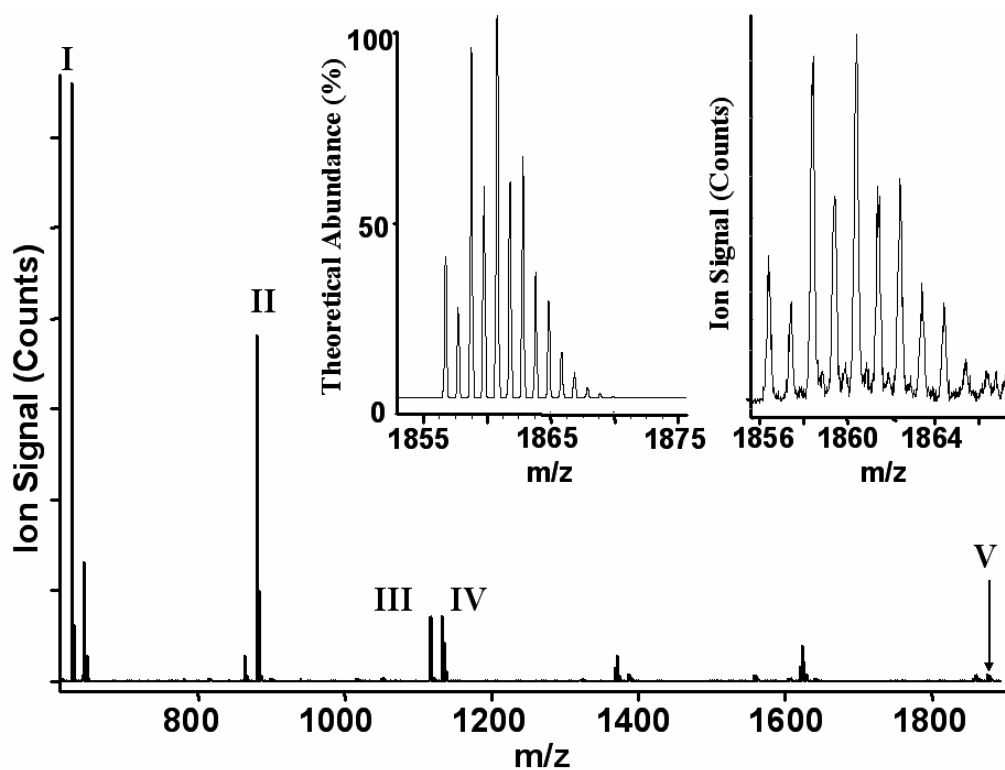


Figure 31: ES-MS spectrum of $[\text{Mn}_4(\text{bptz})_4(\text{CH}_3\text{CN})_8][\text{ClO}_4]_8$. Ion signals at m/z 620.9, 880.7, 1126.7, 1134.5 and 1860.8 (parent ion peak) correspond to $[\text{Mn}_4(\text{bptz})_4(\text{ClO}_4)_7 + 2\text{H}]^{3+}$ (**I**), $[\text{Mn}_4(\text{bptz})_4(\text{ClO}_4)_6]^{2+}$ (**II**), $[\text{Mn}_2(\text{bptz})_3(\text{ClO}_4)_3]^+$ (**III**), $[\text{Mn}_3(\text{bptz})_2(\text{ClO}_4)_5]^+$ (**IV**), and $[\text{Mn}_4(\text{bptz})_4(\text{ClO}_4)_7]^+$ (**V**), respectively. Ion signals due to the progressive loss of bptz molecules are also observed for $[\text{Mn}_4(\text{bptz})_4(\text{ClO}_4)_7 - (\text{bptz})]^+$ and $[\text{Mn}_4(\text{bptz})_4(\text{ClO}_4)_7 - 2(\text{bptz})]^+$ at m/z 1624.6 and 1388.3, respectively. The theoretical and experimental isotopic distribution patterns of the parent ion peak **V** have been expanded in the inset.

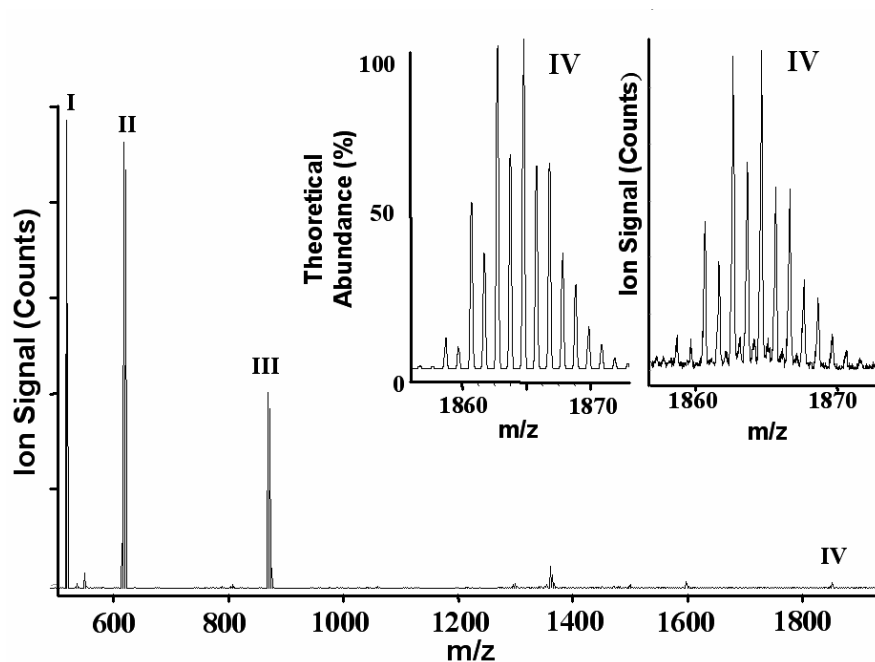


Figure 32: ES-MS spectrum of $[\text{Fe}_4(\text{bptz})_4(\text{CH}_3\text{CN})_8][\text{ClO}_4]_8$. Ion signals at m/z 522.3, 622.1, 882.5, 1864.5 correspond to $[\text{Fe}_4(\text{bptz})_4(\text{ClO}_4)_4 + \text{H}]^{3+}$ (**I**), $[\text{Fe}_4(\text{bptz})_4(\text{ClO}_4)_7 + 2\text{H}]^{3+}$ (**II**), $[\text{Fe}_4(\text{bptz})_4(\text{ClO}_4)_6]^{2+}$ (**III**), $[\text{Fe}_4(\text{bptz})_4(\text{ClO}_4)_7]^+$ (**IV**) (parent ion peak), respectively. Ion signals due to the progressive loss of bptz molecules are also observed for $[\text{Fe}_4(\text{bptz})_4(\text{ClO}_4)_7 - (\text{bptz})]^+$ and $[\text{Fe}_4(\text{bptz})_4(\text{ClO}_4)_7 - 2(\text{bptz})]^+$ at m/z 1628.3 and 1392.0, respectively. The theoretical and experimental isotopic distribution patterns of the parent ion peak **IV** have been expanded in the inset.

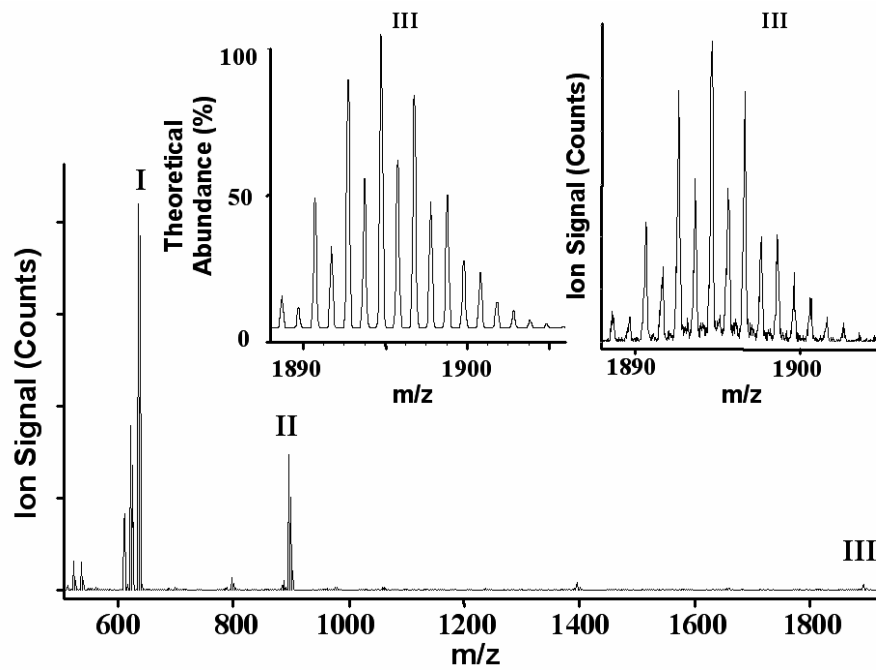


Figure 33: ES-MS spectrum of $[\text{Cu}_4(\text{bptz})_4(\text{CH}_3\text{CN})_8][\text{ClO}_4]_8$. Ion signals at m/z 632.4, 897.9, 1895.2 correspond to $[\text{Cu}_4(\text{bptz})_4(\text{ClO}_4)_7 + 2\text{H}]^{3+}$ (**I**), $[\text{Cu}_4(\text{bptz})_4(\text{ClO}_4)_6]^{2+}$ (**II**), and $[\text{Cu}_4(\text{bptz})_4(\text{ClO}_4)_7]^+$ (**III**) (parent ion peak), respectively. An ion signal due to the loss of a bptz molecule is also observed for $[\text{Cu}_4(\text{bptz})_4(\text{ClO}_4)_7 - 2(\text{bptz})]^+$ at m/z 1422.7. The theoretical and experimental isotopic distribution patterns of the parent ion peak **III** have been expanded in the inset.

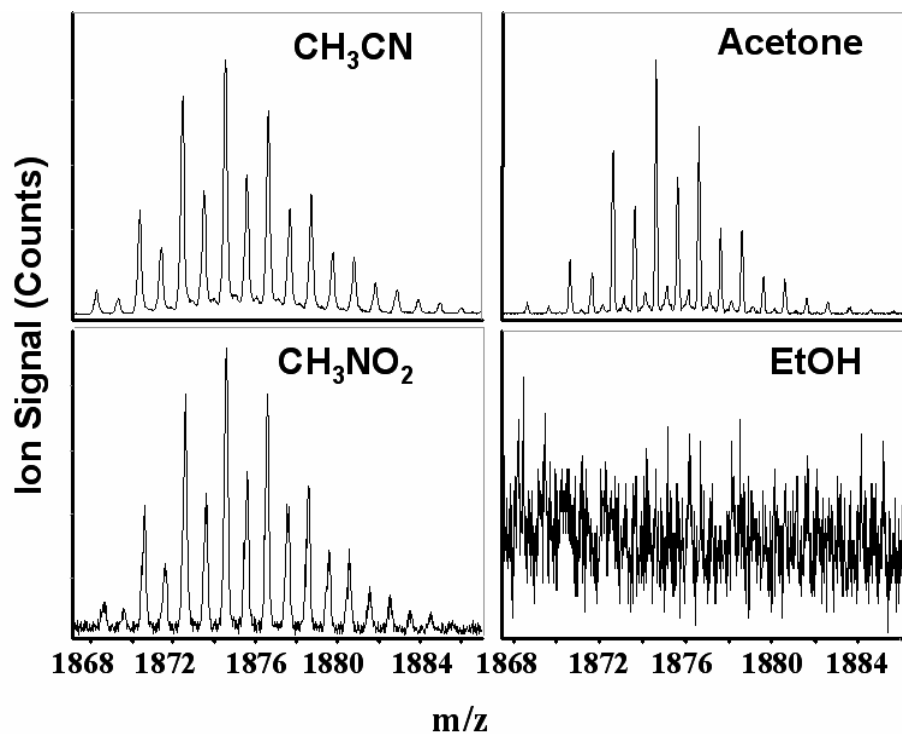


Figure 34: ES-MS spectra of the products from the reaction between $\text{Ni}(\text{ClO}_4)_2 \cdot 6\text{H}_2\text{O}$ and bptz in acetonitrile, acetone, nitromethane, and ethanol. Parent ion peak for $[\text{Ni}_4(\text{bptz})_4(\text{ClO}_4)_7]^+$ at m/z 1875.8. The highly polar solvent ethanol does not favor formation of the $[\text{Ni}_4(\text{bptz})_4(\text{ClO}_4)_7]^+$ square.

To ensure that acetonitrile is the best solvent for promoting the formation of cyclic products with M(II) salts and bptz, a series of mass spectra of the reaction products between $\text{Ni}(\text{ClO}_4)_2 \cdot 6\text{H}_2\text{O}$ and bptz in 1:1 ratio were recorded in several different solvents. The results indicate that in the presence of acetonitrile, acetone, and nitromethane, the square $[\text{Ni}_4(\text{bptz})_4(\text{ClO}_4)_7]^+$ is formed, whereas protic solvents such as water, ethanol, and methanol are unfavorable for its formation (Figure 34). These findings suggest that the solvent is also a controlling element in the self-assembly of the polygons presented.⁵⁴

G. X-ray Crystallographic Studies

1. $[\{\text{Ni}_4(\text{bptz})_4(\text{CH}_3\text{CN})_8\}\text{C}\text{BF}_4][\text{BF}_4] \cdot 4\text{CH}_3\text{CN}$, (1)•4CH₃CN - The essential features of the molecular structure of **1** were reported in a previous communication.⁴⁸ The four pairs of Ni(II) ions and bptz ligands form a molecular square in which each metal ion occupies a vertex and each ligand spans one edge as a bridge between metal centers. The coordination geometry about each Ni(II) ion is distorted octahedral, with four sites being occupied by two different bridging bptz moieties and the two remaining sites being capped by acetonitrile ligands. A plot of the cationic unit $[\{\text{Ni}_4(\text{bptz})_4(\text{CH}_3\text{CN})_8\}\text{C}\text{BF}_4]^{7+}$ is shown in Figure 35; selected bond distances and angles are provided in the corresponding figure caption. The four Ni···Ni···Ni vertex angles are in the range of 85.99-93.55°. There is no imposed symmetry on the $[\{\text{Ni}_4(\text{bptz})_4(\text{CH}_3\text{CN})_8\}\text{C}\text{BF}_4]^{7+}$ unit, consequently there are four different Ni···Ni separations; these are in the range 6.844-6.896 Å. The distances between the centroids of the parallel tetrazine rings are 6.904 and 7.087 Å. The four bptz ligands along the sides of the square create a void space inside the cavity, which is akin to a box with two open faces rather than a square.

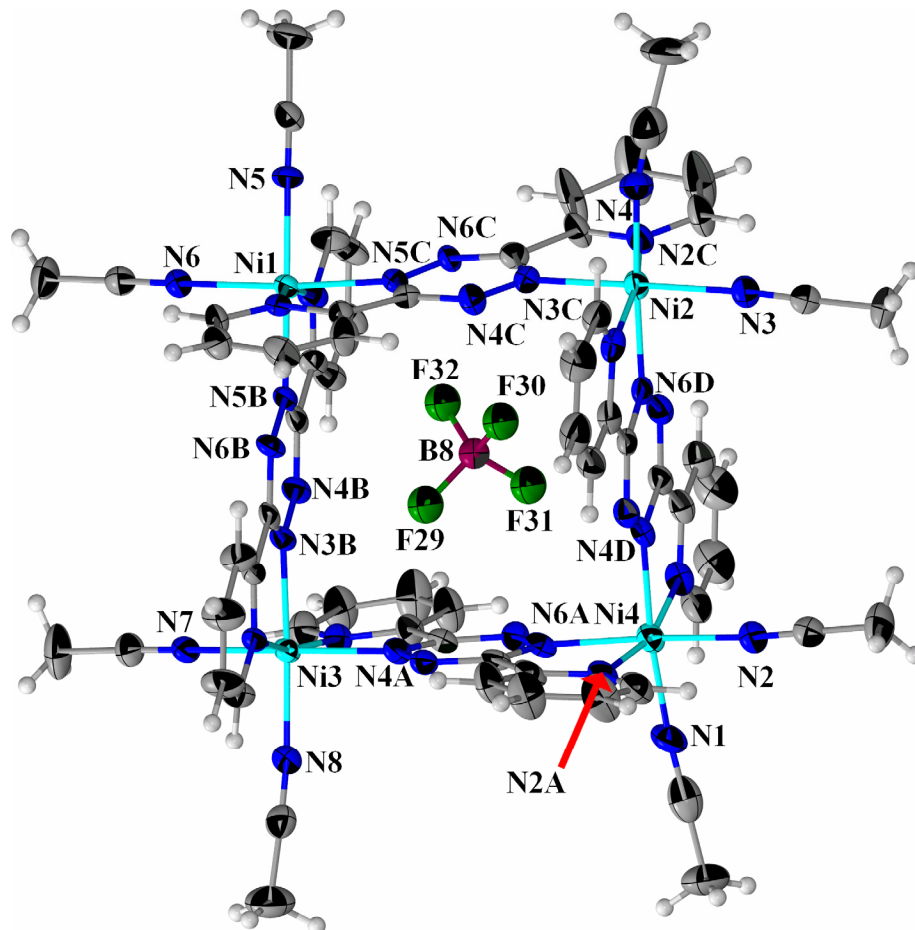


Figure 35: Thermal ellipsoid plot of the cationic unit $[\{\text{Ni}_4(\text{bptz})_4(\text{CH}_3\text{CN})_8\}\text{c}\text{BF}_4]^{7+}$ in $\mathbf{1}\cdot 4\text{CH}_3\text{CN}$. Thermal ellipsoids are represented at the 50% probability level. Selected bond distances (Å) and angles ($^\circ$): Ni1-N5 2.031(7), Ni1-N6 2.043(7), Ni1-N5B 2.097(6), Ni4-N1 2.038(8), Ni4-N2 2.041(7), Ni4-N2A 2.067(7), Ni3-N7 2.041(7), N5C-N6C 1.327(8), N5-Ni1-N6 89.4(3), N2C-Ni2-N3 98.3(3), N5-Ni1-N5B 173.7(3).

2. $[\{\text{Ni}_4(\text{bptz})_4(\text{CH}_3\text{CN})_8\}\text{C}(\text{ClO}_4)](\text{ClO}_4)_7 \cdot 4\text{CH}_3\text{CN} \cdot \text{C}_4\text{H}_8\text{O}$, (2) $\cdot 4\text{CH}_3\text{CN} \cdot \text{C}_4\text{H}_8\text{O}$ -

The molecular structure of **2** is similar to that of the $[\text{BF}_4]^-$ salt, **1**. A thermal ellipsoid plot of the cationic unit $[\{\text{Ni}_4(\text{bptz})_4(\text{CH}_3\text{CN})_8\}\text{C}(\text{ClO}_4)]^{7+}$ is shown in Figure 36 along with selected bond distances and angles. The four $\text{Ni}\cdots\text{Ni}\cdots\text{Ni}$ vertex angles ($87.30\text{-}92.97^\circ$) for this molecular square deviate slightly from ideality; the average $\text{Ni}\cdots\text{Ni}$ vertex separation is 6.846 \AA . The $\text{Ni-N}(\text{bptz})$ bond distances are in the range $2.055(4)$ to $2.112(5) \text{ \AA}$. Although the two pyridyl groups of bptz are free to rotate about the C-C bonds between the tetrazine and pyridine rings, the three rings are nearly coplanar. The distances between the centroids of parallel tetrazine rings are 6.973 and 7.076 \AA .

3. $[\{\text{Zn}_4(\text{bptz})_4(\text{CH}_3\text{CN})_8\}\text{C}(\text{BF}_4)](\text{BF}_4)_7 \cdot 4\text{CH}_3\text{CN}$, (3) $\cdot 4\text{CH}_3\text{CN}$ -

A thermal ellipsoid plot of the cationic unit $[\{\text{Zn}_4(\text{bptz})_4(\text{CH}_3\text{CN})_8\}\text{C}(\text{BF}_4)]^{7+}$ is shown in Figure 37. The molecular structures of complexes **1** and **3** are very similar, but the $[\text{Zn}_4]$ square is slightly larger than the $[\text{Ni}_4]$ analog, with $\text{Zn}\cdots\text{Zn}$ vertex separations in the range $7.129\text{-}7.201 \text{ \AA}$. The distances between centroids of the parallel tetrazine rings are 7.045 and 7.205 \AA . The average $\text{Zn-N}(\text{CH}_3\text{CN})$ distances ($2.070(4)\text{-}2.091(5) \text{ \AA}$) are shorter than the $\text{Zn-N}(\text{bptz})$ distances ($2.090(5)\text{-}2.284(4) \text{ \AA}$). As in the case of the $[\text{Ni}_4]$ analog, a $[\text{BF}_4]^-$ anion is located inside the cavity flanked by the bptz ligands. In addition, an acetonitrile molecule occupies a portion of the cavity volume. The crystal structure of the perchlorate salt $[\text{Zn}_4(\text{bptz})_4(\text{H}_2\text{O})_4(\text{CH}_3\text{CN})_4][\text{ClO}_4]_8 \cdot 2\text{CHCl}_3 \cdot 4\text{CH}_3\text{CN}$, which crystallized in the chiral space group $C222_1$, has already been reported.⁶⁶

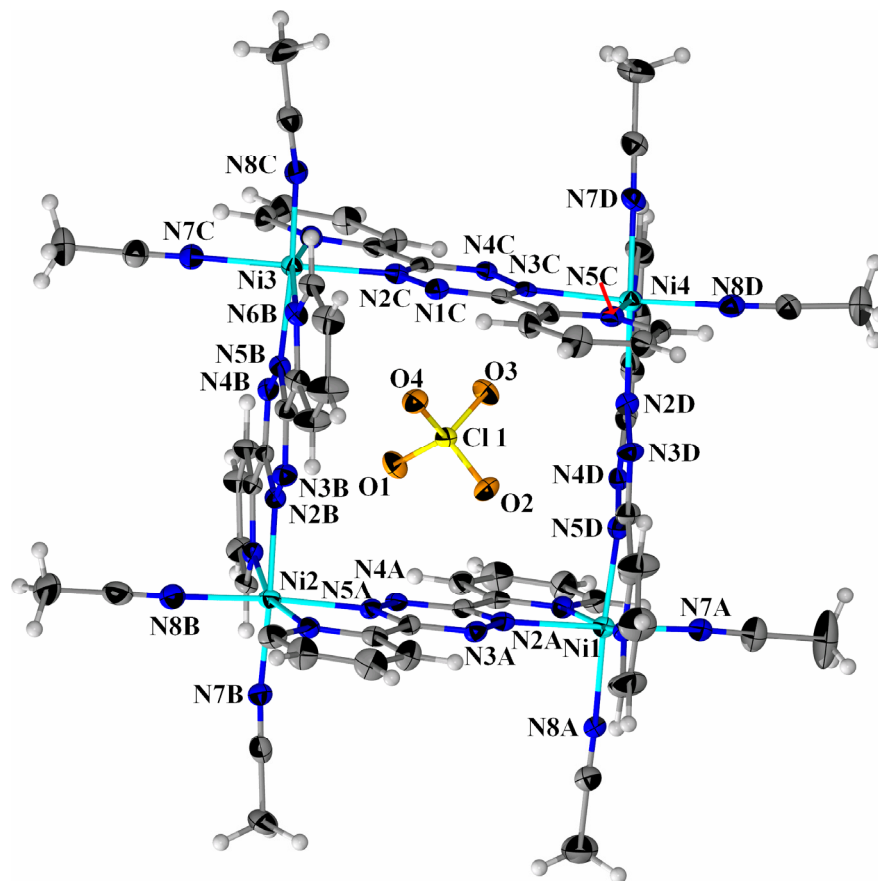


Figure 36: Thermal ellipsoid plot of the cationic unit $[\text{Ni}_4(\text{bptz})_4(\text{CH}_3\text{CN})_8]^{7+}$ in $2 \cdot 4\text{CH}_3\text{CN} \cdot \text{C}_4\text{H}_8\text{O}$. Thermal ellipsoids are represented at the 50% probability level. Selected bond distances (Å) and angles ($^\circ$): Ni4-N7D 2.035(5), Ni4-N3C 2.099(4), Ni4-N8D 2.038(5), Ni1-N2A 2.081(4), Ni1-N5D 2.073(5), Ni4-N5C 2.062(4), N2D-N3D 1.334(6), N2A-Ni1-N8A 90.10(18), N8A-Ni1-N7A 90.59(19), N7A-Ni1-N5D 87.29(18), N2A-Ni1-N7A 174.57(18), N7C-Ni3-N8C 88.21(19), N5B-Ni3-N2C 91.69(16), N2C-Ni3-N6B 87.89(17), N7C-Ni3-N2C 175.43(18).

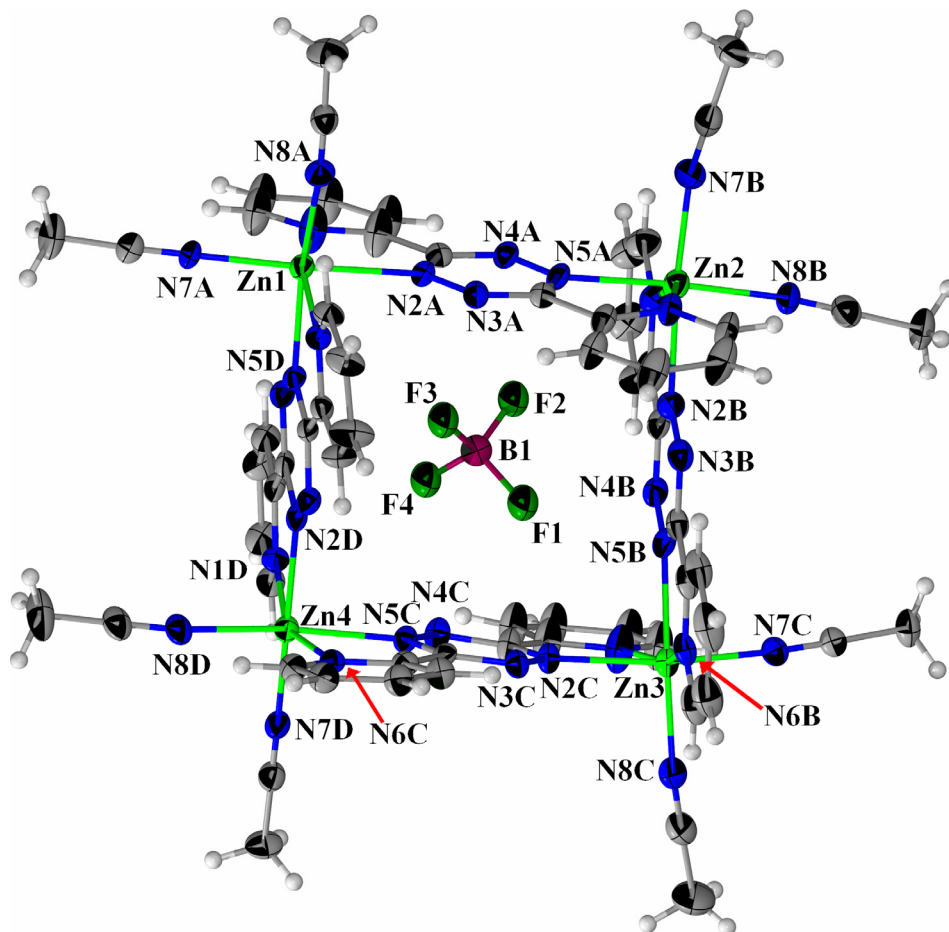


Figure 37: Thermal ellipsoid plot of the cationic unit $[Zn_4(bptz)_4(CH_3CN)_8]^{7+}$ in $3 \cdot 4CH_3CN$. Thermal ellipsoids are represented at the 50% probability level. Selected bond distances (Å) and angles (°): Zn1-N8A 2.074(4), Zn1-N7A 2.080(4), Zn1-N5D 2.260(4), Zn1-N2A 2.293(4), Zn4-N7D 2.070(4), Zn4-N8D 2.074(4), Zn4-N1D 2.095(4), Zn4-N6C 2.129(4), Zn4-N5C 2.246(4), Zn4-N2D 2.273(4), N8A-Zn1-N7A 92.62(17), N8A-Zn1-N5D 170.65(16), N7A-Zn1-N5D 92.98(16), N6B-Zn3-N5B 75.096(16), N8A-Zn1-N2A 89.79(16), N7A-Zn1-N2A 170.11(17), N5D-Zn1-N2A 85.95(14).

4. $[\{\text{Ni}_5(\text{bptz})_5(\text{CH}_3\text{CN})_{10}\}\text{SbF}_6][\text{SbF}_6]_9 \cdot 2\text{CH}_3\text{CN}$, (5**) $\cdot 2\text{CH}_3\text{CN}$** - The essential structural features of **5** were reported in a previous communication.⁴⁹ The thermal ellipsoid plot of the cation $[\{\text{Ni}_5(\text{bptz})_4(\text{CH}_3\text{CN})_8\}\text{SbF}_6]^{7+}$ is depicted in Figure 38. The molecular cation consists of a pentagon in which each metal ion occupies a vertex and five bptz ligands span the edges of the polygon. The cavity of $[\{\text{Ni}_5(\text{bptz})_4(\text{CH}_3\text{CN})_8\}]^{10+}$ is occupied by a $[\text{SbF}_6]^-$ anion and a partially encapsulated acetonitrile molecule. The five Ni \cdots Ni \cdots Ni vertex angles (107.83-108.19°) are close to that of an ideal pentagon (108°) even though the coordination angles N-Ni-N at the vertices are much smaller (91.2(3)-91.7(3)°). Clearly the flexibility of the bptz ligands, which bow inwards to compensate for the strain, allows for the formation of the closed pentagon structure.⁴⁹

5. $[\{\text{Ni}_4(\text{bptz})_4(\text{CH}_3\text{CN})_8\}\text{I}][\text{SbF}_6]_7$ (7**)** - Two significant observations emerged from this X-ray crystal structural determination, namely that the core structure of the pentagon has been transformed into a square, and that an iodide anion is located inside the cavity. A ball and stick plot of the cationic unit $[\{\text{Ni}_4(\text{bptz})_4(\text{CH}_3\text{CN})_8\}\text{I}]^{7+}$ is shown in Figure 39. Selected bond distances and angles are provided in the corresponding Figure caption. In **7**, the cation $[\{\text{Ni}_4(\text{bptz})_4(\text{CH}_3\text{CN})_8\}\text{I}]^{7+}$ has imposed 222 symmetry, therefore the four Ni \cdots Ni \cdots Ni vertex angles (87.52°) are identical and there are two pairs of Ni \cdots Ni distances (6.785 and 6.839 Å). The $[\text{I}]^-$ occupies a smaller molecular square cavity as compared to the analogous $[\text{BF}_4]^-$ and $[\text{ClO}_4]^-$ containing cations.

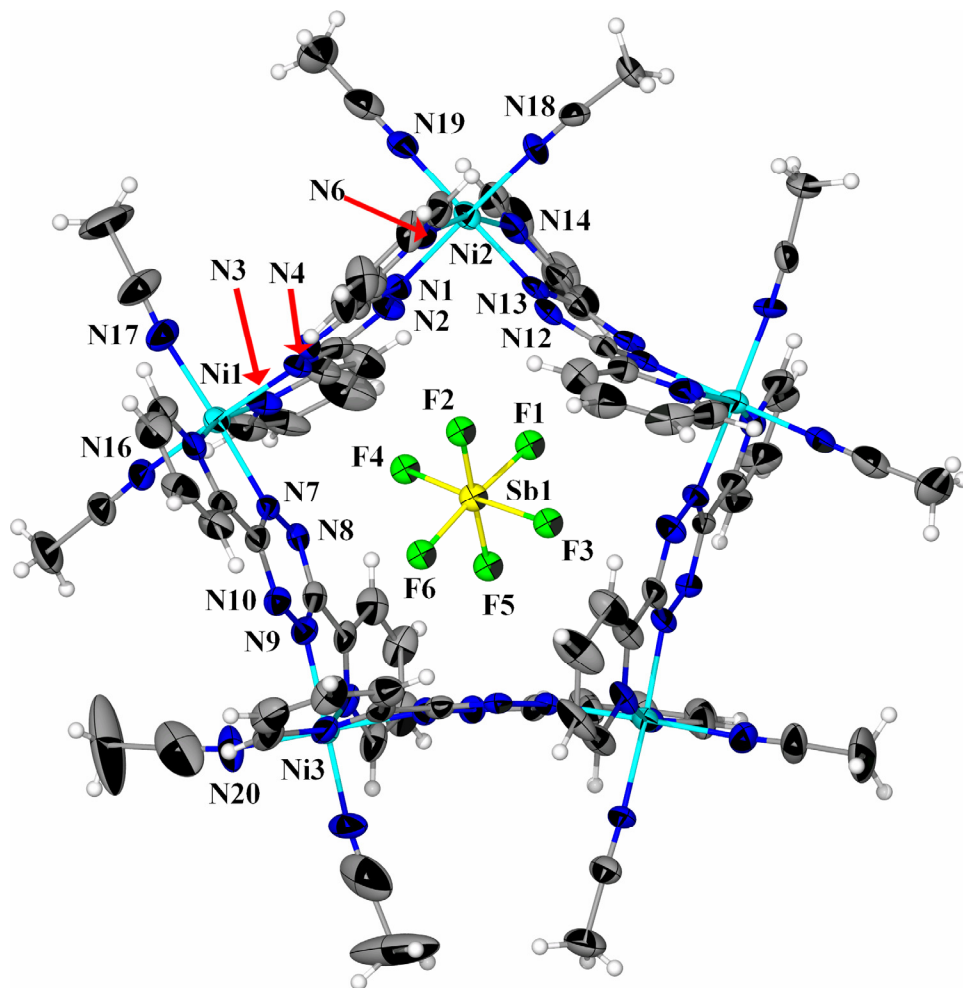


Figure 38: Thermal ellipsoid plot of the cationic unit $[\{\text{Ni}_5(\text{bptz})_5(\text{CH}_3\text{CN})_{10}\} \subset \text{SbF}_6]^{9+}$ in $5 \cdot 2\text{CH}_3\text{CN}$. Thermal ellipsoids are represented at the 50% probability level. Selected bond distances (Å) and angles (°) are: Ni1-N7 2.078(7), Ni1-N3 2.085(7), Ni1-N16 2.039(7), Ni1-N17 2.058(9), Ni1-N4 2.067(6), Ni2-N19 2.026(9), Ni2-N18 2.057(7), Ni2-N13 2.068(7), Ni2-N6 2.055(6), N4-Ni1-N7 91.8(3), N3-Ni1-N7 89.1(3), N17-Ni1-N7 176.8(3), N4-Ni1-N3 78.8(3), N18-Ni2-N19 92.4(3), N6-Ni2-N18 98.5(3), N19-Ni2-N13 177.4(3), N6-Ni2-N13 86.4(3), N18-Ni2-N13 86.4(3).

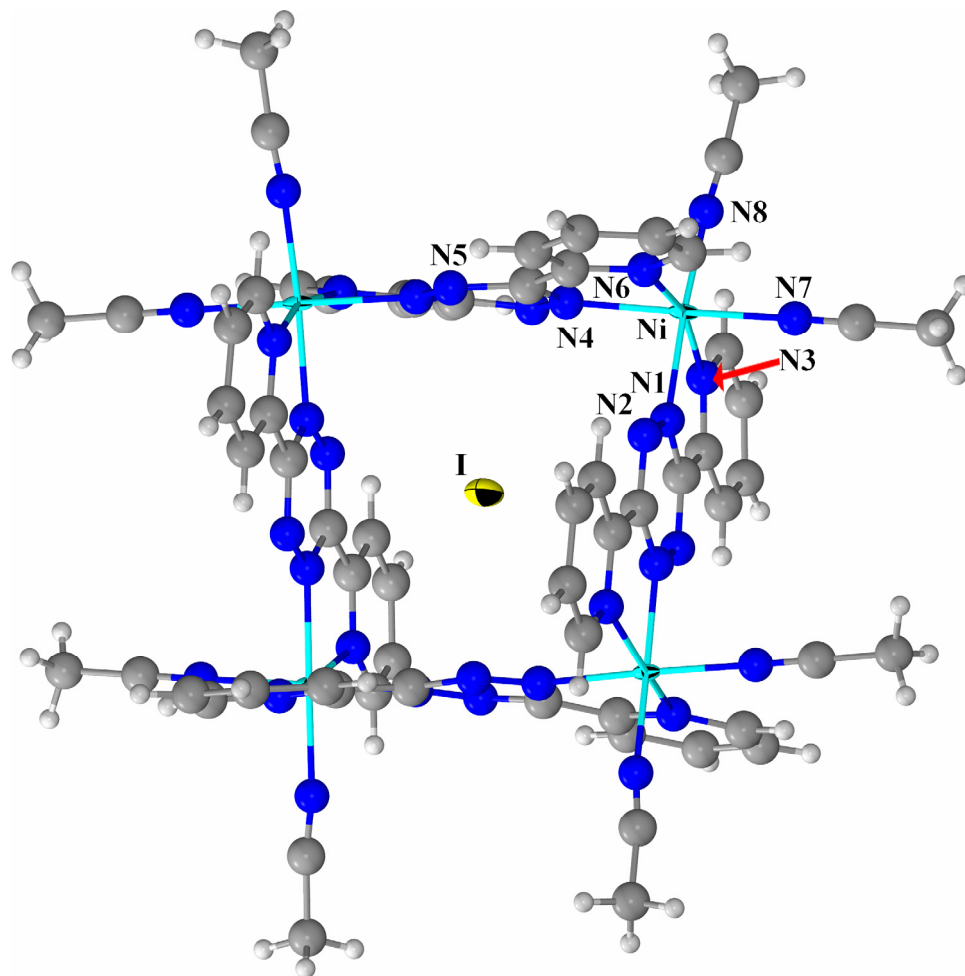
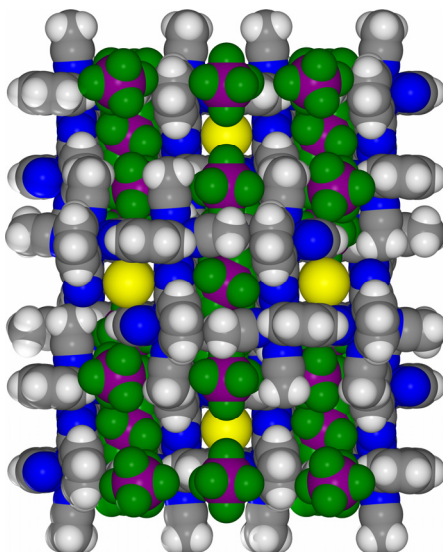


Figure 39: Ball and stick plot of the cationic unit $[\{Ni_4(bptz)_4(CH_3CN)_8\} \subset I]^{7+}$ in **7**. Thermal ellipsoids are represented at the 50% probability level except for the C and N atoms of the bptz ligands, which are circles of arbitrary radii. Selected bond distances (Å) and angles (°): Ni-N8 2.021(7), Ni-N7 2.045(8), Ni-N6 2.067(7), Ni-N1 2.076(6), Ni-N3 2.105(7), Ni-N4 2.103(8), N8-Ni-N7 89.5(3), N8-Ni-N6 97.6(3), N7-Ni-N6 95.2(3), N8-Ni-N1 174.1(3), N7-Ni-N1 88.73(3), N6-Ni-N1 88.1(3), N8-Ni-N3 95.4(3), N7-Ni-N3 91.9(3), N6-Ni-N3 165.2(3), N1-Ni-N3 79.6(3), N8-Ni-N4 92.2(3), N7-Ni-N4 173.1(3), N6-Ni-N4 77.9(3), N1-Ni-N4 90.2(2), N3-Ni-N4 94.6(2).

The two sets of centroid distances of the parallel tetrazine rings are 6.5480 and 7.026 Å. Due to their size, seven outer-sphere [SbF₆]⁻ anions occupy a large fraction of the unit cell volume. A packing diagram viewed along the *a*-axis is depicted in Figure 40a. It is evident from this diagram that the [Ni₄(bptz)₄(CH₃CN)₈]⁸⁺ cations are well suited to accommodate [I]⁻ ions in the square cavities and that the larger [SbF₆]⁻ anions result in a grid-like arrangement of squares in the crystal. A much less efficient packing of the squares is evident in the packing diagram of **2** (Figure 40b).

6. [Ni₄(bptz)₄(CH₃CN)₈][BF₄][PF₆][SbF₆]₆ (8**)** - Although crystals of **8** contain three different anions, the compound crystallizes in the same space group as **7** with similar cell dimensions. A thermal ellipsoid plot of [Ni₄(bptz)₄(CH₃CN)₈][BF₄][PF₆] is shown in Figure 41. Selected bond distances and angles are provided in the corresponding Figure caption. The cationic unit [Ni₄(bptz)₄(CH₃CN)₈]⁸⁺ has point symmetry 222 and the four Ni··Ni vertex angles are identical at 87.89° with two pairs of Ni··Ni distances (6.781 and 6.850 Å). The centroid distances of parallel tetrazine rings are 6.393 and 7.066 Å. The crystallographic symmetry site 222 results in two disordered components for the encapsulated [BF₄]⁻ ion. The [PF₆]⁻ and [SbF₆]⁻ ions are located in the interstices created by the cations. As in the case of **7**, the voids formed by the Ni(II) squares are channels rather than simple cavities. The [BF₄]⁻ ions occupy a portion of the volume inside the channels and are disordered along the channel direction

(A)



(B)

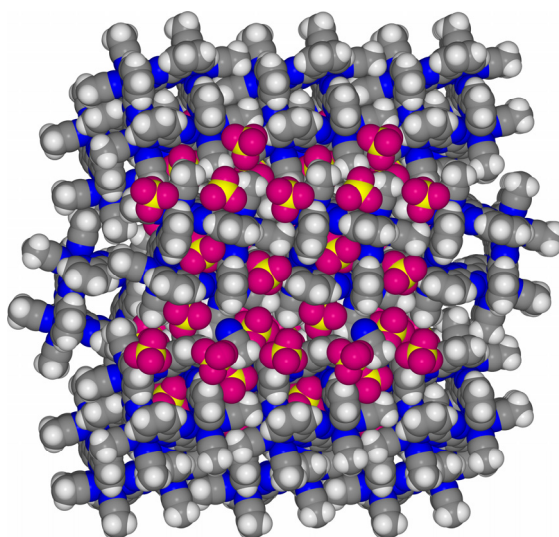


Figure 40: Packing diagram viewed along the a -axis of (A) $[\{\text{Ni}_4(\text{bptz})_4(\text{CH}_3\text{CN})_8\}\text{Cl}]^{7+}$ cations and $[\text{SbF}_6]^-$ anions in compound 7 and (B) $[\{\text{Ni}_4(\text{bptz})_4(\text{CH}_3\text{CN})_8\}\text{ClO}_4]^{7+}$ cations and $[\text{ClO}_4]^-$ anions in compound 2.

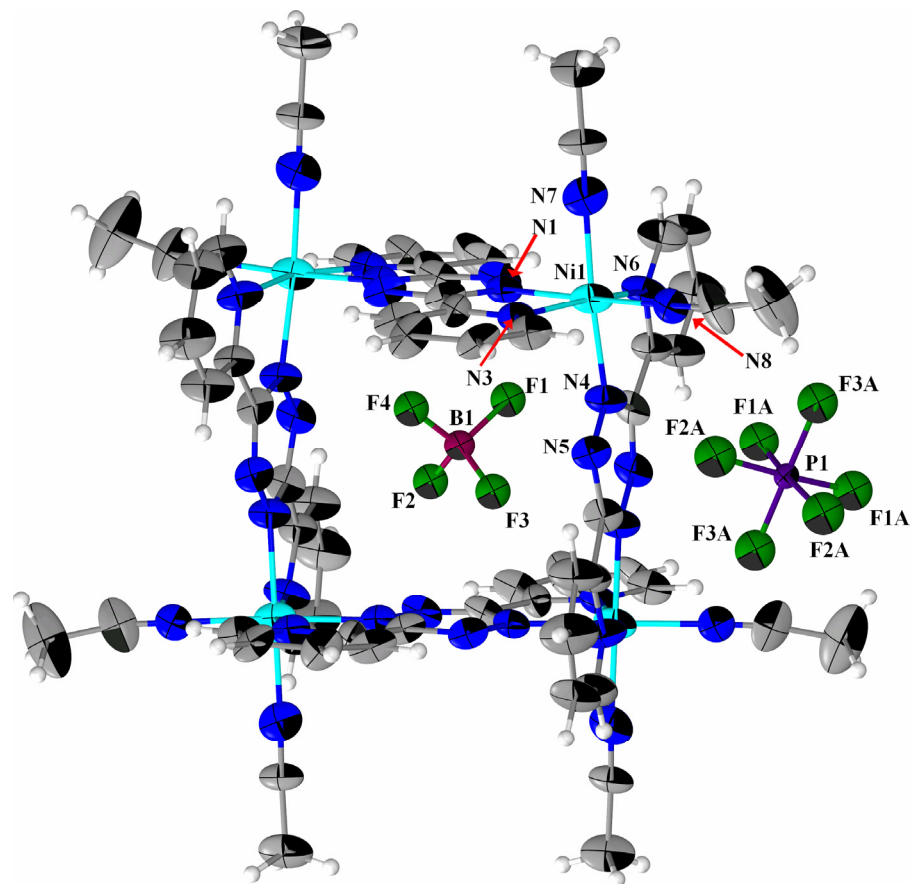


Figure 41: Thermal ellipsoid plot of the cationic unit $\{[\text{Ni}_4(\text{bptz})_4(\text{CH}_3\text{CN})_8]\text{cBF}_4\}[\text{PF}_6]^{6+}$ in **8**. Thermal ellipsoids are drawn at the 50% probability level. Selected bond distances (Å) and angles (°): Ni1-N8 2.008(15), Ni1-N1 2.055(11), Ni1-N7 2.068(13), Ni1-N4 2.095(10), Ni1-N6 2.088(11), Ni1-N3 2.096(11), P1-F2A 1.625(13), B1-F1 1.422(13), N8-Ni1-N1 173.2(4), N8-Ni1-N7 91.0(5), N1-Ni1-N7 86.9(5), N8-Ni1-N4 89.5(5), N1-Ni1-N4 93.3(5), N7-Ni1-N4 173.3(4), N1-Ni1-N6 87.8(5), N7-Ni1-N6 95.6(5), N4-Ni1-N6 77.8(4), N8-Ni1-N3 96.5(5), N1-Ni1-N3 77.1(5), N7-Ni1-N3 90.7(5), N4-Ni1-N3 95.8(4).

7. $[\{\text{Ni}_4(\text{bptz})_4(\text{CH}_3\text{CN})_4(\text{H}_2\text{O})_4\}\text{C}\text{ClO}_4][\text{IO}_4]_7 \cdot 3\text{CH}_3\text{CN}$, (**9**) $\cdot 3\text{CH}_3\text{CN}$ - The molecular structure of **9** is typical of the squares encountered in this study. A thermal ellipsoid plot of the $[\{\text{Ni}_4(\text{bptz})_4(\text{CH}_3\text{CN})_4(\text{H}_2\text{O})_4\}\text{C}\text{ClO}_4][\text{IO}_4]$ unit is shown in Figure 42. The cation $[\text{Ni}_4(\text{bptz})_4(\text{CH}_3\text{CN})_8]^{8+}$ resides on a two-fold axis, thus there are two pairs of Ni...Ni vertex distances (6.826 and 6.834 Å) and two centroid distances between tetrazine rings of parallel bptz ligands (6.913 and 7.038 Å). The coordination environment of the two pairs of Ni(II) ions is completed by two acetonitrile and two water molecules, respectively. The Ni-O (H₂O) distances are 2.031(12) and 2.035(13) Å. The Ni-N distances are in the range observed for the other Ni-bptz complexes reported herein. It is notable that the $[\text{ClO}_4]^-$ anion still occupies the space inside the cavity of the $[\text{Ni}_4(\text{bptz})_4(\text{CH}_3\text{CN})_8]^{8+}$ square whereas the outer-sphere anions are $[\text{IO}_4]^-$.

8. $[\{\text{Ni}_4(\text{bptz})_4(\text{CH}_3\text{CN})\text{Br}_7\}\text{C}\text{Br}_3] \cdot 2\text{CH}_3\text{CN} \cdot 2.5\text{C}_7\text{H}_8$, (**10**) $\cdot 2\text{CH}_3\text{CN} \cdot 2.5\text{C}_7\text{H}_8$ - The structure of the neutral molecular complex **10** is a square with four Ni(II) ions at the vertices and bptz ligands spanning the edges. This compound is unique among the members of the square series in that it is neutral, if the encapsulated $[\text{Br}_3]^-$ is taken into consideration. A thermal ellipsoid plot of the unit $[\{\text{Ni}_4(\text{bptz})_4(\text{CH}_3\text{CN})\text{Br}_7\}\text{C}\text{Br}_3]$ is illustrated in Figure 43. Selected bond distances and angles are provided in the corresponding Figure caption. Each Ni(II) center adopts a pseudo-octahedral coordination geometry with four sites being occupied by two different bptz ligands. The other two coordination sites of the three Ni(II) ions are occupied by bromide ions while the fourth Ni(II) center is coordinated to a bromide ion and an acetonitrile molecule.

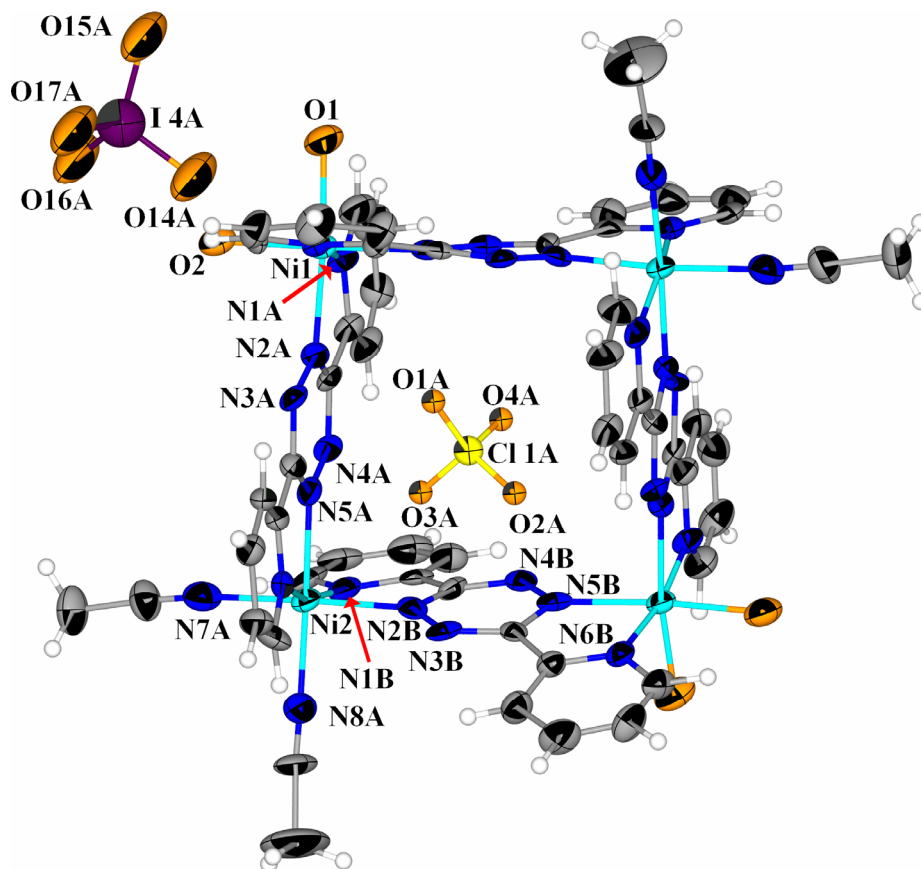


Figure 42: Thermal ellipsoid plot of the cationic unit $\{[\text{Ni}_4(\text{bptz})_4(\text{CH}_3\text{CN})_4(\text{H}_2\text{O})_4]\text{ClO}_4\}^{6+}$ in $\mathbf{9} \cdot 3\text{CH}_3\text{CN}$. Thermal ellipsoids are represented at the 50% probability level. Selected bond distances (Å) and angles (°): Ni1-O2 2.035(13), Ni1-O1 2.031(12), Ni1-N1A 2.072(14), Ni1-N2A 2.067(14), Ni2-N1B 2.053(17), Ni2-N7A 2.08(2), Ni2-N2B 2.056(14), Ni2-N8A 2.067(16), Ni2-N6A 2.077(16), Ni2-N5A 2.103(13), O2-Ni1-O1 86.6(5), O2-Ni1-N1A 93.5(6), O1-Ni1-N1A 92.9(5), O2-Ni1-N2A 87.4(5), O1-Ni1-N2A 169.4(6), N1A-Ni1-N2A 78.7(5), N1B-Ni2-N7A 95.8(6), N1B-Ni2-N2B 78.6(6), N7A-Ni2-N2B 173.7(6), N1B-Ni2-N6A 163.6(6).

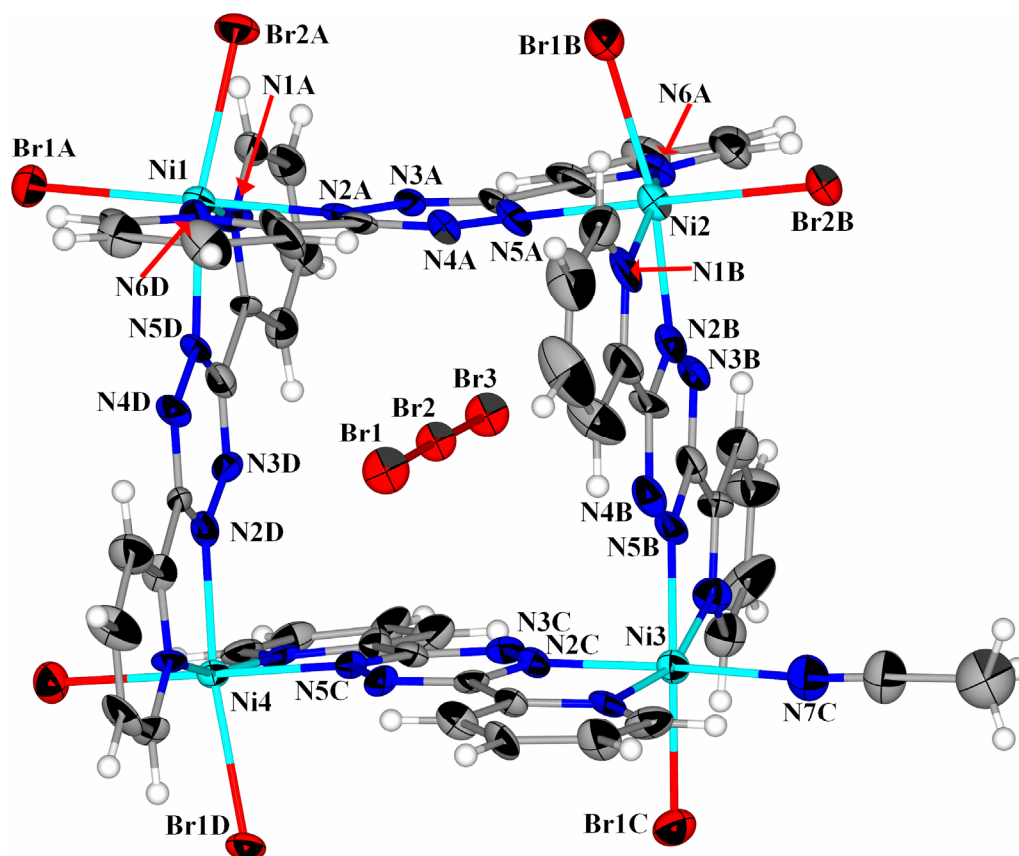


Figure 43. Thermal ellipsoid plot of the unit $[\{\text{Ni}_4(\text{bptz})_4(\text{CH}_3\text{CN})\text{Br}_7\} \cdot \text{Br}_3]$ in $10 \cdot 2\text{CH}_3\text{CN} \cdot 2.5\text{C}_6\text{H}_5\text{CH}_3$. Thermal ellipsoids are represented at the 50% probability level. Selected bond distances (Å) and angles (°): Br1-Br2 2.525(2), Br2-Br3 2.566(2), Ni1-N1A 2.097(10), Ni1-N6D 2.079(10), Ni1-N2A 2.092(10), Ni1-N5D 2.128(9), Ni1-Br1A 2.479(2), Ni1-Br2A 2.537(2), Br1-Br2-Br3 179.17(7), N1B-Ni2-N6A 161.1(4), N1A-Ni1-N2A 78.0(4), N6D-Ni1-N2A 89.1(4), N1A-Ni1-N5D 89.7(4), N6D-Ni1-N5D 77.6(4), N2A-Ni1-N5D 87.7(3), N1A-Ni1-Br1A 96.8(3), N6D-Ni1-Br1A 96.1(3), N2A-Ni1-Br1A 174.8(3), N1A-Ni1-Br2A 94.9(3), N6D-Ni1-Br2A 95.4(3), N2A-Ni1-Br2A 82.5(2), N5D-Ni1-Br2A 168.1(3), Br1A-Ni1-Br2A 97.59(7).

Presumably, replacement of the last acetonitrile by bromide is not favored due to the fact that the molecule with the encapsulated $[\text{Br}_3]^-$ is neutral. The Ni \cdots Ni distances are in the range of 6.806-6.915 Å whereas the *trans* tetrazine ring centroid separations are 6.638 and 7.014 Å. The Ni-N(bptz) distances are in the range 2.072(10)-2.128(9) Å and the Ni-N(CH₃CN) distance is 2.035(13) Å. The bptz ligands are nearly planar and the $[\text{Br}_3]^-$ ion inside the cavity is parallel to the adjacent pairs of bptz ligands. The distances within the $[\text{Br}_3]^-$ anion are Br1-Br2 = 2.525(2) Å and Br2-Br3 = 2.566(2) Å.

9. $[\text{Ni}_2(\text{bptz})(\text{CH}_3\text{CN})_8][\text{ClO}_4]_4$ (11) - Compound **11** consists of a dinuclear cation in which two Ni(II) ions are bridged by a bptz ligand. A thermal ellipsoid plot of the cationic unit $[\text{Ni}_2(\text{bptz})(\text{CH}_3\text{CN})_8]^{4+}$ is shown in Figure 44. Selected bond distances and angles are provided in the corresponding Figure caption. Each metal ion is found in a distorted octahedral environment with two sites being occupied by bptz and the remaining four sites capped by acetonitrile ligands. The midpoint of the tetrazine ring of the bptz ligand lies on an inversion center. The Ni1-N1(bptz-pyridyl) and Ni1-N2 (bptz-tetrazine) distances are 2.067(7) and 2.078(7) Å, respectively, while the Ni1-N(CH₃CN) distances are in the range of 2.045(7)-2.075(7) Å. The Ni1-Ni2 distance is 6.904 Å, which is typical for the bptz bridged Ni \cdots Ni complexes.

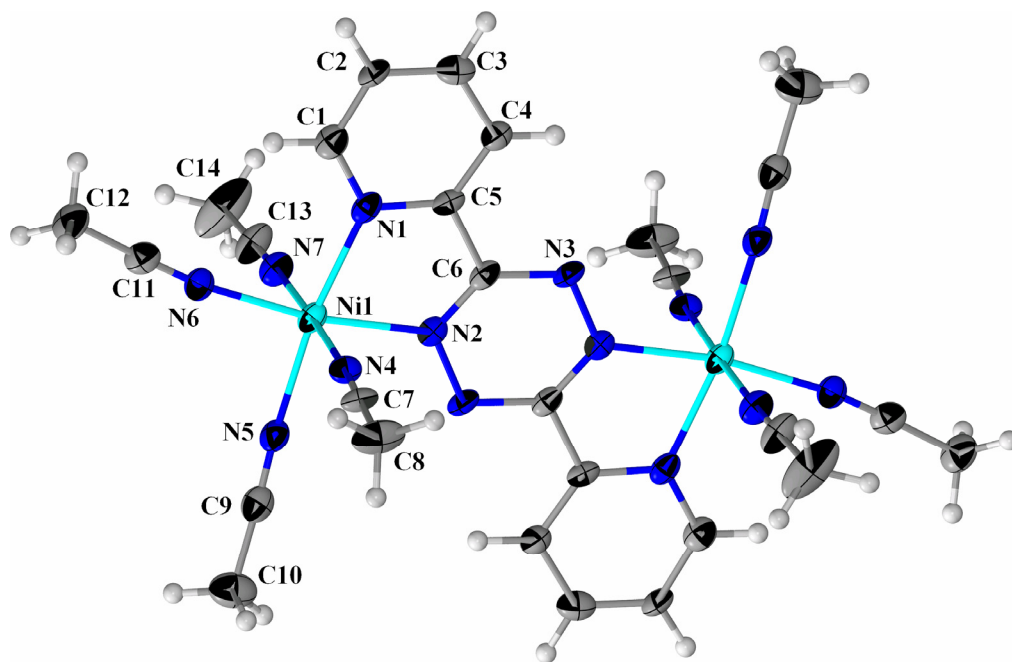


Figure 44: Thermal ellipsoid plot of the cationic unit $[\text{Ni}_2(\text{bptz})(\text{CH}_3\text{CN})_8]^{4+}$ in **11**. Thermal ellipsoids are drawn at a 50% probability level. Selected bond distances (\AA) and angles ($^\circ$): Ni1-N1 2.067(7), Ni1-N2 2.078(6), Ni1-N4 2.072(6), Ni1-N5 2.078(7), Ni1-N6 2.075(7), Ni1-N7 2.045(7), N4-C7 1.131(8), N6-C11 1.145(9), N5-C9 1.153(9), N2-C6 1.294(9), C6-C5 1.497(10), C1-C2 1.375(10), C2-C3 1.335(11), C3-C4 1.384(11), N7-Ni1-N4 177.8(3), N1-Ni1-N5 171.7(2), C13-N7-Ni1 177.5(7), N4-Ni1-N5 86.1(2), N6-Ni1-N5 94.8(2), N2-Ni1-N5 95.0(2), N1-Ni1-N4 89.8(2), N7-Ni1-N6 90.2(2), N1-Ni1-N6 92.4(2), N4-Ni1-N6 88.6(2), N7-Ni1-N2 90.9(2), N1-Ni1-N2 77.8(2), N4-Ni1-N2 90.6(2).

10. $\{[\text{Mn}(\text{bptz})(\text{CH}_3\text{CN})_2][\text{BF}_4]_2 \cdot 1.5\text{CH}_3\text{CN}\}_\infty$ (**12**) $\cdot 1.5n\text{CH}_3\text{CN}$ - The structure of **12** consists of a cationic polymer in which two Mn(II) centers are bridged by bptz ligands that lie on inversion centers. A thermal ellipsoid plot of the $[\text{Mn}_2(\text{bptz})_2(\text{CH}_3\text{CN})_4]$ unit is shown in Figure 45. Selected bond distances and angles are provided in the corresponding Figure caption. The trans arrangement of the Mn-bptz units leads to formation of a polymeric structure rather than a discrete cyclic oligomer. Each Mn(II) center is in a slightly distorted octahedral geometry with two bptz units and two acetonitrile ligands completing the coordination sites. The Mn-N distances follow the same trend as other metallacyclophanes, namely the shorter bonds are to the acetonitrile ligands (2.143(4) and 2.166(4) Å). The Mn-N(pyridyl) bond distances are 2.225(4) and 2.231(4) Å and the Mn-N(tetrazine) distances are 2.318(4) and 2.313(4) Å. The Mn...Mn separation is 7.327 Å.

IV. Discussion

A. Product Nuclearity Dependence on the Anion Identity

Considering the divergent nature of bptz and the absence of protective ligands around the Ni(II) and Zn(II) metal ions, the isolation of the discrete molecular squares **1–4** in high-yields is quite remarkable. The formation of molecular squares is dominant in the presence of both $[\text{BF}_4]^-$ and $[\text{ClO}_4]^-$ ions, regardless of the presence of $[\text{SbF}_6]^-$ ions (Schemes 3, 4). Other metallacages with encapsulated anions⁷⁸ have been reported to form in essentially quantitative yields as judged by NMR spectroscopy, but in many cases a variety of oligomeric species are detected.⁷⁹

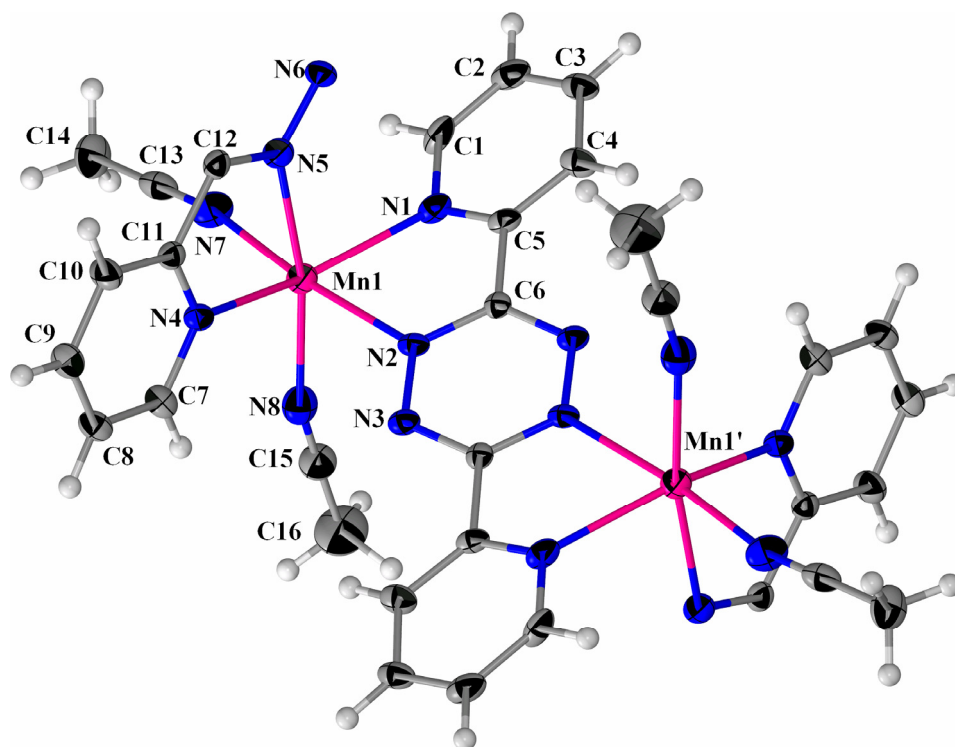


Figure 45: Thermal ellipsoid plot of the cationic repeat unit $[\text{Mn}_2(\text{bptz})_2(\text{CH}_3\text{CN})_4]^{4+}$ in the polymer $\mathbf{12} \cdot 1.5n\text{CH}_3\text{CN}$. Thermal ellipsoids are represented at the 50% probability level. Selected bond distances (Å) and angles (°): Mn1-N8 2.143(4), Mn1-N7 2.166(4), Mn1-N4 2.225(4), Mn1-N1 2.231(4), Mn1-N5 2.313(4), Mn1-N2 2.318(4), N4-C11 1.333(5), N4-C7 1.351(5), N3-N2 1.328(5), Mn1...Mn1' 7.327(1), N7-Mn1-N5 172.45(14), N4-Mn1-N5 71.18(13), N1-Mn1-N2 71.32(13), N5-Mn1-N2 94.54(12), N8-Mn1-N1 97.32(14), N7-Mn1-N1 99.20(14), N8-Mn1-N7 93.81(14), N8-Mn1-N4 108.67(14).

The lability of Zn(II) ions favors the conversion of intermediates into a single product by a *self-reorganization* mechanism, which reduces the likelihood of obtaining insoluble kinetic products and leads to formation of the square in high yields. This is supported by the fact that the presence of excess $[\text{Zn}(\text{CH}_3\text{CN})_4]^{2+}$ ions leads to formation of the square $[\text{Zn}_4(\text{bptz})_4(\text{CH}_3\text{CN})_8][\text{BF}_4]_8$, as evidenced by ^1H NMR spectroscopy. The mass spectrometric data clearly point to the existence of intrinsically stable $[\text{Ni}_4]$ (Figure 26) and $[\text{Zn}_4]$ (Figure 27) species in the gas phase, in the presence of $[\text{BF}_4]^-$ and $[\text{ClO}_4]^-$ anions, with no evidence of higher nuclearity species such as the pentagon. Since both $[\text{BF}_4]^-$ and $[\text{ClO}_4]^-$ anions promote the formation of molecular squares with Ni(II) and Zn(II) ions (Scheme 1), presumably due to similarities in their size and shape,⁶⁷ it is reasonable to expect that molecular polygons of different nuclearities can form, in the presence of other appropriate anions. The single crystal structural determination of $[\text{Ni}_5(\text{bptz})_5(\text{CH}_3\text{CN})_{10}\text{SbF}_6]^{9+}$ revealed that the shape and size of the $[\text{SbF}_6]^-$ anion render it appropriate to occupy a cavity slightly larger than that of the square, *viz.*, that of a pentagon (Figure 38).⁴⁹ Furthermore, the ES-MS studies of **5** in acetonitrile established that the $[\text{Ni}_5]$ moiety persists in solution (Figure 28) for long periods of time with no indication of lower nuclearity products. Therefore, the anion $[\text{SbF}_6]^-$ leads to the exclusive formation of the molecular pentagon both in solid state and in solution.

The dictating role of the anion in these reactions is further corroborated by the formation of **6** from **5** in the presence of an excess amount of $[\text{NO}_3]^-$ anions. The existence of a possible molecular triangular unit is supported by the ion signal at m/z 1194.7, which corresponds to $[\text{Ni}_3(\text{bptz})_3(\text{NO}_3)_5]^+$ (Figure 29). Since X-ray quality single crystals of **6** could not be obtained, in spite of numerous attempts, the identity

of the triangle is supported solely by mass spectral data. It is important to note that the characteristic patterns for the $[\text{Ni}_5]$ and $[\text{Ni}_4]$ polygons are not evident in this spectrum, which suggests that the $[\text{NO}_3]^-$ anion is too small to template these higher nuclearity species.

B. Anion Selectivity of the Cavity

To further probe the anion selectivity in the molecular polygon formation, a solution of the pentagon **5** was treated with an equimolar mixture of $[\text{BF}_4]^-$ and $[\text{PF}_6]^-$ ions (Scheme 6). The X-ray crystal structural determination of the resulting compound **8**, showed it to be a molecular square in which a $[\text{BF}_4]^-$ ion resides inside the cavity (Figure 41) and $[\text{PF}_6]^-$ with six $[\text{SbF}_6]^-$ acting as outer-sphere anions. The $[\text{PF}_6]^-$ anion is not incorporated inside the cavity of the square, nor does its presence lead to a product of different nuclearity, facts which further underscore the importance of the anion size and shape in promoting a particular cyclic structure. Moreover, treatment of **2** with an excess of $[\text{IO}_4]^-$, leads to replacement of all the $[\text{ClO}_4]^-$ anions, except for the one residing inside the cavity (Scheme 7, Figure 42). Conversely, similar treatment of **2** with an excess of $[\text{Br}_3]^-$ ions, leads to displacement of the $[\text{ClO}_4]^-$ with $[\text{Br}_3]^-$ ions (Scheme 8, Figure 43). Obviously, the larger tetrahedral anion $[\text{IO}_4]^-$ cannot replace $[\text{ClO}_4]^-$ inside the cavity, but the linear $[\text{Br}_3]^-$ anion is capable of doing so.

Apart from ‘weakly coordinating’ anions, halides were also probed as possible templates in the chemistry of M(II) with bptz. Although reactions of halide salts with the pentagon **5** led to insoluble solids, in the case of $[n\text{-Bu}_4\text{N}][\text{I}]$, a crop of crystals **7**, consisting of a molecular square with an encapsulated iodide ion (Scheme 5, Figure 39), was collected. The fact that the spherical $[\text{I}]^-$ anion can template the formation of

the square seems contradictory to the requirement of a specific anion geometry (namely tetrahedral) to form the square, unless the size and polarizability of $[I]^-$ are taken into consideration; the large polarizability of iodide ($19.22 \text{ cm}^3 \text{ mol}^{-1}$ in H_2O) allows it to adopt the directionality of a tetrahedral geometry.⁹

C. Stability of the Molecular Pentagon vs. the Square

The competing influence of the anions in stabilizing the different cyclic entities was nicely probed by mass spectrometry and X-ray crystallography. The $[\text{Ni}_5]$ pentagon **5** was found to be less stable compared to its $[\text{Ni}_4]$ analogs **1** and **2**. Ion signals corresponding to the molecular square begin to appear in the MS spectra after addition of $[n\text{-Bu}_4\text{N}][\text{BF}_4]$ or $[n\text{-Bu}_4\text{N}][\text{ClO}_4]$ to a solution of **5** and complete conversion of the Ni(II) pentagon to the square is achieved by adding an excess of either tetrahedral anion (Scheme 3). Moreover, crystals of **1** are obtained from an acetonitrile solution of **5** that is layered over a saturated benzene solution of $[n\text{-Bu}_4\text{N}][\text{BF}_4]$. The aforementioned results underscore the ability of $[\text{BF}_4]^-$ and $[\text{ClO}_4]^-$ anions to template the formation of the molecular square even in the presence of $[\text{SbF}_6]^-$ ions (Figure 30). The reverse conversion, namely that of the square to the pentagon, is also possible, albeit under much harsher conditions, *viz.*, heating and long reaction times (Scheme 6, Figure 46). Given the strain that is evident by the bowing of the bptz ligands in the pentagon (Figure 38),⁴⁹ it is not unreasonable to expect that the square is intrinsically more stable than the pentagon.

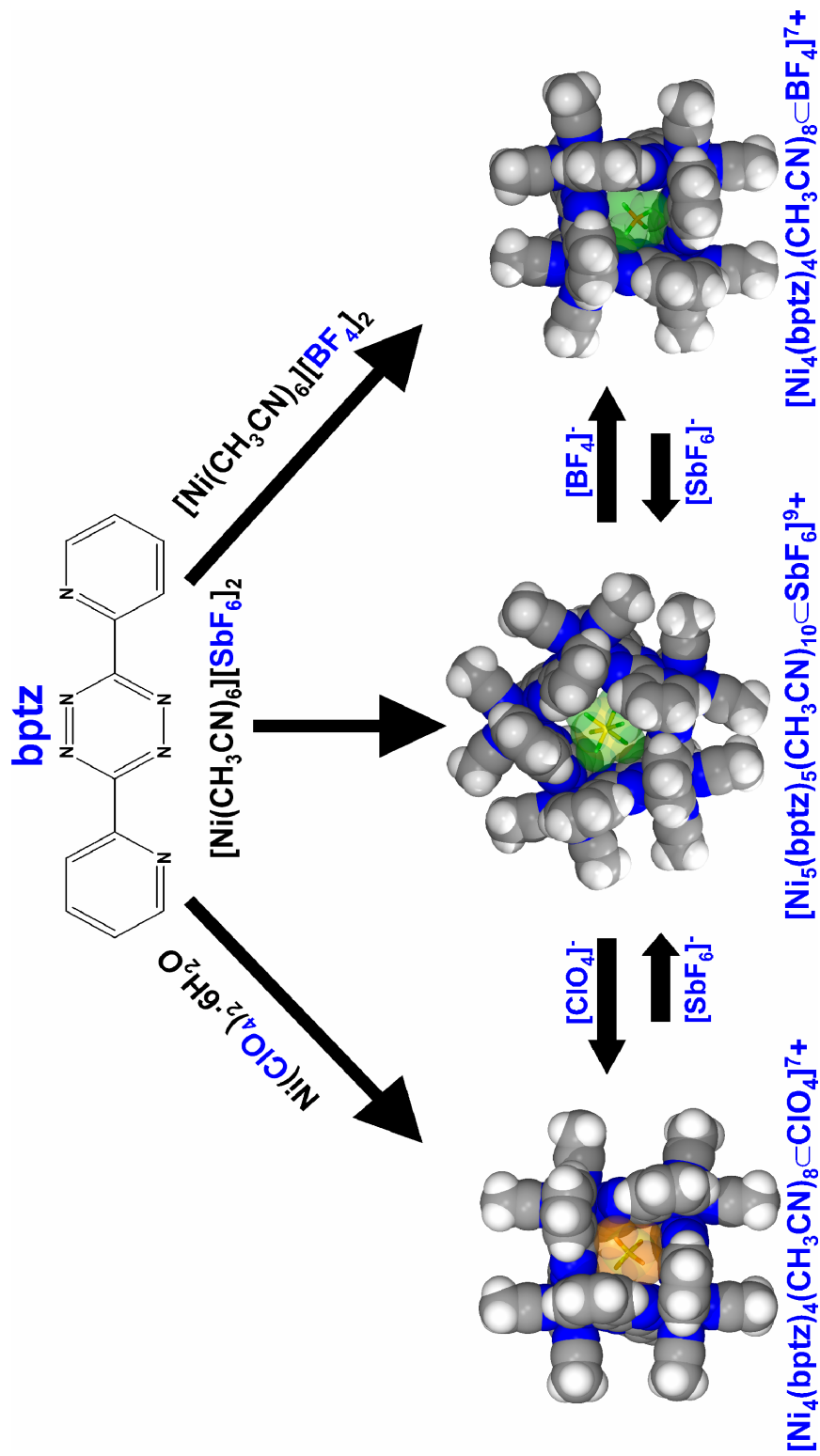


Figure 46: Space-filling representations of the cationic units $[Ni_5(bptz)_5(CH_3CN)_{10}]SbF_6]^{9+}$, $[Ni_4(bptz)_4(CH_3CN)_8]ClO_4]^{9+}$ or $[Ni_4(bptz)_4(CH_3CN)_8]SbF_6]^{9+}$ and their scheme of interconversion.

Mass spectrometric spectra indicate however that, in the absence of competing anions, the square and the pentagon are not interconverting in solution to form equilibrium mixtures (Figures 26, 28). The high stability of the square is further supported by the fact that it is possible to exchange $[\text{ClO}_4]^-$ for $[\text{Br}_3]^-$ in the cavity of **2** (Scheme 8). Single crystal X-ray studies of $[\{\text{Ni}_4\text{Br}_7(\text{bptz})_4(\text{CH}_3\text{CN})\} \subset \text{Br}_3]$ reveal that the anion trapped inside the cavity is $[\text{Br}_3]^-$ and the parent square cation remains intact, despite the fact that seven of the eight acetonitrile ligands have been replaced by bromide ions (Figure 43). This result is also promising in light of the potential to displace the acetonitrile ligands without degradation of the molecular square, a requisite condition for connecting individual square units via bridging ligands.

D. Divalent Transition Metals and Product Identity

The investigation of the reactions of other divalent transition metals, namely Mn(II), Fe(II) and Cu(II) with bptz, supports the importance of the metal identity on the outcome of these reactions. Although the previous metals form the corresponding ‘ $\text{M}_4(\text{bptz})_4$ ’ clusters, as evidenced by ESI-MS data recorded immediately after mixing the $\text{M}(\text{ClO}_4)_2 \cdot x\text{H}_2\text{O}$ precursors with bptz in acetonitrile (Figures 31-33), the ‘ $\text{M}_4(\text{bptz})_4$ ’ clusters are not stable and their ion signals decrease over time with enhancement of the intensities of lower nuclearity species; this is in contrast to the Ni(II) and Zn(II) squares. The reason for the different stabilities, although purely speculative, is attributed to subtle differences in the metal ions; for example $[\text{BF}_4]^-$ or $[\text{ClO}_4]^-$ ions may not have the same tendency to template “ $\text{M}(\text{bptz})$ ” units of various metals, due to insufficient favorable contacts. Cations such as Fe(II) are less kinetically labile than Ni(II) or Zn(II), thus the *self-reorganization* mechanism that leads to the high-yield assembly of the

thermodynamically favorable species may not be efficient. In the case of the Cu(II) ion, the expected Jahn-Teller distortion could affect the formation of stable cyclic architectures such as molecular squares. It is thus apparent that the assembly of various cages arises from an ideal match between the coordination preferences of the metal ions, the symmetry properties of the ligands,⁸⁰ and the anions present.

The reaction of solvated 3d metal ions with divergent ligands can, in principle, give rise to a variety of species. It is rare, however, to find examples in which open chain oligomers or polymers are isolated from the same reaction that favors formation of molecular squares.⁸¹ The reaction of $\text{Ni}(\text{ClO}_4)_2 \cdot 6\text{H}_2\text{O}$ with bptz affords, apart from the tetranuclear cage **2**, a small quantity of the dinuclear product $[\text{Ni}_2(\text{bptz})(\text{CH}_3\text{CN})_8][\text{ClO}_4]_4$ (**11**) (Figure 44), which suggests that the molecular squares **1** and **2** may be forming by dimerization of these intermediates. In the case of bptz reactions with $[\text{Mn}(\text{CH}_3\text{CN})_6][\text{BF}_4]_2$, a small quantity of the zig-zag polymeric chain $\{[\text{Mn}(\text{bptz})(\text{CH}_3\text{CN})_2][\text{BF}_4]_2\}_\infty$ (**12**) (Figure 45) is formed. The isolation of **12** suggests that the formation of discrete cyclic products is not an obvious outcome but the result of the interplay of a variety of factors including anion, metal and solvent identity.

It is important to note that although both the Ni(II) and Zn(II) molecular squares are easily isolated in the solid-state with the encapsulated anions $[\text{BF}_4]^-$ and $[\text{ClO}_4]^-$, their relative stabilities are quite different. Contrary to the Ni(II) squares, which are stable in solution for long periods of time, acetonitrile solutions of the $[\text{Zn}_4]^{8+}$ cations (in **3** and **4**) begin to decompose after approximately one week with deposition of insoluble precipitates, presumably polymeric in nature; this fact may be attributed to the greater lability of the Zn-N bonds. Moreover, unlike the Ni(II)

analog, the formation of $[\text{Zn}_4(\text{bptz})_4(\text{CH}_3\text{CN})_8]^{8+}$ is more sensitive to reaction conditions such as temperature and solvent (mass spectrometric studies indicate that the $[\text{Zn}]^{8+}$ species is formed only in acetonitrile).

E. Anion Interactions with the Cyclic Cations

Anions are known to occupy void spaces inside the cavity of macrocycles, a fact that is largely attributed to efficient crystal packing in the absence of any prominent non-covalent interactions.⁸² In the space-filling representations of **1**, **2** and **5** with the encapsulated anions $[\text{BF}_4]^-$, $[\text{ClO}_4]^-$, $[\text{SbF}_6]^-$, respectively, the efficiency of their packing in the metallacycles is nicely illustrated (Figure 46). Careful examination of the relevant structural parameters for **1-3**, **5** and **7-10**, however, suggests that in the cyclic structures presented herein there may be other stabilizing factors. Short distances are noted between the centroids of the tetrazine rings to the O/F atoms of the encapsulated anions rather than obvious interactions with the cationic metal centers.⁸⁰ Several theoretical studies on this type of contacts, *e.g.*, anion π -interactions, have been undertaken recently.¹² A systematic study of N-heterocyclic ligands, with different degrees of electropositive character on the central π -ring systems, may reveal the degree to which such interactions are dictating the formation and stabilization of a particular cyclic product. It is notable that several reports support the existence of such interactions based on the location of the anion in the cavity.^{35,36,83}

V. Conclusions

The importance of the anions in the formation of cyclic molecules from a set of simple precursors has been demonstrated. The fact that the reaction between divalent metal ions and bptz can be tuned by the choice of counterion to favor a

particular cyclic structure provides compelling evidence for an anion template effect in this chemistry. In particular, the tetrahedral anions $[\text{BF}_4]^-$ and $[\text{ClO}_4]^-$ act as templates in the formation of molecular squares with Ni(II) and Zn(II) ions and the bptz ligand. The anion $[\text{SbF}_6]^-$ was found to lead to the exclusive formation of a molecular pentagon with Ni(II), and mass spectrometric data suggest the existence of a molecular triangle in the presence of $[\text{NO}_3]^-$ anions. The molecular pentagon is less stable than the square, as evidenced by the facile conversion of $[\{\text{Ni}_5(\text{bptz})_5(\text{CH}_3\text{CN})_{10}\}\text{SbF}_6]^{9+}$ to $[\{\text{Ni}_4(\text{bptz})_4(\text{CH}_3\text{CN})_8\}\text{BF}_4]^{7+}$, $[\{\text{Ni}_4(\text{bptz})_4(\text{CH}_3\text{CN})_8\}\text{ClO}_4]^{7+}$ (Figure 46) or $[\{\text{Ni}_4(\text{bptz})_4(\text{CH}_3\text{CN})_8\}\text{I}]^{7+}$, by addition of excess quantities of $[\text{BF}_4]^-$, $[\text{ClO}_4]^-$ or $[\text{I}]^-$ anions to acetonitrile solutions of the pentagon, respectively (Figure 47). The reverse conversion of the square to the pentagon requires heating and does not go to completion. Anion exchange reactions of $[\{\text{Ni}_4(\text{bptz})_4(\text{CH}_3\text{CN})_8\}\text{ClO}_4][\text{ClO}_4]_7$ indicate that, as expected, a larger anion such as $[\text{IO}_4]^-$ cannot replace $[\text{ClO}_4]^-$ inside the cavity, but the linear $[\text{Br}_3]^-$ anion is capable of doing so. It can be concluded from this study that the nuclearity of the cyclic products is strongly influenced by the identity of the anion present in solution during the self-assembly process. The latter may be attributed to a template effect that stabilizes one particular cage over another due to favorable contacts between the anion inside the cavity and the bptz ligands. Given that there are close directional contacts between the anion and the central tetrazine ring of the bptz ligands, it is of interest to further explore the possibility of anion π -interactions being operative in dictating the outcome of these reactions.

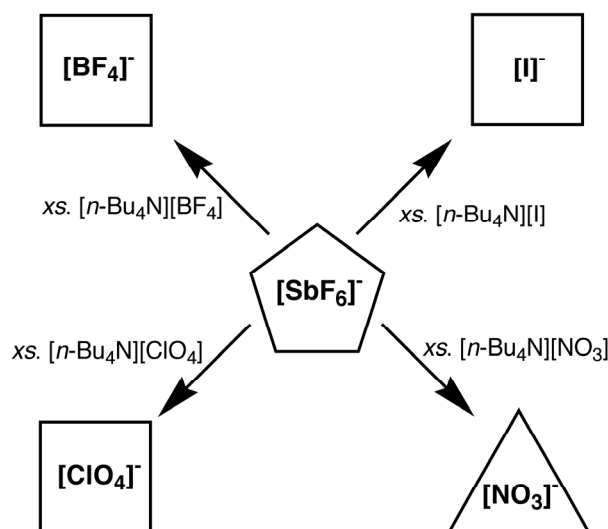


Figure 47: Schematic Diagram of how several compounds that can be synthesized starting with $[\text{Ni}_5(\text{bptz})_5(\text{CH}_3\text{CN})_{10}\text{SbF}_6][\text{SbF}_6]_9$.

CHAPTER III

ANION- Π INTERACTIONS AS CONTROLLING ELEMENTS IN
SELF-ASSEMBLY REACTIONS OF Ag(I) COMPLEXES WITH Π -
ACIDIC AROMATIC RINGS*

I. Introduction

Numerous examples of cation- π interactions in many organic and biochemical systems have been reported,^{84,85} but the electron-donating character of anions and the expected repulsive interactions with aromatic π -systems has limited the development of noncovalent anion- π interaction chemistry. A few NMR studies, however, indicate association between neutral π moieties and negatively charged groups,^{13,43,46} and several theoretical studies suggest that noncovalent electrostatic interactions between anions and π -electron deficient aromatic rings (*i.e.*, hexafluorobenzene, trinitrobenzene, *s*-triazine, *s*-tetrazine), primarily consisting of electrostatic and anion-induced polarization contributions,³⁰ are energetically favorable.^{12,21,23,25-27,30,32,40,46} Recently, the term ‘anion- π interaction’ was coined by Frontera *et al.*, to describe these interactions.^{12c}

* Chapter reproduced with permission from “Anion- Π Interactions as Controlling Elements In Self-Assembly Reactions of Ag(I) Complexes With Π -Acidic Aromatic Rings” Brandi L. Schottel, Helen T. Chifotides, Michael Shatruk, Abdellatif Chouai, Lisa M. Pérez, John Bacsá, and Kim R. Dunbar* *J. Am. Chem. Soc.* **2006**, *128*, 5895-5912.

Previous studies conducted in our laboratories with the bis-bidentate bipyridine ligand 3,6-bis(2'-pyridyl)-1,2,4,5-tetrazine (bptz; Figure 23) and divalent metal ions provide compelling evidence that the anions play a decisive role in the formation of a particular cyclic structure both in the solid state and in solution (See previous chapter). In the case of Ni(II), the tetrahedral anions $[\text{BF}_4]^-$ and $[\text{ClO}_4]^-$ act as templates for the formation of molecular squares $[\text{Ni}_4(\text{bptz})_4(\text{CH}_3\text{CN})_8\text{C}\text{X}][\text{X}]_7$, $\text{X} = [\text{BF}_4]^-$, $[\text{ClO}_4]^-$, (Figures 25, 26)⁴⁸ whereas the anion $[\text{SbF}_6]^-$ leads to the exclusive formation of the molecular pentagon $[\text{Ni}_5(\text{bptz})_5(\text{CH}_3\text{CN})_{10}\text{C}\text{SbF}_6][\text{SbF}_6]_9$. (Figure 28)⁴⁹ Interestingly, the two metallacyclophanes interconvert in solution in the presence of an excess of the appropriate anion.⁴⁹ These transformations are attributed to a template effect that stabilizes one particular cage over another due to favorable interactions between the anion and the central tetrazine rings.⁸⁹

As part of our ongoing interest in bptz chemistry and the desire to further investigate the role of anion π -interactions, we have recently turned our attention to Ag(I) complexes of bptz. Silver is a suitably flexible transition metal that can adopt a variety of coordination numbers and geometries^{90,91} which makes it an attractive candidate for the study of 'self-healing' thermodynamic systems.⁹²⁻⁹⁹ As a backdrop for the current studies we note that the role of the anions in the assembly of Ag(I) species with terpyridine based¹⁰⁰ and ethylenediamine-tetrapropionitrile¹⁰¹ ligands has been investigated. In this regard, Constable *et al.*, reported the 1D polymer $\{[\text{Ag}(\mu\text{-bptz})(\text{bptz})][\text{BF}_4]\}_n$ consisting of Ag(I) ions bridged by bptz ligands in the *anti* orientation and an additional chelating bptz unit binding to each ion.¹⁰² The same group also reported the dinuclear species $[\text{Ag}_2(\text{bptz})_2][\text{CF}_3\text{SO}_3]_2$ with bptz in the *syn* orientation.^{102,103} By using the Ag(I) salt of the $[\text{AsF}_6]^-$ ion, however, we

recently isolated the propeller-type compound $[\text{Ag}_2(\text{bptz})_3][\text{AsF}_6]_2$.⁸³ In this structure, the anion- π interactions that arise from the packing of the $[\text{AsF}_6]^-$ anions in the folds of the cationic propeller molecule appear to be important in the solid state. To further explore similar anion- π interactions in a systematic fashion, X-ray crystallographic as well as theoretical studies of Ag(I) complexes with the ligands bptz and the related ligand 3,6-bis(2'-pyridyl)-1,2-pyridazine (bppn; Figure 48) were undertaken. The ligand bppn was chosen for the present investigation because, on the one hand, it is similar to bptz and can chelate only in the *syn* orientation,¹⁰⁴⁻¹⁰⁶ but on the other hand, the central pyridazine ring of bppn is expected to be much less π -acidic as compared to the tetrazine ring of bptz. Prior to the new studies reported herein, we note that the triflate complexes $[\text{Cu}_4(\text{bppn})_4][\text{CF}_3\text{SO}_3]_4$ ¹⁰⁴ and $[\text{Ag}(\text{bppn})_2][\text{CF}_3\text{SO}_3]_2$ ¹⁰⁶ were prepared and the bis-methyl substituted bppn species $[\text{Ag}_4(\text{Me}_2\text{-bppn})_4][\text{CF}_3\text{SO}_3]_4$ was identified by ¹H NMR spectroscopy to coexist with other Ag(I) mixed-ligand grids.⁹⁵ Due to the insolubility of silver halides, the Ag(I) salts of $[\text{PF}_6]^-$, $[\text{AsF}_6]^-$, $[\text{SbF}_6]^-$, and $[\text{BF}_4]^-$ were used as starting materials. To our knowledge, multiatomic anions have not been systematically explored *vis-à-vis* their role in anion- π interactions. Systems based on multiple anion- π interactions (established in our Ag(I)-bptz complexes) are promising candidates for anion-sensing receptors and transporters in biological systems.³²

In the work reported herein, the free ligands, as well as representative complexes, were subjected to Density Functional Theory (DFT) calculations and pertinent correlations were made between the derived electrostatic potentials and the solid-state structural features of the complexes.

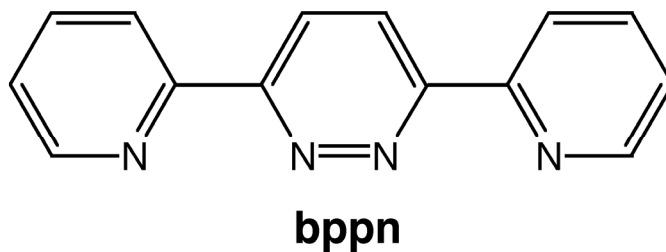


Figure 48: Schematic drawing of 3,6-bis(2'-pyridyl)-1,2,4,5-tetrazine, or bppn.

This study combines crystallographic and computational evidence that anion- π interactions are indeed present in the Ag(I) complexes with π -acidic aromatic rings and that they play an important role in determining the particular structural motif that is observed. This study is the first example of a comprehensive investigation of anion- π interactions as controlling elements in self-assembly reactions.

II. Experimental Section

A. Starting Materials

The reagents AgBF₄, AgPF₆, AgAsF₆, and AgSbF₆ were purchased from Aldrich and used without further purification. The ligands 3,6-bis(2'-pyridyl)-1,2,4,5-tetrazine (bptz)⁵⁷ and 3,6-bis(2'-pyridyl)-1,2-pyridizine (bppn)¹⁰⁷ were prepared by literature procedures and recrystallized from benzene and ethanol, respectively. All reactions were performed under an atmosphere of dry N₂ by Schlenk-line procedures. All solvents were dried by standard methods, distilled under nitrogen, and deoxygenated prior to use.

B. Physical Methods

The ¹H NMR spectra were recorded at 20°C on a 500 MHz Inova spectrometer with a 5-mm switchable probehead. The ¹⁹F spectra were recorded at

22°C on a 400 MHz Unity Inova spectrometer with a 5-mm autoswitchable probe operating at 375.99 MHz. The ^1H NMR spectra were referenced relative to the residual proton impurities of the deuterated solvent ($\text{CD}_3\text{CN}-d_3$ or $\text{CD}_3\text{NO}_2-d_3$). The ^{19}F NMR spectra were referenced relative to CFCl_3 at 0 ppm. Cyclic voltammetric experiments for the free bptz and bppn ligands were carried out in CH_3CN at r.t. with 0.10 M tetra-*n*-butylammonium hexafluorophosphate as supporting electrolyte. The reduction potentials $E_{p,c}$ were referenced to the Ag/AgCl electrode without correction for junction potentials. Electrospray mass spectra were acquired on an MDS Sciex API QStar Pulsar mass spectrometer (Toronto, Ontario, CA) using an electrospray ionization source. All spectra were acquired in positive ion mode in acetonitrile at analyte concentrations ranging between 50 and 100 μM . The spray voltage was ~ 4800 V; the nozzle skimmer potential was adjusted to 10 V to minimize fragmentation.

C. Synthesis of Ag-bptz and Ag-bppn Compounds

1. $\{[\text{Ag}(\text{bptz})][\text{PF}_6]\}_\infty$ (13) - A fuchsia solution of bptz (50 mg, 0.21 mmol) in CH_3CN (20 mL) was added dropwise to a colorless solution of AgPF_6 (53 mg, 0.21 mmol) in CH_3CN (10 mL). The resulting dark purple solution was stirred for a few hours, concentrated to 7 mL and filtered through Celite. The filtrate was layered with 20 mL of toluene. Dark violet plate-like crystals formed within two days. Yield: 66 mg (64%). ^1H NMR in CD_3CN (δ , ppm): 7.88 (ddd, $J = 7.5, 5, 1$ Hz, 5',5''-H), 8.23 (ddd, $J = 7.5, 1.5$ Hz, 4',4''-H), 8.88 (d, $J = 7.7$ Hz, 3',3''-H), 9.05 (ddd, $J = 5$ Hz, 6',6''-H). ^{19}F NMR in $\text{CD}_3\text{CN}-d_3$ (δ , ppm): -72.0 (d, $J_{\text{P-F}} = 706$ Hz,

[PF₆]⁻ free ions). ESI-MS (CH₃CN), *m/z*: 833 [Ag₂(bptz)₂(PF₆)⁺], 579 [Ag(bptz)₂]⁺, 343 [Ag(bptz)]⁺.

2. [Ag₂(bptz)₂(CH₃CN)₂][PF₆]₂ (14) - A fuchsia solution of bptz (140 mg, 0.59 mmol) in CH₃CN (100 mL) was added dropwise to a colorless solution of AgPF₆ (150 mg, 0.59 mmol) in CH₃CN (100 mL). The resulting purple solution was stirred for 12 hours, reduced in volume to ~30 mL, layered with toluene in a thin Schlenk tube, and placed in the refrigerator. Plate-like purple crystals were collected after three days. Yield: 107 mg (34%). ¹H NMR in CD₃CN-*d*₃ (δ , ppm): 7.89 (ddd, *J* = 7.5, 5, 1.5 Hz, 5',5''-H), 8.24 (ddd, *J* = 7.7 Hz, 4',4''-H), 8.88 (d, *J* = 7.7 Hz, 3',3''-H), 9.05 (ddd, *J* = 5 Hz, 6',6''-H). ¹⁹F NMR in CD₃CN (δ , ppm): -72.0 (d, *J*_{P-F} = 706 Hz, [PF₆]⁻ free ions). ESI-MS (CH₃CN), *m/z*: 833 [Ag₂(bptz)₂(PF₆)⁺], 579 [Ag(bptz)₂]⁺, 343 [Ag(bptz)]⁺.

3. [Ag₂(bptz)₂(CH₃CN)₂][AsF₆]₂ (15) - A fuchsia solution of bptz (119 mg, 0.50 mmol) in CH₃CN (85 mL) was added dropwise to a colorless solution of AgAsF₆ (150 mg, 0.50 mmol) in CH₃CN (100 mL) to produce a dark purple solution, which was stirred for 12 hours. The solution was reduced to ~30 mL, layered with toluene in a Schlenk tube and placed in the refrigerator. Plate-like purple crystals were collected after three days. Yield: 149 mg (52%). ¹H NMR in CD₃CN-*d*₃ (δ , ppm): 7.89 (ddd, *J* = 6.5, 5, 1.5 Hz, 5',5''-H), 8.24 (ddd, *J* = 7.9 Hz, 4',4''-H), 8.89 (d, *J* = 7.9 Hz, 3',3''-H), 9.04 (ddd, *J* = 5 Hz, 6',6''-H). ¹⁹F NMR in CD₃CN (δ , ppm): -65.0 (q, *J*_{As-F} = 932 Hz, [AsF₆]⁻ free ions). ESI-MS (CH₃CN), *m/z*: 1111 [Ag₂(bptz)₂(AsF₆)₂(CH₃CN) + H]⁺, 877 [Ag₂(bptz)₂(AsF₆)⁺], 579 [Ag(bptz)₂]⁺, 343 [Ag(bptz)]⁺.

4. $[\text{Ag}_2(\text{bptz})_3][\text{AsF}_6]_2$ (16**)⁸³** - A fuchsia solution of bptz (178 mg, 0.75 mmol) in CH_3CN (130 mL) was added dropwise to a colorless solution of AgAsF_6 (150 mg, 0.50 mmol) in CH_3CN (100 mL). The resulting purple solution was stirred for 24 hours, reduced to ~30 mL, layered with toluene in a Schlenk tube, and placed in the refrigerator. Plate-like purple crystals were collected in a few days. Yield: 56.7 mg (16%). Performance of the same reaction in nitromethane induced immediate precipitation of a blue powder (evidenced by ESI-MS spectra). Yield: 276 mg (78%). ¹H NMR in $\text{CD}_3\text{CN}-d_3$ (δ , ppm): 7.87 (ddd, $J = 8, 5, 1$ Hz, 6H, 5',5''-H), 8.22 (ddd, $J = 7.8, 1.5$ Hz, 6H, 4',4''-H), 8.86 (d, $J = 7.8$ Hz, 6H, 3',3''-H), 9.04 (ddd, $J = 5$ Hz, 6H, 6',6''-H). ¹⁹F NMR in CD_3CN (δ , ppm): -65.0 (q, $J_{\text{As-F}} = 932$ Hz, $[\text{AsF}_6]^-$ free ions). ESI-MS (CH_3CN), m/z : 923 $[\text{Ag}_2(\text{bptz})_3 - \text{H}]^+$, 579 $[\text{Ag}(\text{bptz})_2]^+$, 462 $[\text{Ag}_2(\text{bptz})_3]^{2+}$, 343 $[\text{Ag}(\text{bptz})]^+$.

5. $[\text{Ag}_2(\text{bptz})_3][\text{SbF}_6]_2$ (17a and 17b**)** - A fuchsia solution of bptz (92.5 mg, 0.39 mmol) in CH_3CN (130 mL) was added dropwise to a colorless solution of AgSbF_6 (137.5 mg, 0.40 mmol) in CH_3CN (100 mL). The resulting dark purple solution was stirred for 12 hours and separated into small aliquots. Two types of crystals were grown by slow evaporation in the dark. ¹H NMR in $\text{CD}_3\text{CN}-d_3$ (δ , ppm): 7.81 (ddd, $J = 7, 5, 1$ Hz, 6H, 5',5''-H), 8.20 (ddd, $J = 7.7, 1.8$ Hz, 6H, 4',4''-H), 8.81 (d, $J = 7.9$ Hz, 6H, 3',3''-H), 9.00 (ddd, $J = 5$ Hz, 6H, 6',6''-H). ¹⁹F NMR in CD_3CN (δ , ppm): -123.0 (sextet, $J_{121_{\text{Sb-F}}} = 1917$ Hz, octet, $J_{123_{\text{Sb-F}}} = 1034$ Hz, $[\text{SbF}_6]^-$ free ions). ESI-MS (CH_3CN), m/z : 923 $[\text{Ag}_2(\text{bptz})_3 - \text{H}]^+$, 579 $[\text{Ag}(\text{bptz})_2]^+$, 462 $[\text{Ag}_2(\text{bptz})_3]^{2+}$, 343 $[\text{Ag}(\text{bptz})]^+$.

6. [Ag₄(bppn)₄][PF₆]₄ (18) - A colorless solution of bppn (138 mg, 0.59 mmol) in CH₃NO₂ (130 mL) was added dropwise to a colorless solution of AgPF₆ (150 mg, 0.59 mmol) in CH₃NO₂ (100 mL) resulting in a light yellow solution. The reaction solution was stirred for 12 hours and then concentrated to ~30 mL. Slow diffusion of benzene into the solution for two days resulted in the formation of yellow block-shaped crystals. Yield: 136 mg (42%). ¹H NMR in CD₃NO₂-*d*₃ (δ, ppm): 8.73 (s, 8H, 4,5-H), 8.47 (br, d, 8H, 3',3''-H), 8.26 (d, 8H, 6',6''-H), 8.04 (td, 8H, 4',4''-H), 7.48 (td, 8H, 5',5''-H). ¹⁹F NMR in CD₃NO₂ (δ, ppm): -72.2 (d, J_{P-F} = 706 Hz, [PF₆]⁻ free ions).

7. [Ag₄(bppn)₄][AsF₆]₄ (19) - A colorless solution of bppn (49 mg, 0.21 mmol) in CH₃NO₂ (130 mL) was added dropwise to a colorless solution of AgAsF₆ (64 mg, 0.21 mmol) in CH₃NO₂ (100 mL) resulting in the formation of a light yellow solution. After 12 hours of stirring, the reaction mixture was concentrated to ~30 mL and layered with benzene. After two days, yellow block-shaped crystals were collected. Yield: 42 mg (33%). ¹H NMR in CD₃NO₂-*d*₃ (δ, ppm): 8.71 (s, 8H, 4,5-H), 8.46 (br, d, 8H, 3',3''-H), 8.24 (d, 8H, 6',6''-H), 8.03 (td, 8H, 4',4''-H), 7.47 (ddd, 8H, 5',5''-H). ¹⁹F NMR in CD₃NO₂ (δ, ppm): -65.0 (q, J_{As-F} = 932 Hz, [AsF₆]⁻ free ions).

8. [Ag₄(bppn)₄][SbF₆]₄ (20) - A colorless solution of bppn (49 mg, 0.21 mmol) in CH₃NO₂ (130 mL) was added dropwise to a colorless solution of AgSbF₆ (72 mg, 0.21 mmol) in CH₃NO₂ (100 mL) to give a light yellow solution. After 12 hours of stirring, the reaction mixture was concentrated to ~30 mL and layered with benzene. After two days, yellow block-shaped crystals were collected. Yield: 46 mg (34%). ¹H NMR in CD₃NO₂-*d*₃ (δ, ppm): 8.72 (s, 8H, 4,5-H), 8.47 (br, d, 8H, 3',3''-H), 8.25 (d, 8H, 6',6''-H), 8.04 (td, 8H, 4',4''-H), 7.48 (td, 8H, 5',5''-H). ¹⁹F NMR in

CD₃NO₂ (δ , ppm): -125.9 (sextet, $J_{121_{\text{Sb-F}}} = 1945$ Hz, octet, $J_{123_{\text{Sb-F}}} = 1061$ Hz, [SbF₆]⁻ free ions).

9. [Ag₄(bppn)₄][BF₄]₄ (21) - A colorless solution of bppn (180 mg, 0.77 mmol) in CH₃NO₂ (130 mL) was added dropwise to a colorless solution of AgBF₄ (150 mg, 0.77 mmol) in CH₃NO₂ (100 mL) to afford a light yellow solution. The reaction solution was stirred for 12 hours, concentrated to ~30 mL, and layered with benzene, which led to the formation of yellow block-shaped crystals after two days. Yield: 112 mg (29.4%). ¹H NMR in CD₃NO₂-*d*₃ (δ , ppm): 8.72 (s, 8H, 4,5-H), 8.47 (br, d, 8H, 3',3''-H), 8.26 (d, 8H, 6',6''-H), 8.03 (td, 8H, 4',4''-H), 7.47 (td, 8H, 5',5''-H). ¹⁹F NMR in CD₃NO₂ (δ , ppm): -153 ([BF₄]⁻ free ions).

C. Data Collection and Refinement

Single crystal X-ray data for all compounds were collected on a Bruker APEX CCD X-ray diffractometer equipped with a graphite monochromated Mo-K α radiation source ($\lambda = 0.71073$ Å). In a typical experiment, a crystal of appropriate size was affixed to a nylon loop with mineral oil and placed in a cold stream of N₂(g) at 110(2) K. The data were collected as three or four sets of exposures, each set having a different ϕ angle for the crystal and each exposure covering 0.3° in ω . Crystal decay was monitored by analyzing duplicate reflections and was found to be less than 1%, therefore no decay correction was applied. The frames were integrated with the Bruker SAINT software package⁵⁹ and a semi-empirical absorption correction using multiple-measured reflections was applied using the program SADABS.⁶⁰ The structures were solved and refined using X-SEED,⁶¹ a graphical interface to the SHELX suite of programs.⁶² Additional crystallographic calculations

were performed with PLATON.⁶³ In the final cycles of refinement, all atoms except hydrogen and disordered atoms were refined anisotropically. Aromatic hydrogen atoms were placed in geometrically optimized positions and the bond distances and angles were idealized during refinement with the hydrogen U values set at 1.2 times the equivalent isotropic U of the C atoms to which they are attached. Methyl group hydrogen atoms were placed in regions of maximum electron density and the bond distances and angles were idealized during refinement with the hydrogen U values set at 1.5 times the equivalent isotropic U of the C atoms to which they were attached. The crystal parameters and information pertaining to the data collection and refinement of the crystals of **13-21** are summarized in Table 7. Selected bond distances and angles are provided in the corresponding figure caption of each structure.

1. $\{\text{[Ag(bptz)][PF}_6\text{]}\}_\infty$ (13**)** - An indexing of the preliminary diffraction patterns established that the crystal belonged to the triclinic system. The structure was solved and refined in the space group $P\bar{1}$. The asymmetric unit contains one-half each of a bptz molecule, a silver atom, and a hexafluorophosphate counterion. The final refinement cycle resulted in an R value of 0.0641.

2. $[\text{Ag}_2(\text{bptz})_2(\text{CH}_3\text{CN})_2][\text{PF}_6]_2$ (14**) and $[\text{Ag}_2(\text{bptz})_2(\text{CH}_3\text{CN})_2][\text{AsF}_6]_2$ (**15**)** - An indexing of the preliminary diffraction patterns established that the crystals were monoclinic with a primitive unit cell. The structures were solved and refined in the space group $P2_1/c$. The asymmetric unit of each compound contains one bptz molecule, one silver atom, one acetonitrile ligand, and a disordered counterion ($[\text{PF}_6]^-$ and $[\text{AsF}_6]^-$ for **2** and **3**, respectively). In each case, the disorder of the anion was modeled in two different orientations; the total occupancy of both orientations

was fixed to one. The final refinement cycle resulted in R values of 0.0776 and 0.0512 for **14** and **15**, respectively.

3. $[\text{Ag}_2(\text{bptz})_3][\text{AsF}_6]_2 \cdot 2\text{CH}_3\text{CN}$, (16**) $\cdot 2\text{CH}_3\text{CN}$** ⁸³ - An indexing of the preliminary diffraction patterns established that the crystal was monoclinic with a primitive unit cell. The structure was solved and refined in the space group $P2_1/c$. The asymmetric unit contains a complete $[\text{Ag}_2(\text{bptz})_3]^{2+}$ unit, two $[\text{AsF}_6]^-$ counterions, and two acetonitrile molecules of crystallization. One of the $[\text{AsF}_6]^-$ anions was found to be disordered and was modeled in two different orientations. The final refinement cycle resulted in an R value of 0.0349.

Table 7. Crystal and structural refinement data for **13**, **14**, **15**, **16**•2CH₃CN, **17a**•2CH₃CN, **17b**, **18**•4CH₃NO₂, **19**•4CH₃NO₂, **20**•4CH₃NO₂ and **21**•3CH₃NO₂•C₆H₆.

	13	14	15
Formula	AgC ₁₂ N ₆ PF ₆ H ₈	Ag ₂ C ₂₈ N ₁₄ P ₂ F ₁₂ H ₂₂	Ag ₂ C ₂₈ N ₁₄ As ₂ F ₁₂ H ₂₂
Formula weight	489.08	1060.28	1148.18
Temp (K)	110(2)	110(2)	110(2)
Crystal system	Triclinic	Monoclinic	Monoclinic
Space group	$P\bar{1}$ (No. 2)	$P2_1/c$ (No. 14)	$P2_1/c$ (No. 14)
<i>a</i> (Å)	7.284(2)	8.221(2)	8.288(4)
<i>b</i> (Å)	7.687(2)	12.674(3)	12.736(7)
<i>c</i> (Å)	7.827(2)	17.096(3)	17.504(9)
α (°)	65.05(3)	90	90
β (°)	74.80(3)	97.73(3)	98.529(9)
γ (°)	86.85(3)	90	90
<i>V</i> (Å ³)	382.7(2)	1765.1(6)	1827(2)
Crystal description	Needle	Plate	Block
Color	Violet	Violet	Violet
Crystal size(mm ³)	0.30 x 0.20 x 0.14	0.17 x 0.13 x 0.08	0.30 x 0.21 x 0.15
<i>Z</i>	1	2	2
ρ_{calc} (g/cm ³)	2.122	1.995	2.087
μ (mm ⁻¹)	1.500	1.311	2.976
<i>F</i> (000)	238	1040	1112
θ range (°)	2.90 to 27.51	2.50 to 27.48	1.99 to 27.58
Diffraction limits (<i>h</i> , <i>k</i> , <i>l</i>)	-9 < <i>h</i> < 8 -9 < <i>k</i> < 9 -10 < <i>l</i> < 7	-10 < <i>h</i> < 10 -16 < <i>k</i> < 15 -21 < <i>l</i> < 19	-10 < <i>h</i> < 10 -16 < <i>k</i> < 16 -14 < <i>l</i> < 22
Reflections collected	2282	12888	13632
Independent reflections	1503	3893	4165
Completeness to θ_{max} (%)	[<i>R</i> (int) = 0.0198] 85.6	[<i>R</i> (int) = 0.0638] 96.0	[<i>R</i> (int) = 0.0519] 98.1
Data / parameters/ restraints	1503/ 121/ 0	3893 / 257/ 30	4165 / 318/ 36
$R, {}^1wR^2$ [<i>I</i> > 2 σ (<i>I</i>)]	0.0641, 0.1415	0.0776, 0.1897	0.0512, 0.0854
$R, {}^1wR^2$ (all data)	0.0796, 0.1480	0.1108, 0.2094	0.0748, 0.0922
Goodness-of-fit ³ (<i>F</i> ²)	1.069	1.050	1.079
Largest diff. peak and hole (e Å ⁻³)	1.653 and -1.060	2.213 and -1.212	0.829 and -0.774

$${}^1R = \frac{\sum ||F_o| - |F_c||}{\sum |F_o|}$$

$${}^2wR = \left\{ \frac{\sum [w(F_o^2 - F_c^2)^2]}{\sum w(F_o^2)^2} \right\}^{1/2}$$

³Goodness-of-fit = $\left\{ \frac{\sum [w(F_o^2 - F_c^2)^2]}{(n-p)} \right\}^{1/2}$, where *n* is the number of reflections and *p* is the total number of parameters refined.

Table 7, continued. Crystal and structural refinement data for **13**, **14**, **15**, **16**•2CH₃CN, **17a**•2CH₃CN, **17b**, **18**•4CH₃NO₂, **19**•4CH₃NO₂, **20**•4CH₃NO₂ and **21**•3CH₃NO₂•C₆H₆.

	16 •2CH ₃ CN	17a •2CH ₃ CN	17b
Formula	Ag ₂ C ₄₀ N ₂₀ As ₂ F ₁₂ H ₃₀	Ag ₂ C ₄₀ N ₂₀ Sb ₂ F ₁₂ H ₃₀	Ag ₂ C ₃₆ N ₁₈ Sb ₂ F ₁₂ H ₂₄
Formula weight	1384.42	1478.08	1395.97
Temp (K)	110(2)	110(2)	110(2)
Crystal system	Monoclinic	Orthorhombic	Trigonal
Space group	<i>P2₁/c</i> (No. 14)	<i>Pbcn</i> (No. 60)	<i>R-3</i> (No. 146)
<i>a</i> (Å)	22.879(7)	25.673(9)	12.363(6)
<i>b</i> (Å)	25.283(7)	8.201(3)	12.363(6)
<i>c</i> (Å)	8.125(2)	23.11(2)	49.13(2)
α (°)	90	90	90
β (°)	90.353(6)	90	90
γ (°)	90	90	120
<i>V</i> (Å ³)	4700(2)	4865(3)	6503(5)
Crystal description	Plate	Needle	Plate
Color	Violet	Violet	Violet
Crystal size(mm ³)	0.38 x 0.26 x 0.19	0.35 x 0.18 x 0.07	0.44 x 0.24 x 0.21
<i>Z</i>	4	4	6
ρ_{calc} (g/cm ³)	1.957	2.018	2.139
μ (mm ⁻¹)	2.336	1.994	2.229
<i>F</i> (000)	2712	2856	4020
θ range (°)	0.89 to 27.54	2.61 to 26.37	1.95 to 27.48
Diffraction limits (<i>h</i> , <i>k</i> , <i>l</i>)	-28 < <i>h</i> < 29 -32 < <i>k</i> < 22 -10 < <i>l</i> < 10	-27 < <i>h</i> < 13 -5 < <i>k</i> < 10 -28 < <i>l</i> < 27	-14 < <i>h</i> < 15 -15 < <i>k</i> < 16 -34 < <i>l</i> < 63
Reflections collected	30038	12037	13296
Independent reflections	10051	4617	3316
Completeness to θ_{max} (%)	[<i>R</i> (int) = 0.0262] 92.5	[<i>R</i> (int) = 0.1601] 92.7	[<i>R</i> (int) = 0.0303] 99.6
Data / parameters/ restraints	10051 / 687/ 0	4617/ 332/ 24	3316/ 212/ 0
R , ⁴ <i>wR</i> ⁵ [<i>I</i> > 2 σ (<i>I</i>)]	0.0349, 0.0770	0.0996, 0.1839	0.0304, 0.0715
R , ¹ <i>wR</i> ² (all data)	0.0449, 0.0806	0.2145, 0.2281	0.0366, 0.0743
Goodness-of-fit ⁶ (<i>F</i> ²)	1.088	1.019	1.047
Largest diff. peak and hole (e Å ⁻³)	0.729 and -0.533	1.401 and -0.779	1.628 and -1.014

$$^4R = \sum | |F_o| - |F_c| | / \sum |F_o|$$

$$^5wR = \{ \sum [w(F_o^2 - F_c^2)^2] / \sum w(F_o^2)^2 \}^{1/2}$$

⁶Goodness-of-fit = $\{ \sum [w(F_o^2 - F_c^2)^2] / (n-p) \}^{1/2}$, where *n* is the number of reflections and *p* is the total number of parameters refined.

Table 7, continued. Crystal and structural refinement data for **13**, **14**, **15**, **16**•2CH₃CN, **17a**•2CH₃CN, **17b**, **18**•4CH₃NO₂, **19**•4CH₃NO₂, **20**•4CH₃NO₂ and **21**•3CH₃NO₂•C₆H₆.

	18 •4CH ₃ NO ₂	19 •4CH ₃ NO ₂	20 •4CH ₃ NO ₂
Formula	Ag ₄ C ₆₀ N ₂₀ P ₄ F ₂₄ O ₈ H ₅₂	Ag ₄ C ₆₀ N ₂₀ As ₄ F ₂₄ O ₈ H ₅₂	Ag ₄ C ₆₀ N ₂₀ Sb ₄ F ₂₄ O ₈ H ₅₂
Formula weight	2192.58	2368.38	2555.70
Temp (K)	110(2)	110(2)	110(2)
Crystal system	Monoclinic	Monoclinic	Monoclinic
Space group	C2/c (No. 15)	C2/c (No. 15)	C2/c (No. 15)
<i>a</i> (Å)	23.316(3)	23.414(7)	23.595(5)
<i>b</i> (Å)	14.237(2)	14.424(4)	14.620(3)
<i>c</i> (Å)	25.069(3)	25.155(7)	25.322(5)
α (°)	90	90	90
β (°)	115.972(3)	116.074(4)	116.38(3)
γ (°)	90	90	90
<i>V</i> (Å ³)	7481(2)	7631(4)	7826(3)
Crystal description	Block	Block	Block
Color	Yellow	Yellow	Yellow
Crystal size(mm ³)	0.30 x 0.25 x 0.20	0.32 x 0.19 x 0.17	0.22 x 0.13 x 0.12
<i>Z</i>	4	4	4
ρ_{calc} (g/cm ³)	1.947	2.061	2.169
μ (mm ⁻¹)	1.245	2.858	2.460
<i>F</i> (000)	4320	4608	4896
θ range (°)	1.73 to 27.55	2.78 to 27.51	2.76 to 28.35
Diffraction limits (<i>h, k, l</i>)	-30 < <i>h</i> < 29 -18 < <i>k</i> < 18 -32 < <i>l</i> < 31	-30 < <i>h</i> < 25 -18 < <i>k</i> < 18 -32 < <i>l</i> < 32	-31 < <i>h</i> < 31 -19 < <i>k</i> < 19 -32 < <i>l</i> < 32
Reflections collected	42690	31529	33093
Independent reflections	8547 [<i>R</i> (int) = 0.1080]	8523 [<i>R</i> (int) = 0.0345]	9071 [<i>R</i> (int) = 0.0700]
Completeness to θ_{max} (%)	98.8	97.1	92.7
Data / parameters/ restraints	8547/ 583/ 0	8523/ 587/ 21	9071/ 544/ 0
<i>R</i> , ⁷ <i>wR</i> ⁸ [<i>I</i> > 2 σ (<i>I</i>)]	0.0702, 0.0921	0.0362, 0.0733	0.0489, 0.1149
<i>R</i> , ¹ <i>wR</i> ² (all data)	0.1231, 0.1038	0.0492, 0.0779	0.0609, 0.1211
Goodness-of-fit ⁹ (<i>F</i> ²)	1.108	1.032	1.060
Largest diff. peak and hole (e Å ⁻³)	0.898 and -0.833	0.961 and -0.613	1.535, -1.080

$${}^7R = \Sigma | |F_o| - |F_c| | / \Sigma |F_o|$$

$${}^8wR = \{ \Sigma [w(F_o^2 - F_c^2)^2] / \Sigma w(F_o^2)^2 \}^{1/2}$$

⁹Goodness-of-fit = $\{ \Sigma [w(F_o^2 - F_c^2)^2] / (n-p) \}^{1/2}$, where *n* is the number of reflections and *p* is the total number of parameters refined.

Table 7, continued. Crystal and structural refinement data for **13**, **14**, **15**, **16**•2CH₃CN, **17a**•2CH₃CN, **17b**, **18**•4CH₃NO₂, **19**•4CH₃NO₂, **20**•4CH₃NO₂ and **21**•3CH₃NO₂•C₆H₆.

	21 •3CH ₃ NO ₂ •C ₆ H ₆
Formula	Ag ₄ C ₆₅ N ₁₉ B ₄ F ₁₆ O ₆ H ₅₅
Formula weight	1977.00
Temp (K)	110(2)
Crystal system	Monoclinic
Space group	<i>P</i> 2 ₁ / <i>c</i> (No. 14)
<i>a</i> (Å)	15.655(7)
<i>b</i> (Å)	28.37(1)
<i>c</i> (Å)	16.34(1)
α (°)	90
β (°)	94.79(3)
γ (°)	90
<i>V</i> (Å ³)	7230(7)
Crystal description	Block
Color	Yellow
Crystal size(mm ³)	0.35 x 0.10 x 0.06
<i>Z</i>	4
ρ_{calc} (g/cm ³)	1.816
μ (mm ⁻¹)	1.175
<i>F</i> (000)	3912
θ range (°)	1.44 to 26.37
Diffraction limits (<i>h</i> , <i>k</i> , <i>l</i>)	-19 < <i>h</i> < 19 -35 < <i>k</i> < 35 -20 < <i>l</i> < 15
Reflections collected	77086
Independent reflections	14799 [<i>R</i> (int) = 0.0977]
Completeness to θ_{max} (%)	100
Data / parameters/ restraints	14799/ 1022/ 0
<i>R</i> , ¹⁰ <i>wR</i> ¹¹ [<i>I</i> > 2 σ (<i>I</i>)]	0.0485, 0.1124
<i>R</i> , ¹ <i>wR</i> ² (all data)	0.1308, 0.1582
Goodness-of-fit ¹² (<i>F</i> ²)	1.046
Largest diff. peak and hole (e Å ⁻³)	0.838, 0.803

$$^{10}\text{R} = \sum | |F_o| - |F_c| | / \sum |F_o|$$

$$^{11}\text{wR} = \{ \sum [w(F_o^2 - F_c^2)^2] / \sum w(F_o^2)^2 \}^{1/2}$$

¹²Goodness-of-fit = $\{ \sum [w(F_o^2 - F_c^2)^2] / (n-p) \}^{1/2}$, where *n* is the number of reflections and *p* is the total number of parameters refined.

4. $[\text{Ag}_2(\text{bptz})_3][\text{SbF}_6]_2 \cdot 2\text{CH}_3\text{CN}$, (17a) $\cdot 2\text{CH}_3\text{CN}$ - Routine indexing of the diffraction patterns using the SMART¹⁰⁸ indexing software failed to give a reasonable unit cell. Twin indexing using the program GEMINI¹⁰⁹ gave a primitive orthorhombic cell with reasonable dimensions and indicated that the diffraction patterns consisted of two major components arising from a twinned or split crystal. The reflections from these components were approximately equal to each other. Precise unit-cell parameters and the correct Bravais cell were subsequently obtained using the SMART software.¹⁰⁸ The reflection data were integrated using the orientation matrix for only one component with the spot size and orientation matrix for the crystal being fixed during the integration process. Some reflections overlapped, resulting in a relatively large *R*-index (0.16) for merged equivalent reflections. The structure was solved and refined in the space group *Pbcn* (No. 60). The asymmetric unit contains one-half of a $[\text{Ag}_2(\text{bptz})_3]^{2+}$ molecule, one $[\text{SbF}_6]^-$ counterion, and one acetonitrile molecule of crystallization. Initially, the acetonitrile solvent molecule was refined as occupying one discrete position in the asymmetric unit, but the *U*-values for these atoms and the residual electron density indicated that this molecule was disordered. The atoms belonging to this molecule were split in two parts, and their relative positions were refined. Geometric restraints were applied such that the components of disorder exhibited chemically meaningful bond distances and angles. The total occupancy of both orientations was fixed to one with the isotropic thermal parameters of both components equal. After refinement, two acetonitrile groups were rotated and displaced from each other and the program PLATON⁶³ confirmed that there were no further voids accessible to solvent in the unit cell. This approach yielded a better electron density model than the refinement

including one position for the acetonitrile molecule with anisotropic ellipsoids. The final refinement cycle resulted in an R value of 0.0996.

5. [Ag₂(bptz)₃][SbF₆]₂ (17b) - Large, purple, hexagonal-shaped plates of [Ag₂(bptz)₃](SbF₆)₂ (**17b**) suitable for X-ray analysis grew on the sides of the container along with **17a**. Upon examination of these crystals under crossed-polarizers on an optical microscope, it was determined that they were uniaxial and had at least trigonal symmetry because they did not extinguish polarized light when viewed along their six-fold symmetry axis. The diffraction patterns had trigonal Laue symmetry and were indexed in a rhombohedral unit cell that was much larger than the unit cells determined for **16** and **17a**. The structure was solved and refined in the space group *R*-3 (No. 148). The asymmetric unit contains one-third of a [Ag₂(bptz)₃]²⁺ molecule and two-thirds of a [SbF₆]⁻ counterion. Unlike the previous compounds, there are no solvent molecules of crystallization and the program PLATON⁶³ showed that there are no solvent accessible voids in the unit cell. The calculated density for this crystal is 2.139 as compared to 2.018 g cm⁻³ for compound **5a**. The final refinement cycle resulted in an R value of 0.0304.

6. Ag₄(bppn)₄][PF₆]₄•4CH₃NO₂ (18)•4CH₃NO₂, [Ag₄(bppn)₄][AsF₆]₄•4CH₃NO₂, (19)•4CH₃NO₂, and [Ag₄(bppn)₄][SbF₆]₄•4CH₃NO₂, (20)•4CH₃NO₂ - An indexing of the preliminary diffraction patterns in each case established that the crystals belonged to a monoclinic C-centered unit cell. All the structures were solved and refined in the space group *C*2/*c*. The asymmetric unit of each compound contains two bppn molecules, three silver atoms (one on a special position), two counterions ([PF₆]⁻, [AsF₆]⁻, and [SbF₆]⁻ for **18**, **19**, and **20**, respectively), and two nitromethane molecules. In compounds **18** and **19**, one of the anions was found to be disordered

and was modeled in two different orientations. The final refinement cycle resulted in R values of 0.0702, 0.0362, and 0.0489 for **18**, **19**, and **20**, respectively.

7. $[\text{Ag}_4(\text{bppn})_4][\text{BF}_4]_4 \cdot 3\text{CH}_3\text{NO}_2 \cdot \text{C}_6\text{H}_6$, (**21**) $\cdot 3\text{CH}_3\text{NO}_2 \cdot \text{C}_6\text{H}_6$. - An indexing of the preliminary diffraction patterns of **21** established that the crystals belonged to a monoclinic primitive unit cell. The structure was solved and refined in the space group $P2_1/c$. The asymmetric unit contains four bppn molecules, four silver atoms (one on a special position), four $[\text{BF}_4]^-$ counterions, three nitromethane molecules, and one benzene molecule. One of the $[\text{BF}_4]^-$ anions was found to be disordered and was modeled in two different orientations. The final refinement resulted in an R value of 0.0485.

D. Theoretical Calculations

Density Functional Theory (DFT)¹¹⁰ calculations were undertaken for the ligands bppn and bptz as well as the complexes 15, 16, 17b, and 19. The bptz and bppn ligands were subjected to full geometry optimization in the syn and anti conformations with a triple- ζ quality basis set that had a diffuse function on the heavy atoms and a polarization function on all the atoms (6-311+G(d,p))¹¹¹ at the B3LYP [Becke three-parameter exchange functional (B3)]¹¹² and the Lee-Yang-Parr correlation functional (LYP)¹¹³] level of theory as implemented in Gaussian 03 (G03).¹¹⁴ Full geometry optimizations were also performed with scalar relativistic effects by the zeroth-order regular approximation (ZORA)¹¹⁵ and an all-electron triple- ζ basis set with a polarization function on all atoms (TZP) designed to be used with ZORA¹¹⁵ at the BP86 [Becke exchange functional (B)]¹¹² and Perdew-Wang correlation functional (P86)¹¹⁶] level of theory as implemented in the Amsterdam Density Functional (ADF) program.¹¹⁷ Single-Point Energy (SPE) calculations for

the crystal structure geometries were undertaken for complexes 3, 4, 5b, and 7, with scalar relativistic effects by ZORA¹¹⁵ and an all-electron triple- ζ basis set with a polarization function on all atoms (TZP) designed to be used with ZORA at the BP86 level of theory as implemented in ADF.¹¹⁷

III. Results

A. X-ray Crystallographic Results

1. $\{[\text{Ag}(\text{bptz})][\text{PF}_6]\}_\infty$ (**13**) - The thermal ellipsoid plot of compound **13**, a 1-D coordination polymer, is depicted in Figure 49. Each Ag(I) ion resides on an inversion center and is coordinated to two bptz ligands resulting in a distorted square planar geometry around the metal atom. The two Ag-N bond distances are Ag1-N1 2.218(5) Å and Ag1-N2 2.564(5) Å. The bptz ligands are in an *anti* orientation, which leads to the formation of the polymer. The four Ag-N bonds are coplanar and the ‘bite’ angles of bptz result in N-Ag-N bond angles that deviate considerably from the ideal square-planar coordination geometry (69.9(2) and 110.1(2)°). The 1-D chains interact through π - π contacts between the pyridyl rings (3.46 Å between π -planes) and are separated by $[\text{PF}_6]^-$ anions, which are positioned over the tetrazine rings (Figures 50 and 51a).

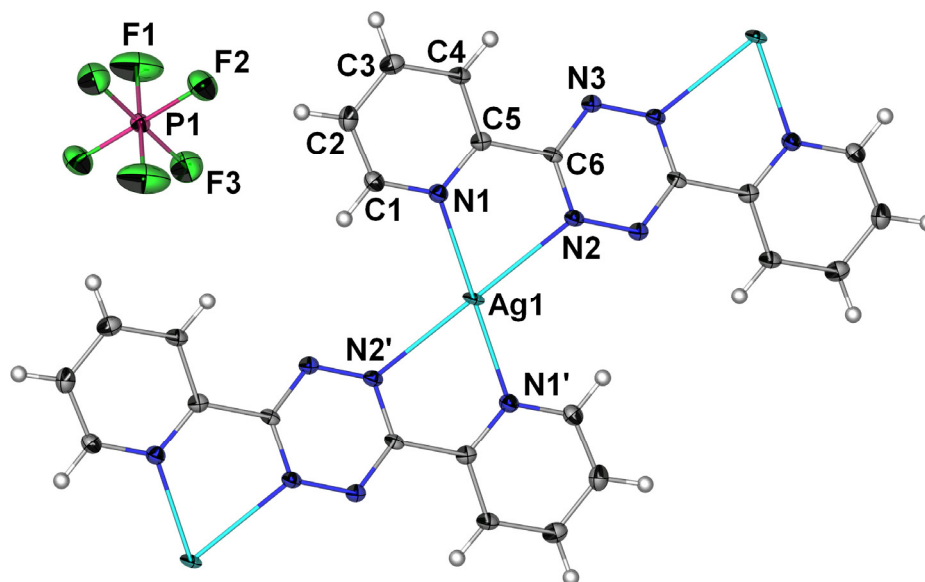


Figure 49: Thermal ellipsoid plot of a fragment of $\{[\text{Ag}(\text{bptz})][\text{PF}_6]\}_\infty$, (**13**), at the 50% probability level. Selected bond distances (\AA) and angles ($^\circ$): Ag1-N1 2.218(5), Ag1-N2 2.564(5), N2-Ag1-N1 69.9(2), N1-Ag1-N1' 180.0(2), N2-Ag1-N1', 110.1(2), N2-Ag1-N2' 180.0(2).

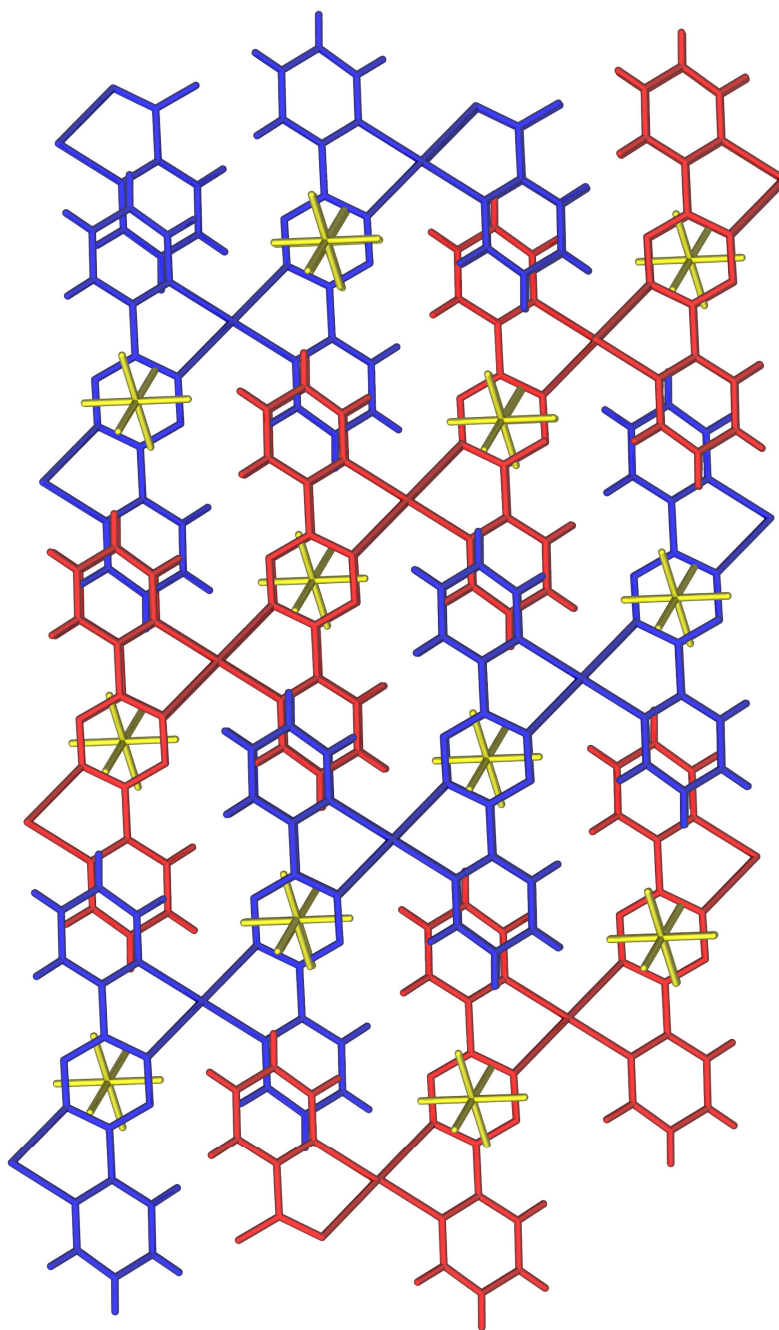


Figure 50: Packing diagram of $\{[\text{Ag}(\text{bptz})][\text{PF}_6]\}_\infty$ along the xx plane with alternating chains in red and blue. The anions (shown in yellow) are clearly in close proximity to the central tetrazine rings of bptz.

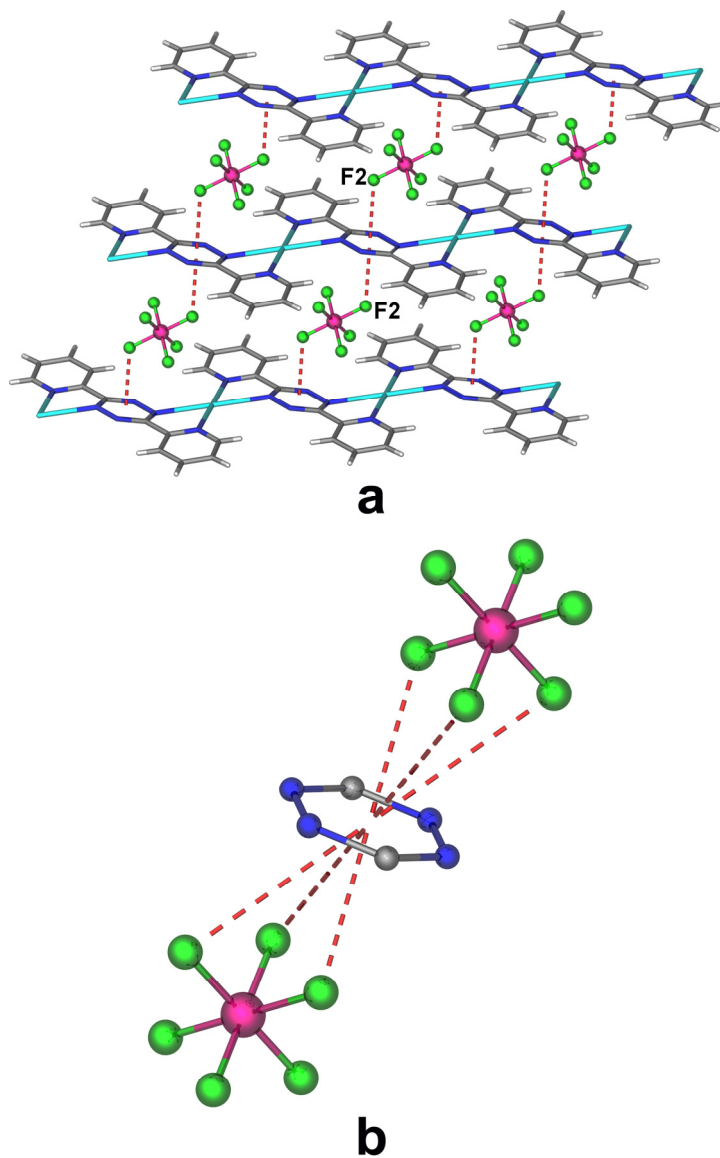


Figure 51: (a) Packing diagram of $\{[Ag(bptz)][PF_6]\}_\infty$ (**1**) depicting the shortest contacts between the $[PF_6]^-$ anions and the tetrazine rings. Shortest F2 \cdots centroid distance 2.840(5) Å; F \cdots tetrazine plane distances in the range 2.785–2.968 Å. (b) Tetrazine ring with two $[PF_6]^-$ anions in **1**, displaying the three F atoms involved in each anion– π interaction (dotted lines drawn to the ring centroid).

Each anion interacts with two tetrazine rings and each tetrazine ring interacts with two different $[\text{PF}_6]^-$ anions (Figure 51a). Each anion- π interaction involves three F atoms oriented towards the tetrazine ring (Figure 51b) with the $\text{F}\cdots$ tetrazine ring plane distances being in the range 2.785-2.968 Å (the shortest $\text{F}\cdots$ tetrazine centroid distance is 2.840(5) Å).

2. $[\text{Ag}_2(\text{bptz})_2(\text{CH}_3\text{CN})_2][\text{PF}_6]_2$ (14**) and $[\text{Ag}_2(\text{bptz})_2(\text{CH}_3\text{CN})_2][\text{AsF}_6]_2$ (**15**)** - The thermal ellipsoid plots of compounds **14** and **15**, which are isostructural, are depicted in Figures 52 and 53, respectively. In these structures, each bptz molecule is bis-chelating to two Ag(I) ions and is in the *syn* orientation resulting in the formation of dinuclear cations $[\text{Ag}_2(\text{bptz})_2(\text{CH}_3\text{CN})_2]^{2+}$ (the $\text{Ag}\cdots\text{Ag}$ separations are 4.660 and 4.644 Å for **2** and **3**, respectively). Each Ag(I) ion is in a square-pyramidal geometry; the fifth coordination site of the metal is occupied by an acetonitrile molecule with the two solvent molecules positioned on opposite sides of the dinuclear unit. The bptz pyridyl rings participate in intermolecular π - π interactions (3.56 and 3.52 Å for **14** and **15**, respectively; Figure 54), whereas each tetrazine ring is involved in two anion- π interactions. Each anion is sandwiched between two tetrazine rings. The anion- π interactions in **14** and **15** are depicted in Figures 55a and b, respectively. As in structure **13** (Figure 51b), each anion interacts with each tetrazine ring through three F atoms oriented towards the ring with the $\text{F}\cdots$ tetrazine ring plane distances being in the ranges 2.791-3.045 and 2.758-3.142 Å for **14** and **15**, respectively. The shortest $\text{F}\cdots$ tetrazine centroid distances are 2.806(7) and 2.784(6) Å for **2** and **3**, respectively.

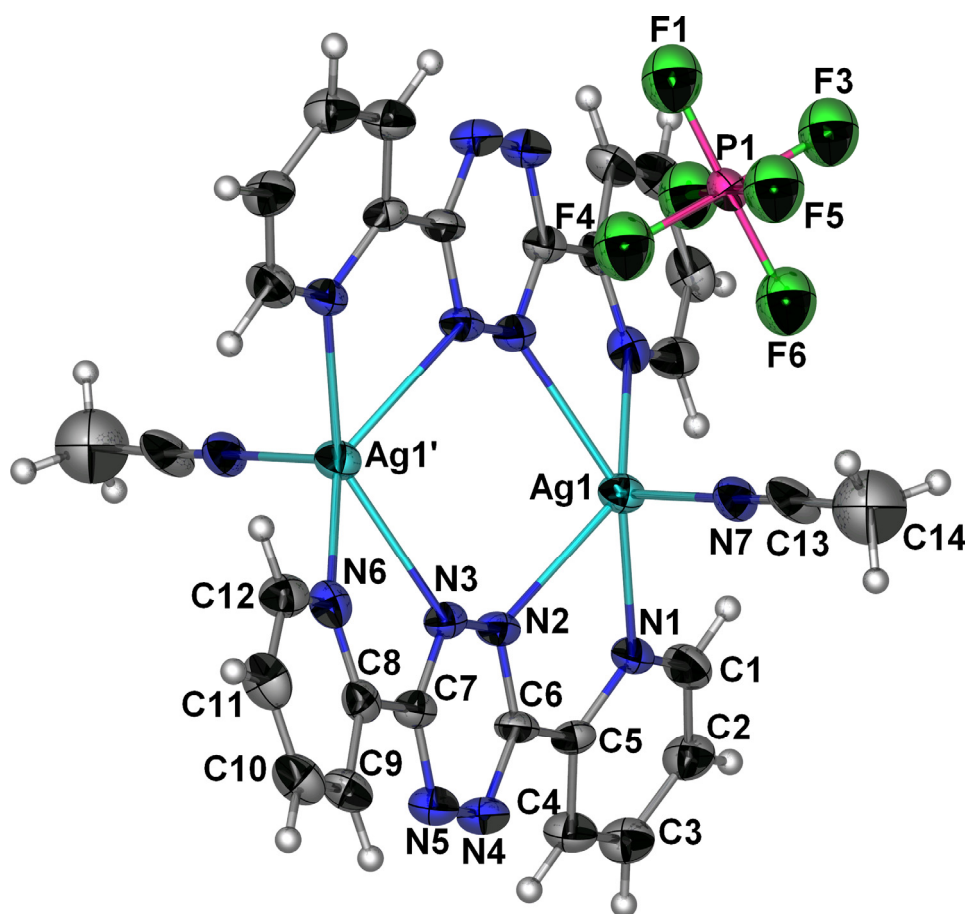


Figure 52: Thermal ellipsoid plot of [Ag₂(bptz)₂(CH₃CN)₂][PF₆]₂ (**14**) at the 50% probability level (one [PF₆]⁻ ion has been omitted for clarity). The methyl carbon atom ellipsoids (C14) are depicted at the 25% probability level for the sake of clarity. Selected bond distances (Å) and angles (°): Ag1-N1 2.376(6), Ag1-N2 2.517(6), Ag1-N7 2.256(6), Ag1'-N6 2.342(6), Ag1-N3 2.580(6), N1-Ag1-N2 68.3(2), N7-Ag1-N1 108.3(2), N7-Ag1-N2 94.7(2), N6-Ag1'-N3 67.0(3).

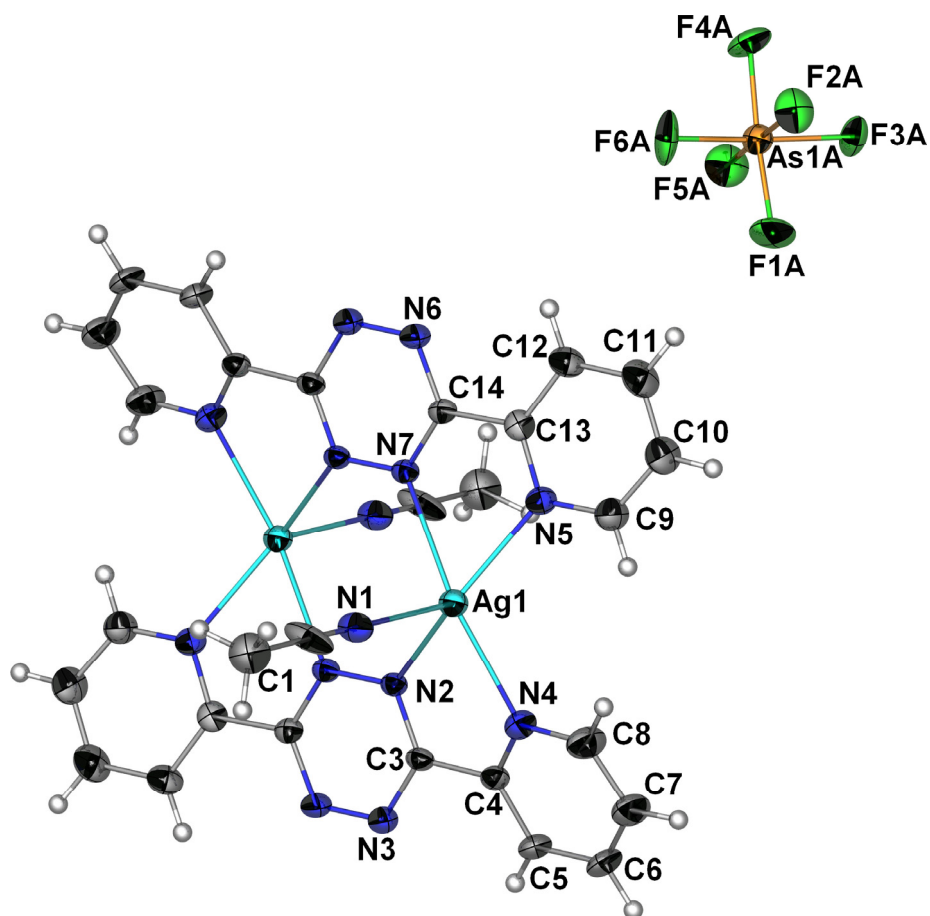


Figure 53: Thermal ellipsoid plot of $[\text{Ag}_2(\text{bptz})_2(\text{CH}_3\text{CN})_2][\text{AsF}_6]_2$ (**15**) at the 50% probability level. The methyl carbon ellipsoids are shown at the 25% probability level for the sake of clarity. Selected bond distances (Å) and angles (°): Ag1-N2 2.524(4), Ag1-N3 2.376(4), Ag1-N4 2.341(4), Ag1-N5 2.567(4), Ag1-N7, 2.268(4), N7-Ag1-N4 118.4(1), N7-Ag1-N3 105.4(2), N7-Ag1-N2 95.3(1), N4-Ag1-N5 67.31(13), N4-Ag1-N2 143.53(1), N3-Ag1-N2 68.4(4), N7-Ag1-N5 99.4(1), N2-Ag1-N5 95.2(1).

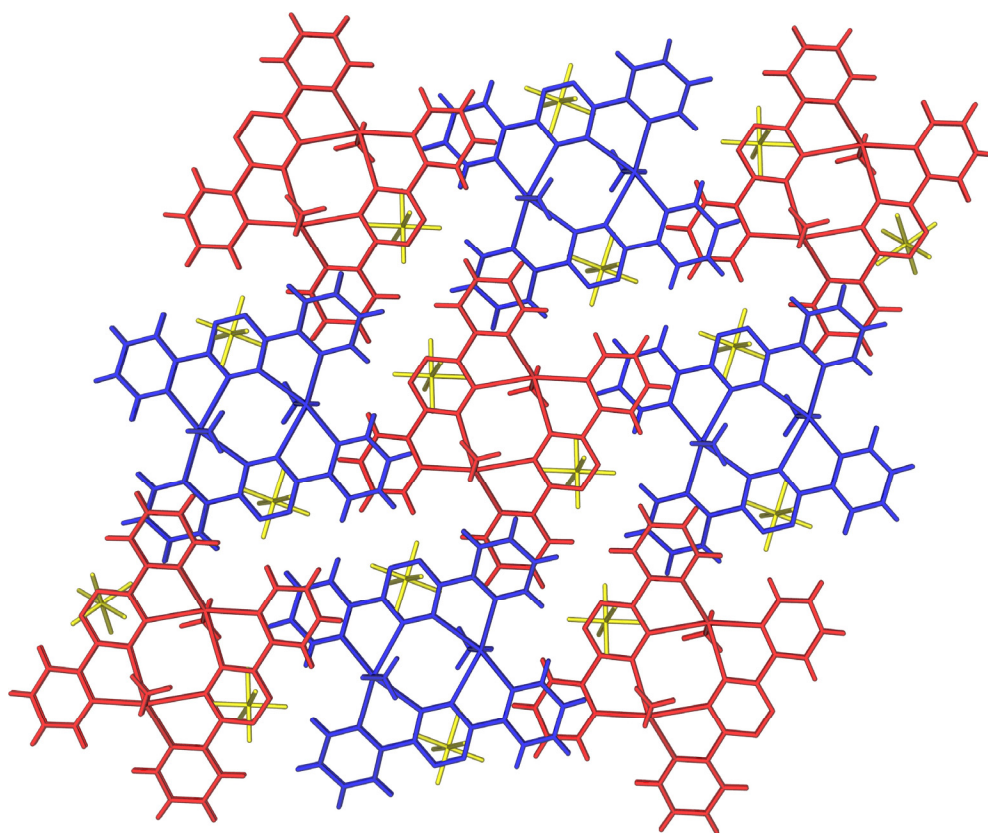


Figure 54: Packing diagram of $[\text{Ag}_2(\text{bptz})_2(\text{CH}_3\text{CN})_2][\text{PF}_6]_2$ (**14**) in the *bc* plane.

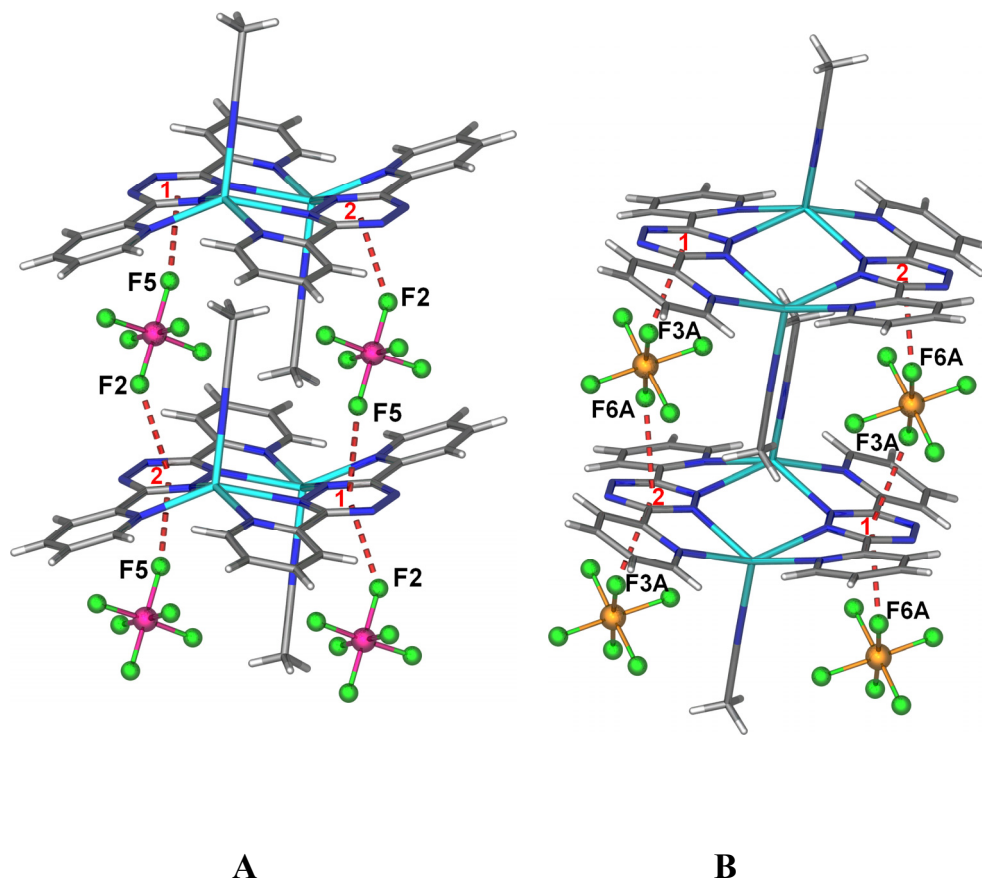


Figure 55: (a) Fragment of the cation/anion arrangements in $[\text{Ag}_2(\text{bptz})_2(\text{CH}_3\text{CN})_2][\text{PF}_6]_2$ (**14**) depicting the shortest contacts between the $[\text{PF}_6]^-$ anions and the tetrazine rings. Shortest F \cdots tetrazine centroid distances (\AA): centroid 1-F2 2.806(7), centroid 2-F5 2.835(7); F \cdots tetrazine plane distances in the range 2.791-3.045 \AA . (b) Fragment of the structure of $[\text{Ag}_2(\text{bptz})_2(\text{CH}_3\text{CN})_2][\text{AsF}_6]_2$ (**15**) depicting the shortest contacts between the $[\text{AsF}_6]^-$ anions and the tetrazine rings. Shortest F \cdots tetrazine centroid distances (\AA): centroid 1-F3A 2.838(6), centroid 2-F6A 2.784(6) \AA ; F \cdots tetrazine ring plane distances in the range 2.758-3.142 \AA .

3. $[\text{Ag}_2(\text{bptz})_3][\text{AsF}_6]_2 \cdot 2\text{CH}_3\text{CN}$, **(16)** $\cdot 2\text{CH}_3\text{CN}$ ⁸³ and $[\text{Ag}_2(\text{bptz})_3][\text{SbF}_6]_2 \cdot 2\text{CH}_3\text{CN}$, **(17a)** $\cdot 2\text{CH}_3\text{CN}$ - Compounds **16** and **17a** are isomorphous; the thermal ellipsoid plots of the dinuclear cations $[\text{Ag}_2(\text{bptz})_3]^{2+}$ in **16** and **17a** are illustrated in Figures 56 and 57, respectively. In both cases, the cation consists of two Ag(I) ions (Ag...Ag separations are 4.283 and 4.320 Å for **16** and **17a**, respectively), each coordinated to six nitrogen atoms from three bptz moieties in a trigonal prismatic arrangement with approximate C_{3v} molecular symmetry. Each bptz moiety is in the *syn* conformation and bridges the two Ag(I) ions in a bis-chelating fashion. There are π - π intermolecular interactions between pyridyl rings of bptz ligands from different propeller-type units (3.52 Å for **16** and 3.51 Å for **17a**; Figures 58a and 58b, respectively). Each anion ($[\text{AsF}_6]^-$ and $[\text{SbF}_6]^-$ for **16** and **17a**, respectively) interacts with two tetrazine rings from one cationic unit $[\text{Ag}_2(\text{bptz})_3]^{2+}$ and one tetrazine ring from another cationic unit (Figure 59). Each anion interacts with each tetrazine ring through three F atoms oriented towards the ring (Figure 59) with the F...tetrazine ring plane distances in the ranges 2.783-3.116 Å and 2.743-3.004 Å for **16** and **17a** (the shortest F...tetrazine centroid distances are 2.941(3) Å for **16** and 2.913(6) Å for **17a**), respectively. The packing of the cations and anions results in the formation of channels along the *c* axis, which are occupied by CH_3CN solvent molecules.

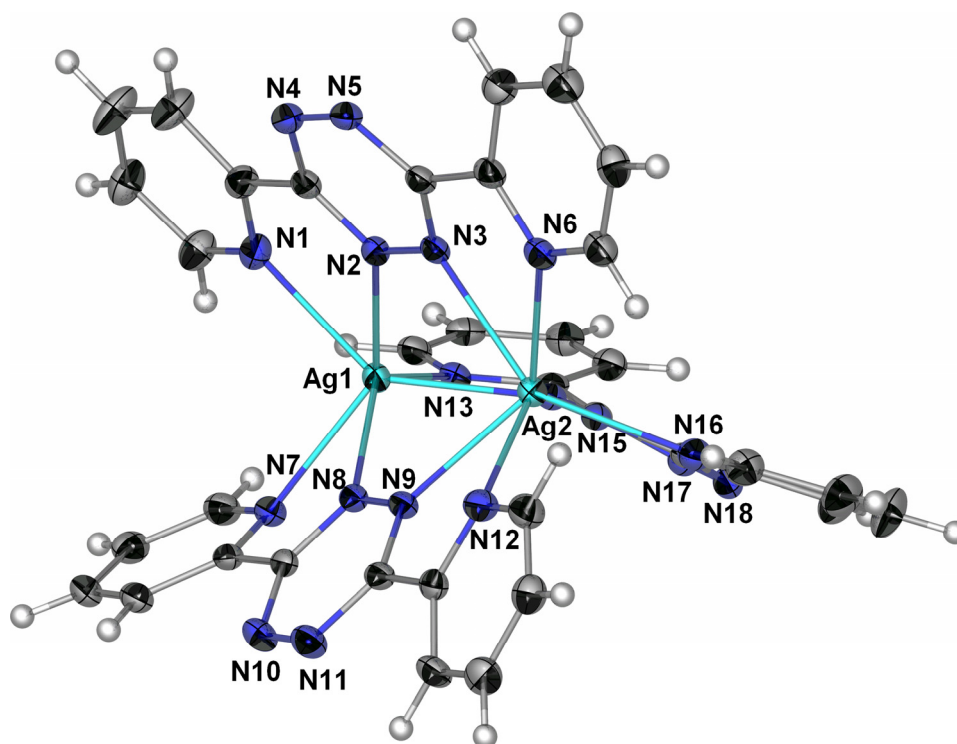


Figure S6: Thermal ellipsoid plot of the cationic unit $[\text{Ag}_2(\text{bptz})_3]^{2+}$ in **16** at the 50% probability level. Selected bond distances (\AA) and angles ($^\circ$): Ag1-N1 2.426(3), Ag1-N2 2.516(3), Ag1-N7 2.418(3), Ag1-N8 2.571(3), Ag1-N13 2.500(3), Ag2-N9 2.439(3), Ag2-N12 2.561(3), Ag2-N16 2.391(3), Ag2-N6 2.420(3), Ag2-N3 2.500(3), N1-Ag1-N2 66.77(10), N1-Ag1-N7 95.60(10), N8-Ag1-N7 66.92(9), N13-Ag1-N2 130.43(9), N9-Ag2-N12 66.67(9), N12-Ag2-N16 93.57(9), N3-Ag2-N16 140.14(9), N6-Ag2-N16 105.07(10).

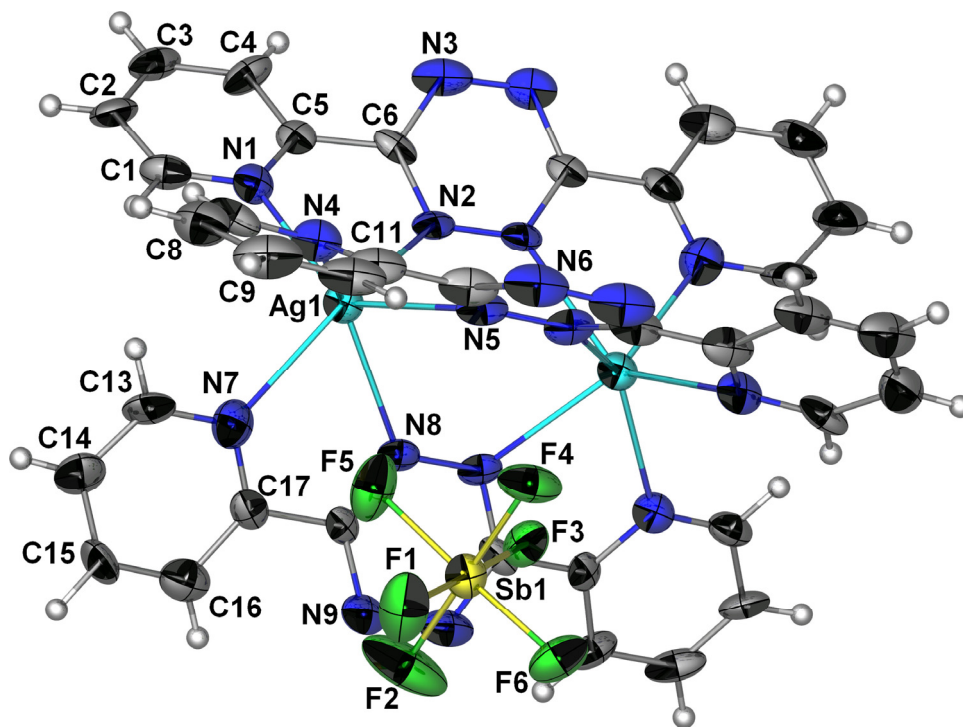


Figure 57: Thermal ellipsoid plot of $[\text{Ag}_2(\text{bptz})_3][\text{SbF}_6]_2$ (**17a**) at the 50% probability level (one $[\text{SbF}_6]^-$ ion has been omitted for clarity). Selected bond distances (\AA) and angles ($^\circ$): Ag1-N1 2.451(9), Ag1-N2 2.487(9), Ag1-N4 2.491(9), Ag1-N5 2.509(8), Ag1-N7 2.41(1), Ag1-N8 2.543(9), N1-Ag1-N2 68.9(3), N2-Ag1-N8 88.5(3), N7-Ag1-N8 66.5(3), N5-Ag1-N7 118.1(3), N4-Ag1-N7 95.2(3), N1-Ag1-N4 93.7(3), N4-Ag1-N5 66.3(3).

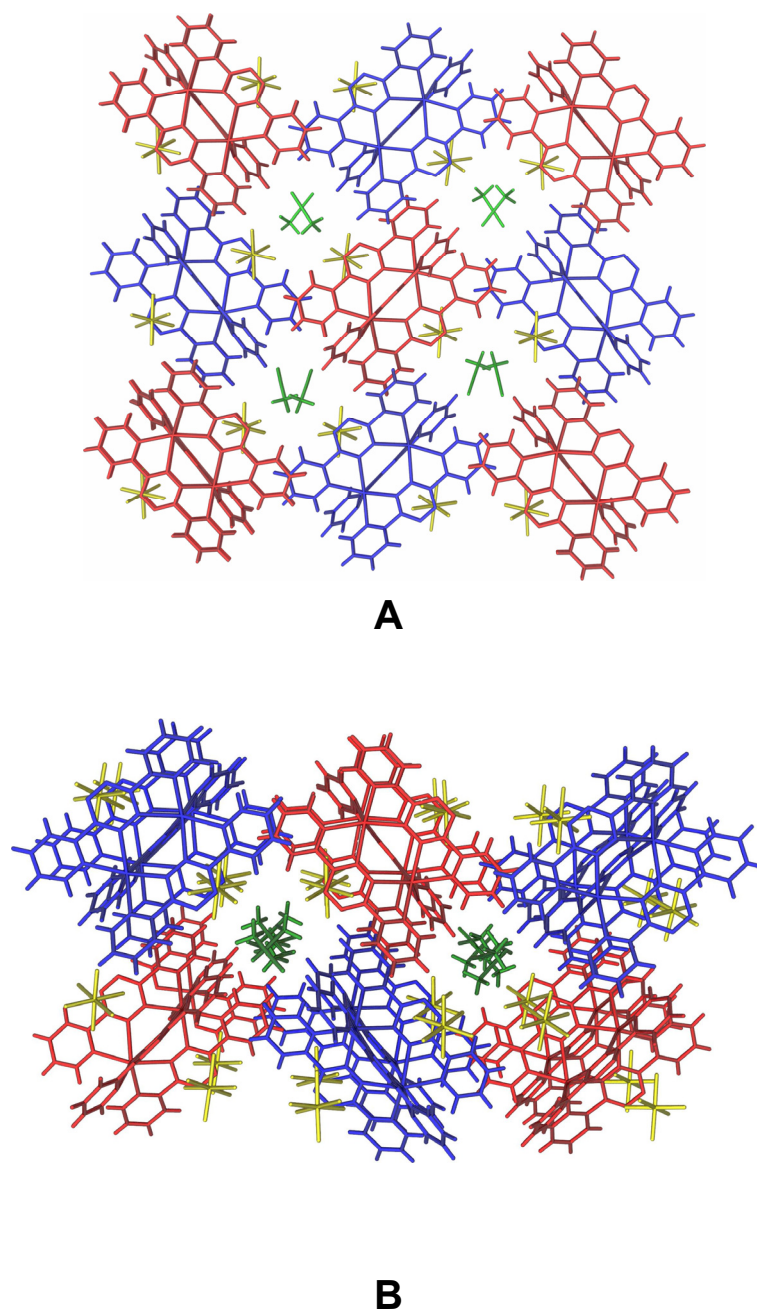


Figure 58: (a) Packing diagram of $[\text{Ag}_2(\text{bptz})_3][\text{AsF}_6]_2$ (**16**) in the ab plane. (b) Packing diagram of $[\text{Ag}_2(\text{bptz})_3][\text{SbF}_6]_2$ (**17a**) depicting the π - π intermolecular interactions between pyridyl rings of bptz ligands from different propeller-type units.

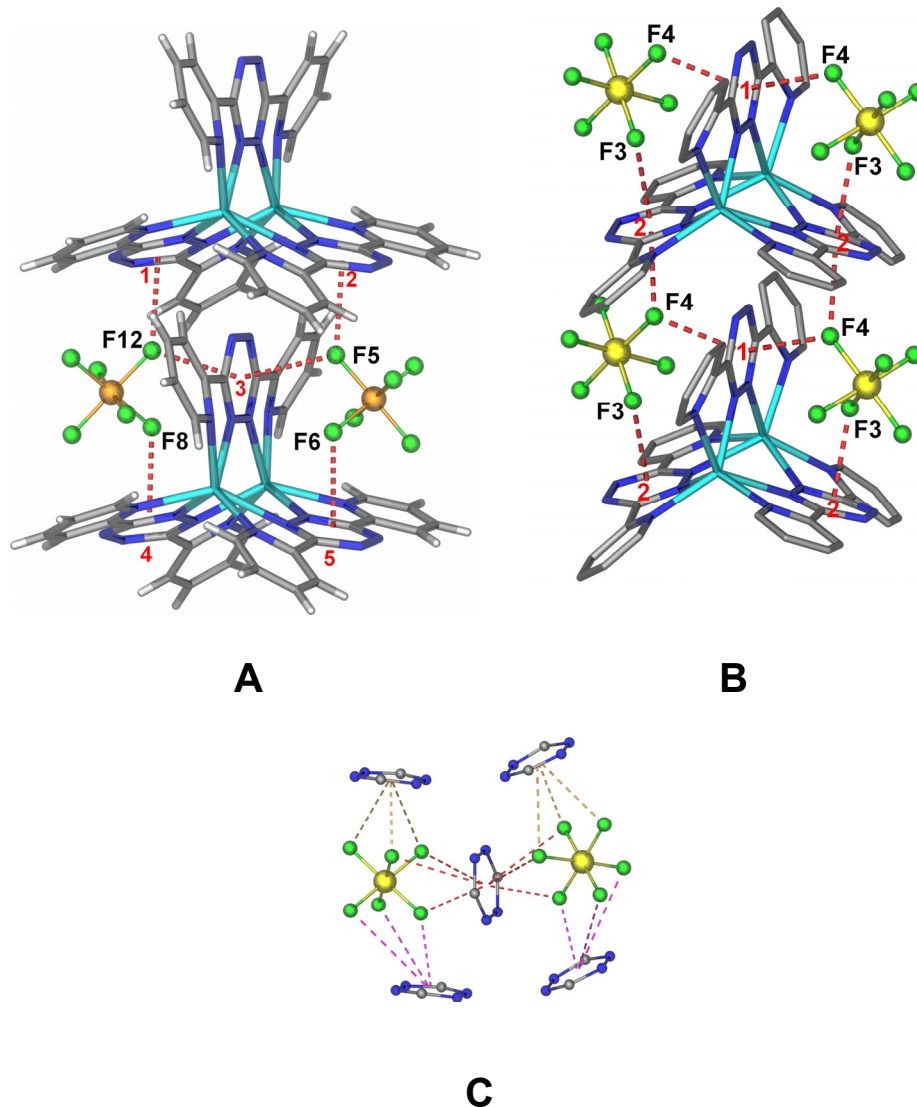


Figure 59: (a) Fragment of the $\text{Ag}_2(\text{bptz})_3[\text{AsF}_6]_2$ (**16**) structure depicting the shortest contacts between the $[\text{AsF}_6]^-$ anions and the tetrazine rings. Shortest $\text{F}\cdots$ tetrazine centroid distances (\AA): centroid 1-F12 2.948(2), centroid 2-F5 2.941(3), centroid 3-F5 2.965(3), centroid 3-F12 2.913(2), centroid 4-F8 3.029(2), centroid 5-F6 3.038(3) \AA ; $\text{F}\cdots$ tetrazine ring plane distances in the range 2.783–3.116 \AA . (b) Fragment of the $[\text{Ag}_2(\text{bptz})_3][\text{SbF}_6]_2$ (**17a**) structure depicting the shortest contacts between the $[\text{SbF}_6]^-$ anions and the tetrazine rings. Shortest $\text{F}\cdots$ tetrazine centroid distances (\AA): centroid 1-F4 2.927(9), centroid 2-F4 2.913(6), centroids 2 and 3-F3 2.952(6); $\text{F}\cdots$ tetrazine plane distances in the range 2.743–3.004 \AA . (c) Tetrazine ring with two $[\text{SbF}_6]^-$ anions in **17a**, displaying the three F atoms involved in each anion- π interaction (dotted lines drawn to the ring centroid).

4. [Ag₂(bptz)₃][SbF₆]₂, (17b) - The thermal ellipsoid plot of compound **17b** is depicted in Figure 60. It crystallizes in the space group *R*-3 which is the highest symmetry space group for this series of compounds. The [Ag₂(bptz)₃]²⁺ unit is located on a 3-fold axis and has *C*_{3v} symmetry, whereas two of the [SbF₆]⁻ anions have point symmetry 3- and the third one is on *C*₃ axis. The Ag...Ag separation is 4.424 Å, and each Ag(I) is in an ideal trigonal prismatic coordination geometry. No solvent molecules are present in the structure (Figure 61a). Unlike the other structures, this crystal does not contain cavities but consists of alternating layers of [Ag₂(bptz)₃]²⁺ and [SbF₆]⁻ ions which are parallel to the *ab* plane (Figure 61b). One of the crystallographically independent [SbF₆]⁻ ions is not incorporated into the layers; rather it participates in multiple anion- π interactions. The topology of these interactions, however, is different from that observed in **16** and **17a**. The [SbF₆]⁻ anion is surrounded by six tetrazine rings, and each anion- π interaction involves one F atom facing the tetrazine ring plane at a crystallographically unique distance of 2.844 Å (the shortest tetrazine centroid contact being 3.265(3) Å) (Figure 62). The bptz molecules in each [Ag₂(bptz)₃]²⁺ unit establish intermolecular π - π interactions with the bptz moieties of three other cationic units (Figure 62).

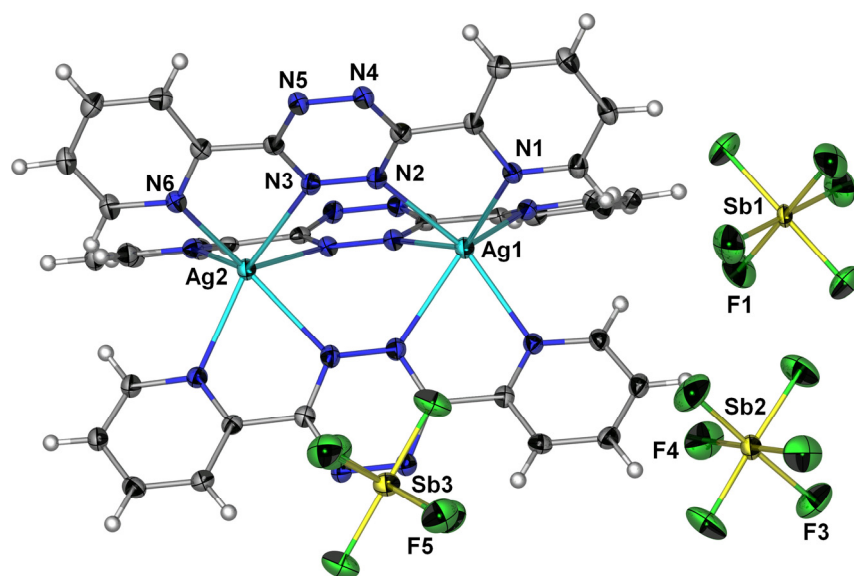


Figure 60: Thermal ellipsoid plot of $[\text{Ag}_2(\text{bptz})_3][\text{SbF}_6]_2$ (**17b**) at the 50% probability level. Selected bond distances (\AA) and angles ($^\circ$): Ag1-N1 2.438(3), Ag1-N2 2.554(3), Ag2-N3 2.575(3), Ag2-N6 2.434(3), N1-Ag1-N2 67.41(9), N3-Ag2-N6 66.19(9).

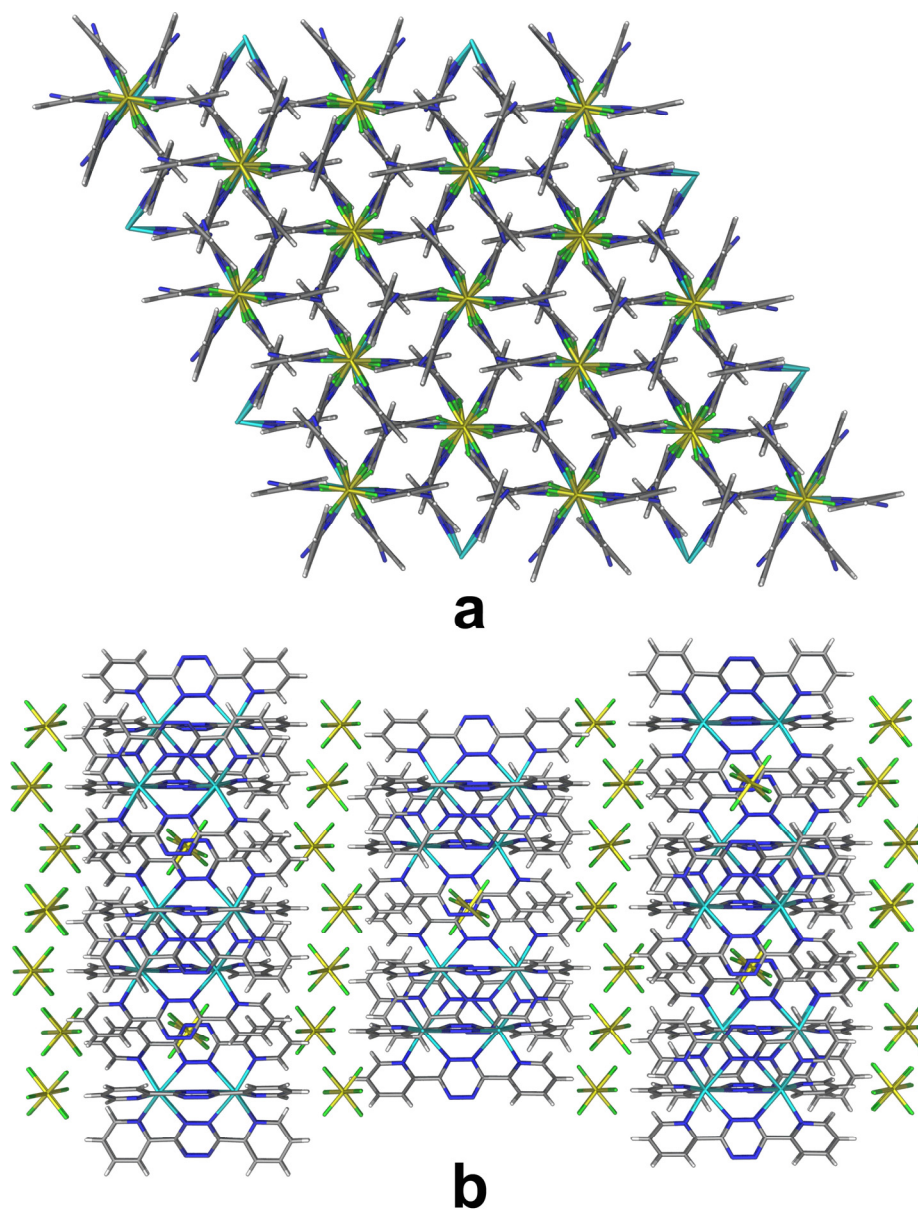


Figure 61: (a) Packing diagram of $[Ag_2(bptz)_3][SbF_6]_2$ (**17b**) along the c axis; and (b), view perpendicular to the c axis.

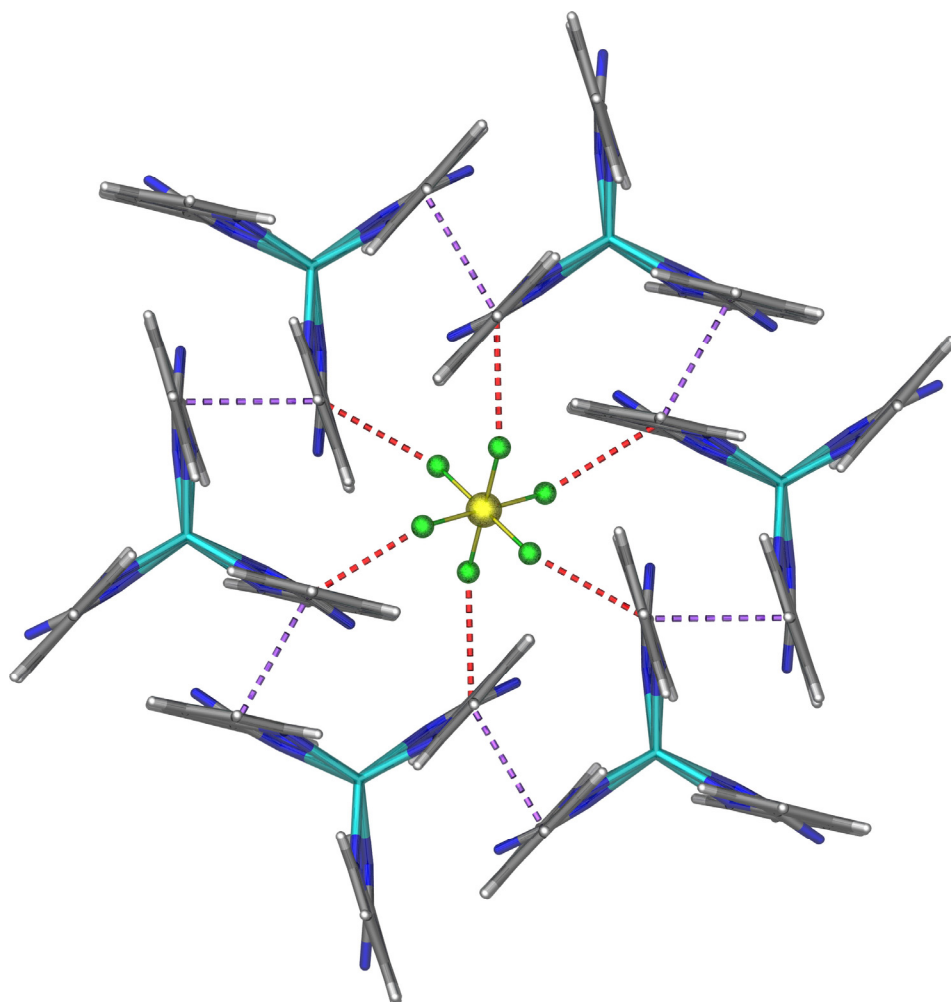


Figure 62: Anion- π interactions between a $[\text{SbF}_6]^-$ anion and six tetrazine rings in $[\text{Ag}_2(\text{bptz})_3][\text{SbF}_6]_2$ (**17b**). The F-centroid distance is 3.265(3) Å (red dash lines); F-tetrazine plane distance 2.844 Å. The π - π contacts (3.36 Å) are indicated with purple dash lines.

Unlike **16** and **17a**, wherein only the bptz pyridyl rings participate in π - π interactions, the π - π contacts in **17b** are maximized by involvement of both the pyridyl and tetrazine rings. The intermolecular π - π stacking between the bptz rings (3.36 Å) results in a highly symmetric crystal packing arrangement (Figures 61a and 62).

5. [Ag₄(bppn)₄][PF₆]₄•4CH₃NO₂ (18**)•4CH₃NO₂, [Ag₄(bppn)₄][AsF₆]₄•4CH₃NO₂ (**19**)•4CH₃NO₂, and [Ag₄(bppn)₄][SbF₆]₄•4CH₃NO₂ (**20**)•4CH₃NO₂** - Compounds **18-20** are isostructural. The thermal ellipsoid plots of **18**, **19**, and **20** are illustrated in Figures 63, 64 and 65, respectively. Despite similar reaction conditions, compounds **18-20** differ considerably from the compounds obtained with bptz. In all cases, [2x2] silver grids [Ag₄(bppn)₄]⁴⁺, similar to the cationic unit in the compound [Cu₄(bppn)₄][CF₃SO₃]₄,¹⁰⁴ are formed. The Ag(I) ions in each grid are in a distorted tetrahedral geometry, and the bppn moieties are in the *syn* orientation. The Ag...Ag separations in **18-20** are 3.73 Å. The Ag-N (pyridazine) and the Ag-N (pyridine) distances for **18-20** are in the ranges 2.220-2.370 and 2.260-2.331 Å, respectively. The grids are stabilized by intramolecular π - π interactions between both the pyridine and pyridazine rings of the bppn molecules (Figure 66a, b; 3.38, 3.38 and 3.33 Å for **18**, **19** and **20**, respectively). No intermolecular π - π interactions are present (the packing diagram of **18** is shown in Figure 67). In **6-8** there is only one anion- π interaction per pyridazine ring (Figure 66a); each anion interacts with only one ring through three F atoms (Figure 66c), and the F...pyridazine ring plane distances are in the ranges 2.902-3.181, 2.780-3.092, and 2.937-3.033 Å for **18**, **19**, and **20**, respectively. The shortest F...tetrazine ring centroid distances are 3.095(6), 3.096(3), and 3.260(5) Å for **18**, **19**, and **20**, respectively.

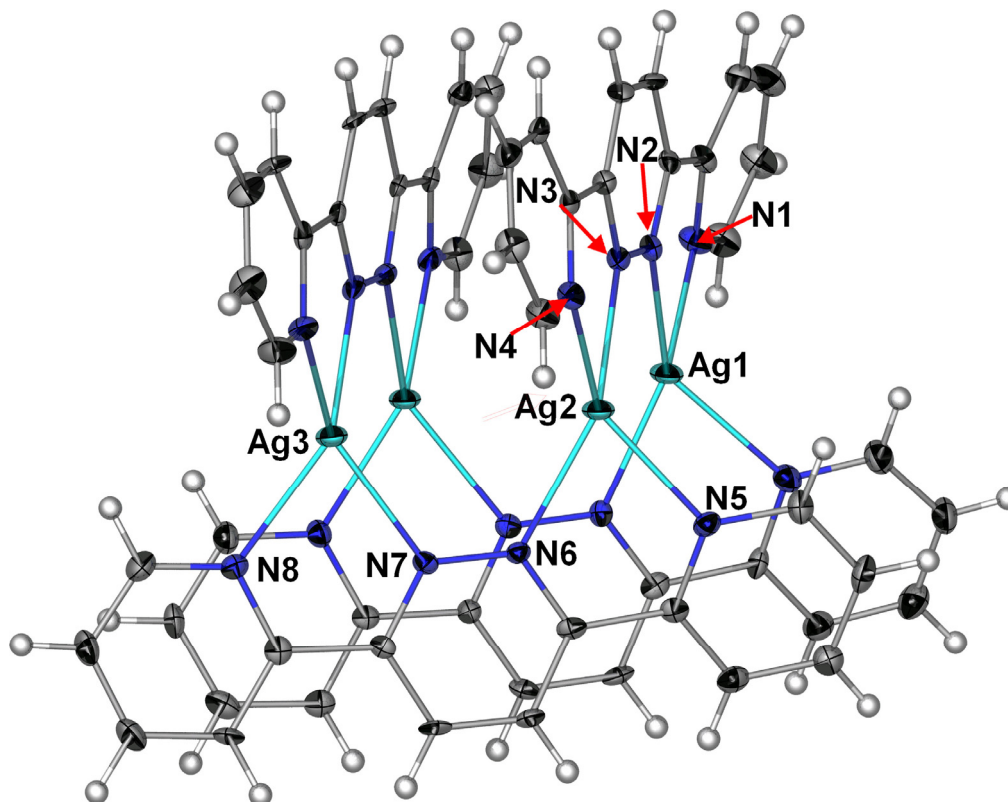


Figure 63: Thermal ellipsoid plot of the cationic unit $[\text{Ag}_4(\text{bppn})_4]^{4+}$ in **18** at the 50% probability level. Selected bond distances (Å) and angles ($^\circ$): Ag1-N1 2.319(5), Ag1-N2 2.222(4); Ag2-N3 2.369(4), Ag2-N4 2.272(4), Ag2-N5 2.288(5), Ag2-N6, 2.338(4), Ag3-N7 2.284(4), Ag3-N8 2.305(4), N1-Ag1-N2 72.5(2), N3-Ag2-N4 70.7(2), N4-Ag2-N6 129.1(1), N6-Ag2-N5 71.2(2), N5-Ag2-N3 117.7(1), N7-Ag3-N8 72.2(2).

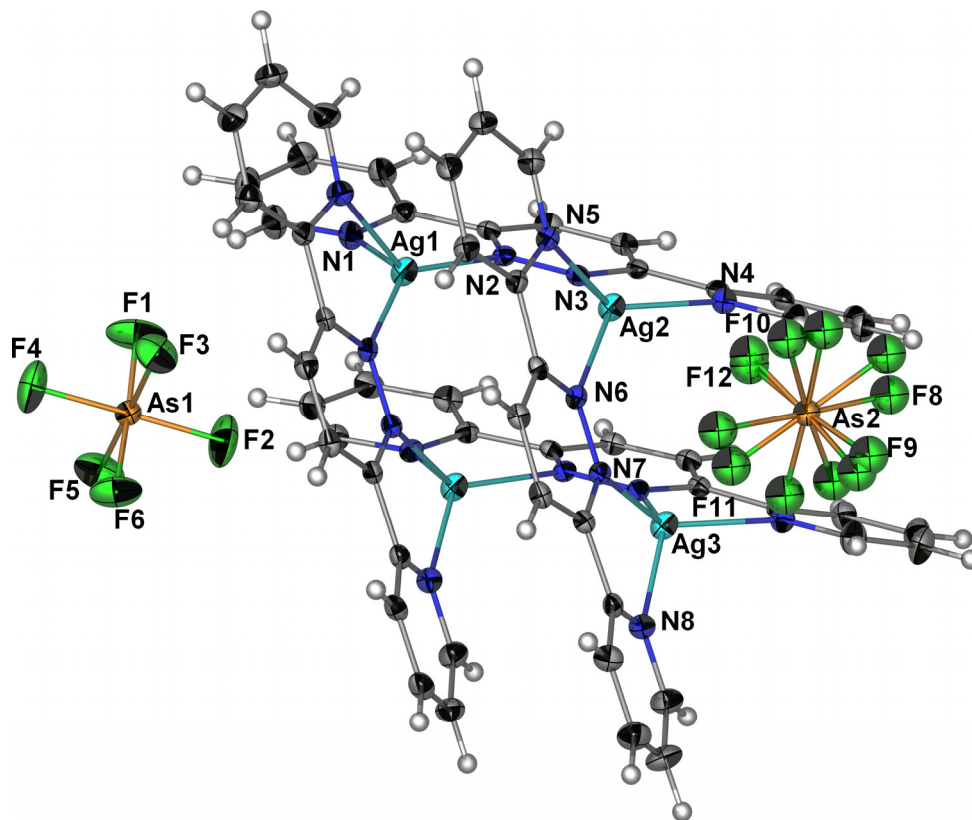


Figure 64: Thermal ellipsoid plot of the cationic unit $\{[Ag_4(bppn)_4][AsF_6]_2\}^{2+}$ in **19** at the 50% probability level. Selected bond distances (Å) and angles (°): N1-Ag1 2.331(3), N2-Ag1 2.225(3), N5-Ag2 2.295(3), N6-Ag1 2.338(3), N4-Ag2 2.273(3), N3-Ag2 2.370(3), N7-Ag3 2.293(3), N8-Ag3 2.303(3), N8-Ag3-N7 70.7(1), N6-Ag2-N5 71.3(1), N1-Ag1-N2 72.2(1), N3-Ag2-N4 70.6(1).

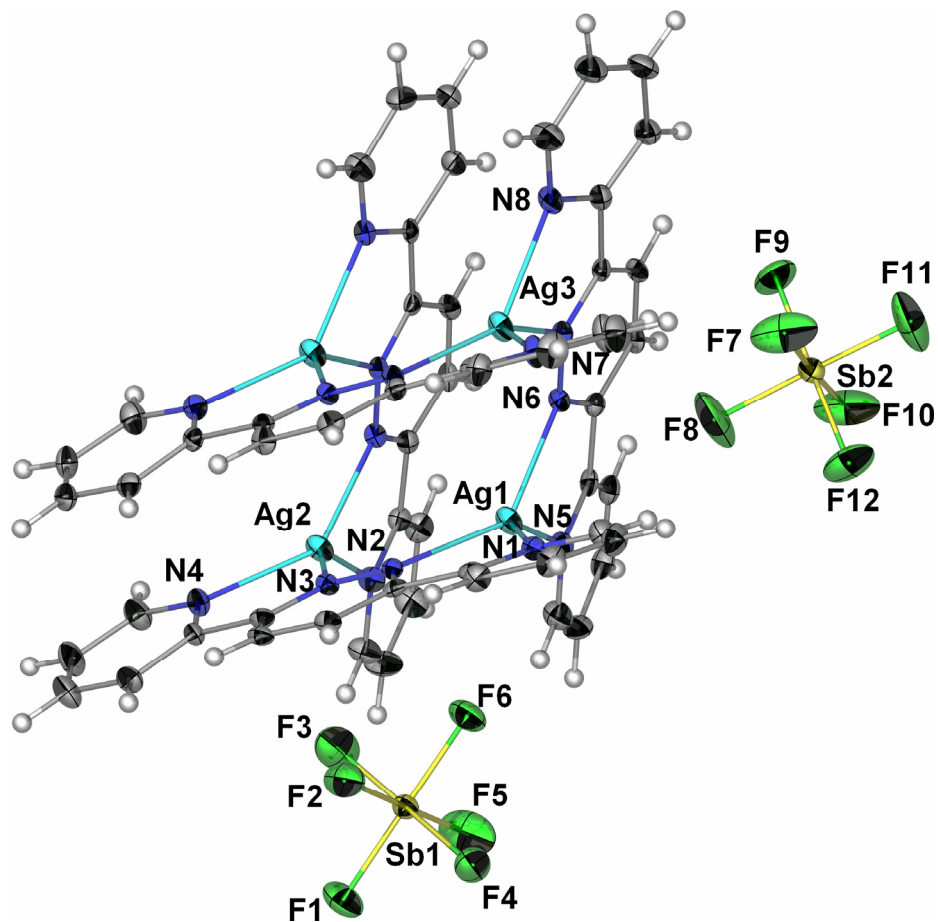


Figure 65: Thermal ellipsoid plot of the cation $\{[Ag_4(bppn)_4][SbF_6]_2\}^{+2}$ in **20** at the 50% probability level. Selected bond distances (Å) and angles (°): N1-Ag1 2.298(4), N2-Ag1 2.325(4), N5-Ag1 2.281(4), N6-Ag1 2.364(4), N3-Ag2 2.294(4), N4-Ag2 2.308(4), N8-Ag3 2.334(4), N7-Ag3 2.230(4), N8-Ag3-N7 72.0(2), N5-Ag1-N6 70.8(1), N1-Ag1-N2 71.1(2), N2-Ag1-N5 130.3(2), N3-Ag2-N4 71.7(2).

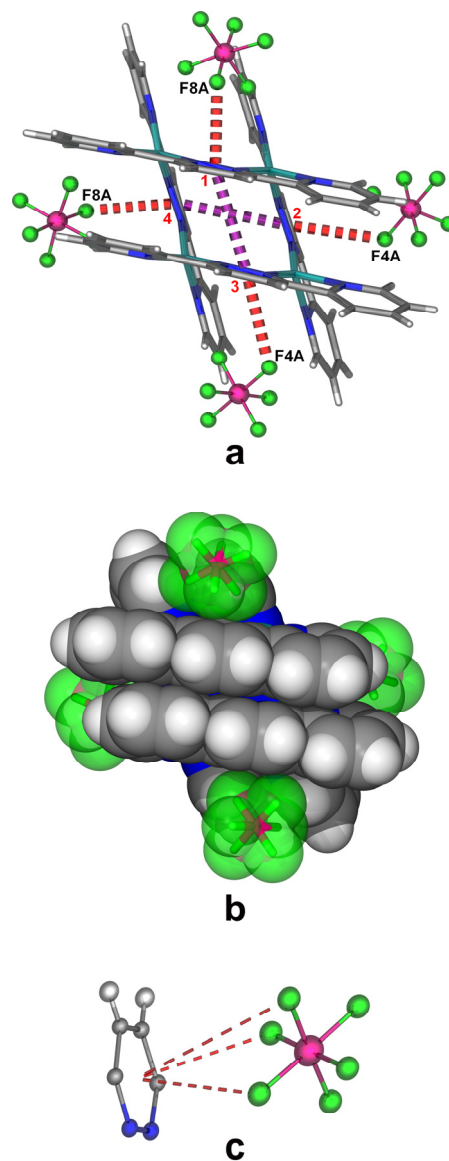


Figure 66: (a) Grid-type structure of $[\text{Ag}_4(\text{bppn})_4][\text{PF}_6]_4$ (**18**) depicting the π - π (3.38 Å; purple dashed lines) and anion- π interactions (red dashed lines); the F \cdots pyridazine ring plane distances are in the range 2.902-3.181 Å; shortest F \cdots tetrazine ring centroid distances (Å): centroids 1 and 4-F8A 3.095(6) and centroids 2 and 3-F4A 3.336(4). (b) Space-filling representation of **18**. (c) Pyridazine ring with one $[\text{PF}_6]^-$ anion in **18**, displaying the three F atoms involved in each anion- π interaction (dotted lines drawn to the ring centroid).

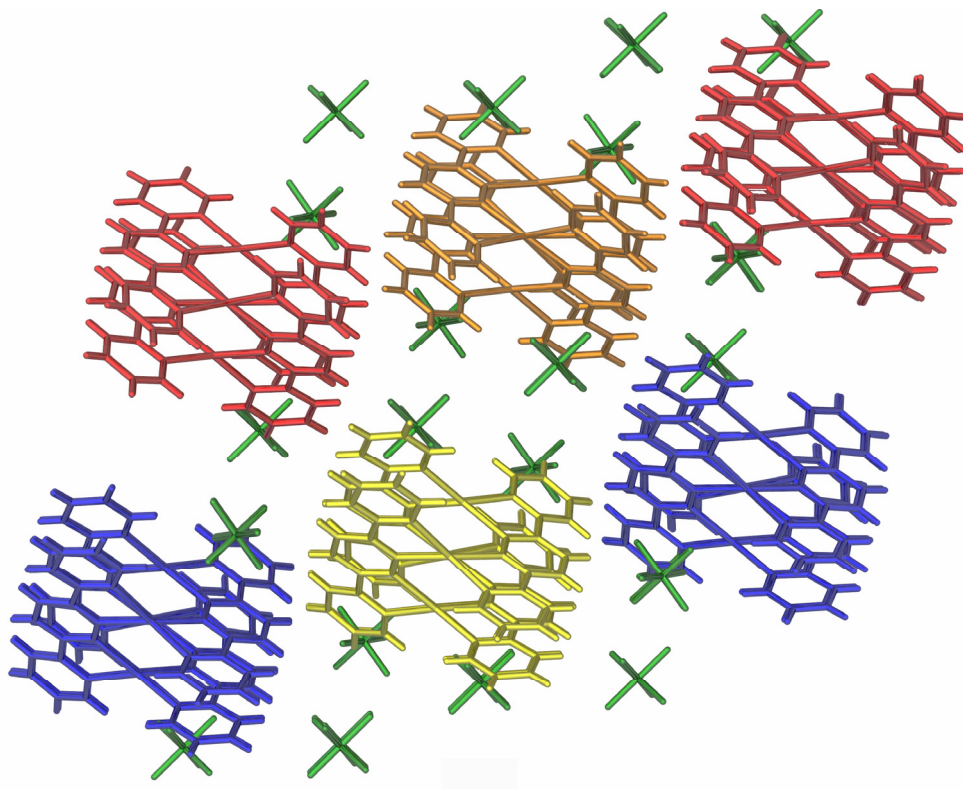


Figure 67: Packing diagram of **6** in the *ab* plane. Solvent molecules have been omitted for the purpose of clarity.

6. $[\text{Ag}_4(\text{bppn})_4][\text{BF}_4]_4 \cdot 3\text{CH}_3\text{NO}_2 \cdot \text{C}_6\text{H}_6$, (**21**) $\cdot 3\text{CH}_3\text{NO}_2 \cdot \text{C}_6\text{H}_6$ - The thermal ellipsoid plot of **21** is illustrated in Figure 68. The structure of **21** is analogous to those of compounds **18-20**. Due to the lower symmetry of this structure, there are four different Ag \cdots Ag separations in the range 3.677-3.770 Å. Each Ag(I) ion is in a distorted tetrahedral geometry, and the Ag-N (pyridazine) and Ag-N (pyridine) distances are in the ranges 2.264(5)-2.360(5) Å and 2.279(5)-2.348(5) Å, respectively. Intramolecular π - π stacking interactions at a distance of 3.53 Å between the bppn rings of the grid are present as in **18-20** (Figure 66a, b). In contrast to compounds **18-20**, however, only three out of the four pyridazine rings of each grid participate in anion- π interactions. The F \cdots pyridazine ring plane distances are in the range 2.835-3.261 Å (the shortest F to tetrazine ring centroid distance is 2.90(4) Å).

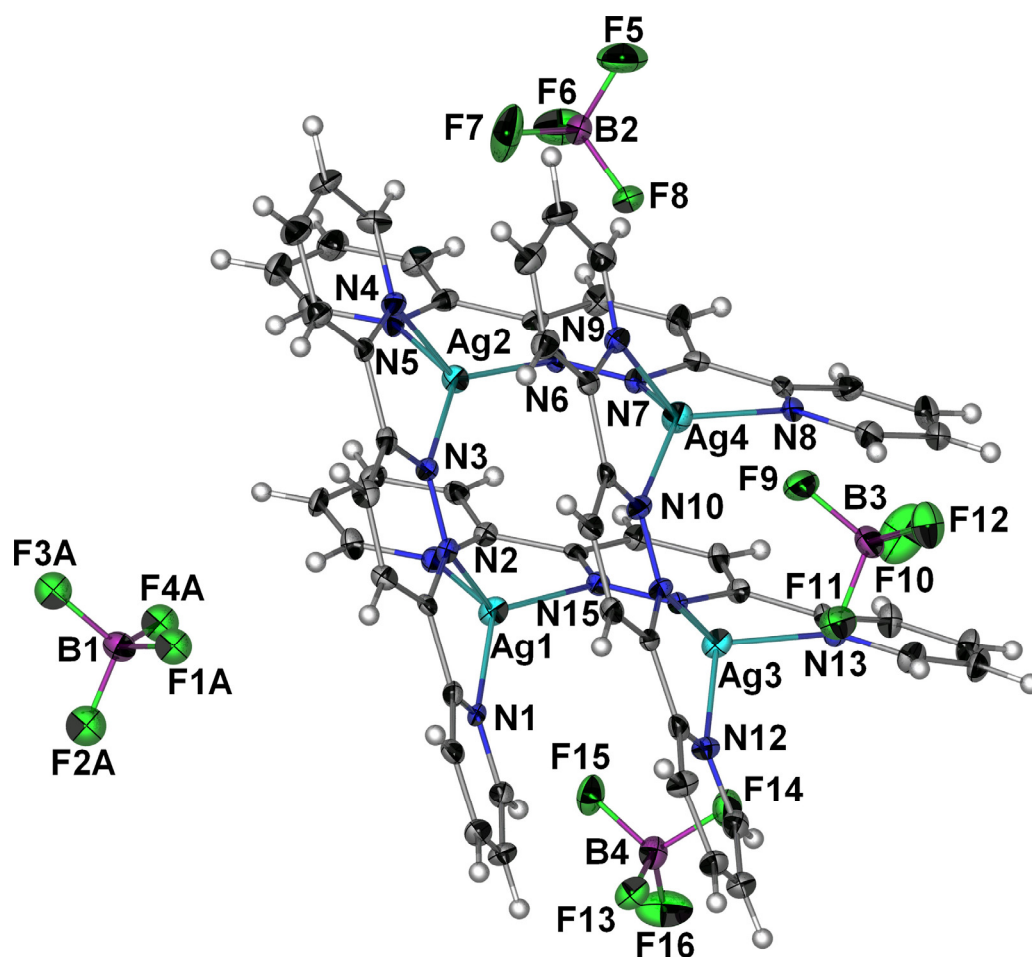


Figure 68: Thermal ellipsoid plot of $[\text{Ag}_4(\text{bppn})_4][\text{BF}_4]_4$ (**21**) at the 50% probability level. Selected bond distances (Å) and angles (°): Ag2-N3 2.284(5), Ag2-N6 2.290(5), Ag2-N4 2.355(5), Ag2-N5 2.360(5), N3-Ag2-N4 70.9(2), N6-Ag2-N5 70.5(2), N3-Ag2-N6 138.4(2), N6-Ag2-N4 138.9(2), N3-Ag2-N5 141.0(2), N4-Ag2-N5 104.4(2).

B. NMR and Mass Spectrometry Studies

1. Ag(I)-bptz complexes - The aromatic region of the ^1H NMR spectra of the Ag(I) bptz compounds **13-17b** in $\text{CD}_3\text{CN-}d_3$ exhibits four sets of resonances, which indicate that the bptz ligands are binding to the Ag(I) ions in a symmetric fashion in all cases. Complexes **13-17b** exhibit resonances at $\delta \sim 9.1, 8.9, 8.2,$ and 7.9 ppm in $\text{CD}_3\text{CN-}d_3$, which are ascribed to the $6',6'', 3',3'', 4',4'',$ and $5',5''$ protons of the pyridyl rings (Figure 69), respectively. Unbound bptz exhibits resonances at δ 8.93 ($6',6''$), 8.64 ($3',3''$), 8.10 ($4',4''$), and 7.65 ($5',5''$) ppm in $\text{CD}_3\text{CN-}d_3$ for the corresponding protons.⁸⁹ Thus, the $6',6'', 3',3'', 4',4'',$ and $5',5''$ protons of the Ag(I) complex pyridyl rings shift downfield by $\Delta\delta \sim 0.2, 0.2, 0.1,$ and 0.2 ppm, with respect to the corresponding free bptz protons due to the inductive effect of the metal.¹¹⁸

The ESI-MS spectra of compounds **13-15** in CH_3CN exhibit peaks at m/z 579, with the appropriate isotopic distributions, which correspond to $[\text{Ag}(\text{bptz})_2]^+$. Other disilver species observed at m/z 832 and 877 for **13-15** correspond to the ion clusters $[\text{Ag}_2(\text{bptz})_2(\text{PF}_6)]^+$ and $[\text{Ag}_2(\text{bptz})_2(\text{AsF}_6)]^+$, respectively. Compounds **13-15** also exhibit peaks at m/z 343, which indicate the presence of $[\text{Ag}(\text{bptz})]^+$ ions in solution. No evidence of any higher nuclearity species in solution was obtained for the polymeric compound **13**.

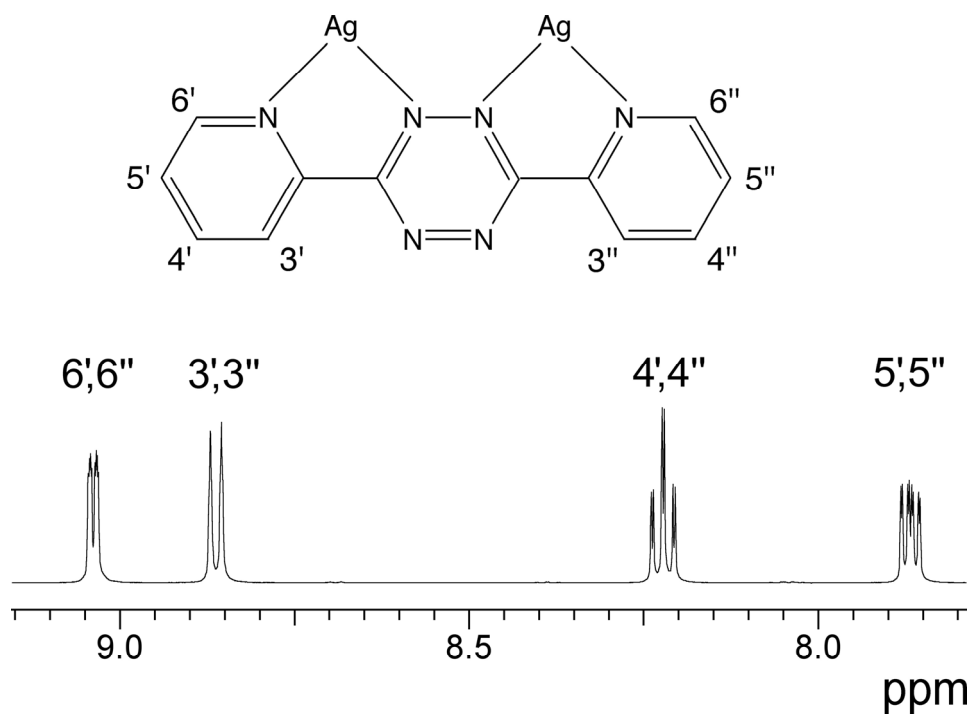


Figure 69: Aromatic region of the ^1H NMR spectrum of $[\text{Ag}_2(\text{bptz})_3][\text{AsF}_6]_2$ (**16**) in $\text{CD}_3\text{CN}-d_3$.

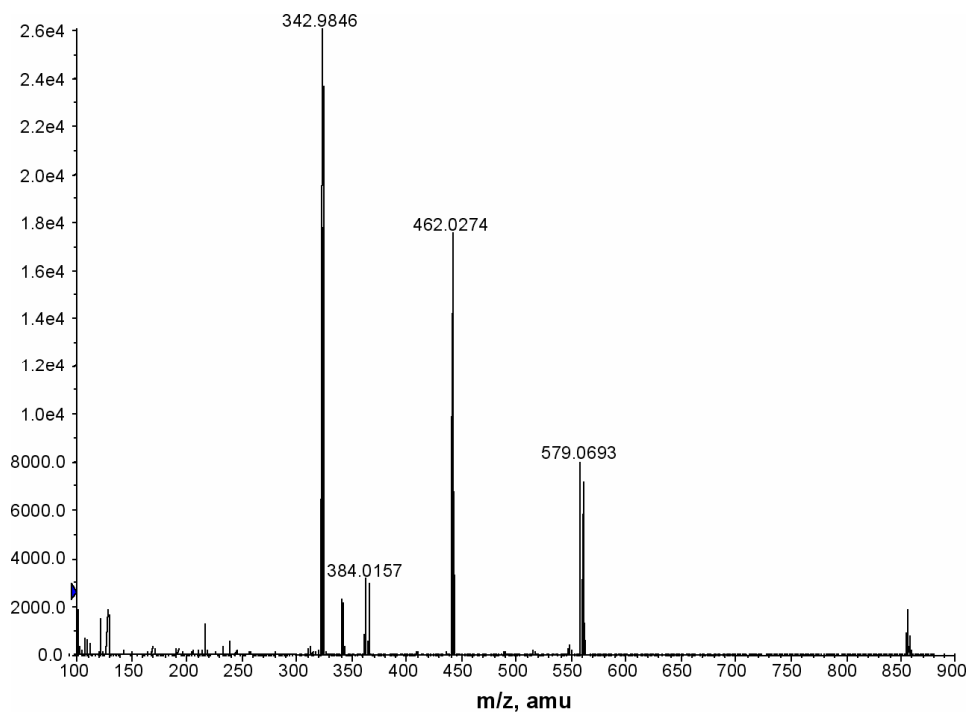


Figure 70: ESI-MS spectrum of $\text{Ag}_2(\text{bptz})_3[\text{AsF}_6]_2$ (**16**).

These observations are similar to those reported for the $[\text{CF}_3\text{SO}_3]^-$ and $[\text{BF}_4]^-$ salts of $[\text{Ag}_2(\text{bptz})_2]^{2+}$.^{102,103} The ESI-MS spectra of compounds **16-17b** exhibit peaks at m/z 462 and 923, corresponding to $[\text{Ag}_2(\text{bptz})_3]^{2+}$ and $[\text{Ag}_2(\text{bptz})_3 - \text{H}]^+$, respectively (Figure 70 for **16**), which indicate the presence of the doubly and singly charged intact cationic units in solution. The presence of the $[\text{Ag}_2(\text{bptz})_3]^{2+}$ ions under the conditions required for the mass spectral studies are indicative of the unusual stability of the Ag(I) propeller-type compounds **16-17b**. Compounds **16-17b** also exhibit peaks at m/z 579 and 343 in their ESI-MS spectra, which indicate the presence of the $[\text{Ag}(\text{bptz})_2]^+$ and $[\text{Ag}(\text{bptz})]^+$ ions in solution, as in the cases of compounds **13-15**.

Despite the fact that compound **1** is a polymer while **14** and **15** are dimers in the solid state, the shifts of their ^1H NMR resonances are similar and their ESI-MS spectra indicate the presence of mononuclear and dinuclear Ag(I) species in solution.^{102,103} Although the ESI-MS spectra of the propeller-type compounds **16-17b** support the presence of the species $[\text{Ag}_2(\text{bptz})_3]^{2+}$, their ^1H NMR spectra are very similar to those of **13-3**. Therefore, it is evident that for compounds **13-17b**, the lower nuclearity Ag(I)-bptz species present in solution are similar in all cases.⁹⁶ Apparently, the different Ag(I):bptz stoichiometries among compounds **13-17b** are not reflected by their ^1H NMR spectra. The downfield shifts of the protons of the Ag(I)-bptz species relative to the free ligand, albeit relatively small, indicate that there is an interaction between the Ag(I) ions and bptz units in solution,⁹⁶ but the inductive effect of the Ag(I) ions on the aromatic rings is approximately the same,¹¹⁹ and the ligands are binding to the Ag(I) ions in a symmetric fashion in all cases.

2. Ag(I)-bppn complexes - Free bppn exhibits resonances at δ 8.77 (dd, 6',6''-H), 8.70 (dd, 3',3''-H), 8.70 (d, 4,5-H), 8.02 (dt, 4',4''-H), and 7.53 (ddd, 5',5''-H) ppm in $\text{CD}_3\text{NO}_2-d_3$ (Figure 71a). The aromatic region of the ^1H NMR spectra of the Ag(I) bppn compounds **18-21** in $\text{CD}_3\text{NO}_2-d_3$ exhibits five sets of resonances, which indicate that the bppn ligands are binding to the Ag(I) ions in a symmetric fashion in accord with grid-like rather than oligomeric structures. Complexes **18-21** exhibit resonances at $\delta \sim 8.7$, 8.46, 8.24, 8.03, and 7.47 ppm in $\text{CD}_3\text{NO}_2-d_3$ (Figure 71b for **21**), which are attributed to the (4,5), 3',3'', 6',6'', 4',4'', and 5',5'' protons of bppn, respectively. The resonances of protons 3',3'', 6',6''-H are shifted upfield by ~ 0.25 , 0.50 ppm, respectively, and have switched relative positions with respect to the free ligand resonances, features that were also observed in the ^1H NMR spectra of other Cu(I)-bppn and Ag(I)-functionalized bppn grid-type molecules.^{104,120} The considerable upfield shift of the resonances for protons 6',6''-H, adjacent to the binding sites of the Ag(I) ions is attributed to a shielding effect from the neighboring pyridyl bppn aromatic rings of the grid.^{94,121-123} Mass spectra are not reported for the Ag(I)-bppn complexes due to the unsuitability of nitromethane as a solvent for such studies (the compounds decompose in other solvents).

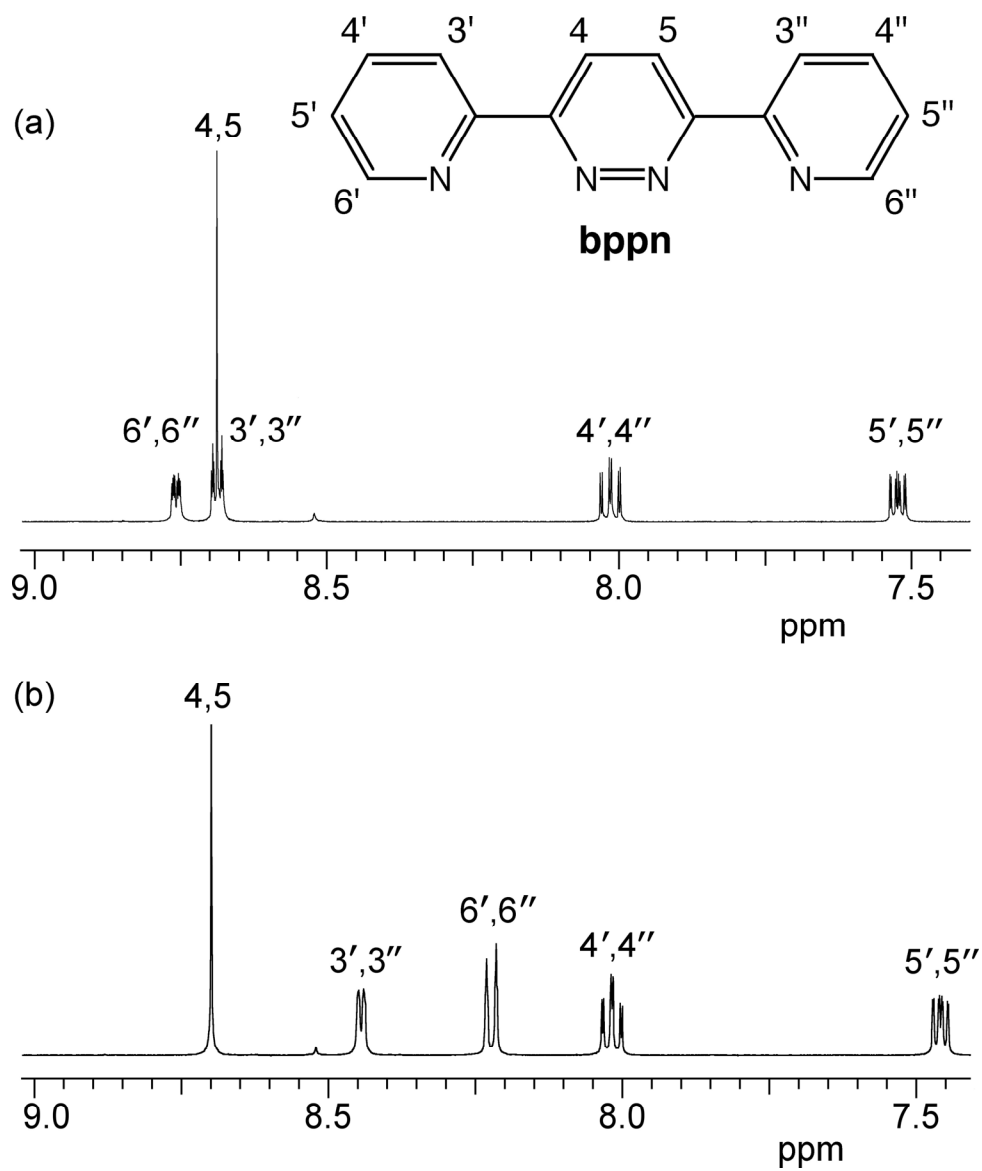


Figure 71. Aromatic region of the ^1H NMR spectrum of (a) **bppn**, and (b) $[\text{Ag}_4(\text{bppn})_4][\text{AsF}_6]_4$ (**20**) in $\text{CD}_3\text{NO}_2-d_3$.

C. Bptz and Bppn Ligand Calculations

The ligands bptz and bppn were subjected to DFT geometry optimization calculations to determine the effect of the different number of nitrogen atoms of the central rings on the corresponding electrostatic potential. Based on the reduction potentials $E_{p,c}$ of the free ligands,¹²⁴ bptz is expected to be more electropositive than bppn. Both ligands were optimized in the low-energy *anti* orientation (Figures 72a, b and 73a, b), but due to the fact that the ligands are *syn* in complexes **14-21**, they were also optimized in the higher-energy *syn* orientation (Figures 72c, d and 73c, d). The differences between the optimized geometries calculated by the B3LYP/6-311+G(d,p) and BP86/TZP optimizations are negligible for both the *syn* and *anti* orientations of bptz and bppn.

The B3LYP/6-311+G(d,p) (Figure 72) and BP86/TZP (Figure 73) optimizations afforded similar electrostatic potential maps (electrostatic potential mapped on the electron density with an isodensity value of 0.02). The electrostatic potential maps derived from B3LYP/6-311+G(d,p) and BP86/TZP calculations clearly indicate an area of positive charge, illustrated by the blue color, in the center of the bptz tetrazine ring (Figures 72a, c, and 73a, c), which is more intense as compared to the bppn central pyridazine ring (Figures 72b, d, and 73b, d). Moreover, in the bptz ligand, the electrostatic potential maps suggest that the central ring is significantly more electropositive as compared to the outer pyridyl rings (Figures 72a, c and 73a, c).

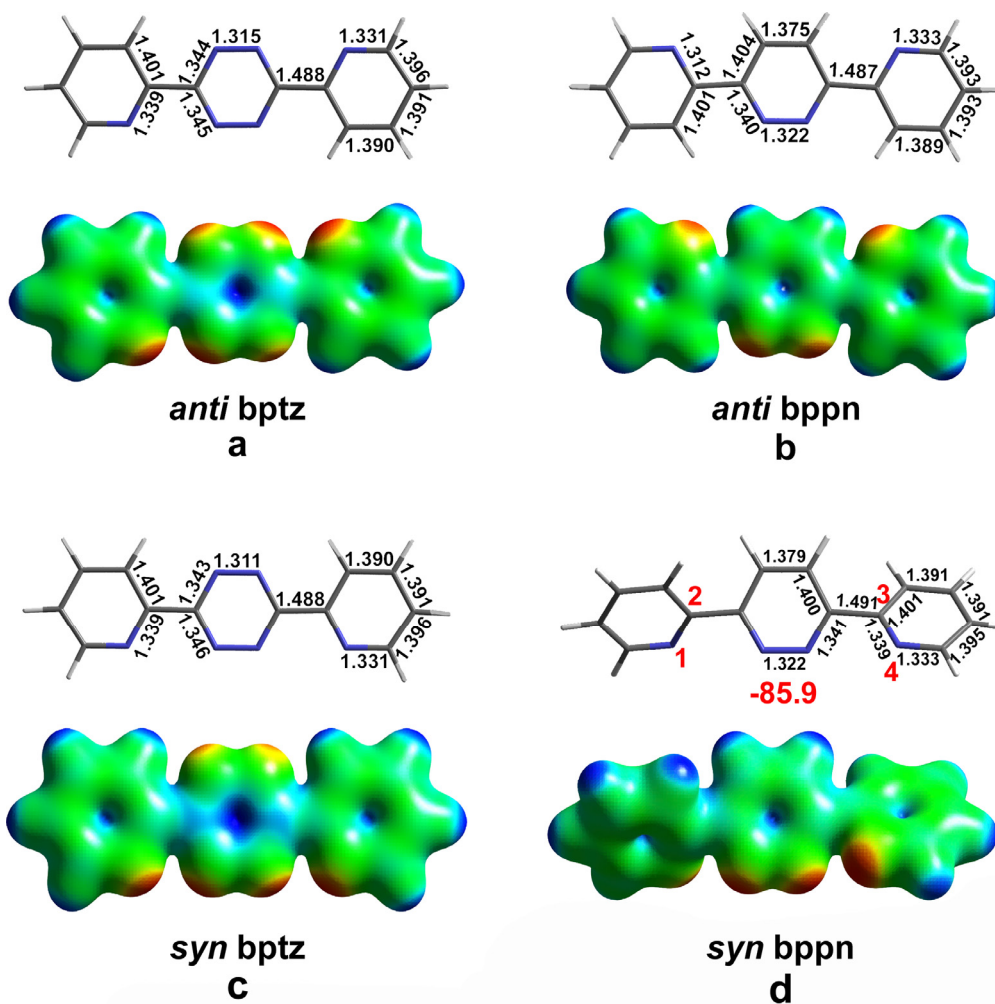


Figure 72: B3LYP/6-311+G(d,p) geometry optimization and electrostatic potential maps for (a) bptz in the *anti* orientation, (b) bppn in the *anti* orientation, (c) bptz in the *syn* orientation, and (d) bppn in the *syn* orientation (the dihedral angle defined by the atoms labeled with red numbers is -85.9°). The maps were generated with Cerius² 4.8 (Accelrys, Inc.) at a 0.02 isodensity value and a color scale of 126 (blue) to -63 (red) kcal/mol.

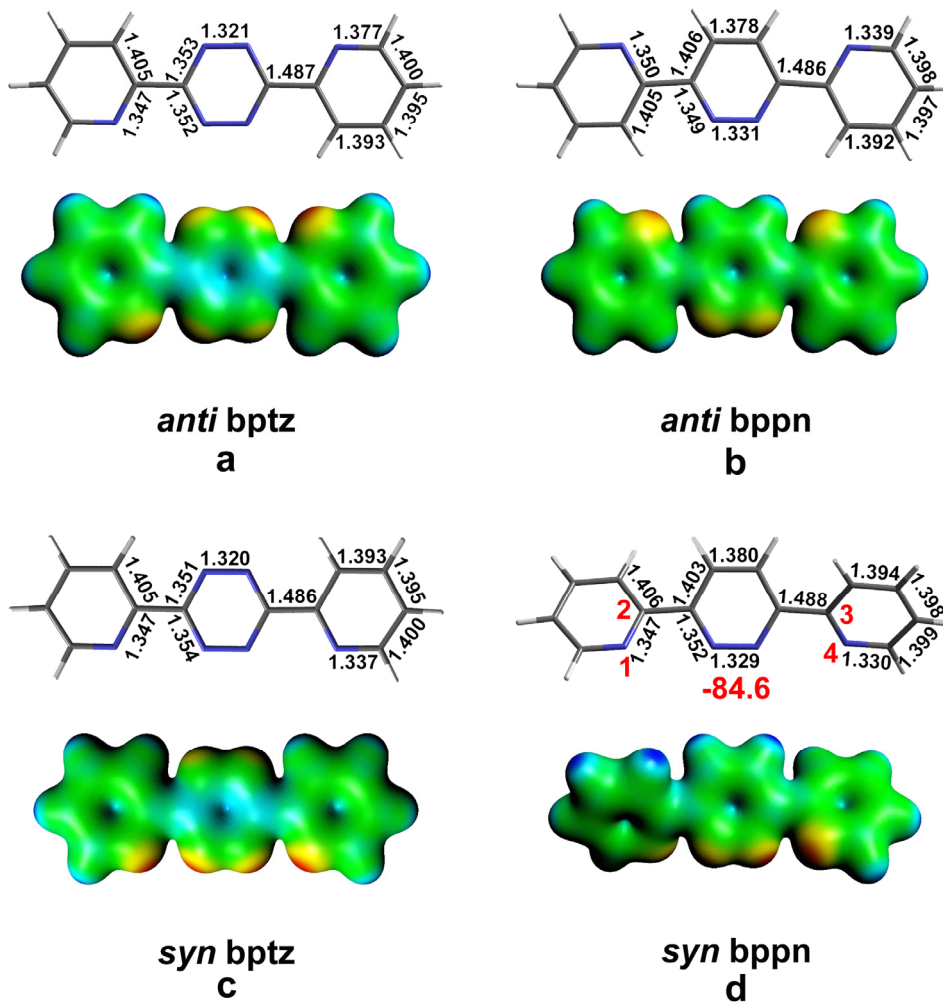


Figure 73: BP86/TZP geometry optimization and electrostatic potential maps for (a) bptz in the *anti* orientation, (b) bppn in the *anti* orientation, (c) bptz in the *syn* orientation, and (d) bppn in the *syn* orientation (the dihedral angle defined by the atoms labeled with red numbers is -84.6°). The maps were generated with the ADFView¹²⁵ interface at a 0.02 isodensity value and a color scale of 126 (blue) to -63 (red) kcal/mol.

On the contrary, the three bppn rings are very similar in charge distribution, with the central pyridazine ring being only slightly more electropositive than the outer pyridyl rings (Figures 72b, d and 73b, d).

An important observation is that, for both ligands, the electrostatic potentials do not change significantly between the low-energy *anti* and the higher-energy *syn* conformations (Figures 72, 73). The bptz ligand displays the same increase in electropositive charge of its central tetrazine ring in both the *anti* and *syn* conformations (Figures 72a, c and Figures 73a, c) and bppn displays a more electronegative central ring than bptz for both conformations (Figures 72b, d and Figures 73b, d). Therefore, the charge density distributions in the Ag(I)-bptz and bppn complexes should not be affected by the conformations of the ligands which, except for **13**, are *syn* oriented.

D. Silver Complex Calculations

BP86/TZP Single-Point Energy (SPE) calculations were undertaken for the crystal structure geometries of the neutral or cationic species of **15**, **16**, **17b**, and **19**, and their electrostatic potential maps are depicted in Figures 74-77.

The electrostatic potential map scales derived from the SPE calculations (and thus the color ranges) of the doubly charged cation $[\text{Ag}_2(\text{bptz})_2(\text{CH}_3\text{CN})_2]^{2+}$ (Figure 74a) and the neutral complex **15** (Figure 74b), were adjusted to be the same for the outer pyridyl rings of the bptz ligands in the two differently charged species. Thus a direct comparison of colors between the electrostatic maps in Figures 74a and 74b is viable.

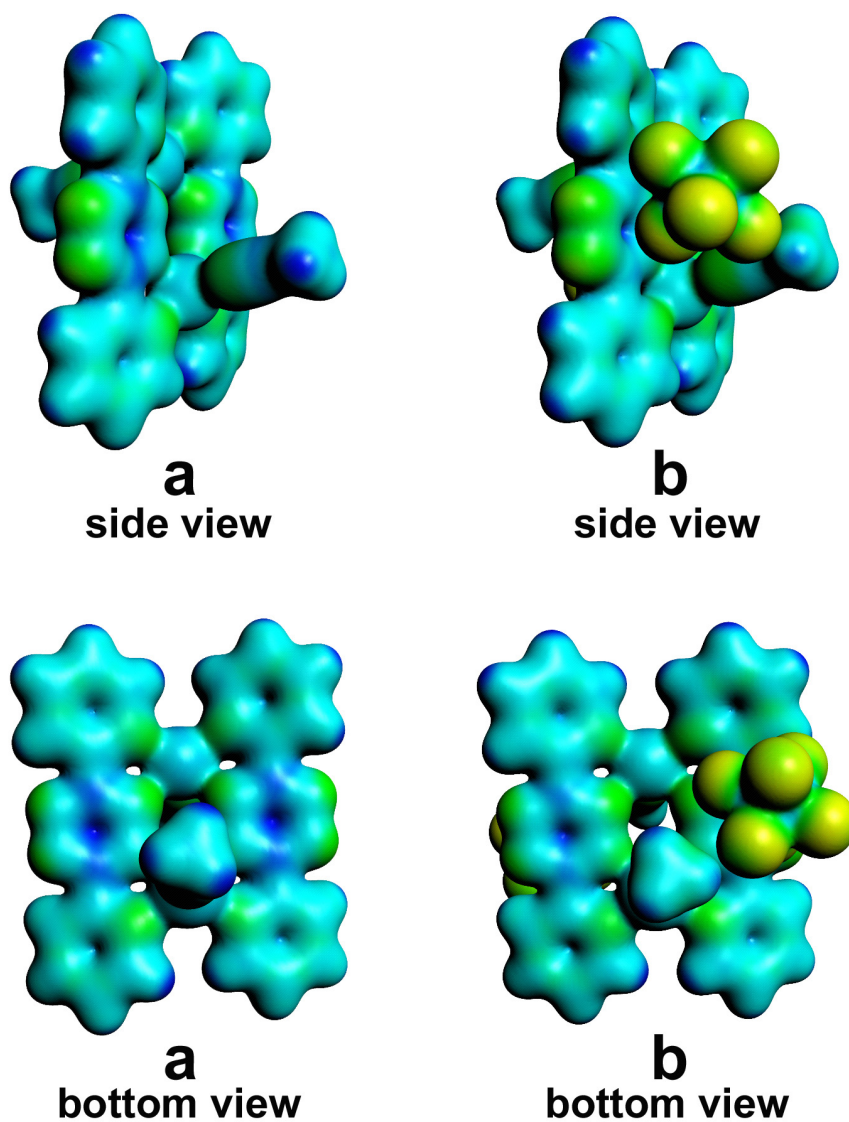


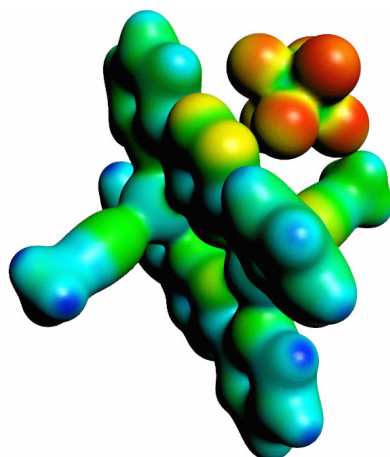
Figure 74. Electrostatic potential map from the BP86/TZP SPE calculations of **3** for (a) doubly charged cation $[\text{Ag}_2(\text{bptz})_2(\text{CH}_3\text{CN})_2]^{2+}$ with a color scale of 220 (blue) to -31 (red) kcal/mol, and (b) neutral complex $[\text{Ag}_2(\text{bptz})_2(\text{CH}_3\text{CN})_2][\text{AsF}_6]_2$ with a color scale of 126 (blue) to -126 (red) kcal/mol. The maps were generated with ADFView¹²⁵ at a 0.02 isodensity value.

The SPE calculations performed for **15** indicate that, in the absence of the $[\text{AsF}_6]^-$ counter anions, the cationic subunit $[\text{Ag}_2(\text{bptz})_2(\text{CH}_3\text{CN})_2]^{2+}$ displays a highly electropositive area in the central tetrazine ring of both bptz units as compared to the outer pyridyl rings (Figure 74a) comparable to that observed in the electrostatic maps of free bptz (Figures 72c and 73c). In the neutral complex **15**, there is equivalent charge density distribution on the two bptz ligands. The two tetrazine rings of the bptz ligands in close proximity to the $[\text{AsF}_6]^-$ anions become less electropositive as compared to the tetrazine rings in the cationic unit $[\text{Ag}_2(\text{bptz})_2(\text{CH}_3\text{CN})_2]^{2+}$, but the central tetrazine rings still remain more electropositive than the outer pyridyl rings (Figures 74a, 74b). The decrease in the electropositive character of the central tetrazine rings in the neutral complex is attributed to a flow of electron density from the $[\text{AsF}_6]^-$ anions to the bptz π -acidic central rings and the establishment of favorable anion- π interactions between the $[\text{AsF}_6]^-$ anions and the tetrazine rings. Although both central tetrazine rings of the neutral complex **15** are more electronegative as compared to free bptz and the dication of **15**, each tetrazine ring is electropositive enough to participate in an additional anion- π interaction, which is corroborated by the X-ray crystallographic data (*vide supra*; Figures 53, 54b and 55b).

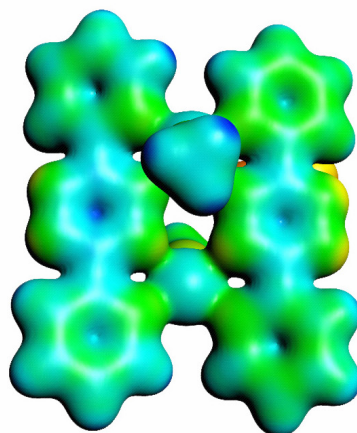
The presence of only one $[\text{AsF}_6]^-$ anion in the singly charged species $\{[\text{Ag}_2(\text{bptz})_2(\text{CH}_3\text{CN})_2][\text{AsF}_6]\}^+$ of **15** disrupts the equivalent electrostatic potential distributions between the two bptz ligands (Figure 75; bottom view), as compared to the neutral species of **15** (Figure 74b); the color range of the outer pyridyl rings in Figure 75 does not match that of the species in 74a and 74b, which prohibits direct comparison with them. The tetrazine ring of the bptz ligand in close proximity to the

[AsF₆]⁻ anion (right ligand in Figure 75; bottom view) has less electropositive character as compared to the other tetrazine ring of the molecule. Moreover, the anion fluorine atoms closest to the tetrazine ring are slightly less electronegative than the distal ones (Figure 75; side view) and the difference in the color intensities between the central tetrazine and the outer pyridyl rings in the bptz ligand in proximity to the anion has decreased as compared to the free ligand (Figure 75, bottom view; right ligand). The difference in the color intensities between the central tetrazine and the outer pyridyl rings in the distal bptz ligand from the anion (Figure 75; bottom view), however, is comparable to that in free bptz (Figures 72c and 73c). The aforementioned observations suggest a flow of electronic charge from the anion to the proximal bptz π -acidic central ring and the establishment of an anion- π interaction between the [AsF₆]⁻ anion and the adjacent bptz tetrazine ring in the cationic species {[Ag₂(bptz)₂(CH₃CN)₂][AsF₆]}⁺.⁸³

In the electrostatic potential maps of the doubly charged propeller-type unit [Ag₂(bptz)₃]²⁺ of **17b**, there is equivalent charge density distribution on the three ligands and the three central tetrazine rings display a more intense electropositive area as compared to the outer pyridyl rings (Figure 76a). Since in the crystal structure of **17b** only one [SbF₆]⁻ anion is in proximity with each tetrazine ring (*vide supra*: Figure 62), the SPE calculation of the singly charged cation {[Ag₂(bptz)₃][SbF₆]}⁺ was undertaken.



side view



bottom view

Figure 75: Electrostatic potential map from the BP86/TZP SPE calculations for the singly charged cation $\{[\text{Ag}_2(\text{bptz})_2(\text{CH}_3\text{CN})_2][\text{AsF}_6]\}^+$ of **15** with a color scale of 188 (blue) to -31 (red) kcal/mol. The maps were generated with ADFView¹²⁵ at a 0.02 isodensity value.

In the electrostatic potential map of $\{[\text{Ag}_2(\text{bptz})_3][\text{SbF}_6]\}^+$, the electropositive charge in the central tetrazine ring close to the anion has decreased, as compared to the bptz ligand distal to it (Figure 76b). Furthermore, the anion fluorine atoms closest to the tetrazine ring are less electronegative than the distal ones. The previous observations suggest a flow of electronic charge from the anion to the proximal π -acidic ring and thus the presence of an anion- π interaction between the $[\text{SbF}_6]^-$ anion and the bptz tetrazine ring.¹²⁶

In the electrostatic potential map of the doubly charged cationic unit $[\text{Ag}_2(\text{bptz})_3]^{2+}$ of **16** (Figure 77a), the three tetrazine rings display a more electropositive area than the outer pyridyl rings of the bptz ligands, as observed in the free bptz ligand (Figures 72c and 73c). The higher positive charge on one of the central tetrazine rings of the dication $[\text{Ag}_2(\text{bptz})_3]^{2+}$ (upper ring; Figure 77a, side view) originates from the bonding and geometry in the molecular crystal structure of **16** that was used for the SPE calculations. Apparently, the structural features of the propeller-type compound **16** render it less symmetric than **17b** in the solid state and account for the unequal positive charge density distribution on the three tetrazine rings of each doubly charged propeller unit $[\text{Ag}_2(\text{bptz})_3]^{2+}$ (in contrast to equal distribution in the doubly charged species of **17b**; Figure 76a).

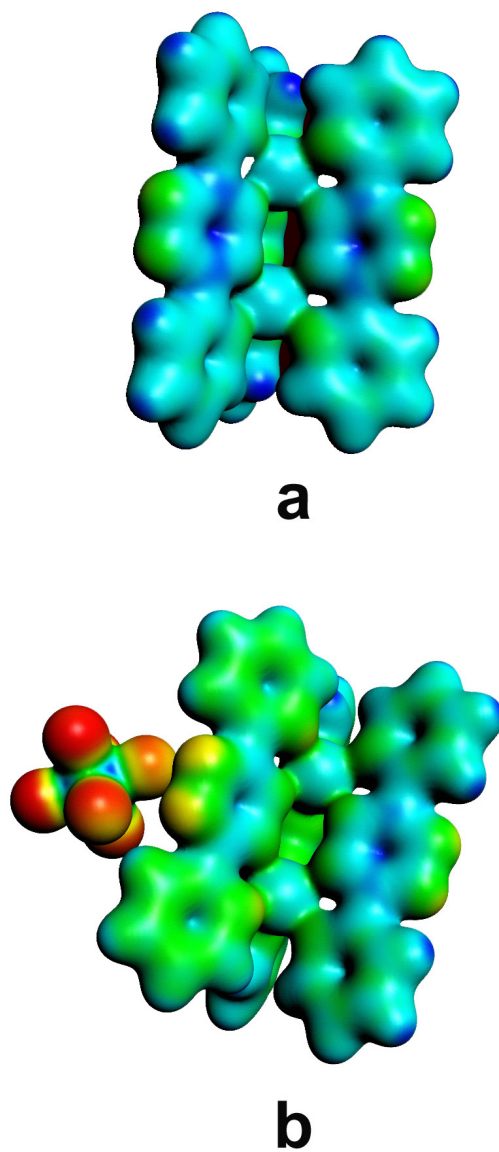


Figure 76: Electrostatic potential map from the BP86/TZP SPE for **17b** (a) doubly charged $[\text{Ag}_2(\text{bptz})_3]^{2+}$ with a color scale of 220 (blue) to -31 (red) kcal/mol, and (b) singly charged cation $\{[\text{Ag}_2(\text{bptz})_3][\text{SbF}_6]\}^+$ with a color scale of 188 (blue) to -31 (red) kcal/mol. The maps were generated with ADFView¹²⁵ at a 0.02 isodensity value.

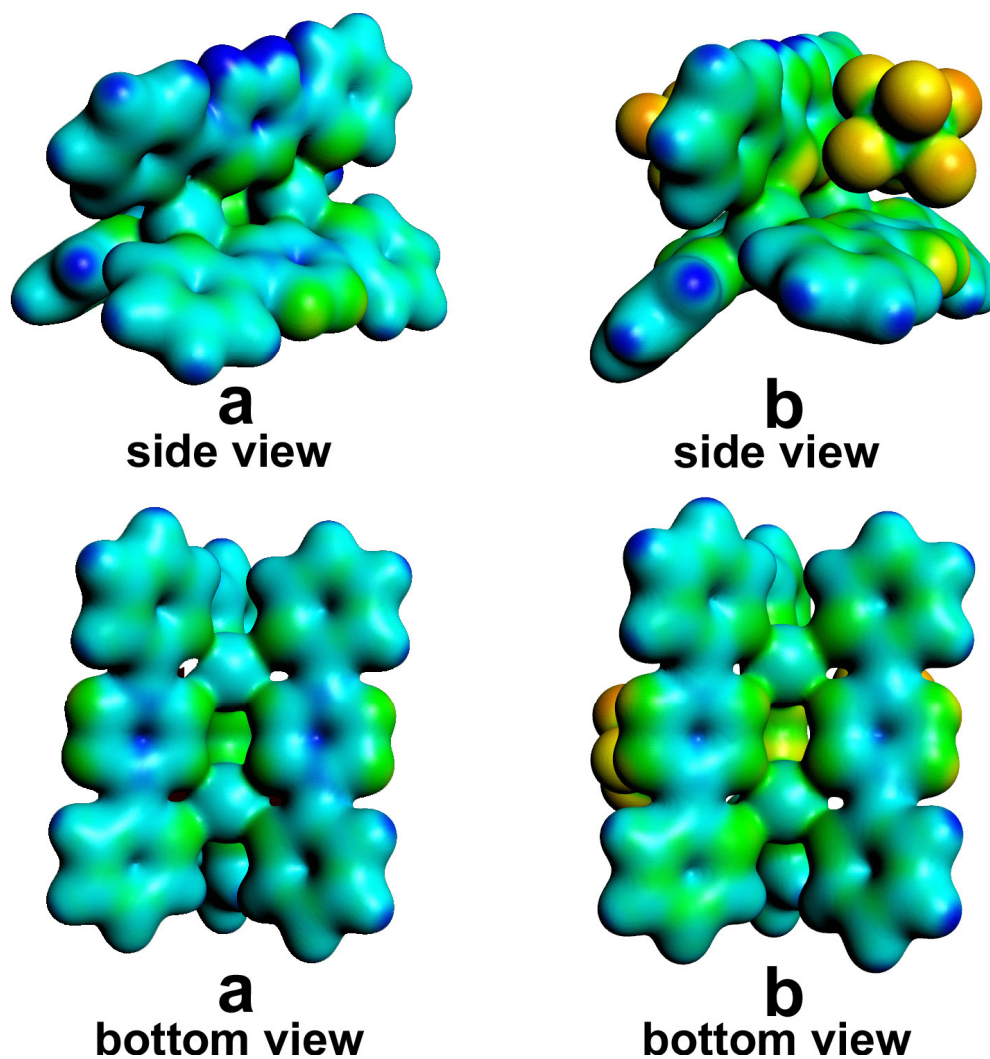


Figure 77: Electrostatic potential map from the BP86/TZP SPE calculations for **16** (a) doubly charged cation $[Ag_2(bptz)_3]^{2+}$ with a color scale of 200 (blue) to -31 (red) kcal/mol, and (b) neutral complex $[Ag_2(bptz)_3][AsF_6]_2$ with a color scale of 126 (blue) to -94 (red) kcal/mol. The maps were generated with ADFView¹²⁵ at a 0.02 isodensity value.

In contrast to the propeller-type complex **17b**, wherein only one $[\text{SbF}_6]^-$ anion is in proximity with each tetrazine ring in the crystal structure (*vide supra*: Figure 62), in **16**, both $[\text{AsF}_6]^-$ anions are close to tetrazine rings (Figure 59b). Thus, single point energy (SPE) calculations of the neutral complex $[\text{Ag}_2(\text{bptz})_3][\text{AsF}_6]_2$ were undertaken. The color scales for the dication and the neutral species in Figure 77 were adjusted to be the same for the pyridyl rings; therefore direct color comparison between them is meaningful. In the neutral complex **16**, the positive charge density on all the central tetrazine rings has decreased (Figure 77b, bottom view), as compared to the doubly charged species (Figure 77a, bottom view), due to flow of electronic charge from the anions to the π -acidic rings in proximity to them (each anion interacts with two tetrazine rings from one cationic unit; Figure 59b). These findings corroborate the presence of anion- π interaction between the $[\text{AsF}_6]^-$ anions and the bptz tetrazine rings.¹²⁶ The decrease in the electropositive character of the tetrazine ring in the upper bptz ring of the neutral complex (Figure 77b, side view), however, is more appreciable than in the other two tetrazine rings (Figure 77b, bottom view), in spite of the former being more electropositive than the latter two in the doubly charged species. This difference is attributed to two anions interacting with the upper tetrazine ring as compared to one anion per ring for the two lower rings (Figure 77b, side view). The fact that the changes in the electron density maps between the dication and the neutral species for the propeller-type complex **16** (Figure 77) follow the same trends as those in **17b**, which is a propeller-type compound with more symmetric structural characteristics (Figure 76), indicates that the anion- π interactions claimed for **16** based on the electrostatic potential maps, are indeed viable.

As a representative of the bppn grid-type complexes, the cationic unit $[\text{Ag}_4(\text{bppn})_4]^{4+}$ (Figure 78a), as well as the neutral complex $[\text{Ag}_4(\text{bppn})_4][\text{AsF}_6]_4$ (**19**) (Figure 78b), were subjected to SPE calculations. In the cationic unit $[\text{Ag}_4(\text{bppn})_4]^{4+}$, the slightly larger difference in the charge between the central and outer rings (Figure 78a), as compared to that of free bppn (Figures 72d and 73d), can be attributed to an induced positive charge on the central pyridazine ring due to the Ag(I) cation binding. This difference in electron density between the central and outer rings of the bppn ligands in the cationic complex, however, is still much less than the difference between the tetrazine and pyridyl rings of free bptz (Figures 72c and 73c). Additionally, the change in electropositive character of the central rings of the bppn ligands in the cationic unit $[\text{Ag}_4(\text{bppn})_4]^{4+}$ is very small upon addition of the $[\text{AsF}_6]^-$ anions (Figures 78a, b; the color scales for the outer pyridyl rings were adjusted to be the same, therefore direct color comparison between the cationic and neutral species is possible), which indicates the negligible flow of electron density from the anion to the pyridazine ring in the neutral complex. These results concur with a more electron-rich bppn central pyridazine ring and, thus, much weaker anion- π interactions in **19** as compared to those established in the bptz complexes **15**, **16** and **17b**.

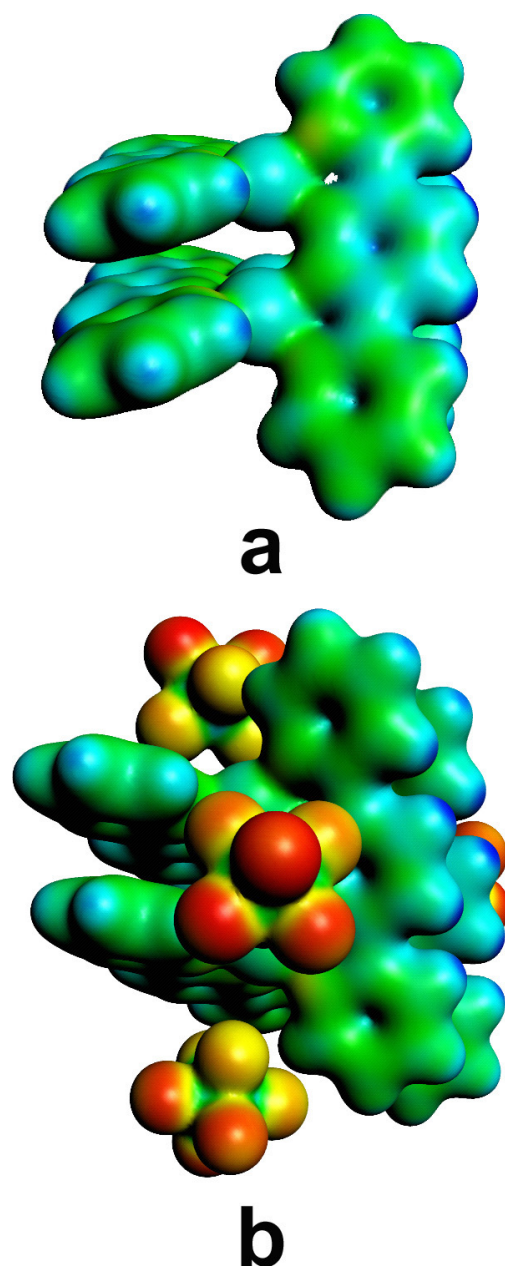


Figure 78. Electrostatic potential map from the BP86/TZP SPE calculations of **19** for (a) cationic unit $[\text{Ag}_4(\text{bppn})_4]^{4+}$ with a color scale of 314 (blue) to -126 (red) kcal/mol, and (b) neutral complex $[\text{Ag}_4(\text{bppn})_4][\text{AsF}_6]_4$ with a color scale of 157 (blue) to -63 (red) kcal/mol. The maps were generated with ADFView¹²⁵ at a 0.02 isodensity value.

It is notable in **19** that the *syn* orientation of the bound bppn ligand is different from the optimized geometry of the free ligand. In the free bppn ligand the N-C-C-N dihedral angles are in the range -84.6 to -85.9° (Figures 72d, 73d; atoms labeled with red numbers), whereas in structures **18-21**, the corresponding N-C-C-N dihedral angles range from -17.7 to -22.3° . As mentioned earlier, however, the ligand conformation appears to have little effect on the electrostatic potential maps.

IV. Discussion

A. Effect of Anion Identity and Anion- π Interactions on the Products

The reactions of bptz with the appropriate Ag(I)X salts ($X = [\text{PF}_6]^-$, $[\text{AsF}_6]^-$, $[\text{SbF}_6]^-$) afford complexes of three different structural types depending on the experimental conditions and the anion used. Reactions of Ag(I):bptz, in a 1:1 ratio, in the presence of $[\text{PF}_6]^-$ ions, afford either the polymer **13** or the discrete molecular compound **14** (more concentrated solutions favor the polymer), whereas in the presence of $[\text{AsF}_6]^-$ ions, the reaction produces only the dinuclear product **15**. When the ratio of Ag(I):bptz is 2:3, the propeller-type compound $[\text{Ag}_2(\text{bptz})_3][\text{AsF}_6]_2$ (**16**) is formed in high yield in the presence of the $[\text{AsF}_6]^-$ ions, but not in the presence of $[\text{PF}_6]^-$ ions. At a $[\text{AgPF}_6]:\text{bptz}$ ratio of 2:3, only the polymer **13** or the dimer **14** are obtained in low yields (depending on the concentrations of the initial solutions). Reactions of Ag(I):bptz in a 1:1 ratio in the presence of $[\text{SbF}_6]^-$ ions, however, yield the propeller-type compounds **17a** and **17b**, as indicated by the single crystal X-ray structural determinations. When the reaction is performed in a $[\text{AgSbF}_6]:\text{bptz}$ ratio of 2:3, no crystals are obtained, but the propeller-type species $[\text{Ag}_2(\text{bptz})_3]^{2+}$ is formed as suggested by an ESI-MS spectrum of the reaction solution (ion peaks are observed at m/z 923 and 462 corresponding to the singly and doubly charged species

$[\text{Ag}_2(\text{bptz})_3 - \text{H}]^+$ and $[\text{Ag}_2(\text{bptz})_3]^{2+}$, respectively). Attempts to react AgBF_4 with bptz in a 1:1 ratio leads to immediate precipitation of an insoluble product. Dissolution of the solid after prolonged heating and layering with toluene affords crystals of the previously reported compound $\{[\text{Ag}(\mu\text{-bptz})(\text{bptz})][\text{BF}_4]\}_n$.¹⁰²

Apart from the anion size (the size of the anions increases in the order $[\text{PF}_6]^- < [\text{AsF}_6]^- < [\text{SbF}_6]^-$),¹²⁷ which plays a role in the packing of the resulting structures, anion- π interactions appear to be a dictating factor in determining the preferred structural motif. This conclusion is corroborated by the fact that reactions of bptz with the Ag(I)X salts ($X = [\text{PF}_6]^-$, $[\text{AsF}_6]^-$, $[\text{SbF}_6]^-$, $[\text{BF}_4]^-$) in a 1:1 ratio lead only to the grid-type structures **18-21**, regardless of the anion present. Even when the reactions are performed with a Ag(I):bptz ratio 2:3, no propeller-type compounds are obtained with this ligand. Despite the different shapes and sizes of the various anions, all the bptz structures adopt the grid motif, which is stabilized by intramolecular π - π stacking interactions between the bptz aromatic rings.

B. Solid State Evidence for Anion- π Interactions

Compound **13** is a 1D polymer, whereas compounds **14-17b** consist of discrete molecular units. In **13**, the bptz units are in the *anti* orientation (Figure 49), which is necessary for the formation of the polymer, whereas the bptz units in **14-17b** are in the *syn* orientation (Figures 52, 53, 56, 57, and 60). Bptz ligands in the *anti* orientation were also observed in the recently reported 1D polymers $\{[\text{Ag}(\mu\text{-bptz})(\text{bptz})][\text{BF}_4]\}_n$ ¹⁰² and $[\text{Cd}(\mu\text{-bptz})(\text{NO}_3)_2]_n$.¹²⁸ The metals are six-coordinate in both the latter cases, in contrast to the square planar geometry of the Ag(I) ions in **13**. Compounds **14** and **15** are 1:1 isomorphous Ag(I):bptz complexes

consisting of dinuclear cationic units $[\text{Ag}_2(\text{bptz})_2(\text{CH}_3\text{CN})_2]^{2+}$ (Figures 52 and 53) similar to that in $[\text{Ag}_2(\text{bptz})_2][\text{CF}_3\text{SO}_3]_2$ ^{102,103} with the exception that the Ag(I) ions are in a five-coordinate square pyramidal geometry instead of being square planar. The previously mentioned bptz cationic units in **14** and **15** are favored over the [2 x 2] grids encountered in the cations $[\text{Ag}_4(\text{bppn})_4]^{4+}$ of the bppn compounds **18-21** as well as in $[\text{Cu}_4(\text{bppn})_4][\text{CF}_3\text{SO}_3]_4$ ¹⁰⁴ grid-like structures were predicted by Constable et al., to result from reactions of Ag(I) salts ($X = [\text{BF}_4]^-$, $[\text{NO}_3]^-$, or $[\text{CF}_3\text{SO}_3]^-$) with bptz, but the products are, in fact, dinuclear.¹⁰² The formation of the dinuclear cations in **14** and **15**, instead of grids, is attributed to the favorable anion- π interactions established between the anions and the π -acidic central tetrazine ring of bptz.

In the propeller-type compounds **16** and **17a**, three bptz ligands span two Ag(I) ions in the *syn* orientation (Figures 56 and 57) with the anions being situated in the folds of the cations (Figure 58); each anion establishes anion- π interactions with three tetrazine rings (Figure 53). Likewise, in the reported 2D sheet-like structure of $\{[\text{Ag}_2(\text{dpztz})_3][\text{SbF}_6]_2\}_\infty$ ⁹⁶ (dpztz: 3,6-di-pyrazin-2-yl-(1,2,4,5)-tetrazine), each $[\text{SbF}_6]^-$ anion interacts with three tetrazine rings at $\text{F}\cdots\text{ring}$ distances in the range 2.764-3.111 Å. In **17b**, the $[\text{SbF}_6]^-$ anion that is participating in the anion- π interactions is surrounded by six tetrazine rings, each F atom facing a ring at a crystallographically unique distance of 2.844 Å from the ring plane (Figure 62). To our knowledge, complex **17b** represents the first crystallographic example of an anion- π_6 system with six anion- π interactions per participating anion. Precedent of an anion establishing anion- π interactions with four or five electron-deficient tetrazine rings was obtained from the crystal structures of the molecular Ni(II) and

Zn(II) squares or the Ni(II) pentagon, respectively, with the anion encapsulated in the cavity.^{48,49}

Unlike compounds **13-17a**, wherein only the pyridyl rings of bptz participate in π - π intermolecular stacking interactions, in **17b**, all the bptz rings engage in such interactions. The structural features of compounds **17a** and **17b** render them good candidates to estimate the strength of anion- π interactions. Compound **17b** is the only bptz complex in which the central tetrazine ring of bptz participates in π - π stacking interactions. Apart from π - π stacking interactions, the central tetrazine ring of bptz in **17b** establishes anion- π interactions on the other side of the ring (Figure 62), whereas in **17a** it is participating only in anion- π interactions on both sides of the ring (Figure 59). Based on the fact that one cannot favor the crystallization of **17a** over **17b** and vice versa, it may be claimed that the two compounds have approximately the same overall energy, which suggests that the strength of the anion- π interactions in these compounds is comparable to that of π - π stacking (1-50 kJ/mol).¹²⁹ For purposes of comparison, the interacting energies obtained by Frontera et al.²³ for *s*-tetrazine with [Cl]⁻ and [Br]⁻ anions, and by Mascari et al.^{12a} for *s*-triazine with anions are less than 42 kJ/mol.

Compounds **18-21** form Ag(I) [2 x 2] square grids consisting of discrete [Ag₄(bppn)₄]⁴⁺ cationic units (Figures 63, 64, 65, 68) similar to those encountered in [Cu₄(bppn)₄][CF₃SO₃]₄,¹⁰⁴ instead of dinuclear or propeller-type structures. A [2 x 3] rectangular mixed-ligand Ag(I) grid, as well as the square [2 x 2] grid [Ag₄(Me₂-bppn)₄]⁴⁺, were obtained with the bis-methyl substituted form of bppn.⁹⁵ The recently reported salt [Ag(bppn)₂][CF₃SO₃] is not a grid-type compound, however, and no anion- π interactions are present; instead there is extensive π - π stacking

between all the rings of the coplanar ligands within the dinuclear unit as well as between dinuclear units of the arrays.¹⁰⁶ Likewise, in compounds **18-21**, the three rings of bppn, including the central pyridazine ring, participate in intramolecular π - π stacking interactions within the grids (Figure 66a, b), with the anion- π interactions being weaker and secondary to the structure formation. On the contrary, in **13-17b**, there are no intramolecular π - π interactions; in **13-17a**, intermolecular π - π stacking is established only between the bptz outer pyridyl rings. Instead, the highly π -acidic central tetrazine rings in **13-17a** prefer to engage in multiple anion- π interactions. In compounds **13-17a**, each anion establishes anion- π interactions with several tetrazine rings (Table 8) and each central tetrazine ring interacts with two different anions positioned on either side of the ring (Figures 51, 52, and 58). Moreover, as mentioned earlier, in **17b**, one of the two $[\text{SbF}_6]^-$ anions present in the molecule participates in anion- π interactions with six tetrazine rings (Figure 62; Table 8). In compounds **18-20**, however, only one anion- π interaction is established per pyridazine ring (the opposite side of the pyridazine ring is involved in π - π stacking) and each anion interacts with one ring only (Figure 66a, c; in **21**, only three out of the four pyridazine rings of each grid interact with a $[\text{BF}_4]^-$ ion). The multiple anion- π interactions per anion established in the case of the bptz complexes (as compared to one per anion in the bppn complexes) and the difference in the preferred structural motifs between the bptz and bppn structures are in accord with the higher π -acidic character of the bptz central tetrazine ring as compared to the more electron-rich bppn pyridazine ring.

Favorable anion- π interactions exist between the anions and the tetrazine rings in the previously reported compounds $\{[\text{Ag}(\mu\text{-bptz})(\text{bptz})][\text{BF}_4]\}_n$ ¹⁰² (one per anion; F \cdots tetrazine ring plane 2.98 Å) and $\{[\text{Ag}_2(\text{dpztz})_3][\text{SbF}_6]_2\}_\infty$ ⁹⁶ (three per $[\text{SbF}_6]^-$ anion; F \cdots tetrazine ring plane 2.7-3.1 Å) and the F \cdots tetrazine distances are in the same range as those for the Ag(I)-bptz structures reported herein. The F \cdots tetrazine ring (plane) distances (for the F atoms facing the rings) in the Ag(I)-bptz compounds **13-17b** are in the range 2.7-3.1 Å, whereas the F \cdots pyridazine ring distances in the Ag(I)-bppn compounds **18-21** are in the range 2.9-3.3 Å (a non-bonded anion- π contact is considered to be present when the distance between the anion and the π -ring is less than the sum of the van der Waals radii, according to Frontera et al.¹³⁰). The distances of the anion F atoms facing the central ring (from the central ring plane) in the bppn compounds **18-21** are, in general, longer by 0.15-0.20 Å as compared to those encountered in the bptz structures **13-17b**, except for **19** (Table 8 the shorter distance in **19** may be attributed to the disorder of the $[\text{AsF}_6]^-$ anion, which reduces the average degree of interaction between the anion and the pyridazine ring). Since it is logically anticipated that longer anion- π distances correlate with weaker interactions of this type,¹³⁰ the 0.15-0.20 Å difference in the F \cdots central ring distances between the bptz and bppn complexes reflects the stronger anion- π interactions involved in the bptz complexes. The 0.15-0.20 Å difference in the F \cdots central ring distances between the bptz and bppn complexes is comparable to that in the calculated distances between the fluorinated F₃triazine + halogen and triazine + halogen systems (and the same anion) reported by Mascàl *et al.*,^{12b} the energies of the (more π -acidic) F₃triazine systems with the shorter anion- π

interactions are twice as low as the energies of the triazine systems).^{12b} Furthermore, stronger anion- π interactions in the bptz as compared to bppn complexes can be argued based on the multiple (between two to six) tetrazine rings participating in anion- π interactions per anion in the bptz complexes **13-17b**, in contrast to only one pyridazine ring interacting per anion in the bppn complexes 18-21 (Table 8). The additivity of anion- π interactions was recently reported by Frontera et al.;³² the binding energies obtained from *ab initio* studies, performed on complexes of halide ions ($[\text{Cl}]^-$, $[\text{Br}]^-$) interacting with two (or three) trifluoro *s*-triazine (or *s*-triazine) rings, are approximately two (or three) times the binding energy of the corresponding complex with only one ring interacting with the anion.³²

Table 8: Anion- π and π - π Distances for the Central Rings in Compounds **13-21**.

Bptz Complexes					
Compound	Anion involved	Rings per anion ^a	F distance range (Å) ^c	shortest F-centroid distance (Å)	π - π distance between tetrazine rings (Å)
13	[PF ₆] ⁻	2	2.785-2.968	2.840(5)	^d
14	[PF ₆] ⁻	2	2.791-3.045	2.806(7)	^d
15	[AsF ₆] ⁻	2	2.758-3.142	2.784(6)	^d
16	[AsF ₆] ⁻	3	2.783-3.111	2.913(2)	^d
17a	[SbF ₆] ⁻	3	2.743-3.004	2.913(6)	^d
17b	[SbF ₆] ⁻	6 ^b	2.844	3.265(3)	3.36

Bppn Complexes					
Compound	Anion involved	Rings per anion ^e	F distance range (Å) ^g	shortest F-centroid distance (Å)	π - π distance between pyridazine rings (Å) ^h
18	[PF ₆] ⁻	1	2.902-3.181	3.095(6)	3.38
19	[AsF ₆] ⁻	1	2.780-3.092	3.096(3)	3.38
20	[SbF ₆] ⁻	1	2.937-3.033	3.260(5)	3.33
21	[BF ₄] ⁻	1 ^f	2.835-3.261	2.90(4)	3.53

^aNumber of tetrazine rings involved in anion- π interactions with each anion.

^bOnly one of the two anions per molecule participates in anion- π interactions.

^cF-tetrazine plane distances.

^dNo π - π interactions established.

^eNumber of pyridazine rings involved in anion- π interactions with each anion.

^fOnly three of the four anions per molecule participate in anion- π interactions.

^gF-pyridazine plane distances.

^hIntramolecular interactions.

C. Theoretical Evidence of Anion- π Interactions

B3LYP/6-311+G(d,p) and BP86/TZP geometry optimizations and electrostatic potential calculations indicate that bptz is more likely to participate in anion- π interactions than bppn (Figures 73 and 74). In both ligands, the central rings display a more electropositive area compared to the outer pyridyl rings, but due to the four electron-withdrawing nitrogen atoms on the central ring of bptz compared to two in bppn, a significantly more electropositive area is observed in the bptz central tetrazine ring. An enhancement of the positive charge in the ring with the higher number of electronegative atoms, comparable to that between the bptz and the bppn central rings, has been observed between trifluoro-1,3,5-triazine and 1,3,5-triazine^{12a} as well as between C₆F₆ and benzene.^{12b} The relatively higher positive charge and the higher polarization²³ of the bptz central tetrazine ring (Figures 72a, c and 73a, c) suggest that bptz is likely to participate in stronger anion- π interactions as compared to bppn. This is corroborated by *ab initio* calculations on the *s*-tetrazine ring indicating that it is a good candidate for establishing favorable anion- π interactions. On the other hand,²³ the weaker polarization of the bppn central pyridazine ring, indicated by the charge distribution in the electrostatic potential maps (Figures 72b, d and 73b, d), suggests that it will participate in weaker anion- π interactions.

The SPE calculations for the dicationic units of the Ag(I)-bptz complexes **15** (Figure 74a), **16** (Figure 77a), and **17b** (Figure 76a) reveal the expected positive charge accumulation in the central tetrazine rings of the three bptz ligands. In their electrostatic potential maps, the difference in the color intensities between the central tetrazine and the outer pyridyl rings of the complex bptz ligands (Figures 74a, 76a, 77a) is comparable to the difference in free bptz (Figures 72a, c and 73a, c). In the

electrostatic potential map of the singly charged cationic unit $\{[\text{Ag}_2(\text{bptz})_2(\text{CH}_3\text{CN})_2][\text{AsF}_6]\}^+$ of **15** (Figure 75), this difference is also comparable to that in free bptz for the distal bptz ligands from the anion. In the electrostatic potential maps of the neutral bptz complexes **15** and **16** (Figures 74b and 77b), and in the singly charged cationic units of **15** (Figure 75 bottom view) and **17b** (Figure 76b), however, the difference in the color intensities between the central tetrazine and the outer pyridyl rings in the bptz ligands in proximity to the anions decreases considerably compared to the free ligand (Figures 72a, c and 73a, c). In the same vein, when the electrostatic map colors are adjusted properly, the F atoms closest to the tetrazine ring are less electronegative than the distal ones to the bptz moieties (Figures 75 side view and 76b). Additionally, in the electrostatic potential maps of the neutral bptz complexes **15**, **16** (Figures 74b and 77b), and in the singly charged cationic units of **15** (Figure 75 bottom view) and **17b** (Figure 76b), a reduction of the electropositive character on the tetrazine rings closest to the anions is evident. Particularly in the case of the neutral complex **16**, the decrease in the electropositive character of the tetrazine ring sandwiched between the two anions (Figure 77b, side view; upper ring), is more appreciable than in the other two tetrazine rings (Figure 77b, bottom view), due to two anions interacting with the upper tetrazine ring as compared to one anion per ring for the two lower rings (Figure 77b, side view). These observations strongly suggest a flow of electronic charge from the anions to the π -acidic rings (supported by previous reports that an increase in the aromaticity of the ring is observed upon interaction with the anion)³⁰ and provide unambiguous computational evidence that favorable anion- π interactions are established between the anions and the bptz tetrazine rings in **15**, **16**, and **17b**. A notable observation

about the dicationic unit $[\text{Ag}_2(\text{bptz})_3]^{2+}$ in **16** is that one of the bptz ligands is more electropositive than the other two (upper ring; Figure 77a, side view); the more electropositive central tetrazine ring is the one closest to the $[\text{AsF}_6]^-$ anions in the crystal structure of $[\text{Ag}_2(\text{bptz})_2(\text{CH}_3\text{CN})_2][\text{AsF}_6]_2$ (Figure 59a), which implies that stronger anion- π interactions are established with higher π -acidity rings.¹²

The lack of an appreciable electropositive character in the central pyridazine ring of bppn (Figures 72b, d and 73b, d) renders it less likely to participate in anion- π interactions as compared to bptz. The more electron-rich bppn central pyridazine ring is retained even after binding to Ag(I) ions, as indicated by the electrostatic potential map of the cationic unit $[\text{Ag}_4(\text{bppn})_4]^{4+}$ (Figure 78a). The negligible difference in electropositive character between the central and outer rings of bppn in free bppn and in the cationic unit $[\text{Ag}_4(\text{bppn})_4]^{4+}$ upon addition of the $[\text{AsF}_6]^-$ anions (Figure 78b), concurs with the preference of bppn for grid-type structures such as in **9** wherein the π - π stacking interactions of bppn are maximized (e.g., Figure 66a, b for **18**) at the expense of anion- π interactions. Since the change in electropositive character of the central rings of the bppn ligands in the cationic unit $[\text{Ag}_4(\text{bppn})_4]^{4+}$ is negligible upon addition of the $[\text{AsF}_6]^-$ anions, the anion- π interactions present in complexes **18-21** are expected to be weaker than those in the bptz complexes **13-17b**. The fact that for all the neutral Ag(I)-bptz complexes studied, the difference in the color intensities (and thus of the electron densities) between the central tetrazine ring of the complexes and that of the corresponding dication (in the absence of anions) is greater than the corresponding color difference between the central pyridazine rings of the neutral Ag(I)-bppn complexes and that of the corresponding dication, suggests that stronger anion- π interactions are established in the case of the bptz complexes.

The strength of the anion- π interactions has been correlated to the magnitude of the permanent quadrupole moment ($Q_{zz} = 10.70, -4.922$ and -7.99 Buckingham for *s*-tetrazine, pyridazine and benzene, respectively)¹³¹ and the molecular polarizability (*ab initio* calculations on the *s*-tetrazine ring with $[F]^-$ ions demonstrate the significant contribution of the polarization term to the total binding energy of the anion- π interaction, which is consistent with the high polarizability of the *s*-tetrazine ring, $\alpha_{||} = 58.7$ a.u.²³) of the π -system.^{25,27,30} The larger quadrupole moment of the bptz central rings as compared to bppn results in stronger anion- π interactions for the bptz complexes, which is corroborated by the shorter F \cdots central ring⁴² as well as the presence of multiple anion- π interactions per anion³² in the bptz complexes **13-17b** (Table 8).³²

V. Conclusions

In summary, we have undertaken a tandem crystallographic and computational investigation of the effect of anion- π interactions on the preferred structural motifs of Ag(I) complexes containing π -acidic aromatic rings. The higher π -acidic character of the bptz tetrazine ring as compared to the more electron-rich bppn pyridazine ring, suggested by the electrostatic potential maps of the free ligands, renders bptz more likely to participate in anion- π rather than π - π interactions. This preference is reflected in the resulting structural motifs of the Ag(I)-bptz complexes (polymers, planar dinuclear or propeller-type dinuclear, depending on the anion) versus grid-type structures for the Ag(I)-bppn compounds, regardless of the anion. In the Ag(I)-bptz compounds **13-17b**, multiple and shorter (thus stronger) anion- π interactions are established between the anions and the

central tetrazine rings, whereas in the grids **18-21**, intramolecular π - π interactions are maximized at the expense of anion- π interactions. The solid-state evidence of stronger anion- π interactions in the bptz complexes is supported by the results of DFT calculations (B3LYP/6-311+G(d,p) and BP86/TZP). The electrostatic potential maps of the Ag(I)-bptz species of **15**, **16**, and **17b** suggest a flow of electronic charge from the anions to their proximal π -acidic rings and the establishment of anion- π interactions between the anions and the bptz tetrazine rings. On the other hand, the small difference in electropositive character between the central and outer rings of bppn in the free ligand and the cationic unit $[\text{Ag}_4(\text{bppn})_4]^{4+}$ of the grid-type complex **19** suggests relatively weak anion- π interactions between the bppn central rings and the anions. Further studies on similar systems are underway to gain additional insight into the nature of anion- π interactions with multiatomic anions, their interplay with π - π interactions, and the extent to which they influence the outcome of self-assembly reactions.

CHAPTER IV
COMPUTATIONAL INVESTIGATIONS OF ANION- π
INTERACTIONS BETWEEN TETRAHEDRAL AND OCTAHEDRAL
ANIONS AND, $C_3N_3X_3$, $C_2N_4X_2$, and $C_4X_4N_2$ (X = Br, Cl, F, or CN)
RING SYSTEM

I. Introduction

Investigations of supramolecular interactions are exceedingly difficult due to the weak, cooperative effect these interactions exert on self-assembled structures. The cooperativity of multiple self-assembly factors provides numerous complications when attempting to experimentally evaluate these factors one at a time. Theoretical studies, however, afford a convenient companion to experimental studies when used in the context of a comparative tool. Currently, many supramolecular interactions have been successfully modeled by theoretical methods including hydrogen bonds,¹³² cation- π interactions,¹³³ as well as the focus of this study, anion- π interactions.^{12,21,23,25,26,27,30,32}

Recent studies in our group have revealed multiple coordination complexes that depend on anion- π interactions in order to form,^{83,89,134} with several other laboratories also noting this interaction in their structures as well. Our group recently published an experimental study that examined the impact anion- π interactions have on the formation of coordination compounds that included π -acidic ring systems (see Chapter III).¹³⁴ Despite the success of this study, it was difficult to relate many of these structures to the calculations already performed on anion- π interactions. The use of Ag(I) salts in the synthesis of the compounds precluded the use of halide

counterions, the anions that have been so thoroughly studied in computational papers; instead the complex anions $[\text{BF}_4]^-$, $[\text{PF}_6]^-$, $[\text{AsF}_6]^-$, and $[\text{SbF}_6]^-$ were employed to yield crystalline materials. While multiple theoretical studies on the geometry, equilibrium distances, and additivity of anion- π interactions with halides and $[\text{NO}_3]^-$ anions have been performed, none involving tetrahedral or octahedral anions have been considered to date.

The reasons for this deficiency lie in the inherent difficulty of studying anion- π interactions in a setting that requires optimized geometries. Anions have a propensity for hydrogen bonding, a much stronger secondary interaction than most supramolecular forces, and lead to optimized structures that maximize hydrogen-anion contacts with the ring. To avoid this problem, most studies employ symmetry constraints on the system to keep the anions centered over the aromatic rings. This is an acceptable compromise with spherical halides, but due to the geometry of tetrahedral and octahedral anions, it can be strictly limiting. For example, 1,3,5-trinitrobenzene, which has C_{3h} symmetry, when paired with the tetrahedral $[\text{BF}_4]^-$ anion, can only produce a system with restrained C_{3v} or C_{2v} symmetry. This limits the orientations allowed for the $[\text{BF}_4]^-$ anion, orientations that could lead to better and more realistic anion- π overlap in the molecular orbitals of the system.

In order to fill this gap in the computational literature, we have undertaken a comprehensive computational study to examine anion- π interactions involving complex anions. To avoid hydrogen-bonding interactions without imposing symmetry restraints on the investigated systems, we have only employed ring systems that are devoid of hydrogen atoms. For comparison, all of the rings used in this study have been examined at the MP2¹⁴ and B3LYP^{112,113} levels of theory and

compared to their counterparts with hydrogen atoms through electrostatic potential maps (Figures 79 and 80). By studying these rings with different R groups attached, hydrogen-bonding interactions were avoided, and the effect of increasing π -acidity of the rings under investigation on the strength on anion- π interactions could be examined. By using the appropriate systems, conclusive statements have been made on the effects of the π -acidity of the ring systems, the geometry of the ring systems, and the geometry of the anions on anion- π interactions involving tetrahedral and octahedral complex anions. AIM (Atoms in Molecules) analyses were carried out to help elucidate the strength and position of the interactions, and the results obtained from these computational studies are compared with several structures obtained in Chapters II⁸⁹ and III¹³⁴.

II. Methods and Materials

All of the aromatic ring systems were subjected to full geometry optimizations with a triple- ζ quality basis set that had a diffuse function on the heavy atoms and a polarization function on all the atoms (6-31++G(d',p'))¹¹¹ at the B3LYP [Becke three-parameter exchange functional (B3)¹¹² and the Lee-Yang-Parr correlation functional (LYP)¹¹³] and the MP2¹⁴ levels of theory as implemented in Gaussian 03 (G03).¹¹⁴ All of the single rings with single anion systems were optimized with the same basis set at the same levels of theory, but, due to the large size of both chlorine and bromine, effective core potentials (ECPs) were employed in order to lower the computational cost using the LANL2DZ basis set.¹³⁵ All systems containing only C, H, N, F, B and F atoms were subjected to AIM (Atoms in Molecules)¹⁸ analysis to determine the types and values of critical points present.

Due to the use of ECPs on all systems containing Cl and Br, AIM analysis is not accurate because of the lack of core electron potentials calculated for these atoms.

III. Results

A. π -System Analysis

The first step of this investigation was to examine the π -acidic ring system derivatives of pyridazine, *s*-triazine, and *s*-tetrazine without anions present. Figures 1 and 2 show both the MP2 and B3LYP geometry optimization results and electrostatic potential maps for all the ring systems considered. Although they were not used for the rest of the study, those rings containing hydrogen atoms are presented for the sake of comparison. All of the ESP maps are shown at the same color scale for easy comparison. It can be seen that the π -systems in which the hydrogen atoms are replaced with cyano groups are the most electropositive and most likely to form strong anion- π interactions and possible charge-transfer complexes with anions. The fluorinated derivatives are second in terms of strength, while the chlorine and bromine substituted rings are nearest in electrostatic potential to the hydrogen analogues. It is interesting to note that, when considering the major symmetry axis of the ring plane (the area that the anion is most likely to approach when added to the computation), the symmetry of the ring systems is mirrored in the patterns of their electrostatic potential maps. For instance, in the case of the tetrazine derivatives (bottom rows of Figures 79 and 80), the electropositive character is centered across the ring between the two core carbon atoms, displaying C_2 symmetry central plane axes. In the triazine derivatives, this pattern is three-fold, and spreads to contact all three core carbon atoms of the ring a C_3 axis (second row, Figures 79 and 80).

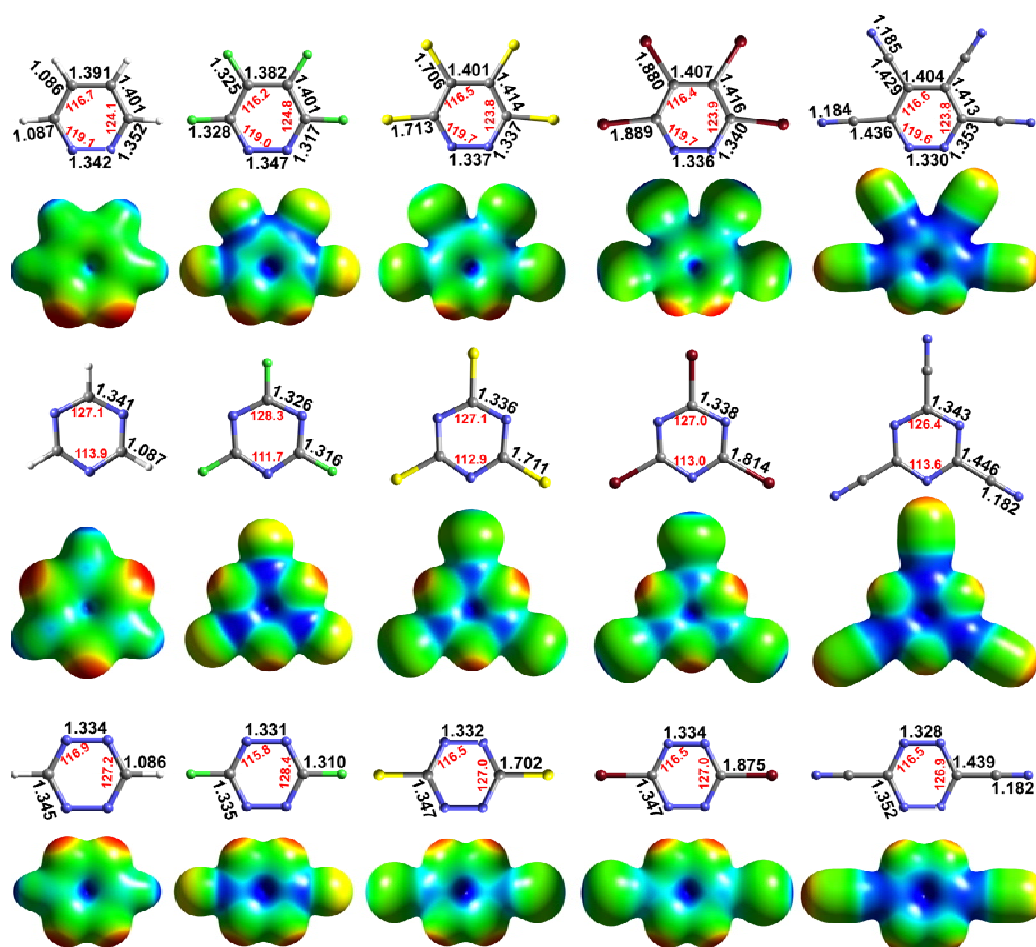


Figure 79: Geometry-optimized MP2/6-31++G(d',p') results of the $C_4N_2X_4$, $C_3N_3X_3$, and $C_2N_4X_2$ systems along with each rings' ESP map. The ESP maps are shown at an isodensity value of 0.02 with a color range of -40.66 kcal/mol (red) – 133.46 kcal/mol (blue). Atom colors are as follows: Carbon = gray, hydrogen = white, nitrogen = blue, fluorine = green, chlorine = yellow, and bromine = red. Theoretical bond distances (Å) and angles (°) are shown in black and red, respectively.

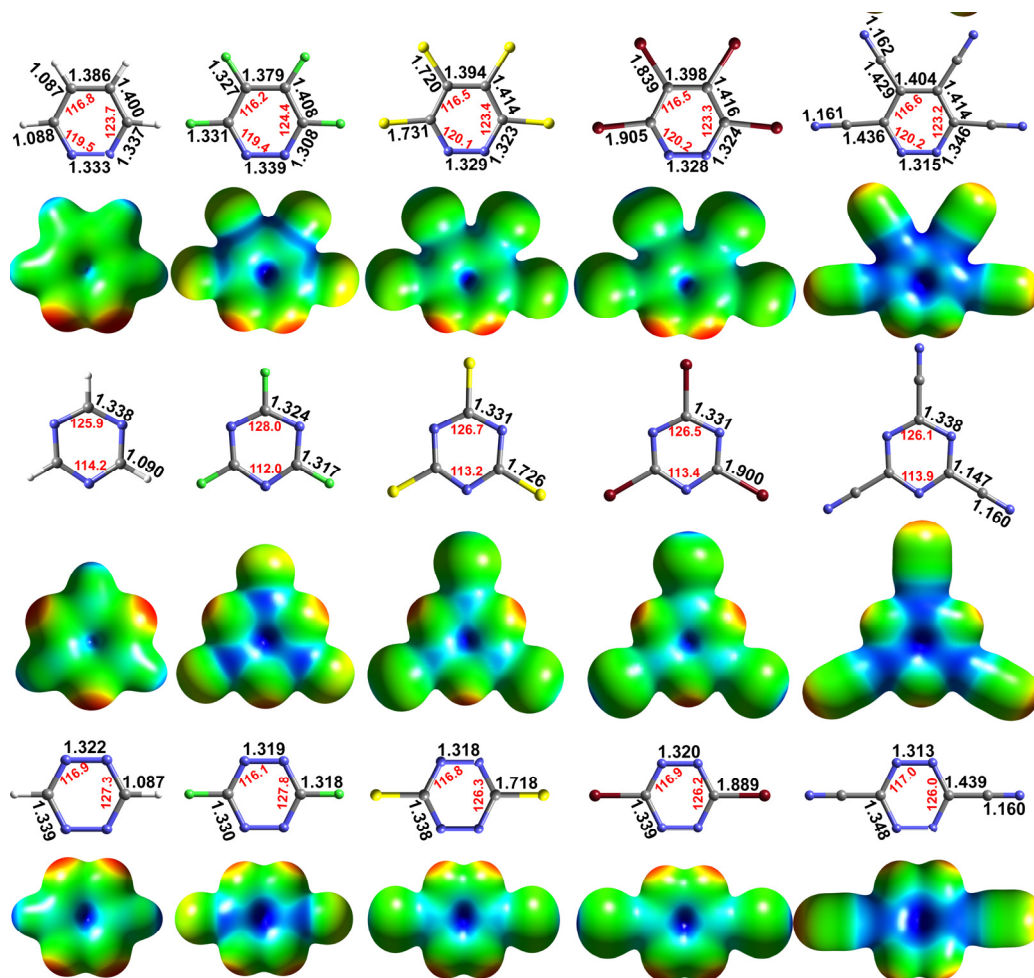


Figure 80: Geometry-optimized B3LYP/6-31++G(d',p') results of the $C_4N_2X_4$, $C_3N_3X_3$, and $C_2N_4X_2$ systems along with each rings' ESP map. The ESP maps are shown at an isodensity value of 0.02 with a color range of -40.66 kcal/mol (red) – 133.46 kcal/mol (blue). Atom colors are as follows: Carbon = gray, hydrogen = white, nitrogen = blue, fluorine = green, chlorine = yellow, and bromine = red. Theoretical bond distances (Å) and angles (°) are shown in black and red, respectively.

The pyridazine rings, which have only a C_1 axis of symmetry perpendicular to the ring plane, have matching areas of electropositive character residing closest to the core carbon atoms of the rings (first row, Figures 79 and 80). These patterns on the ESP maps prove to be important when complex anions are added to the computational geometry optimizations.

B. Computational Analysis of Anion- π Interactions Involving Complex Anions and Ring Systems with Obvious Matching Symmetry

1. $C_3X_3N_3$ Systems with $[BF_4]^-$ and $[PF_6]^-$ – Displayed in Figures 81 and 82 are the MP2 and B3LYP computed geometries of $C_3X_3N_3$ systems interacting with either $[BF_4]^-$ or $[PF_6]^-$. The meaningful bond distances and angles are listed in Table 9. It can be noticed, that, although total system symmetry is evident in the results (especially in the case of $[PF_6]^-$), the anion is positioned over the ring in order to line up three fluorine atoms with the three carbon atoms of the triazine ring to give the interaction a pseudo C_3 central axis. The core ring bonds in all the complexes are shorter than those of the rings optimized alone (Figures 79 and 80 and Tables 9 and 10-Figure 83 describes the bond labels used in the Tables), and the B-F and P-F bond distances of the three anion F atoms participating in anion- π interactions with triazine derivatives are longer than the bond distances of the F anion atoms not participating (See Tables 9 and 10). The corresponding distances between these three fluorine atoms and the carbon atoms, as well as the F-ring centroid and either B- or P-ring centroid distances, are listed in Table 9 along with the interaction energies of each system. In the case of both of the $[BF_4]^-$ and $[PF_6]^-$ systems, the anion resides closer to the ring as the ring substituents become more electronegative.

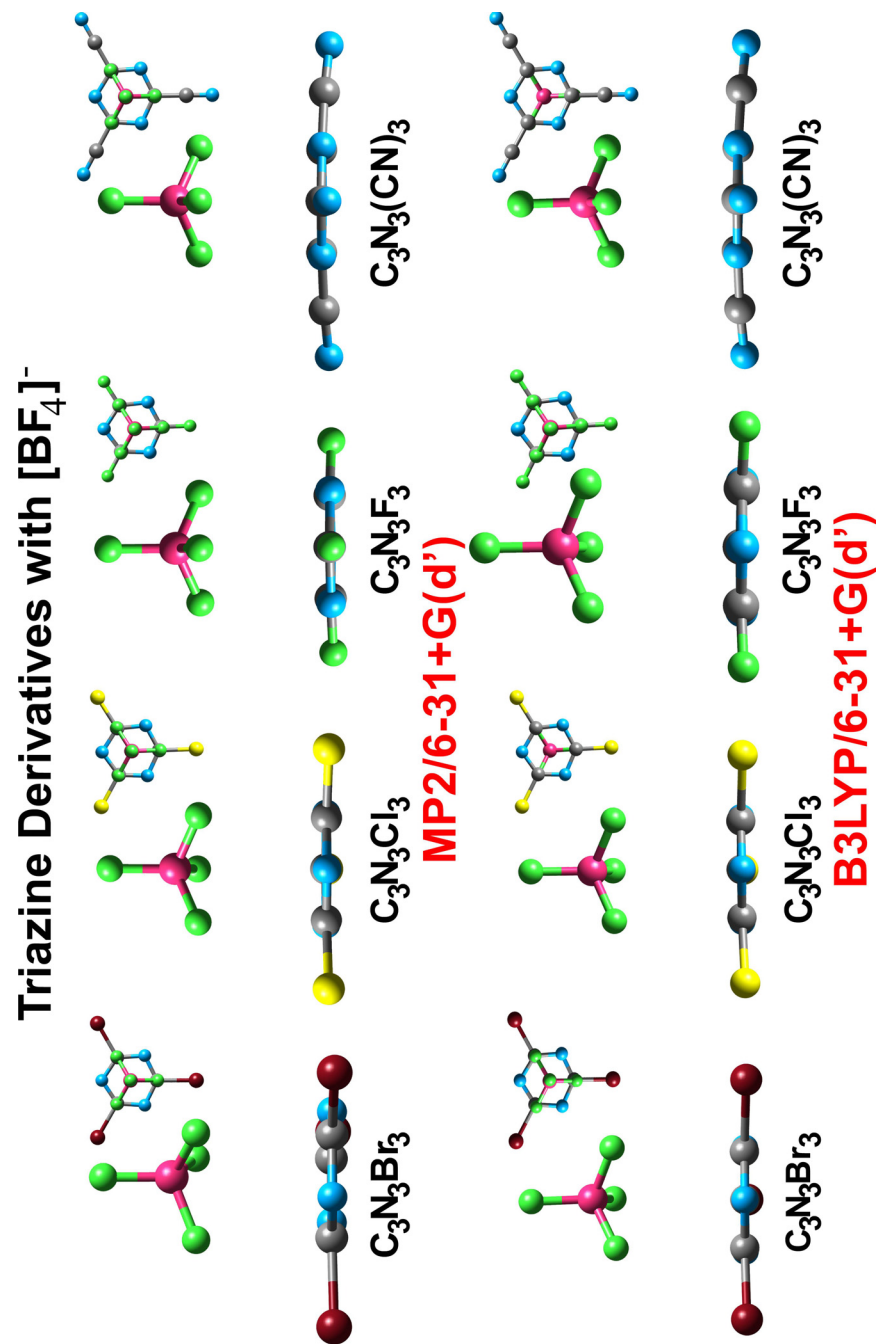


Figure 81: Geometry optimization results of the $\text{C}_3\text{N}_3\text{X}_3$ ring systems with $[\text{BF}_4]^-$ computed by the 6-31++G(d',p') basis set at both the MP2 and B3LYP levels of theory. Colors: C = grey, N = blue, B = pink, F = green, Cl = yellow, and Br = red

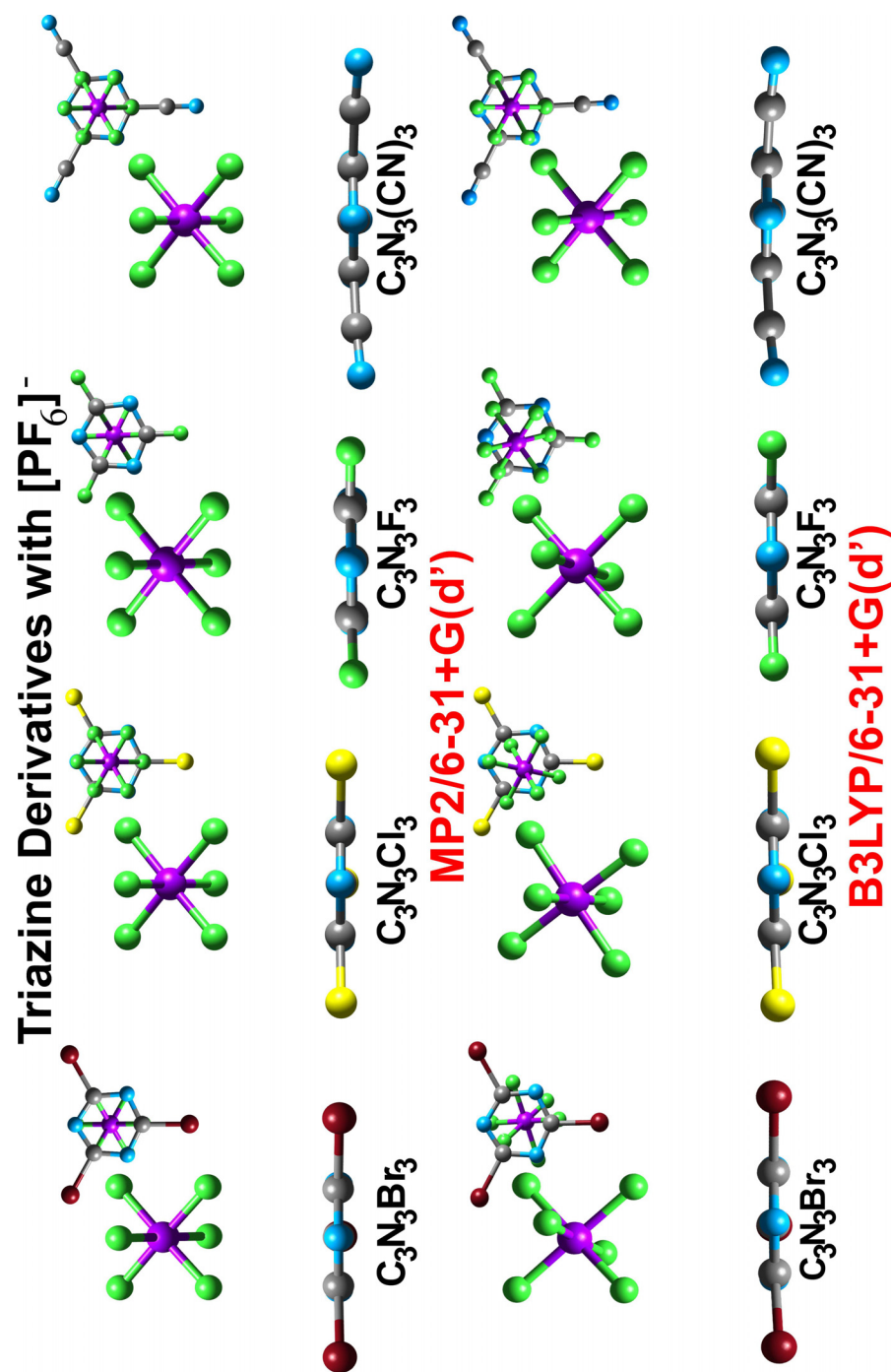


Figure 82: Geometry optimization results of the $\text{C}_3\text{N}_3\text{X}_3$ ring systems with $[\text{PF}_6]^-$ computed by the 6-31++G(d',p') basis set at both the MP2 and B3LYP levels of theory. Colors: C = grey, N = blue, P = purple, F = green, Cl = yellow, and Br = red.

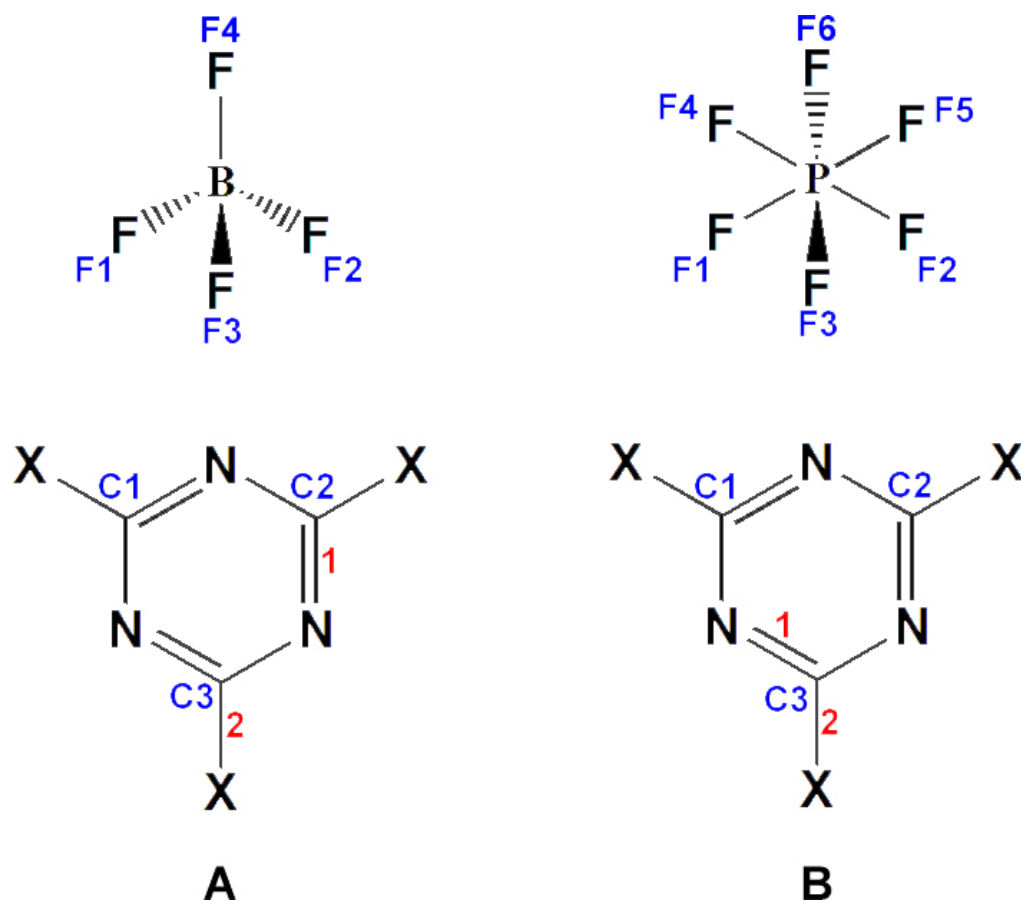


Figure 83: Line diagrams of generic $\text{C}_3\text{N}_3\text{X}_3$ rings with $[\text{BF}_4]^-$ and $[\text{PF}_6]^-$ that assign labels to the values given in Tables 9 and 10. Bond labels are red, and atom labels are blue.

Table 9: MP26-31++G(d') bond distances and binding energies (E_t) for the $C_3N_3F_3$ complexes with $[BF_4]^-$ and $[PF_6]^-$. See Figure 83 for bond and atom labels.

System/MP2	1 (Å)	2 (Å)	B/P-Centroid (Å)	F1-C1 (Å)	F2-C2 (Å)	F3-C3 (Å)	B/P-F 1, 2, 3 (Å)	B-F4/P-F4,5,6 (Å)	E_t (kcal/mol)
$[BF_4]^-$	--	--	--	--	--	--	1.420	1.420	--
$[PF_6]^-$	--	--	--	--	--	--	1.650	1.650	--
X = H	1.314	1.087	--	--	--	--	--	--	--
X = Br	1.336	1.338	--	--	--	--	--	--	--
$[BF_4]^-$, X = Br	1.334	1.868	3.297	2.790	2.796	2.789	1.423-1.424	1.406	0.483
$[PF_6]^-$, X = Br	1.335	1.890	3.756	2.786	2.776	2.775	1.651	1.635	10.433
X = Cl	1.338	1.711	--	--	--	--	--	--	--
$[BF_4]^-$, X = Cl	1.333	1.712	3.278	2.771	2.769	2.779	1.424	1.406	-0.375
$[PF_6]^-$, X = Cl	1.333	1.717	3.731	2.758	2.751	2.751	1.651	1.634	9.604
X = F	1.326	1.316	--	--	--	--	--	--	--
$[BF_4]^-$, X = F	1.321	1.322	3.374	2.753	2.703	2.751	1.424	1.403	-18.558
$[PF_6]^-$, X = F	1.324	1.332	3.690	2.712	2.711	2.712	1.652	1.634	-17.485
X = CN	1.343	1.146	--	--	--	--	--	--	--
$[BF_4]^-$, X = CN	1.341	1.448	3.181	2.662	2.663	2.662	1.427	1.394	-30.229
$[PF_6]^-$, X = CN	1.341	1.447	3.649	2.661	2.661	3.265	1.658	1.629	-27.992

Table 10: B3LYP/6-31++G(d',p') bond distances and binding energies (E_t) for the $C_3N_3F_3$ complexes with $[BF_4]^-$ and $[PF_6]^-$. See Figure 83 for bond and atom labels.

System/B3LYP	1 (Å)	2 (Å)	B/IP-Centroid (Å)	F1-C1 (Å)	F2-C2 (Å)	F3-C3 (Å)	B/IP-F 1, 2, 3 (Å)	B-F4/P-F4,5,6 (Å)	E_t (kcal/mol)
$[BF_4]^-$	--	--	--	--	--	--	1.421	1.421	--
$[PF_6]^-$	--	--	--	--	--	--	1.644	1.644	--
X = H	1.338	1.090	--	--	--	--	--	--	--
X = Br	1.331	1.900	--	--	--	--	--	--	--
$[BF_4]^-$, X = Br	1.328	1.907	3.500	3.008	3.040	2.954	1.422-1.424	1.407	-4.295
$[PF_6]^-$, X = Br	1.329	1.907	4.082	2.889	3.533	3.092	1.650-1.611	1.643-1.644	0.589
X = Cl	1.331	1.726	--	--	--	--	--	--	--
$[BF_4]^-$, X = Cl	1.328	1.735	3.462	2.977	3.243	2.953	1.423	1.406	-5.411
$[PF_6]^-$, X = Cl	1.328	1.735	4.080	3.293	2.270	3.384	1.651-1.663	1.642-1.643	-0.341
X = F	1.324	1.312	--	--	--	--	--	--	--
$[BF_4]^-$, X = F	1.322	1.324	3.374	2.853	2.903	2.851	1.423-1.424	1.404	-12.170
$[PF_6]^-$, X = F	1.323	1.322	3.956	2.921	3.320	2.840	1.651-1.662	1.641	-9.697
X = CN	1.338	1.147	--	--	--	--	--	--	--
$[BF_4]^-$, X = CN	1.336	1.450	3.301	1.297	2.741	2.828	1.426-1.428	1.396	-21.494
$[PF_6]^-$, X = CN	1.336	1.450	3.821	2.857	2.818	2.826	1.662-1.664	1.636	-18.311

The interaction energies between the anion and the ring systems become more favorable as the included rings become more electropositive as well, indicating a stronger anion- π interactions. One clear trend is that the B3LYP interaction energies are underestimated in magnitude as compared to the corresponding MP2 interaction energies when a favorable anion- π interaction occurs (F- and CN-substituted ring systems), while those systems that are weakly binding (Cl- and Br-substituted ring systems) have much more unfavorable MP2 interaction energies than those obtained with B3LYP computations. This is expected, since MP2 calculations overestimate the attraction between the rings and the anions, while B3LYP computations, which estimate electron correlation as a function of energy, and therefore overestimate dispersion forces, underestimate the overall binding energy.¹³⁴ A slight geometry effect of this trend is that, in all B3LYP results (except with the extremely electropositive $C_3N_3(CN)_3$ ring), the $[PF_6]^-$ anion is slightly off-centered for direct overlap between the C atoms of the rings and the three F-atoms of the anion (See Figure 81, bottom row). The stronger repulsion introduced by the B3LYP computation keeps the anion from maximizing its overlap with the ring. Since $[PF_6]^-$ is more diffuse than $[BF_4]^-$, the geometry effect is noticeable. (Table 10). This closer positioning of the anion to the ring systems has a minor effect on the resulting binding energies. Those $[PF_6]^-$ and $[BF_4]^-$ complexes which include the electropositive $C_3N_3F_3$ and $C_3N_3(CN)_3$ rings have much more favorable MP2 binding energies than can be expected, while the same anions with the predominantly electroneutral $C_3N_3Cl_3$ and $C_3N_3Br_3$ rings produce repulsive binding energies at the MP2 level of theory.

An examination of the ring N-C and C-X bond distances (bonds 1 and 2, see Figure 83 for labels) in the anionic complexes reveal subtle shifts in the electron density of the rings due to the proximity of the anions. In all cases where the binding energies are favorable (negative), the N-C bond gets slightly shorter, or just stays the same when compared to the free ring calculations (see Tables 9 and 10). The slight shortening of this bond is evidence that the electron density of this bond has increased, and that empty degenerate π -bonding orbitals have become occupied. More startling, however, is the significant increase in the length of bond 2 (C-X) in the anionic complex compared to the same distance computed for the free ring. The lengthening of this bond indicates that the core conjugated ring system has become more stable (more electron rich) due to the proximity of the anion.

Further examinations of the anion- π complexes involving $C_3N_3F_3$ and $C_3N_3(CN)_3$ were performed by the AIM program for critical point analyses; the results mirrored those obtained from an examination of the geometry optimizations (See Figure 84 for examples). Unfortunately, due to the use of Effective Core Potentials (ECPs)¹³⁵ on the Cl and Br atoms, the AIM results of these systems are inconclusive. The (3,-1), (3,+1), and (3,+3) (bond, ring and cage, respectively) critical points were considered in the examined anion- π complexes. For a complete list of values, see Table 11. Figure 84 provides the labels for each critical point value in the table. Larger values for these critical points (e^-/α_e^3) indicate more electron density (ρ) at that point.

For these strongly binding complexes, the first important observation is that the bond (3,-1) critical points of the ring C-N conjugated bonds increase slightly in density value (ρ) as a result of the anion proximity. Likewise, the values of the (3,-1)

critical points of the P-F and B-F bonds pointing toward the rings are reduced. These two results alone indicate that the anion is losing electron density to the ring system as compared to the free ion. Three weak (3,-1) bond critical points were detected between the three core ring C atom and the 3 anion F atoms pointed at the ring plane, indicating that the electron sharing is occurring between these points. The central (3,+3) CP suspended between the centroid of the ring and the central point of the anion, surrounded by the ring (3,+1) critical points in a symmetric fashion, indicates that an electrostatic attraction is occurring between the anion and the ring system. These (3,+1) critical points show that a new “rings” of density (indicated by the new (3,-1) critical points between the anions and the rings) are created between two sets of anion F atoms and the corresponding C pairs.

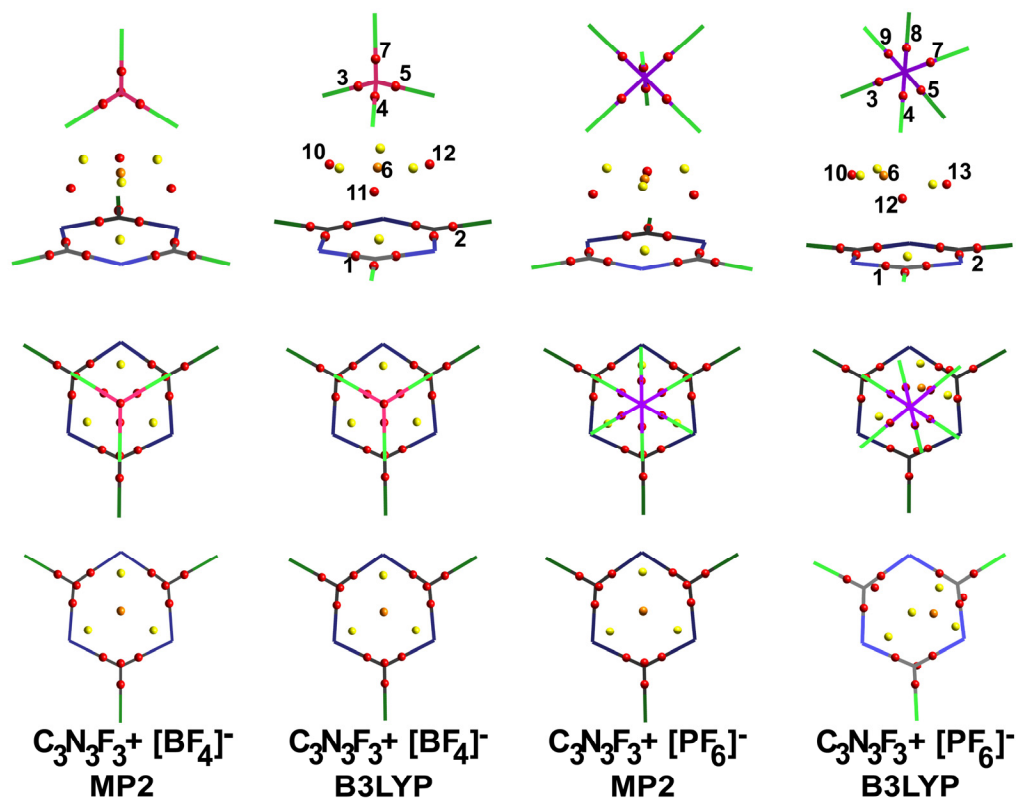


Figure 84: Examples of the AIM critical point analyses of $\text{C}_3\text{N}_3\text{X}_3$ systems for both the MP2 and B3LYP/6-31++G(d',p') wavefunctions. The top row displays entire complexes from the side, the middle row shows these same complexes from the top, and the bottom row has the same view with the anion removed. The numbers assigned to the critical points are labels for the values used in Table 11. Atom colors: C = grey, N = blue, B = pink, P = purple, F = green. Critical point colors: (3,-1) = red, (3,+1) = yellow, (3,+3) = orange.

Table 11: Critical point ρ values (e^2/a_0^3) recorded for the $C_3N_3X_3$ ($X = F$ or CN) systems at both the MP2 and B3LYP Levels of Theory. The labels for the CPs can be found in Figure 84.

System (MP2)	Ring (3,+1)	1 (3,-1)	2 (3,-1)	3 (3,-1)	4 (3,-1)	5 (3,-1)	6 (3,+3)	7,8,9 (3,-1)	10, 11, 12 (3,-1)
[BF ₄] ⁻	--	--	--	0.143	0.143	0.143	--	0.143	--
[PF ₆] ⁻	--	--	--	0.140	0.140	0.140	--	0.140	--
X = H	0.012	0.244	0.210	--	--	--	--	--	--
X = F	0.029	0.371	0.278	--	--	--	--	--	--
[BF ₄] ⁺ , X = F	0.029	0.393	0.271	0.141	0.141	0.141	0.003	0.151	0.011
[PF ₆] ⁺ , X = F	0.029	0.372	0.272	0.137	0.137	0.137	0.002	0.143	0.011
X = CN	0.027	0.352	0.296	--	--	--	--	--	--
[BF ₄] ⁺ , X = CN	0.027	0.354	0.292	0.140	0.140	0.140	0.003	0.155	0.013
[PF ₆] ⁺ , X = CN	0.027	0.354	0.292	0.135	0.135	0.135	0.002	0.145	0.013
System (B3LYP)	Ring (3,+1)	1 (3,-1)	2 (3,-1)	3 (3,-1)	4 (3,-1)	5 (3,-1)	6 (3,+3)	7,8,9 (3,-1)	10, 11, 12 (3,-1)
[BF ₄] ⁻	--	--	--	0.149	0.149	0.149	--	0.149	--
[PF ₆] ⁻	--	--	--	0.144	0.144	0.144	--	0.144	--
X = H	0.028	0.347	0.288	--	--	--	--	--	--
X = F	0.030	0.363	0.281	--	--	--	--	--	--
[BF ₄] ⁺ , X = F	0.030	0.364	0.275	0.148	0.148	0.148	0.002	0.156	0.008
[PF ₆] ⁺ , X = F	0.030	0.364	0.276	0.140	0.142	0.144	0.003	0.146	0.003-0.010
X = CN	0.028	0.349	0.281	--	--	--	--	--	--
[BF ₄] ⁺ , X = CN	0.027	0.354	0.292	0.140	0.140	0.140	0.003	0.155	0.013
[PF ₆] ⁺ , X = CN	0.028	0.350	0.280	0.140	0.140	0.140	0.002	0.148	0.009-0.010

The symmetric nature of the critical point positions that arise from anion- π binding indicate that the interaction is strongest when the anion is arranged to maximize the contact between the F atoms and the three carbon atoms of the ring, and when the orientation matches the original ESP map patterns (See Figures 79 and 80, second row) of π -acidity seen on major axes of the free triazine derivatives.

2. $C_2N_4X_2$ Systems with $[BF_4]^-$ and $[PF_6]^-$ -The complexes obtained for both of the $[BF_4]^-$ and $[PF_6]^-$ anions in the presences of the tetrazine derivatives indicate the same trends displayed for the triazine derivative results described in the previous section. The major difference is that the anions are positioned so that only two of the fluorine atoms from the complex anions are aligning with the carbon atoms of the rings (Figures 85 and 86). Although none of these calculations were symmetry-enforced, and all officially settled into C_1 symmetry, the anion- π interaction clearly has attempted to create a C_2 symmetry axis perpendicular to the ring plane. This is most clear in the complexes involving the $[BF_4]^-$ anion. All anion-tetrazine ring complexes in their final geometries are shown in Figures 85 and 86, and the bond distances, anion- π distances, and complex interaction energies are given in Tables 12 and 13 (See Figure 87 for bond label guide).

Complexes resulting in favorable binding energies exhibit decreased N-C core ring bond distances (bond # 2) as compared to the rings without the anion present. In systems with positive (unfavorable) binding energies, these bond distances do not change. Bond 3, the C-X bond, like with the corresponding $C_3N_3X_3$ systems, increases in all anionic complexes when compared to the C-X distances calculated for the free tetrazine ring derivatives.

Tetrazine Derivatives with $[\text{BF}_4]^-$

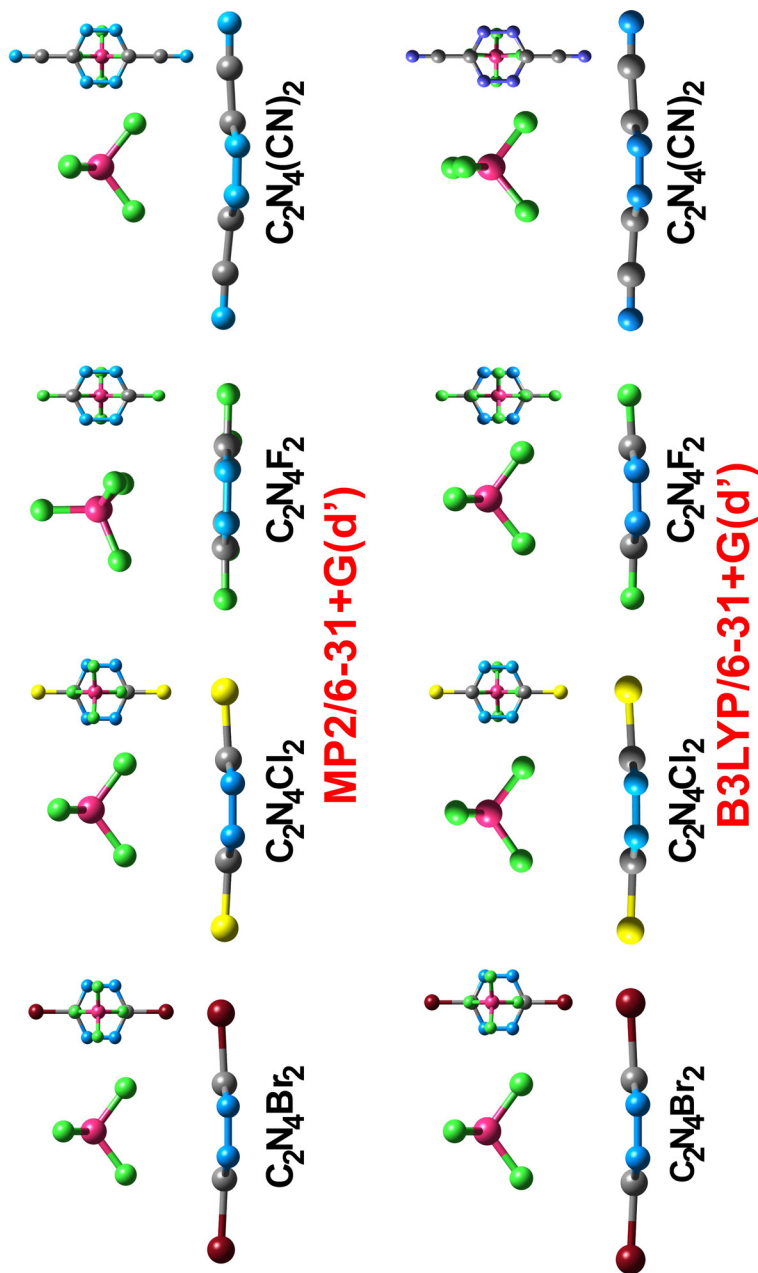


Figure 85: Geometry optimization results of the $\text{C}_2\text{N}_4\text{X}_2$ ring systems with $[\text{BF}_4]^-$ computed by the 6-31++G(d',p') basis set at both the MP2 and B3LYP levels of theory. Colors: C = grey, N = blue, P = purple, F = green, Cl = yellow, and Br = red

Tetrazine Derivatives with $[\text{PF}_6]^-$

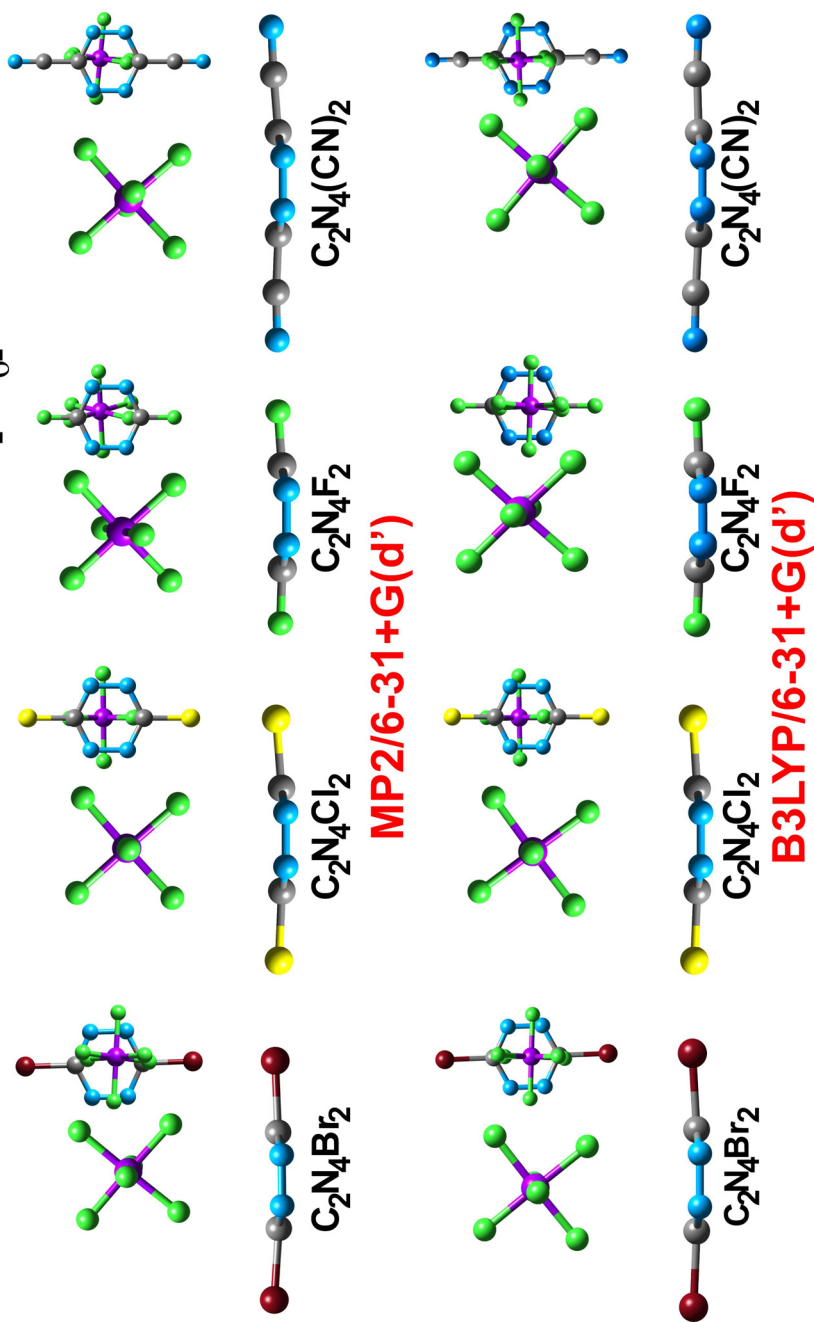


Figure 86: Geometry optimization results of the $\text{C}_2\text{N}_4\text{X}_2$ ring systems with $[\text{PF}_6]^-$ computed by the 6-31++G(d', d') basis set at both the MP2 and B3LYP levels of theory. Colors: C = grey, N = blue, P = purple, F = green, Cl = yellow, and Br = red

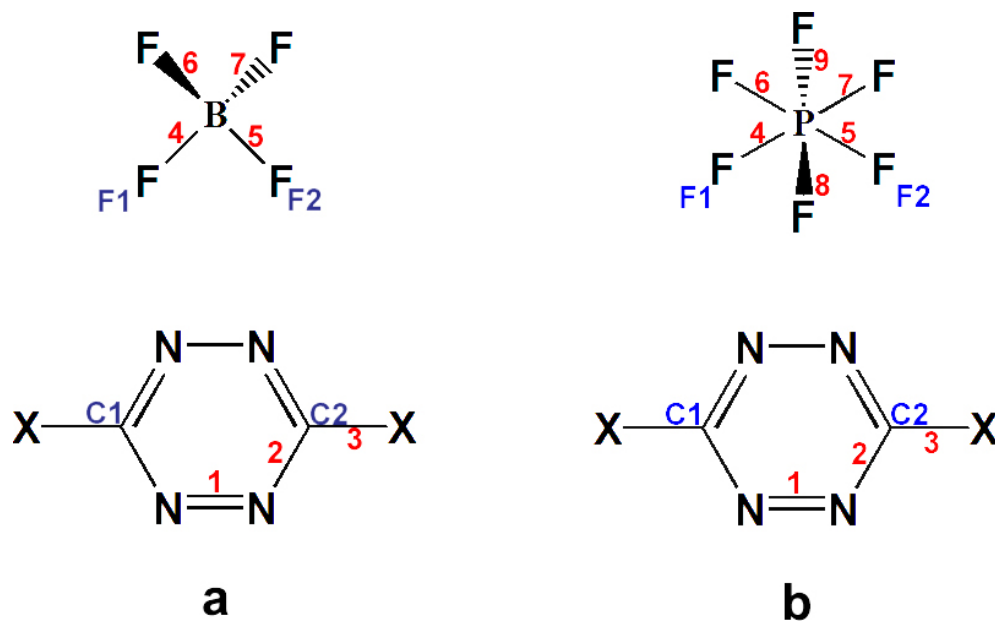


Figure 87: Line drawings of generic $[BF_4]^-$ and $[PF_6]^-$ anion + $C_2N_4X_2$ ring systems. The atom numbers are labeled in blue, and the bonds are labeled in red. These designations correspond to the values in Tables 12 and 13.

Table 12: MP2/6-31++G(d',p') geometry optimization results of $C_2N_4X_2$ ring systems with the $[BF_4]^-$ and $[PF_6]^-$ anions, and the interaction energies (E_I) resulting from these geometries. The labels for the distances listed are found in Figure 87.

System/MP2	1 (Å)	2 (Å)	3 (Å)	4 (Å)	5 (Å)	6, 7, 8, 9 (Å)	F1-C1 (Å)	F2-C2 (Å)	B/P-Centroid (Å)	E_t (kcal/mol)
$[BF_4]^-$	--	--	--	1.421	1.421	1.421	--	--	--	--
$[PF_6]^-$	--	--	--	1.644	1.644	1.644	--	--	--	--
X = H	1.334	1.345	1.086	--	--	--	--	--	--	--
X = Br	1.334	1.347	1.875	--	--	--	--	--	--	--
$[BF_4]^-$, X = Br	1.334	1.345	1.879	1.430	1.430	1.408	2.616	2.618	3.519	-0.884
$[PF_6]^-$, X = Br	1.344	1.344	1.880	1.659	1.651	1.634-1.638	2.583	2.730	3.874	9.796
X = Cl	1.332	1.347	1.702	--	--	--	--	--	--	--
$[BF_4]^-$, X = Cl	1.322	1.334	1.703	1.430	1.430	1.408	2.592	2.592	3.500	-1.371
$[PF_6]^-$, X = Cl	1.332	1.344	1.706	1.659	1.652	1.634-1.638	2.564	2.684	3.851	8.757
X = F	1.331	1.335	1.310	--	--	--	--	--	--	--
$[BF_4]^-$, X = F	1.332	1.334	1.318	1.432	1.432	1.407	2.520	2.521	3.434	-20.697
$[PF_6]^-$, X = F	1.322	1.333	1.320	1.663	1.654	1.633-1.639	2.539	2.617	3.770	-18.728
X = CN	1.328	1.352	1.439	--	--	--	--	--	--	--
$[BF_4]^-$, X = CN	1.327	1.350	1.440	1.437	1.436	1.401	2.497	2.500	3.422	-27.702
$[PF_6]^-$, X = CN	1.326	1.351	1.441	1.669	1.659	1.629-1.636	2.510	2.598	3.782	-25.028

Table 13: B3LYP/6-31++G(d') geometry optimization results of $C_2N_4X_2$ ring systems with the $[BF_4]^-$ and $[PF_6]^-$ anions, and the interaction energies (E_I) resulting from these geometries. The labels for the bonds listed are found in Figure 87

System/B3LYP	1 (Å)	2 (Å)	3 (Å)	4 (Å)	5 (Å)	6, 7, 8, 9 (Å)	F1-C1 (Å)	F2-C2 (Å)	BIP-Centroid (Å)	E (kcal/mol)
$[BF_4]^-$	--	--	--	1.420	1.420	1.420	--	--	--	--
$[PF_6]^-$	--	--	--	1.650	1.650	1.650	--	--	--	--
X = H	1.322	1.359	1.087	--	--	--	--	--	--	--
X = Br	1.320	1.339	1.889	--	--	--	--	--	--	--
$[BF_4]^-$, X = Br	1.319	1.336	1.893	1.429	1.429	1.409	2.792	2.791	3.679	-6.185
$[PF_6]^-$, X = Br	1.319	1.336	1.894	1.657	1.665	1.642-1.645	2.784	3.018	4.104	-0.772
X = Cl	1.318	1.338	1.718	--	--	--	--	--	--	--
$[BF_4]^-$, X = Cl	1.318	1.335	1.719	1.431	1.427	1.409	2.739	2.800	3.657	-7.246
$[PF_6]^-$, X = Cl	1.317	1.332	1.720	1.655	1.668	1.642-1.644	2.750	3.060	4.029	-1.773
X = F	1.319	1.330	1.318	--	--	--	--	--	--	--
$[BF_4]^-$, X = F	1.318	1.328	1.322	1.431	1.431	1.407	2.682	2.682	3.575	-13.792
$[PF_6]^-$, X = F	1.319	1.327	1.322	1.666	1.662	1.641-1.644	2.741	2.776	3.991	-10.866
X = CN	1.313	1.348	1.439	--	--	--	--	--	--	--
$[BF_4]^-$, X = CN	1.311	1.345	1.441	1.437	1.435	1.401-1.402	2.619	2.636	3.533	-20.271
$[PF_6]^-$, X = CN	1.311	1.345	1.441	1.674	1.665	1.636-1.642	2.760	3.240	3.953	-16.213

This indicates that the core π -system of the tetrazine ring derivatives have increased electron density due to the proximity of the anion. All of the $C_2N_4X_2 +$ anion complexes display longer B-F and P-F bonds for the F anion atoms pointing toward the two core ring carbon atoms, indicating a decrease in electron density in these anion bonds in exchange for a stronger anion- π overlap.

Similar to the trend seen with the C3N3X3 anionic systems, the interaction energies of the $[BF_4]^-$ complexes are more favorable than those with the $[PF_6]^-$ anions complexed with the corresponding ring systems (at the same levels of theory), and, in the case of both anions, the more electropositive the ring system, the closer the anion approaches in the final geometry of the complex. Similarly, the binding energies become more favorable the closer the anion is to the ring system as well.

The same predictable trend caused by the MP2 and B3LYP levels of theory is evident when examining the binding energies of the tetrazine ring + anion systems. For the MP2 results, those systems involving the π -acidic F- and CN-substituted rings have favorable, yet overestimated, interaction energies, while those systems that include Cl and Br substituted rings have large, unfavorable, interaction energies as compared to the B3LYP results. In all cases but one, $C_2N_4Br_2$ with $[PF_6]^-$, the B3LYP level of theory yields favorable binding energies (albeit weak in all other cases involving Cl and Br substituted tetrazine rings). This double repulsive result, found with both levels of theory, suggests that the $[PF_6]^-$ anion is incapable of participating in anion- π interactions with $C_2N_4Br_2$.

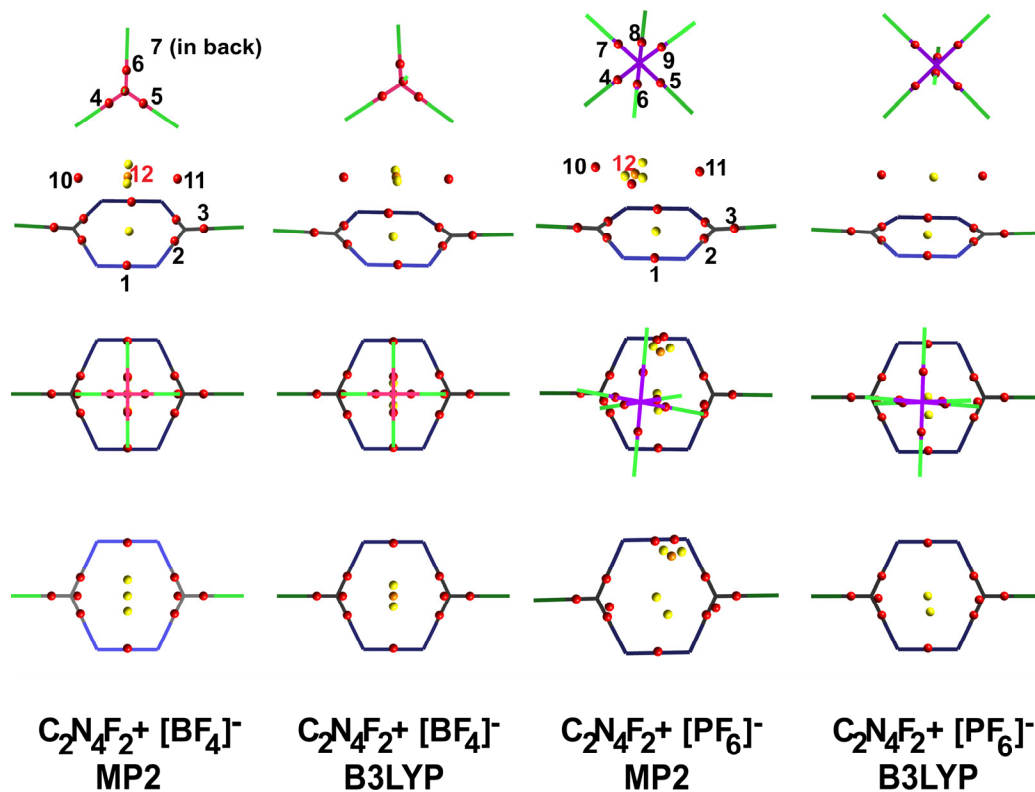


Figure 88: Examples of the AIM critical point analyses of $\text{C}_2\text{N}_4\text{F}_2$ systems for both the MP2 and B3LYP/6-31++G(d',d') wavefunctions. The top row displays entire complexes from the side, the middle row shows these same complexes from the top, and the bottom row has the same view with the anion removed. The numbers assigned to the critical points are labels for the values used in Table 14. Atom colors: C = grey, N = blue, B = pink, P = purple, F = green. Critical point colors: (3,-1) = red, (3,+1) = yellow, (3,+3) = orange. The numerical label for the orange (3,+3) cage point is orange.

Table 14: Critical point ρ values (e^{-3/a_0^3}) recorded for the $C_2N_4X_2$ ($X = F$ or CN) systems at both the MP2 and B3LYP Levels of Theory. The labels for the critical points are found in Figure 88.

System/MP2	Ring, (3,+1)	1 (3,-1)	2 (3,-1)	3 (3,-1)	4 (3,-1)	5 (3,-1)	6,7,8,9 (3,-1)	10 (3,-1)	11 (3,-1)	12 (3,+3)
[BF ₄] ⁻	--	--	--	--	0.143	0.143	0.143	--	--	--
[PF ₆] ⁻	--	--	--	--	0.140	0.140	0.140	--	--	--
X = H	0.025	0.398	0.346	0.296	--	--	--	--	--	--
X = F	0.025	0.398	0.364	0.280	--	--	--	--	--	--
[BF ₄] ⁻ , X = F	0.026	0.397	0.366	0.272	0.137	0.137	0.150	0.018	0.018	0.004
[PF ₆] ⁻ , X = F	0.026	0.397	0.365	0.274	0.133	0.136	0.142-0.143	0.017	0.014	0.002
X = CN	0.025	0.403	0.348	0.294	--	--	--	--	--	--
[BF ₄] ⁻ , X = CN	0.026	0.404	0.349	0.294	0.134	0.135	0.152	0.020	0.019	0.004
[PF ₆] ⁻ , X = CN	0.026	0.404	0.349	0.294	0.130	0.134	0.143-0.145	0.019	0.015	0.005
System/B3LYP	Ring, (3,+1)	1 (3,-1)	2 (3,-1)	3 (3,-1)	4 (3,-1)	5 (3,-1)	6,7,8,9 (3,-1)	10 (3,-1)	11 (3,-1)	12 (3,+3)
[BF ₄] ⁻	--	--	--	--	0.149	0.149	0.149	--	--	--
[PF ₆] ⁻	--	--	--	--	0.144	0.144	0.144	--	--	--
X = H	0.027	0.399	0.348	0.289	--	--	--	--	--	--
X = F	0.028	0.398	0.364	0.279	--	--	--	--	--	--
[BF ₄] ⁻ , X = F	0.028	0.398	0.365	0.275	0.145	0.145	0.155	0.013	0.013	0.003
[PF ₆] ⁻ , X = F	0.028	0.399	0.365	0.276	0.139	0.140	0.146-0.148	0.011	0.010	--
X = CN	0.027	0.406	0.347	0.284	--	--	--	--	--	--
[BF ₄] ⁻ , X = CN	0.027	0.407	0.348	0.283	0.142	0.143	0.158	0.015	0.015	0.004
[PF ₆] ⁻ , X = CN	0.027	0.407	0.348	0.285	0.136	0.139	0.147-0.148	0.013	0.010	0.004

The AIM results for the anion complexes involving $C_2N_4F_2$ and $C_2N_4(CN)_2$ are in accord with the bond distance observations and display the same C_2 symmetry axes observed in the geometry optimizations (See Figure 88, and Table 14). Two (3,-1) bond critical points appear between the F anion atoms pointing at the C core atoms of the ring. In the case of the $C_2N_4F_2 + [BF_4]^-$ complexes, a (3,+3) cage critical point, surrounded by two equidistant (3,+1) ring critical points (all positioned between the anion and the ring) suggest that an electrostatic interaction is occurring. In the MP2 $[PF_6]^- +$ dicyanotetrazine result, this (3,+3) critical point, which designates electrostatic interactions, is missing, suggesting that this complex is participating in a stronger charge transfer interaction (in the gas phase). The values of the (3,-1) critical points of the ring C-N conjugated bonds increase from the values reported for the free systems, indicating that these bonds have increased electron density due to the proximity of the anion (Table 6). Furthermore, the (3,-1) bond critical points between the two B-F and P-F bonds of each system have decreased in value from the free $[BF_4]^-$ and $[PF_6]^-$ values, indicating a decrease in electron density from these bonds. The most staggering difference observed between the anionic systems and the free rings is the value reported for bond 3. In the anionic tetrazine ring derivative complexes, this value has decreased drastically, an expected result when considering that this bond is longer in these anionic complexes than in the free ring tetrazine derivatives. This indicates that this bond is weaker due to the increased amount of electron density of the ring core π -system as a result of the proximity of the anion.

As observed with the $C_3N_3X_3$ results, the symmetry of the ESP map from the free $C_2N_4X_2$ rings is preserved in the anion- π systems with both anions (or as close to it as possible with the $[PF_6]^-$ complexes due to the larger size of this anion) based on

the results presented in this section. An anomaly, however, can be seen with the MP2 results of $[\text{PF}_6]^-$ with the $\text{C}_2\text{N}_4\text{F}_2$ ring. A third (3,-1) and (3,+1) critical point appears between the anion and the ring system, a consequence of a third P-F bond being slightly angled toward the ring plane. (See Figures 86 and 88). It should be noted that, despite the fact that the B3LYP $\text{C}_2\text{N}_4(\text{CN})_2 + [\text{PF}_6]^-$ complex shares the same geometry anomaly, it is not pronounced enough to add these extra (3,-1) and (3,+1) critical points. This observation, and the fact that the strongly favorable MP2 result of $[\text{PF}_6]^-$ with $\text{C}_2\text{N}_4(\text{CN})_2$ also does not have this third F-ring interaction, suggests that the slight difference in these geometry results, while allowing for a larger anion- π overlap, is small enough to be roughly equal to those that have only two obvious F---C anion- π contacts.

C. Structural Analysis of $\text{C}_4\text{N}_2\text{X}_4$ with $[\text{BF}_4]^-$ and $[\text{PF}_6]^-$: No Clear Interaction Symmetry Evident

1. B3LYP/6-31++G(d',p') geometries of $\text{C}_4\text{N}_2\text{X}_4$ rings with $[\text{BF}_4]^-$ - The most complicated results obtained thus far, the $[\text{BF}_4]^-$ and $[\text{PF}_6]^-$ optimizations with the $\text{C}_4\text{N}_2\text{X}_4$ derivatives, give unique insight into how complex anions interact with heteroaromatic ring π -systems (See Figures 89, 90, and Tables 15, 17, 19 and 21). The most obvious trend is that the $[\text{BF}_4]^-$ anion is closer than the $[\text{PF}_6]^-$ anion when paired with the same π -system, most likely a result of the more diffuse nature of the larger $[\text{PF}_6]^-$ anion. In all cases, the binding energies of the B3LYP complexes are less favorable than the corresponding MP2 energies (when binding occurs-this trend is opposite when the Cl and Br substituted rings are employed as discussed in the previous sections), and the in the case of all the $[\text{BF}_4]^-$ systems, the binding energies

are more favorable than those obtained with identical ring systems paired with $[\text{PF}_6]^-$ anions.

Anion position proves to be the most difficult result to describe. The B3LYP $[\text{BF}_4]^-$ results with the $\text{C}_4\text{N}_2\text{F}_4$ and $\text{C}_4\text{N}_2(\text{CN})_4$ systems have the anion positioned such that three of the fluorine atoms are closest to carbon atoms 2, 3, and 4 or 1, 2, and 4 for $\text{C}_4\text{N}_2\text{F}_2$ and $\text{C}_4\text{N}_2(\text{CN})_4$, respectively (see Figure 91 for C atom labels). The B3LYP optimization results of either $\text{C}_4\text{N}_2\text{Cl}_4$ or $\text{C}_4\text{N}_2\text{Br}_4$ with $[\text{BF}_4]^-$ only have close anion- π contacts between two F anion atoms and C atoms 2 and 3 on the pyridazine rings, a position as far away as possible from the electronegative N atoms of the rings. These mixed results are most likely due to the greater π -acidity of the F- and CN-substituted pyridazine rings; the anion is closer to carbon atoms which reside next to the electronegative core N ring atoms in these two cases creating a system with more anion- π overlap. As a result, the $[\text{BF}_4]^-$ anion is able to move closer to these two more electropositive rings than to $\text{C}_4\text{N}_2\text{Cl}_4$ and $\text{C}_4\text{N}_2\text{Br}_4$ for more anion- π contacts. In the complex containing $\text{C}_4\text{N}_2(\text{CN})_4$, this trend of moving closer to the ring surface becomes more evident; two of the possible three F-C anion-to-ring contacts are with carbon atoms 1 and 4, those closest to the two electronegative N pyridazine ring atoms. The extreme π -acidity of this ring (see Figures 79 and 80, first row) enables these particular contacts to occur despite the fact that this orientation appears to be counter-intuitive. The position of the anion, however, is such that nearly the entire ring surface is facing the anion, whereas in the complex with $\text{C}_4\text{N}_2\text{F}_4$, it is slightly slipped to the side of the ring furthest from the N-N conjugated bond.

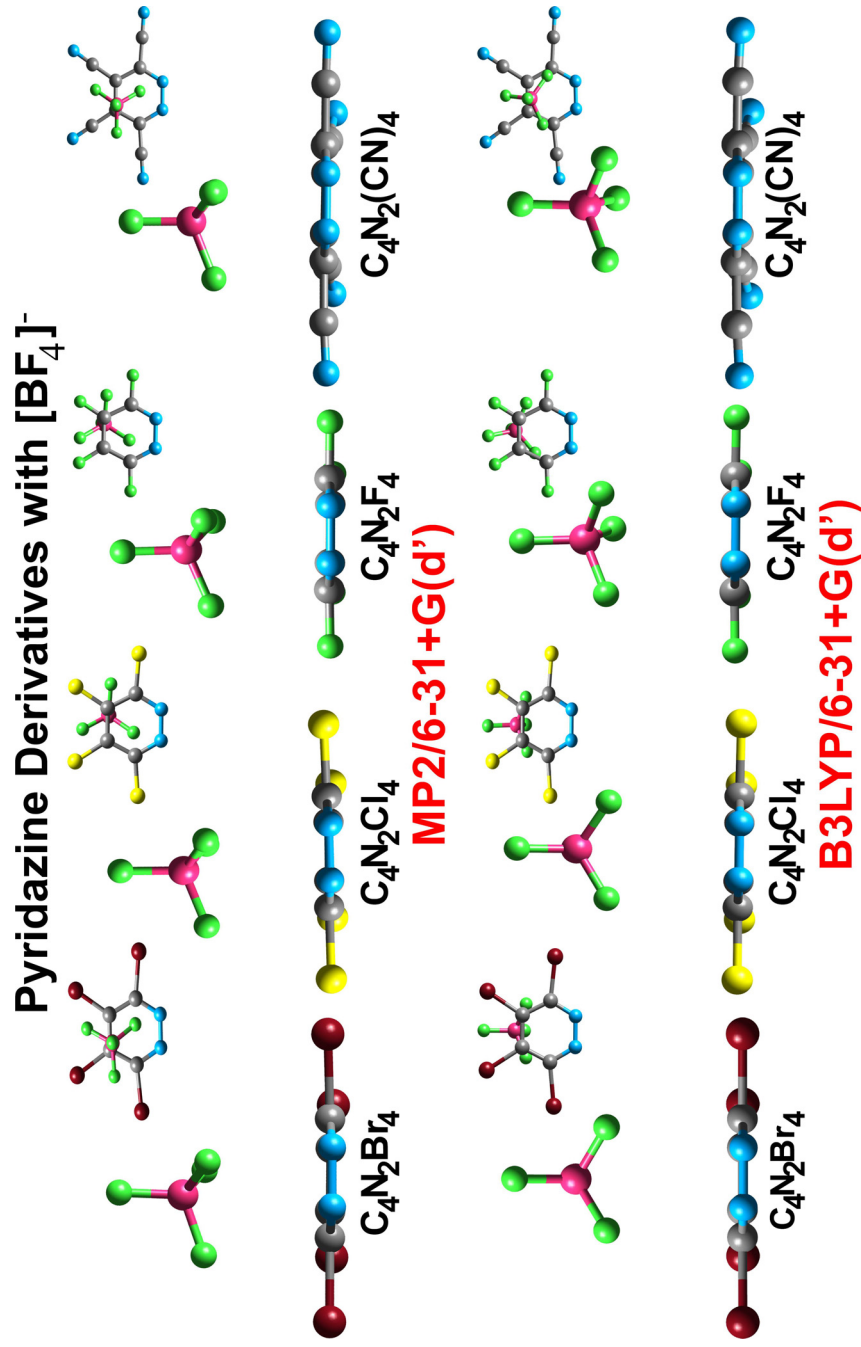


Figure 89: Geometry optimization results of the $\text{C}_4\text{N}_2\text{X}_4$ ring systems with $[\text{BF}_4]^-$ computed by the 6-31++G(d',d') basis set at both the MP2 and B3LYP levels of theory. Colors: C = grey, N = blue, P = purple, F = green, Cl = yellow, and Br = red.

Pyridazine Derivatives with $[\text{PF}_6]^-$

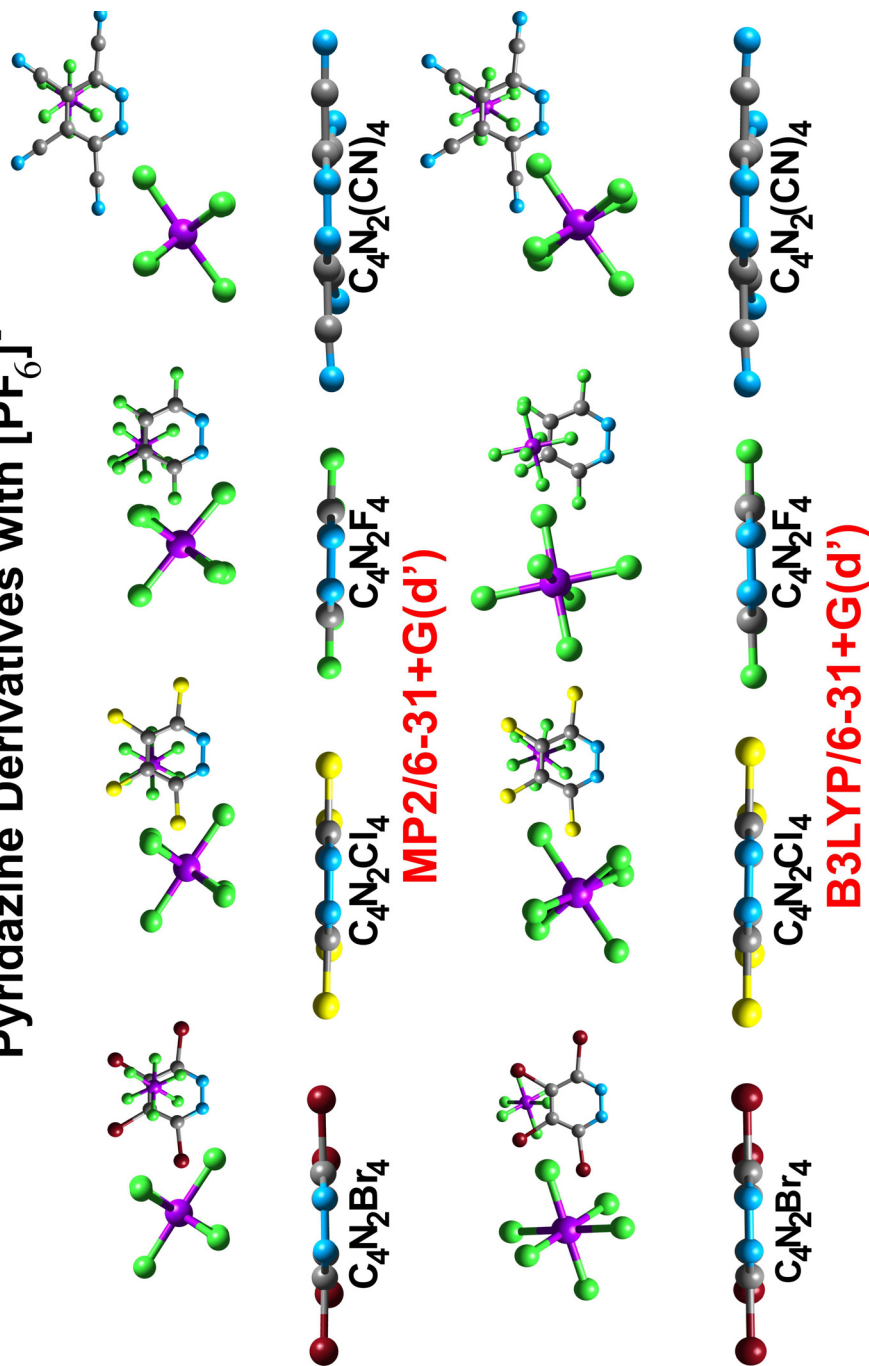


Figure 90: Geometry optimization results of the $\text{C}_4\text{N}_2\text{X}_4$ ring systems with $[\text{PF}_6]^-$ computed by the 6-31++G(d', d') basis set at both the MP2 and B3LYP levels of theory. Colors: C = grey, N = blue, F = purple, Br = green, Cl = yellow, and Br = red.

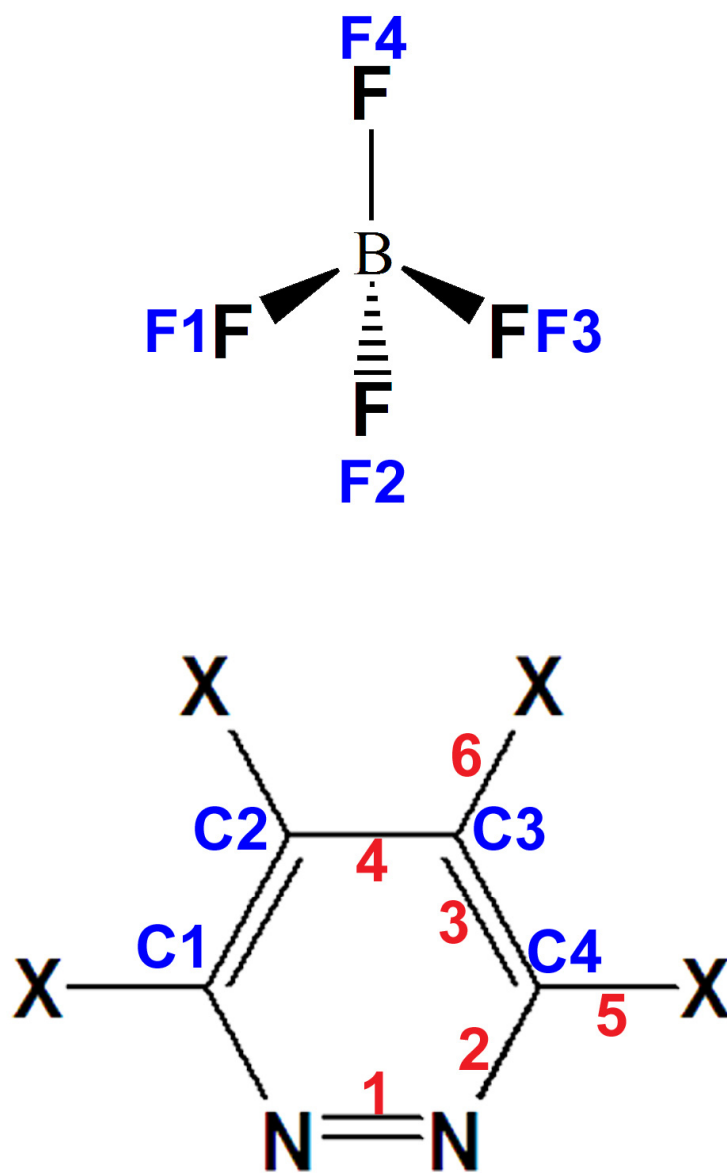


Figure 91: Generic line drawing of $[\text{BF}_4]^-$ paired with a $\text{C}_4\text{N}_2\text{X}_4$ ring. The bond labels (red) and atom labels (blue) correspond to the values listed in Tables 15 and 17.

Table 15: Bond distances, anion- π contact distances and binding energies (E_T) for the B3LYP/6-31+G(d',p') geometry results of $C_4N_2X_4$ with $[BF_4]^-$. The closest F-C contact for each $[BF_4]^-$ fluorine atom pointing toward the ring is in bold. The atom and bond labels used in this table are designated in Figure 91.

System/B3LYP	$[BF_4]^-$	$C_4N_2H_4$	$C_4N_2Br_4$	$C_4N_2Br_4 + [BF_4]^-$	$C_4N_2Cl_4$	$C_4N_2Cl_4 + [BF_4]^-$	$C_4N_2F_4$	$C_4N_2F_4 + [BF_4]^-$	$C_4N_2(CN)_4$	$C_4N_2(CN)_4 + [BF_4]^-$
1 (Å)	--	1.333	1.328	1.332	1.329	1.333	1.399	1.342	1.315	1.315
2 (Å)	--	1.337	1.324	1.320	1.323	1.318	1.308	1.306	1.346	1.343
3 (Å)	--	1.400	1.416	1.415	1.414	1.414	1.408	1.408	1.414	1.412
4 (Å)	--	1.386	1.398	1.395	1.394	1.390	1.379	1.376	1.404	1.399
5 (Å)	--	1.088	1.905	1.190	1.731	1.736	1.331	1.338	1.436	1.438
6 (Å)	--	1.087	1.893	1.858	1.720	1.718	1.327	1.327	1.429	1.429
B-F1 (Å)	1.420	--	--	1.426	--	1.427	--	1.425	--	1.427
B-F2 (Å)	1.420	--	--	1.426	--	1.427	--	1.424	--	1.426
B-F3 (Å)	1.420	--	--	1.416	--	1.415	--	1.421	--	1.427
B-F4 (Å)	1.420	--	--	1.409	--	1.408	--	1.405	--	1.393
F1-C1 (Å)	--	--	--	3.164	--	3.019	--	3.003	--	2.872
F1-C2 (Å)	--	--	--	3.011	--	2.961	--	2.979	--	3.001
F1-C3 (Å)	--	--	--	3.505	--	3.462	--	3.563	--	3.569
F1-C4 (Å)	--	--	--	4.015	--	3.974	--	4.033	--	3.916
F2-C1 (Å)	--	--	--	4.013	--	3.934	--	4.064	--	3.781
F2-C2 (Å)	--	--	--	3.506	--	3.453	--	3.171	--	2.949
F2-C3 (Å)	--	--	--	3.011	--	2.954	--	3.131	--	2.914
F2-C4 (Å)	--	--	--	3.160	--	3.065	--	4.001	--	3.730
F3-C1 (Å)	--	--	--	4.854	--	4.830	--	3.743	--	3.660
F3-C2 (Å)	--	--	--	4.041	--	4.028	--	3.464	--	3.469
F3-C3 (Å)	--	--	--	4.038	--	4.001	--	3.095	--	3.059
F3-C4 (Å)	--	--	--	4.849	--	4.788	--	3.058	--	2.883
E_T (kcal/mol)	--	--	--	-4.347	--	-5.638	--	-12.763	--	-25.149

The anion position in the complexes containing the $C_4N_2Cl_4$ and $C_4N_2Br_4$ rings is even further slipped from the surface of the ring away from the two ring N atoms due to the electroneutral character of these rings (Figures 79 and 80, top row), and, as a result, fewer anion- π F-C anion ring contacts occur.

Due to an odd angle, the three F-C contacts in the $[BF_4]^-$ + F- or CN-substituted pyridazine derivatives are difficult to visualize in Figure 89. These contacts, however, become evident upon viewing the AIM computed bond paths depicted in Figure 92. The red (3,-1) bond critical points between the anion and the ring C atoms are created as a result of the F atoms of $[BF_4]^-$ interacting with this ring system. As the ring substituents become increasingly electronegative, more electron density is directed away from these carbon atoms, and the anion moves closer to the ring for shorter F-C contacts to replace this depleted ring density. The three B-F bonds aligned for the interaction (or the two B-F bonds, in the cases of systems containing the Cl and Br-substituted pyridazine rings) are lengthened as compared to those same B-F bonds in the free anion. Furthermore, the (3,-1) critical points of the B-F bonds pointed toward the pyridazine ring C atoms have decreased in comparison to the values determined for the free anion, indicating a donation of density from the anions to the ring systems (Figure 93 and Table 16). The C-N bonds (2) and the C-C bonds (3 and 4) are shorter in all the B3LYP $C_4N_2X_4 + [BF_4]^-$ complexes as compared to the values found in the free rings (see Table 15). The critical point values of these bonds in complexes that contain F- and CN- substituted pyridazine molecules (see Figure 93 and Table 16) also increase, further supporting the contention that electron density is being donated from the anion to the ring. The C-X bonds 5 and 6 lengthen in all of the B3LYP complex results when compared to the

same bonds in the free rings, and the (3,-1) critical points of the bonds (in the F- and CN- substituted pyridazine derivatives) decrease in value when compared to the free ring values. These observations indicate that the core ring π -system has increased electron density due to the proximity of the $[\text{BF}_4]^-$ anion. A final point worth mentioning is that the three ring (3,+1) critical points and a cage (3,+3) critical point present between the anion and the ring indicate that 3-fold F-C anion-ring binding occurs in the complexes containing F- and CN- substituted pyridazine rings, and also that an electrostatic attraction is present between the anion and the ring.

2. MP2/6-31++G(d',p') geometries of $\text{C}_4\text{N}_2\text{X}_4$ rings with $[\text{BF}_4]^-$ - The $\text{C}_4\text{N}_2\text{X}_4 + [\text{BF}_4]^-$ MP2 results all have three F-C anion- π contacts between the anion F atoms and the pyridazine ring C atoms 2, 3, and 4 except for the complex that contains the CN-substituted pyridazine in which C ring atoms 1, 3, and 4 are involved (see Figure 91 for bond labels and Table 17 for bond distances and interaction energies). Unfortunately, due to the 2-D quality of Figure 89, this is difficult to visualize. Figure 94 depicts the AIM results of the MP2 $\text{C}_4\text{N}_2\text{F}_4$ and $\text{C}_4\text{N}_2(\text{CN})_4 + [\text{BF}_4]^-$ complexes revealing the bond paths between 3 of the anion F atoms and 3 of the ring carbon atoms. The CN, F, Cl and Br-substituted rings, when complexed with $[\text{BF}_4]^-$ at the MP2 level of theory, interact with the two carbon ring atoms that are most distal from the electronegative ring atoms. The third contact is to carbon atom 4 on the ring, which is right next to an electronegative N atom.

The three B-F bonds aligned for all of the anion- π interactions have lengthened when compared to the free anion B-F distances, and the (3,-1) critical point density values of these bonds, in the cases of the F- and CN-substituted pyridazine derivatives, have decreased in comparison to the values of the free anion

B-F (3,-1) critical points, indicating a donation of density from this part of the anion to the ring system (Tables 17 and 18). Three ring (3,+1) CPs are created by the buildup of electron density between the F-C interaction, a further indication that the anion- π interaction is 3-fold. In all cases, a (3,+3) cage point is present, indicating an electrostatic interaction is occurring between the ring and the anion. Examples of MP2 $C_4N_2X_4 + [BF_4]^-$ AIM critical point results are shown in Figure 95.

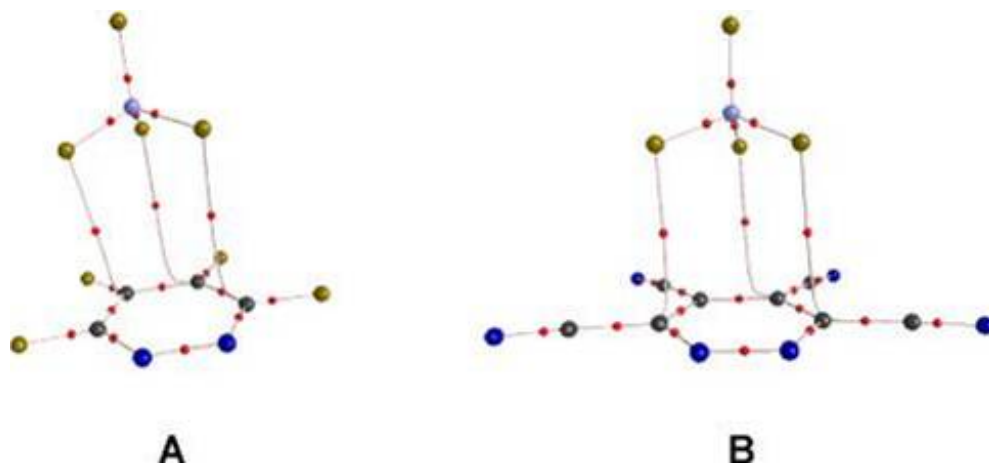


Figure 92: AIM calculated bond paths for complexes of $C_4N_2X_4$ ($X = F$ or CN) from the B3LYP/6-31++G(d',p') computation results. Colors: Gray = C, blue = N, gold = F, pink = B, and (3,-1) CPs are red.

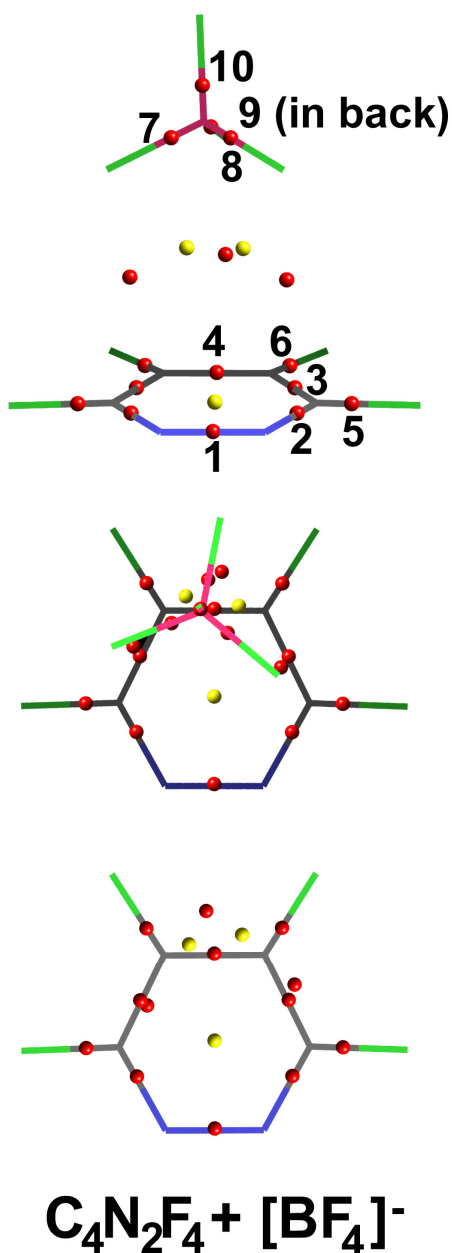


Figure 93: Example of the AIM critical point analysis results of $C_4N_2F_4 + [BF_4]^-$ systems for the B3LYP/6-31++G(d',p') wavefunction. The top row displays the entire complex from the side, the middle row shows the same complex from the top, and the bottom row depicts the same view with the anion removed. The numbers assigned to the critical points are labels for the values used in Table 16. Atom colors: C = grey, N = blue, B = pink, , F = green. Critical point colors: (3,-1) = red, (3,+1) = yellow, (3,+3) = orange.

Table 16: AIM critical point ρ values (e/α_3) obtained from the B3LYP/6-31++G(d',p') geometry optimization results of the $C_4N_2X_4$ rings with $[BF_4]^-$ ($X = F$ or CN). The numerical labels for each critical point are detailed in Figure 93.

System/B3LYP	$[BF_4]^-$	$C_4N_2H_4$	$C_4N_2F_4$	$C_4N_2F_4 + [BF_4]^-$	$C_4N_2(CN)_4$	$C_4N_2(CN)_4 + [BF_4]^-$
Ring (3,+1)	--	0.023	0.023	0.023	0.022	0.022
1	--	0.388	0.376	0.373	0.402	0.402
2	--	0.346	0.374	0.376	0.345	0.347
3	--	0.309	0.310	0.311	0.301	0.303
4	--	0.316	0.326	0.329	0.305	0.308
5	--	0.284	0.268	0.263	0.282	0.282
6	--	0.280	0.268	0.268	0.284	0.284
7	0.149	--	--	0.148	--	0.142
8	0.149	--	--	0.149	--	0.149
9	0.149	--	--	0.148	--	0.146
10	0.149	--	--	0.156	--	0.162
11	--	--	--	0.008	--	0.010
12	--	--	--	0.005	--	0.010
13	--	--	--	0.007	--	0.009

Table 17: Bond distances and anion- π contact distances and binding energies (E_T) for the MP2/6-31++G(d',p,) geometry results of $C_4N_2X_4$ with $[BF_4]^-$. The closest F-C contact for each $[BF_4]^-$ fluorine atom pointing toward the ring is shown in bold. The atom and bond labels used in this table are designated in Figure 91.

System/MP2	$[BF_4]^-$	$C_4N_2H_4$	$C_4N_2Br_4$	$C_4N_2Br_4 + [BF_4]^-$	$C_4N_2Cl_4$	$C_4N_2Cl_4 + [BF_4]^-$	$C_4N_2F_4$	$C_4N_2F_4 + [BF_4]^-$	$C_4N_2(CN)_4$	$C_4N_2(CN)_4 + [BF_4]^-$
1 (Å)		1.342	1.336	1.337	1.337	1.337	1.347	1.348	1.330	1.330
2 (Å)		1.345	1.340	1.336	1.337	1.333	1.317	1.314	1.353	1.350
3 (Å)		1.401	1.416	1.413	1.414	1.411	1.407	1.404	1.413	1.410
4 (Å)		1.391	1.417	1.404	1.401	1.399	1.382	1.379	1.404	1.400
5 (Å)		1.087	1.889	1.895	1.713	1.717	1.328	1.337	1.436	1.438
6 (Å)		1.086	1.880	1.878	1.706	1.703	1.325	1.326	1.429	1.429
B-F1 (Å)	1.421	--	--	1.422	--	1.422	--	1.424	--	1.427
B-F2 (Å)	1.421	--	--	1.424	--	1.424	--	1.423	--	1.428
B-F3 (Å)	1.421	--	--	1.424	--	1.424	--	1.425	--	1.427
B-F4 (Å)	1.421	--	--	1.406	--	1.406	--	1.403	--	1.391
F1-C1 (Å)	--	--	--	2.999	--	2.956	--	2.870	--	2.830
F1-C2 (Å)	--	--	--	2.984	--	2.939	--	2.807	--	2.763
F1-C3 (Å)	--	--	--	3.716	--	3.679	--	3.551	--	3.559
F1-C4 (Å)	--	--	--	4.256	--	4.227	--	4.139	--	4.174
F2-C1 (Å)	--	--	--	3.911	--	3.874	--	3.818	--	3.751
F2-C2 (Å)	--	--	--	3.095	--	3.049	--	2.959	--	2.890
F2-C3 (Å)	--	--	--	3.009	--	2.963	--	2.837	--	2.779
F2-C4 (Å)	--	--	--	3.764	--	3.726	--	3.631	--	3.570
F3-C1 (Å)	--	--	--	3.180	--	3.183	--	3.207	--	3.026
F3-C2 (Å)	--	--	--	3.176	--	3.179	--	3.194	--	3.053
F3-C3 (Å)	--	--	--	3.033	--	3.039	--	3.059	--	2.973
F3-C4 (Å)	--	--	--	2.883	--	2.891	--	2.935	--	2.848
E_T (kcal/mol)		--	--	-1.244	--	-2.269	--	-20.117	--	-35.500

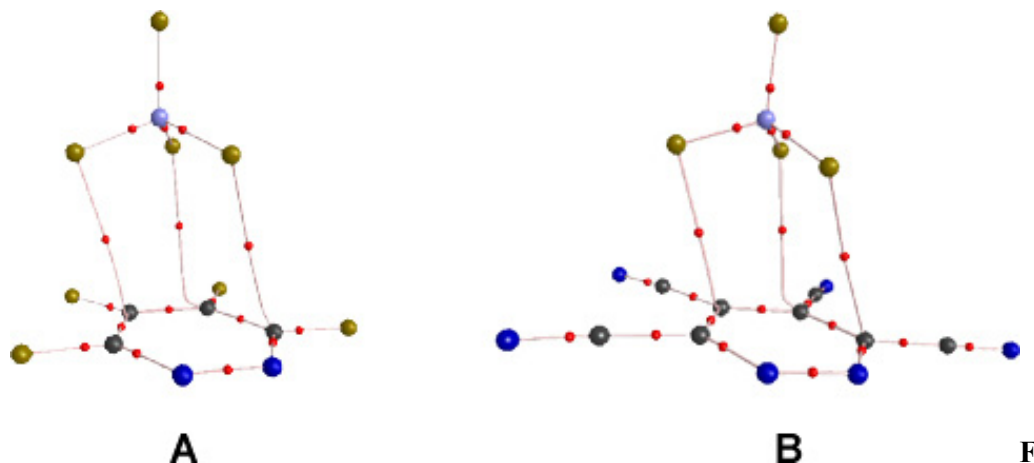


Figure 94: AIM calculated ring bond paths for the MP2/6-31++G(d',p') geometry optimization results of $[\text{BF}_4]^-$ complexed with (a) $\text{C}_4\text{N}_2\text{F}_4$ and (b) $\text{C}_4\text{N}_2(\text{CN})_4$. Colors: C = grey, N = blue, F = gold, B = light blue, and the (3,-1) CPs are red.

An examination of the ring bond distances of the MP2 calculated $\text{C}_4\text{N}_2\text{X}_4 + [\text{BF}_4]^-$ systems reflects these observations (See Figure 91, and Table 17). Generally, the core ring bonds have shortened between the carbon atoms (bonds 3 and 4-see Figure 91 for bond labels), but in the case of the N-N conjugated ring bond (1), the bond length stays the same, except for a slight increase in value for the complex containing the Br-substituted pyridazine ring. This increase of the N-N distance suggests that electron density is being donated into the π^* orbitals of the N-N conjugated bond as a result of the proximity of the anion. The 2 unique C-X bonds of the systems (bonds 4 and 5) display a length increase in the anionic complex when compared to the free ring results, indicating that the core ring π -system has become more electron rich. The AIM results containing the F and CN-substituted rings exhibit the same trends observed for the bond distances (see Figure 95 and Tables 17 and 18). The shortened ring bonds in the complexes show larger density values for their (3,-1) bond critical points, while the longer ring C-X and anion B-F bonds have a reduced value for their (3,-1) critical points as compared to the free anion results.

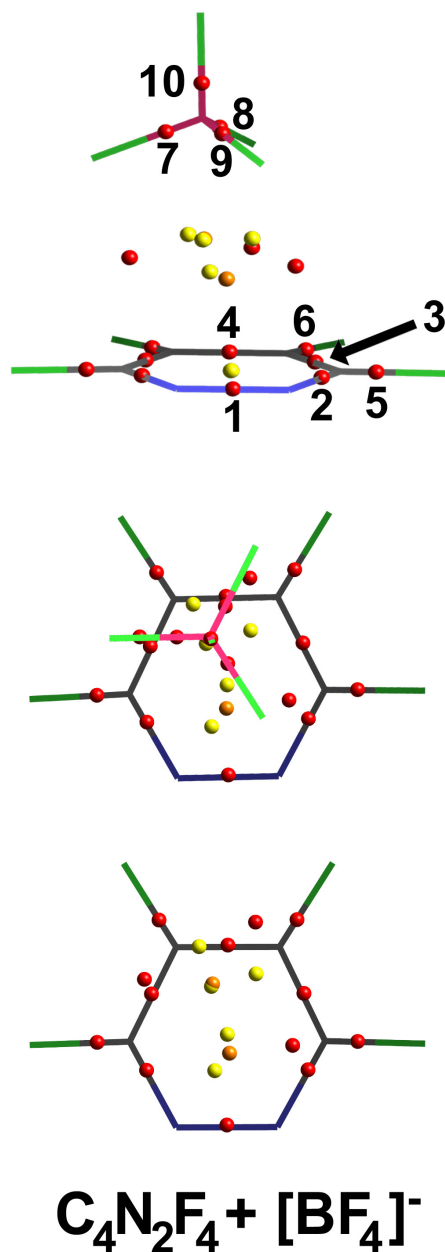


Figure 95: Examples of the AIM critical point analysis results of $C_4N_2F_4 + [BF_4]^-$ systems for the MP2/6-31++G(d',p') wavefunction. The top row displays the entire complex from the side, the middle row shows the same complex from the top, and the bottom row depicts the same view with the anion removed. The numbers assigned to the critical points are labels for the values used in Table 18. Atom colors: C = grey, N = dark blue, B = light blue, F = green. Critical point colors: (3,-1) = red, (3,+1) = yellow, (3,+3) = orange.

Table 18: AIM critical point ρ values (e^{-3}/α_0^3) obtained from the MP2/6-31++G(d',p') geometry optimization results of the $C_4N_2X_4$ rings with $[BF_4]^-$ (X = F or CN). The numerical labels for each CP are detailed in Figure 95

System/MP2	$[BF_4]^-$	$C_4N_2H_4$	$C_4N_2F_4$	$C_4N_2F_4 + [BF_4]^-$	$C_4N_2(CN)_4$	$C_4N_2(CN)_4 + [BF_4]^-$
Ring (3,+1)	--	0.022	0.021	0.021	0.021	0.021
1	--	0.390	0.381	0.379	0.399	0.400
2	--	0.343	0.347	0.375	0.345	0.346
3	--	0.317	0.322	0.324	0.311	0.313
4	--	0.320	0.344	0.336	0.314	0.316
5	--	0.290	0.265	0.256	0.293	0.291
6	--	0.286	0.266	0.263	0.293	0.293
7	0.143	--	--	0.141	--	0.140
8	0.143	--	--	0.140	--	0.140
9	0.143	--	--	0.142	--	0.139
10	0.143	--	--	0.151	--	0.157
11	--	--	--	0.011	--	0.013
12	--	--	--	0.010	--	0.012
13	--	--	--	0.009	--	0.010

The patterns of the bond (3,-1), ring (3,+1) and cage (3,+3) critical points between the anion and the ring reflect the observations regarding the anion position. In the cases in which the F atoms are positioned over C atoms, a weak bond (3,-1) CP exists (giving a total of 3 indicated F-C contacts between the rings and the anion).

3. MP2/6-31++G(d',p') geometries of $C_4N_2X_4$ rings with $[PF_6]^-$ - While it is difficult to see from Figure 90, the same F-ring carbon atom trends noted in the previous sections are observed in the $C_4N_2X_4 + [PF_6]^-$ MP2 geometry optimization results. The P-F bond distances, indicate that three F atoms of the anion are participating in anion- π overlap. Carbon atoms 1, 2, and 3 (or the equivalent 4, 3, and 2 C atoms) are in contact with three different F atoms from the $[PF_6]^-$ anion. This can be visualized easily from the AIM bond-path computation result (see Figure 97-Figure 96 for atom labels). The highly π -acidic $C_4N_2(CN)_4$ ring, however, has one F atom interacting with two C atoms at once, leading to a complex wherein all four C atoms of the ring are participating in anion- π interactions (according to the AIM calculation-see Figure 97).

As found before, systems involving the Br and Cl substituted rings have favorable (positive) binding energies, while the anionic MP2 optimized systems containing the CN- and F- substituted pyridazine rings have favorable (negative) calculated binding energies (Table 19). All three P-F bonds oriented toward the core ring carbon atoms are longer than the values obtained for the free anion, and the C-C and C-N bonds of the systems with favorable binding energies are shorter than those found in the pyridazine ring derivatives alone (see Table 19 and Figure 96 for bond lengths and atom labels). Also similar, the C-X bonds of the anionic species have lengthened in comparison the free ring bond distances. The AIM critical point analyses of the

complexes containing the F- and CN-substituted pyridazine rings mirror these trends, i.e., shorter bonds in the rings exhibit larger (3,-1) critical point density values than in the free rings, and the longer C-X ring bonds and the P-F bonds involved in the anion- π interactions have smaller (3,-1) bond critical point values as compared to the free rings and anions (see Table 20 and Figure 98). Furthermore, as seen in Figures 97 and 98, weak bond (3,-1) critical points exist between 3 of the $[\text{PF}_6]^-$ fluorine anion atoms and 3 core carbon atoms from the $\text{C}_4\text{N}_2\text{F}_4$ and $\text{C}_4\text{N}_2(\text{CN})_4$ rings. As mentioned before, in $\text{C}_4\text{N}_2(\text{CN})_4 + [\text{PF}_6]^-$ complex, 1 of the 3 participating F atoms actually has two (3,-1) critical points positioned between it and the ring; one for each C atom with which it is interacting.

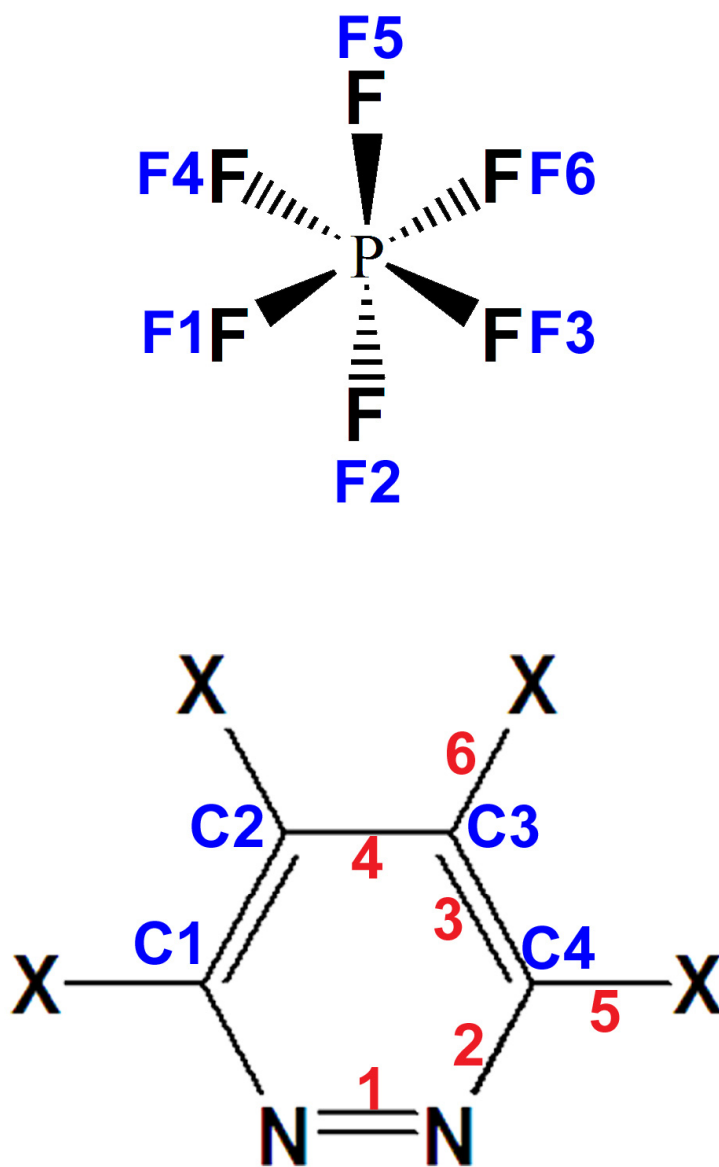


Figure 96: Generic line drawing of $[PF_6]^-$ paired with a $C_4N_2X_4$ ring. The bond labels (red) and atom labels (blue) correspond to the values listed in Tables 19 and 21.

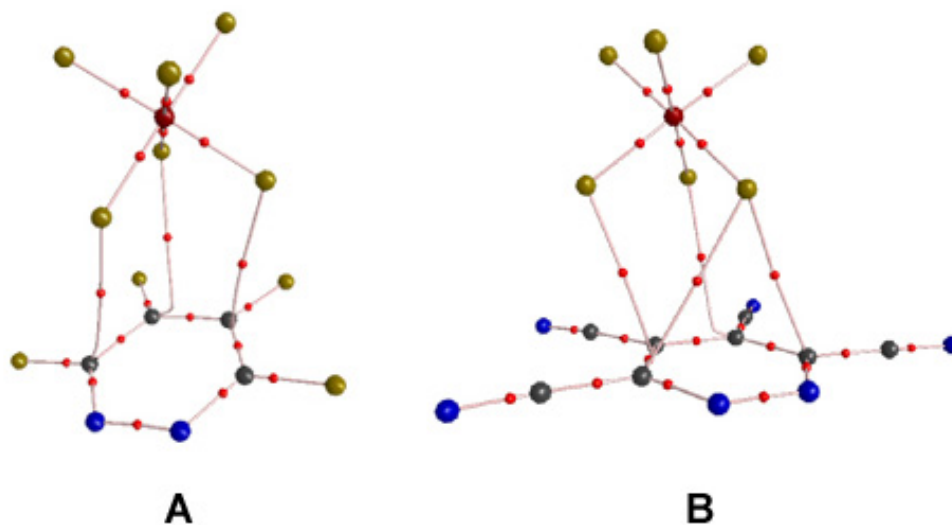


Figure 97: AIM calculated bond paths for the MP2/6-31++G(d',p') optimized geometries of $[\text{PF}_6]^-$ interacting with (a) $\text{C}_4\text{N}_2\text{F}_4$ and (b) $\text{C}_4\text{N}_2(\text{CN})_4$. Colors: Grey = C, dark blue = N, gold = F, dark red = P, and red = (3,+1) CPs.

4. B3LYP/6-31++G(d',p') geometries of $\text{C}_4\text{N}_2\text{X}_4$ rings with $[\text{PF}_6]^-$ - The B3LYP results, when three F-C anion-ring contacts are present, are similar. This 3-fold anion- π contact only occurs in the anionic complexes containing $\text{C}_4\text{N}_2\text{Cl}_4$ (C atoms 2, 3, and 4) or $\text{C}_4\text{N}_2(\text{CN})_4$ (C atoms 1, 3, and 4). The Cl-pyridazine derivative is not very π -acidic (see Figures 79 and 80, top row), and the three anion- π contacts are arranged in the one orientation that provides the least amount of overlap. Two of the contacts involve C atoms 2 and 3, those C atoms most distal from the electronegative ring N atoms, with the third F-C contact occurring at one of the C atoms closest to these 2 ring N atoms. This is opposite of the anion orientation in the more favorable $\text{C}_4\text{N}_2(\text{CN})_4 + [\text{PF}_6]^-$ B3LYP geometry-optimized complex which has two F atoms positioned in contact with the two C atoms closest to the electronegative pyridazine

N atoms (C atoms 1 and 3). The third (leftover) F-C contact is with C atom 3, one of the remaining, electrostatically equal, two C atoms most distal from the N atoms. As mentioned before, this position is closer to the ring overall, and allows for better anion- π overlap. Most likely, this is due to the highly electron-deficient character of the core ring atoms of $C_4N_2(CN)_4$ (see Figures 79 and 80, top row). The strong 3-fold contacts in this system (as well as the single contact in the B3LYP $C_3N_2F_4 + [PF_6]^-$ complex) can be most easily viewed with the AIM bond path result pictured in Figure 99b.

The two remaining results, the B3LYP optimized complexes of $C_4N_2Br_4$ and $C_4N_2F_4$ with $[PF_6]^-$, have only one anion F atom contact close to the ring planes. In both cases, this atom is closest to the conjugated C-C bond between ring C atoms 2 and 3 (See Figure 96 for atom labels). The complex containing the Br-substituted pyridazine ring, which has an unfavorable interaction (positive) energy (see Table 21), might be expected to have this single weak anion- π contact due to the electroneutral nature of the $C_4N_2Br_2$ molecule (See Figures 79 and 80, top row). The $C_4N_2F_4$ pyridazine molecule, however, is very electron-deficient (see Figures 79 and 80, top row), so three anion-ring contact points would be expected. Unlike the complex containing $C_4N_2Br_4$, however, this result has a very favorable interaction energy, which suggests that this B3LYP geometry result is similar in energy to one where three anion F atoms are facing the pyridazine ring plane. For a better view of this 1 F-C anion ring contact orientation, the AIM calculated bond paths are displayed in Figure 99a.

Table 19: Bond distances and anion- π contact distances and binding energies (E_T) for the MP2/6-31++G(d',p') geometry results of $C_4N_2X_4$ with $[PF_6]^-$. The closest F-C contact for each $[PF_6]^-$ fluorine atom pointing toward the ring is in bold. The atom and bond labels used in this table are designated in Figure 96.

Ring/MP2	$[PF_6]^-$	$C_4N_2H_4$	$C_4N_2Br_4$	$C_4N_2Br_4$	$C_4N_2Br_4 + [PF_6]^-$	$C_4N_2Cl_4$	$C_4N_2Cl_4$	$C_4N_2Cl_4 + [PF_6]^-$	$C_4N_2F_4$	$C_4N_2F_4 + [PF_6]^-$	$C_4N_2(CN)_4$	$C_4N_2(CN)_4 + [PF_6]^-$
1 (A)	--	1.342	1.336	1.337	1.337	1.337	1.337	1.337	1.347	1.347	1.330	1.330
2 (A)	--	1.345	1.340	1.338	1.338	1.337	1.335	1.317	1.317	1.317	1.353	1.510
3 (A)	--	1.401	1.416	1.415	1.415	1.414	1.413	1.407	1.407	1.405	1.413	1.410
4 (A)	--	1.391	1.417	1.405	1.405	1.401	1.399	1.382	1.382	1.380	1.404	1.400
5 (A)	--	1.087	1.889	1.891	1.891	1.731	1.716	1.328	1.328	1.331	1.436	1.438
6 (A)	--	1.086	1.880	1.876	1.876	1.706	1.703	1.325	1.325	1.323	1.429	1.429
P-F1 (A)	1.650	--	--	1.651	1.651	--	1.651	--	--	1.652	--	1.658
P-F2 (A)	1.650	--	--	1.650	1.650	--	1.650	--	--	1.653	--	1.659
P-F3 (A)	1.650	--	--	1.648	1.648	--	1.649	--	--	1.652	--	1.600
P-F3 (A)	1.650	--	--	1.633	1.633	--	1.636	--	--	1.633	--	1.628
P-F5 (A)	1.650	--	--	1.636	1.636	--	1.635	--	--	1.634	--	1.627
P-F6 (A)	1.650	--	--	1.633	1.633	--	1.633	--	--	1.635	--	1.626
F1-C1 (A)	--	--	--	2.879	2.879	--	2.893	--	--	2.948	--	2.833
F1-C2 (A)	--	--	--	3.024	3.024	--	3.031	--	--	3.062	--	2.788
F1-C3 (A)	--	--	--	3.157	3.157	--	3.154	--	--	3.167	--	3.589
F1-C4 (A)	--	--	--	3.151	3.151	--	3.147	--	--	3.155	--	4.195
F2-C1 (A)	--	--	--	3.754	3.754	--	3.712	--	--	3.610	--	3.738
F2-C2 (A)	--	--	--	2.989	2.989	--	2.935	--	--	2.814	--	2.891
F2-C3 (A)	--	--	--	3.067	3.067	--	3.013	--	--	2.937	--	2.789
F2-C4 (A)	--	--	--	3.883	3.883	--	3.841	--	--	3.795	--	3.573
F3-C1 (A)	--	--	--	4.273	4.273	--	4.249	--	--	4.174	--	3.001
F3-C2 (A)	--	--	--	3.727	3.727	--	3.690	--	--	3.567	--	3.048
F3-C3 (A)	--	--	--	2.986	2.986	--	2.937	--	--	2.806	--	2.976
F3-C4 (A)	--	--	--	2.991	2.991	--	2.950	--	--	2.877	--	2.841
E_T (kcal/mol)	--	--	--	8.733	8.733	--	7.804	--	--	-18.932	--	-32.873

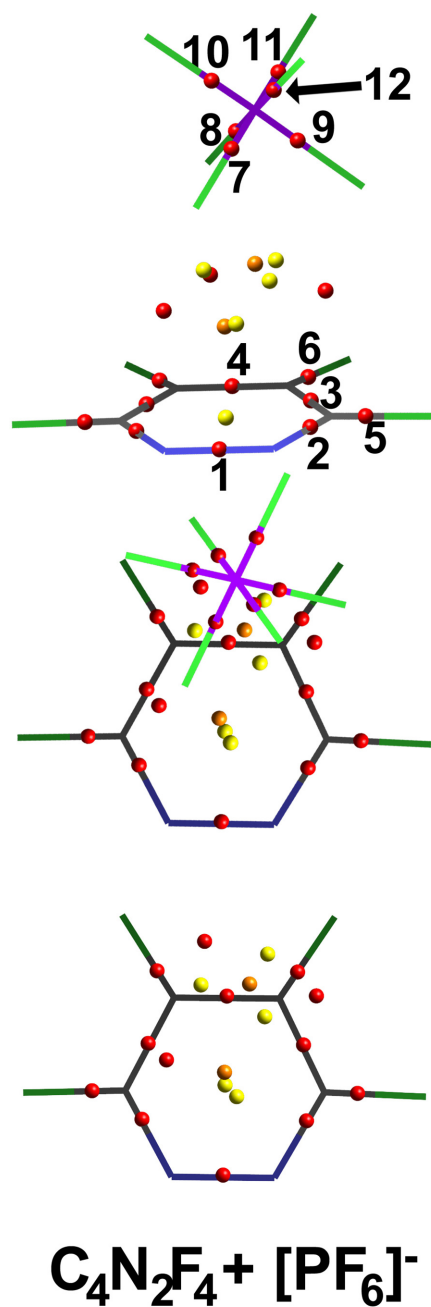


Figure 98: Example of the AIM critical point analysis results of the $C_4N_2F_4 + [PF_6]^-$ system the MP2/6-31++G(d',p') wavefunction. The top row displays the complex from the side, the middle row shows the same complex from the top, and the bottom row depicts the same view with the anion removed. The numbers assigned to the critical points are labels for the values used in Table 20. Atom colors: C = grey, N = blue, P = purple, F = green. Critical point colors: (3,-1) = red, (3,+1) = yellow, (3,+3) = orange

Table 20: AIM critical point ρ values (e^{-}/a_0^3) obtained from the MP2/6-31++G(d',p') geometry optimization results of the $C_4N_2X_4$ rings with $[PF_6]^-$ (X = F or CN). The numerical labels for each CP are detailed in Figure 98.

Ring/MP2	$[PF_6]^-$	$C_4N_2H_4$	$C_4N_2F_4$	$C_4N_2F_4 + [PF_6]^-$	$C_4N_2(CN)_4$	$C_4N_2(CN)_4 + [PF_6]^-$
Ring (3,+1)	--	0.022	0.021	0.021	0.021	0.021
1	--	0.390	0.381	0.379	0.399	0.400
2	--	0.343	0.347	0.374	0.345	0.346
3	--	0.317	0.322	0.324	0.311	0.313
4	--	0.320	0.344	0.366	0.314	0.316
5	--	0.290	0.265	0.261	0.293	0.291
6	--	0.286	0.266	0.265	0.293	0.294
7	0.144	--	--	0.137	--	0.135
8	0.144	--	--	0.137	--	0.135
9	0.144	--	--	0.137	--	0.134
10	0.144	--	--	0.143	--	0.146
11	0.144	--	--	0.143	--	0.146
12	0.144	--	--	0.143	--	0.147
13	--	--	--	0.008	--	0.008
14	--	--	--	0.010	--	0.012
15	--	--	--	0.011	--	0.010

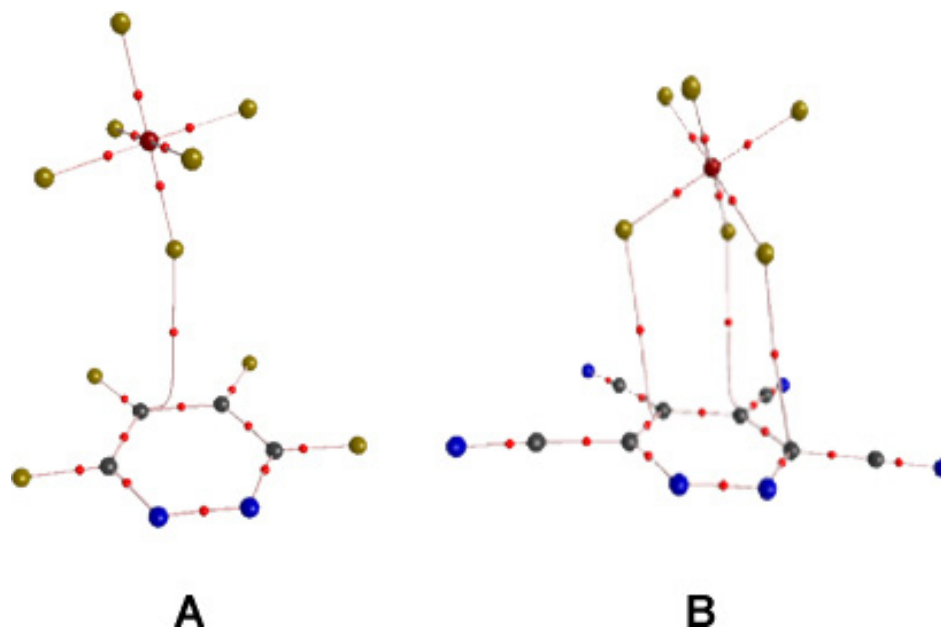


Figure 99: AIM calculated bond paths for the B3LYP/6-31++G(d',p') optimized geometries of $[\text{PF}_6]^-$ interacting with (a) $\text{C}_4\text{N}_2\text{F}_4$ and (b) $\text{C}_4\text{N}_2(\text{CN})_4$. Colors: Grey = C, dark blue = N, gold = F, dark red = P, and red = (3,+1) critical points.

The AIM critical point analyses of these systems support the conclusions drawn from the $\text{C}_4\text{N}_2\text{X}_2 + [\text{PF}_6]^-$ B3LYP geometry optimization results ($\text{X} = \text{F}$ or CN), namely the C-C bonds have increased (3,-1) density values, the participating P-F bonds all have decreased (3,-1) density values, and (3,-1) weak critical points are positioned between the participating F anion atoms and the C atoms of the pyridazine ring derivatives (see Table 22 and Figure 100).

Table 21: Bond distances and anion- π contact distances and binding energies (E_T) for the B3LYP/6-31+G(d') geometry results of $C_4N_2X_4$ with $[PF_6]^-$. The closest F-C contact for each $[PF_6]^-$ fluorine atom pointing toward the ring is in bold. The atom and bond labels used in this table are designated in Figure 96.

System/B3LYP	$[PF_6]^-$	$C_4N_2H_4$	$C_4N_2Br_4$	$C_4N_2Br_4 + [PF_6]^-$	$C_4N_2Cl_4$	$C_4N_2Cl_4 + [PF_6]^-$	$C_4N_2F_4$	$C_4N_2F_4 + [PF_6]^-$	$C_4N_2(CN)_4$	$C_4N_2(CN)_4 + [PF_6]^-$
1 (A)	--	1.333	1.328	1.330	1.329	1.330	1.399	1.339	1.315	1.315
2 (A)	--	1.337	1.324	1.322	1.323	1.319	1.308	1.307	1.346	1.343
3 (A)	--	1.400	1.416	1.414	1.414	1.413	1.408	1.405	1.414	1.412
4 (A)	--	1.386	1.398	1.398	1.394	1.391	1.379	1.377	1.404	1.400
5 (A)	--	1.088	1.905	1.911	1.731	1.737	1.331	1.336	1.436	1.430
6 (A)	--	1.087	1.893	1.886	1.720	1.719	1.327	1.326	1.429	1.429
P-F1 (A)	1.650	--	--	1.633	--	1.655	--	1.671	--	1.664
P-F2 (A)	1.650	--	--	1.644	--	1.655	--	1.645	--	1.665
P-F3 (A)	1.650	--	--	1.646	--	1.657	--	1.645	--	1.665
P-F3 (A)	1.650	--	--	1.649	--	1.643	--	1.647	--	1.635
P-F5 (A)	1.650	--	--	1.651	--	1.643	--	1.648	--	1.634
P-F6 (A)	1.650	--	--	1.645	--	1.641	--	1.642	--	1.633
F1-C1 (A)	--	--	--	3.511	--	3.236	--	4.337	--	2.951
F1-C2 (A)	--	--	--	3.012	--	3.169	--	4.242	--	2.953
F1-C3 (A)	--	--	--	3.004	--	3.838	--	4.833	--	3.642
F1-C4 (A)	--	--	--	3.444	--	4.363	--	5.382	--	4.168
F2-C1 (A)	--	--	--	3.599	--	4.159	--	3.393	--	3.893
F2-C2 (A)	--	--	--	5.268	--	3.331	--	2.804	--	3.074
F2-C3 (A)	--	--	--	4.255	--	3.247	--	2.828	--	2.935
F2-C4 (A)	--	--	--	4.081	--	4.029	--	3.429	--	3.683
F3-C1 (A)	--	--	--	4.817	--	3.557	--	4.841	--	3.341
F3-C2 (A)	--	--	--	4.254	--	3.441	--	4.794	--	3.329
F3-C3 (A)	--	--	--	4.762	--	3.215	--	4.789	--	3.124
F3-C4 (A)	--	--	--	5.643	--	3.126	--	4.830	--	2.941
E_T (kcal/mol)	--	--	--	0.174	--	-7.351	--	-9.091	--	-21.498

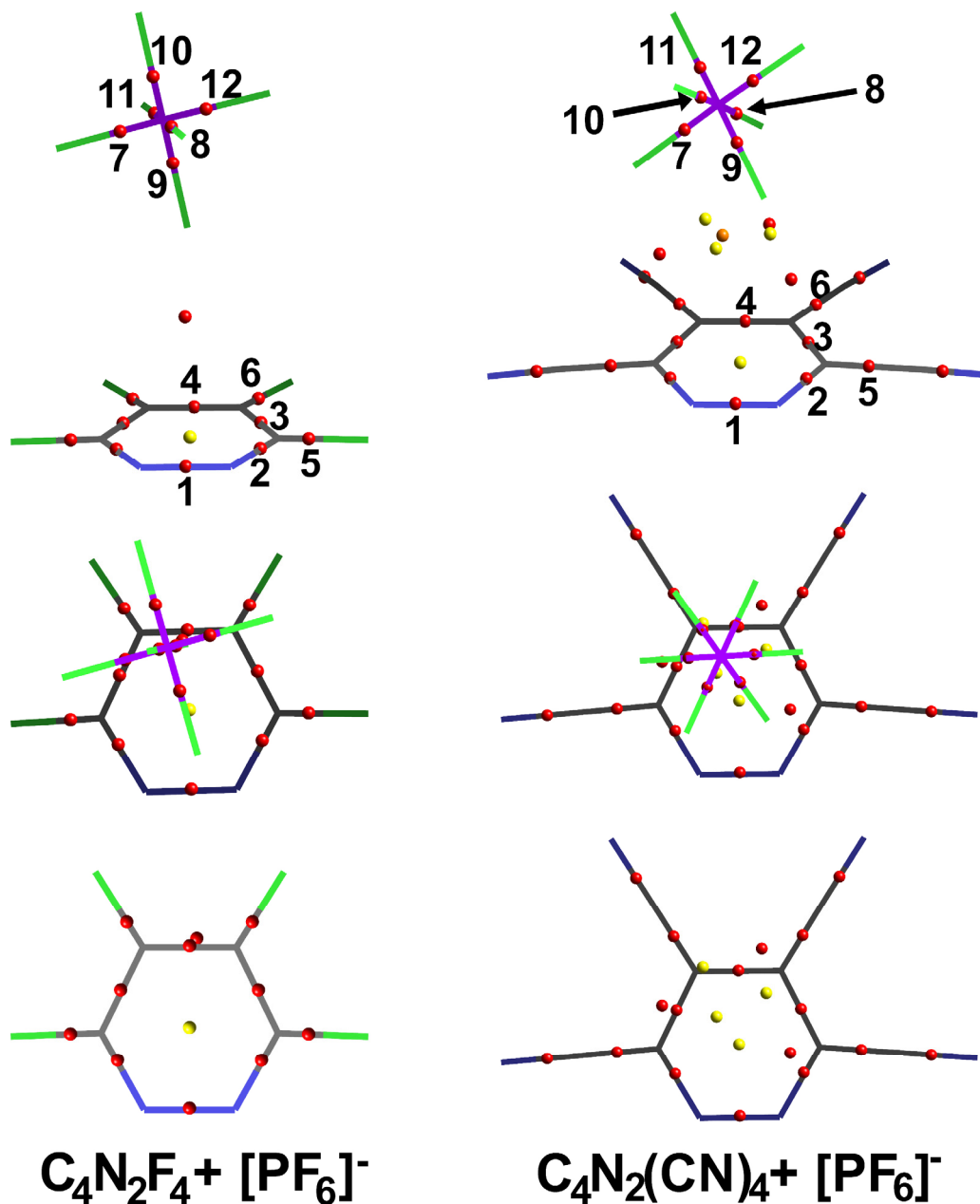


Figure 100: Examples of the AIM critical point analysis results of $C_4N_2X_4 + [PF_6]^-$ systems ($X = F$ or CN) for the B3LYP/6-31++G(d',p') wavefunctions. The top row displays the complexes from the side, the middle row shows the same complexes from the top, and the bottom row depicts the same view with the anion removed. The numbers assigned to the critical points are labels for the values used in Table 22. Atom colors: C = grey, N = blue, P = purple, F = green. Critical point colors: (3,-1) = red, (3,+1) = yellow, (3,+3) = orange.

Table 22: AIM determined important critical point ρ values ($e^{-3}/\text{a.u.}^3$) for the $\text{C}_4\text{N}_2\text{X}_4 + [\text{PF}_6]^-$ ($\text{X} = \text{F}$ or CN) complexes from the B3LYP/6-31++G(d', p') geometry optimizations. Critical point labels are detailed in Figure 100.

Ring/B3LYP	$[\text{PF}_6]^-$	$\text{C}_4\text{N}_2\text{H}_4$	$\text{C}_4\text{N}_2\text{F}_4$	$\text{C}_4\text{N}_2\text{F}_4 + [\text{PF}_6]^-$	$\text{C}_4\text{N}_2(\text{CN})_4$	$\text{C}_4\text{N}_2(\text{CN})_4 + [\text{PF}_6]^-$
Ring (3,+1)	--	0.023	0.023	0.023	0.022	0.022
1	--	0.388	0.376	0.376	0.402	0.402
2	--	0.346	0.374	0.374	0.345	0.346
3	--	0.309	0.310	0.312	0.301	0.307
4	--	0.316	0.326	0.238	0.305	0.307
5	--	0.284	0.268	0.263	0.282	0.282
6	--	0.280	0.268	0.267	0.284	0.284
7	0.140	--	--	0.145	--	0.139
8	0.140	--	--	0.137	--	0.140
9	0.140	--	--	0.145	--	0.140
10	0.140	--	--	0.145	--	0.149
11	0.140	--	--	0.145	--	0.149
12	0.140	--	--	0.145	--	0.149
13	--	--	--	--	--	0.009
14	--	--	--	0.011	--	0.008
15	--	--	--	--	--	0.008

IV. Discussion

A. The Effect of Ring π -Acidity

The effect that π -acidity of the participating aromatic ring on the anion- π complex geometry and energy results is clearly evident in this study. As observed before in earlier studies involving halides, the more electropositive the ring systems, the closer the anion approaches the ring system, and the lower the total binding energy of the system.^{12c} The results of the ring-only optimizations (Figures 79 and 80) indicate that the anion should be closer to the CN-substituted systems, second closest to the F-substituted systems, third closest to the Cl-substituted systems, and most distal from the Br-substituted systems. While this proximity trend could be explained by the size of the ring substituents, it should be noted that the more favorable results of the F- and CN- substituted anionic complexes have closer anion- π contacts than the less favorable B3LYP results. Both the complex geometries and binding energies follow these trends at the MP2 (see Tables 9, 12, 17, and 19) and B3LYP (see Tables 10, 13, 15, and 21) levels of theory. In all the cases involving Br-substituted rings and the large $[\text{PF}_6]^-$ anion, the binding energy is not favorable. Since the ESP maps of the Br ring derivatives most closely match those obtained for pyridazine, *s*-triazine, and *s*-tetrazine, most likely the $[\text{PF}_6]^-$ anion will not be attracted to these rings. The systems involving $[\text{BF}_4]^-$ and Br-substituted rings, while still slightly favorable in the B3LYP computational result, will most likely not participate in the anion- π interactions with the Br-substituted, and therefore H-substituted, rings. This claim can be affirmed because all of the computations performed were in the gas phase, and when experimental conditions such as solvent choice enter the equation, anion- π interactions will be even more difficult to form.

B. The Effect of Symmetry

There is no question that interactions involving complex anions and π -acidic rings have a different set of rules than those defined by halides with ring systems. The orbitals available from complex anions are more complicated and have more strict requirements for strong anion- π overlap. Both the $[\text{BF}_4]^-$ and $[\text{PF}_6]^-$ anions have the ability to orient one, two, or three F atoms toward the ring plane, but the larger size and octahedral geometry of $[\text{PF}_6]^-$ makes the approach more difficult than that of the smaller tetrahedral $[\text{BF}_4]^-$ anion. In the case of the ring systems that can easily accommodate these two or three F atoms oriented toward them, for the $\text{C}_2\text{N}_4\text{X}_2$ and $\text{C}_3\text{N}_3\text{X}_3$ systems, the anions are nearly perfectly aligned to give rise to either C_2 or C_3 symmetry axes through the anion- π interactions, respectively (See Figures 81, 82, 85, and 86). The resulting anion-ring complex geometries support this statement, and the corresponding bond distances of the anion and rings suggest that the orientation is required for maximum overlap (See Tables 9, 10, 12, and 13). The anion P-F and B-F bonds oriented towards the rings are longer than the P-F and B-F bonds of the free anions while, noticeably, those B-F and P-F bonds not pointing towards the ring are shorter than the distances encountered in the free anions. The C-N bonds from both the triazine and tetrazine derivatives are shortened in instances where the overall binding energy is favorable for the system. Electron density is being added to the π bonding orbitals of these C-N bonds, making them shorter, possibly making the ring more aromatic. The tetrazine ring N-N bond distances do not change, however, when the anion is added to the computation (in the case of systems with favorable binding energies) since the π -bonding orbitals between these two atoms are fully occupied. The C-X distances in both the tetrazine and triazine

systems have increased compared to the same distances in the free ring substituents as a result of the close proximity of the anions signifying that the core ring has become more electron rich due to anion- π contacts.

The critical point analyses also support the theory that the anions are oriented to preserve the major symmetry axes of the ring plane ESP maps (C_3 and C_2 rotation axes for the triazine and tetrazine derivatives, respectively). Bond (3,-1) critical points are positioned directly between the participating F atoms and the core ring C atoms, indicating that the anion- π interaction is strongest in these places (See Figures 84 and 85 Tables 11 and 14). Also, the ring N-C bonds that have decreased in length often display a larger (3,-1) bond critical point value than the same bonds in the free ring computational results. Furthermore, those P-F and B-F bonds oriented toward the rings have lower (3,-1) critical point density values than found in the free anions, indicating that electron density is lost from these bonds to the ring systems.

To fully explain why the anions are orienting in specific geometries when interacting with the triazine and tetrazine derivatives, an examination of a ring system without a clear symmetry anion-ring match is required. In the case of $C_4N_2X_4$ derivatives, both the $[BF_4]^-$ and the $[PF_6]^-$ (except for the two B3LYP results with F- and Br- substituted pyridazine rings), the anion is positioned to orient two or three F atoms directly at two or three carbon atoms of the pyridazine rings. The bond paths and critical points computed by the AIM method on the complexes containing $C_4N_2F_4$ and $C_4N_2(CN)_2$ (except for the $C_4N_2F_4 + [PF_6]^-$ B3LYP result) confirm this observation by detecting three different bond paths between the anion F atoms and three of the ring core carbon atoms (and a fourth F-C contact, two from the same F atom, in the MP2 $C_4N_2(CN)_4 + [PF_6]^-$ result). The P-F and B-F bond distances of the

participating F atoms all increase when compared to the free anion bond distances, while the (3,-1) bond values in the complexes containing $C_4N_2X_4$ ($X = F$ or CN) also decrease from those in free anion, an indication of electron density donation from the anion to the ring. Furthermore, the C-C bonds in the rings (when the interaction is favorable) are shortened, indicating more electron density is added to the π bond orbitals between the two carbon atoms, an effect that can be seen in the increased corresponding bond (3,-1) critical point values as compared to those in the free ring systems. The N-N bond does not get shorter in any of the anion-pyridazine ring derivative complexes which result in favorable binding energies. In all cases, the C-X bonds increase in length in the anionic complexes, and in the F- and CN-substituted anionic species, the (3,-1) critical point density value decreases, indicating that these bonds have been destabilized due to the anion- π contacts. This bond lengthening is a result of the increase stabilization of the core ring π -system due to increased electron density obtained from the $[BF_4]^-$ and $[PF_6]^-$ anions.

Clearly, in the results of all three ring systems, the anion is aligned in order to maximize contact with carbon atoms of the ring. Overall, the more F atoms that contact the ring, the more favorable are the binding energies when comparing similar ring derivatives (i.e., the CN-substituted pyridazine and triazine ring derivatives with $[BF_4]^-$ have more favorable binding energies than the CN-substituted tetrazine ring derivative with $[BF_4]^-$), most likely a result of increased anion- π overlap. Although it would seem that the tetrazine ring derivatives + $[BF_4]^-$ (or $[PF_6]^-$) complexes would be more stable if three of the anion F atoms pointed toward the ring plane, this does not appear to be the case. The anion avoids orienting F atoms toward the core N atoms of the rings. The conclusion to be drawn from this observation is that the

anion- π interaction is favorable only when the aromaticity of the ring can be increased. The most likely place for electron density donation is across C-C and C-N ring bonds that do not have all of their binding π orbitals filled. If the anion were to donate density to one of the N ring atoms, this density would reside, in part, across the N-N bond which only has π^* bonding orbitals available to occupy. Thus, anion- π systems that include heteroaromatics and complex anions have strict directionality requirements, namely the anion must be oriented towards the least electronegative atom on the ring in order to provide favorable anion- π overlap.

C. Corrections on Previous Results

It is important to point out some oversights in the literature as well as in our own research. First and foremost, the original study reported by Deyà and coworkers defined an angle of interaction between the anion and the ring system (see Figure 3, Chapter I), namely that the interaction is most favorable if the center point of the anion is directly over the centroid of the anion. While this may be true for halides, complex anions (especially those that are not symmetric such as triflate), do not conform to this standard when heteroaromatic rings are involved in the interaction. This previous study also indicated that the interaction strength could be measured by the distance of the anion to the centroid. The results in this investigation reveal that the distance of the anion from the most electropositive ring atoms is more important, and that the ring centroid is not where the anion is donating its electron density! Recently, a study published by Berryman and coworkers has indicated that this is also true for halide anion- π interactions, and that many of the assumptions previously made by Deyà and coworkers involving the nature of anion- π interactions were flawed.¹³⁶

For the second major correction, as stated in the introduction, the systems examined thus far in this group involve complex tetrahedral and octahedral anions. Originally theorized from the structure analysis in Chapter III, anion- π interactions with tetrazine and pyridazine rings were both thought to have three anion F atoms from the anions interacting with the synthesized complexes based on the F anion atom-ring centroid distances.¹³⁴ These assumptions, while considered sound when examining the evidence obtained through anion- π theoretical studies with halides, were not accurate. Closer examinations of several of the structures obtained both in Chapters II and III reveal our incorrect assumptions. Figures 101, 102, 103, and 104 show several of these structures to help illustrate this point.

The first compound, $[\text{Ni}_4(\text{bptz})_4(\text{CH}_3\text{CN}_8\text{C}\text{BF}_4)[\text{BF}_4]_7]$, (Figure 101, **1**), contains a $[\text{BF}_4]^-$ anion with two distinctly disordered positions.⁸⁹ The original assumption that anion- π interactions were occurring between the anion and the bptz tetrazine rings of this complex was sound, but it was determined from an incorrect distance measurement of the anion F atoms to the centroid of these tetrazine rings. The anion is disordered in such a way that 50% of the time, two of the bptz central tetrazine rings have two F atoms lined up with their carbon atoms, while the other two bptz rings of the structure achieve the same anion- π overlap from the anion in its other disordered position. The actual anion- π contact distances are 2.709-3.017 Å.

Figure 102 shows how the bptz ligand actually interacts with $[\text{PF}_6]^-$ in structure **16**. The same overestimation of anion-F participation was made in Chapter III-but can be seen to be inaccurate after this study. Only two of the F atoms from the anion interact on one side of the ring with F-C distances of 2.976-3.553 Å.

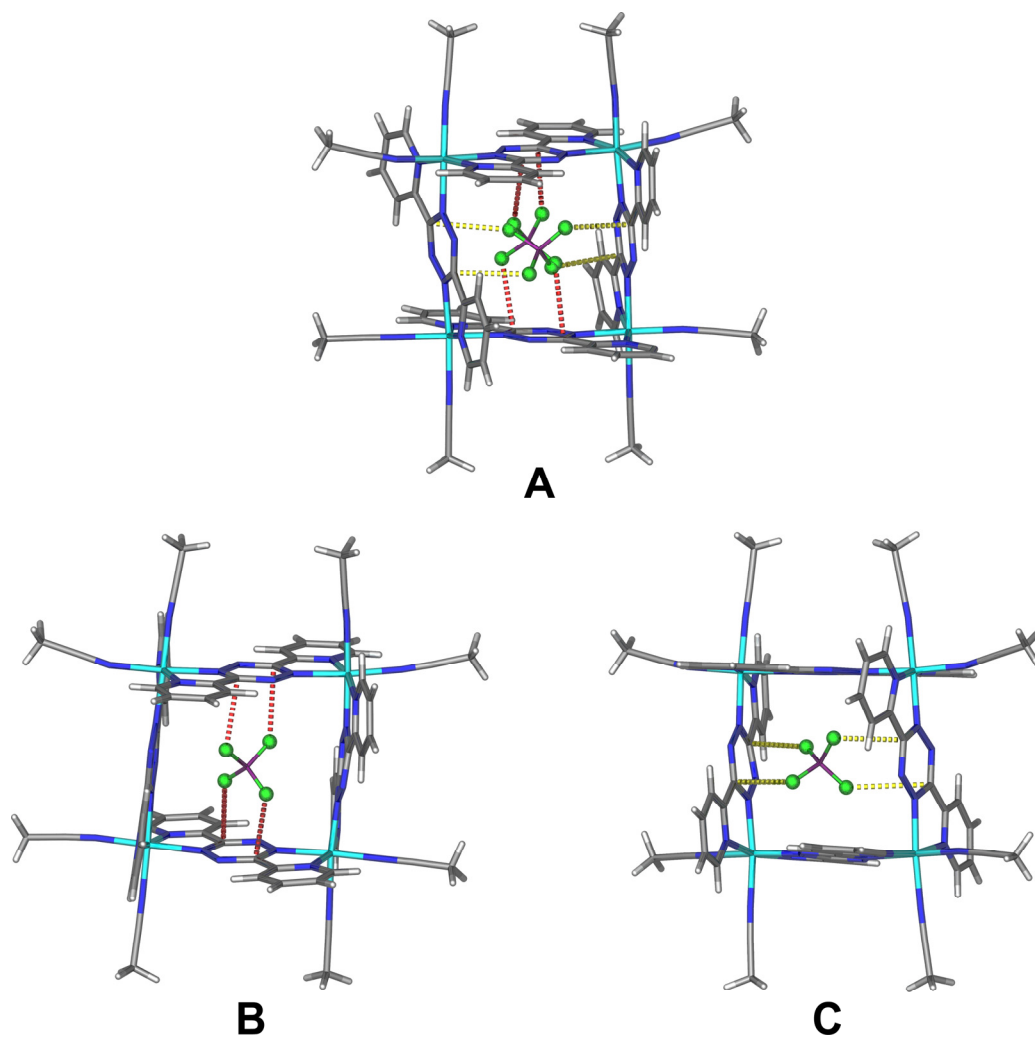


Figure 101: (a) Compound **1** with both encapsulated $[\text{BF}_4]^-$ disorder positions shown, (b) Compound **1** with one $[\text{BF}_4]^-$ disorder position shown with the anion- π contacts between the anion and the tetrazine ring diagrammed with red dashed lines, (anion- π contacts = 2.709-2.971 Å), and (c) Compound **1** with the second $[\text{BF}_4]^-$ disorder position shown with the anion- π contacts between the anion and the tetrazine ring diagrammed with yellow dashed lines, (anion- π contacts = 2.799-3.017 Å)

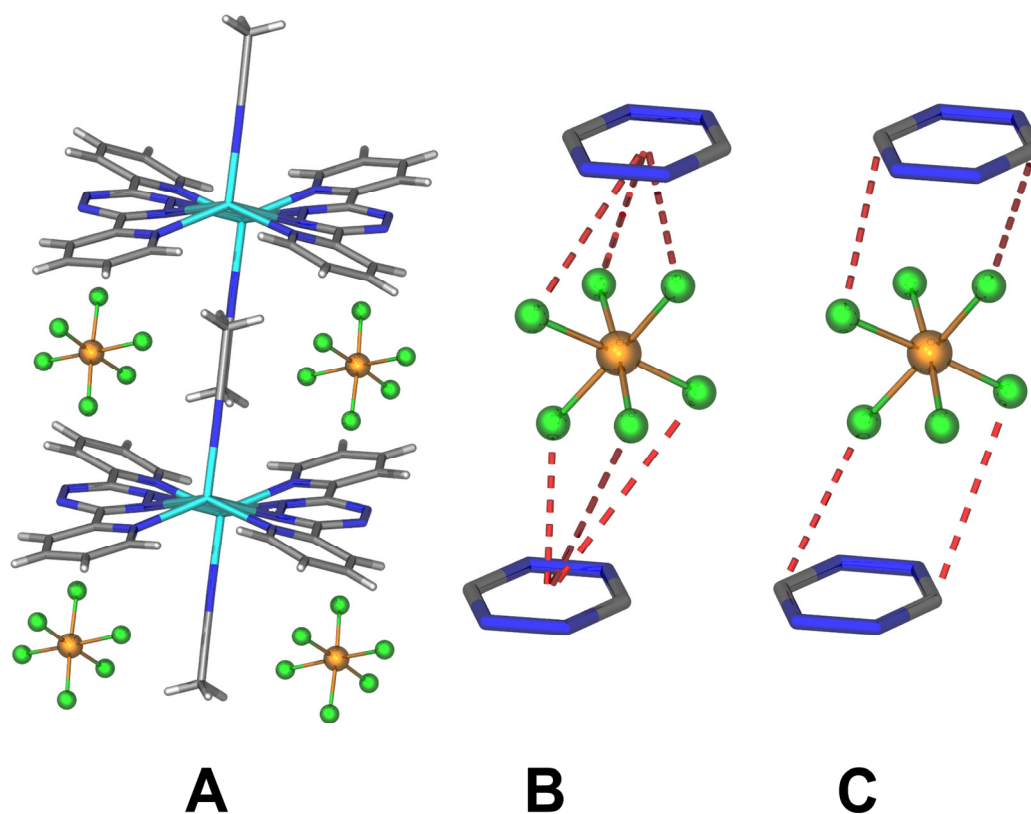


Figure 102: (a) Truncated packing diagram of compound **16**, (b) close-up view of two bptz tetrazine rings interaction with one anion (anion- π contacts shown with red dashed lines) drawn from the F anion atoms to the centroids of the tetrazine rings (F-centroid distances = 3.656, 4.280, 2.785, 2.840, 3.956, and 4.121 Å), and (c) a corrected version of the anion- π contacts between the same two rings (F-C distances = 3.138, 2.976, 3.122, and 3.553 Å)

While this error may seem slight, especially since these distances are clearly short enough for van der Waals overlap between the anion F atoms and the carbon atoms of the bptz tetrazine ring, it brings to light the importance of selecting specific heteroaromatic rings when attempting to induce anion- π interactions.

Structure **17b** described in Chapter III contains bptz tetrazine rings that participate in both an anion- π interactions and π - π stacking interactions at the same time, one on each side of the ring. It is clear from the $[\text{SbF}_6]^-$ position that it is participating in six anion- π interactions at once. In this instance, it seems even more appropriate to draw the anion- π contact to the centroids of the tetrazine ring (distance = 3.260 Å-all six F-centroid distances equivalent). Due to the results obtained in this study, this structure was revisited, and the anion F-tetrazine ring C distances were measured. The two differing distances of 3.249 and 3.698 Å clearly indicate that the anion is interacting with one of the C atoms only, and this contact distance of 3.249 Å is shorter than the distance measured from the F anion atom to the tetrazine ring centroid (3.26 Å - see Figure 103).

Complexes **18-21** in Chapter III also are subject to incorrect anion- π contact analysis. It was speculated that three F-pyridazine ring contacts existed for each anion in these structures, but after the results of this computational study were analyzed, it became appropriate to revisit the anion- π contacts in these structures. A revised analysis revealed that each anion in these structures was only contacting the pyridazine rings of bppn through one F atom (this one atom in close, overlapping contact with 2 carbon atoms at once).

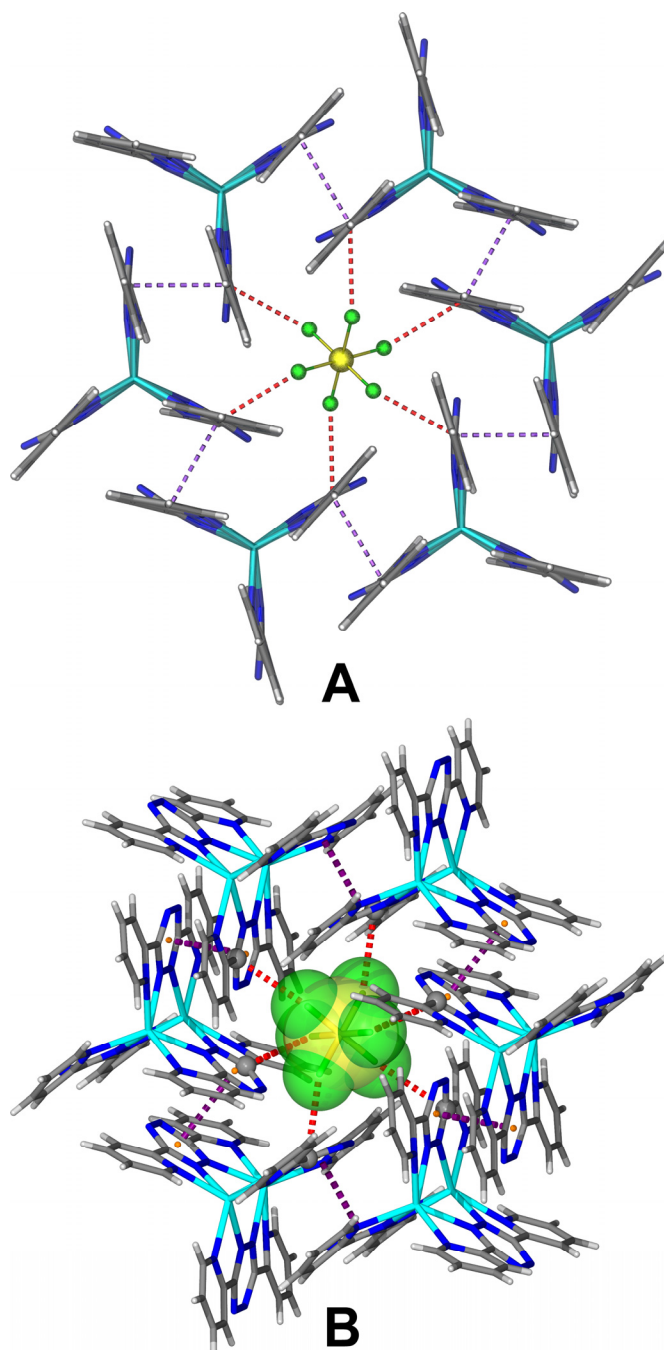


Figure 103: (a) Packing diagram of compound **17b** with anion- π contacts (red dashed lines) drawn from the F anion atoms to the centroids of the tetrazine rings (distance = 3.269 Å), and (b) corrected packing diagram of compound **17b** with the anion- π contacts drawn from the anion F atoms to a carbon atom on the bptz tetrazine rings (distance = 3.249 Å). The carbon atoms that are participating in anion- π contact are shown at a larger scale, and the centroids of the tetrazine rings are indicated with orange spheres.

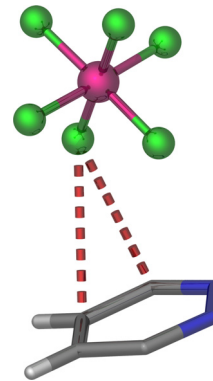
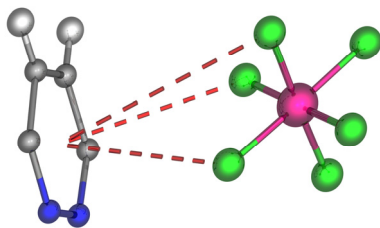
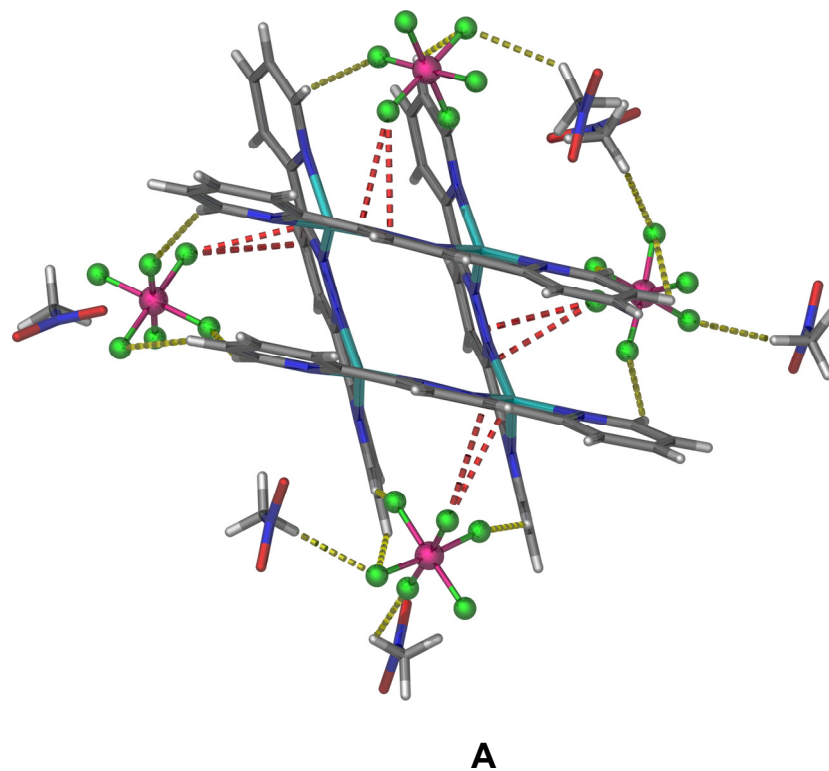


Figure 104: (a) Truncated packing diagram of compound **18** showing the corrected anion- π contacts (red dashed lines) and the multiple hydrogen bond interactions (yellow dashed lines) between the $[\text{PF}_6]^-$ anions and the bppn ligands as well as the hydrogen bond interactions between the anions and nitromethane molecules (yellow dashed lines) in the crystal interstices. (b) Original (incorrect) anion- π contacts speculated in Chapter III for compound **18** from the $[\text{PF}_6]^-$ fluorine atoms to the ring centroid (distances = 2.902-3.181 Å), and (c) corrected F-ring anion- π contacts from compound 17 (anion- π distances = 2.991 and 3.161 Å and 3.124 and 3.240 Å for the two unique $[\text{PF}_6]^-$ anions, respectively).

The majority of the anion contacts were instead participating in hydrogen bond interactions with hydrogen atoms from the bppn ligands or with nitromethane solvent trapped in the structure (See Figure 104 for comparisons and distances).

While these newly measured anion- π contact distances are different than those measured in Chapter III, the conclusions drawn from the results in that chapter are correct. The structures that contain bptz clearly rely strongly on multiple anion- π contacts (or anion- π coupled with strong π - π stacking interactions as in the case of compound **17b**), while those that contain bppn have fewer anion- π contacts, indicating that the complexes only include these interactions due to crystal packing requirements.

When attempting to synthesize complexes that are templated by anion- π interactions, or when designing anion-traps based on these interactions, the anion must be able to position itself to provide maximum overlap with the least electronegative ring atoms. Complex anions, due to their strict geometries, can provide specific contact requirements for such anion- π systems. For example, if a complex is for trapping tetrahedral anions in preference over octahedral anions is desired, a ligand set containing tetrazine rings should be used. Tetrahedral anions can provide maximum anion- π overlap with two tetrazine rings, one ring on each side of this anion being rotated 90° from each other. This geometry is found in compounds **1**, **2**, **3**, and **4**, the Ni and Zn square complexes (See Figures 35, 36, 37, and 103). For octahedral anions, an environment with excess triazine rings would be more appropriate since the anion can face two of these ring planes on opposite sides and still engage in 3 anion F atom-C atom ring contacts.

V. Conclusions

This chapter reports computational results that the symmetry of heteroaromatic rings have on anion- π interactions with tetrahedral and octahedral anions. The major conclusion is that the least electronegative atoms on the ring core, and thus the symmetry of the positive regions of the electrostatic potential of the rings, is an indication that specific ring systems can be tailored to trap specifically shaped anions. Other ring systems, such as the benzene derivatives as well as the N_6 ring, provide interesting possibilities for future studies. Furthermore, complex anions with no clear symmetry need to be investigated in the same manner to lend more evidence to these conclusions as well as to determine the aromatic ring systems that are appropriate to trap such anions.

CHAPTER V

CONCLUSIONS*

Within five short years, anion- π interactions have captured the attention of the supramolecular chemistry community. The results presented herein indicate that, while anion- π interactions involving large complex anions are indeed instrumental in the self-assembly interactions with π -acidic ring systems, they are not structured in the same manner as those involving spherical halide anions.

Chapter II details initial investigations into the anion-template process involving anion- π interactions. Several previously reported structures from our group showed evidence for considerable influence on the part of the anion during the self-assembly process.^{48,49} In order to determine if the anion is indeed the final controlling element in the self-assembly of these compounds, reactions of 3,6-bis(2-pyridyl)-1,2,4,5-tetrazine (bptz) with solvated first-row transition metals M(II) (M(II) = Ni(II), Zn(II), Mn(II), Fe(II), Cu(II)) were explored with an emphasis on the factors that influence the identity of the resulting cyclic products for Ni(II) and Zn(II).⁸⁹

*Portions reproduced with permission from “Anion Template Effect on the Self-Assembly and Introconversion of Metallacyclophanes” by Cristian Saul Campos-Fernández, Brandi L. Schottel, Helen T. Chifotides, Jitendra K. Bera, John Bacsá, John M. Koomen, David H. Russel, and Kim R. Dunbar, *J. Am. Chem. Soc.* **2005**, *127*, 12909-12923, and (2) “Anion- π Interactions as Controlling Elements in Self-Assembly Reactions of Ag(I) Complexes with π -Acidic Ring Systems” by Brandi L. Schottel, Helen T. Chifotides, Mikhail Shatruk, Abdellatif Chouai, Lisa M. Pérez, John Bacsá, and Kim R. Dunbar *J. Am. Chem. Soc.* **2006**, *128*, 5895-5912.

The results demonstrate that relatively small anions of similar volume and geometry, namely $[\text{ClO}_4]^-$ and $[\text{BF}_4]^-$, lead to the formation of molecular squares of general formulae $[\text{M}_4(\text{bptz})_4(\text{CH}_3\text{CN})_8\text{cX}][\text{X}]_7$, ($\text{M} = \text{Zn}(\text{II}), \text{Ni}(\text{II}); \text{X} = [\text{BF}_4]^-, [\text{ClO}_4]^-$), whereas the larger anion $[\text{SbF}_6]^-$ favors the molecular pentagon $[\{\text{Ni}_5(\text{bptz})_5(\text{CH}_3\text{CN})_{10}\}\text{cSbF}_6][\text{SbF}_6]_9$. The molecular pentagon is capable of easily converting to the square in the presence of excess $[\text{BF}_4]^-$, $[\text{ClO}_4]^-$ and $[\text{I}]^-$ anions, whereas the Ni(II) square can be partially converted to the less stable cyclic pentagon under more harsh conditions, in the presence of excess $[\text{SbF}_6]^-$ ions. No evidence for the presence of the molecular square in equilibrium with the pentagon was observed in the ESI mass spectra of the individual square and pentagon samples. The reaction of bptz with $[\text{Ni}(\text{CH}_3\text{CN})_6][\text{NO}_3]_2$ does not afford a crystalline product, but ESI-MS studies of the sample indicate that it is trinuclear in nature. Anion exchange reactions of the encapsulated ion in $[\{\text{Ni}_4(\text{bptz})_4(\text{CH}_3\text{CN})_8\}\text{cClO}_4][\text{ClO}_4]_7$ indicate that a larger anion such as $[\text{IO}_4]^-$ cannot replace $[\text{ClO}_4]^-$ inside the cavity, but the linear $[\text{Br}_3]^-$ anion is also capable of doing so. Although X-ray structures were not obtained for the products of bptz reactions with Mn(II), Fe(II) and Cu(II) in the presence of $[\text{ClO}_4]^-$ anions, mass spectral studies support the conclusion that these ions also produce molecular squares. Evidence gleaned from these results is presented as confirmation that these structures are predominantly controlled by the presence of a specifically-shaped and sized anion.

In Chapter III, it is shown that these previously mentioned complexes were ultimately controlled by anion- π interactions through the examination of Ag(I) compounds with bptz and bppn (3,6-bis(2'-pyridyl)-1,2-pyridazine), in the presence

of specific complex anions.¹³⁷ Reactions of bptz and bppn with the AgX salts [X]⁻ ([PF₆]⁻, [AsF₆]⁻, [SbF₆]⁻, and [BF₄]⁻) afforded complexes of different structural motifs depending on the π -acidity of the ligand central ring and the outer-sphere anion. The bptz reactions led to the polymeric {[Ag(bptz)][PF₆]}_∞ (**13**) and the dinuclear compounds [Ag₂(bptz)₂(CH₃CN)₂][PF₆]₂ (**14**) and [Ag₂(bptz)₂(CH₃CN)₂][AsF₆]₂ (**15**), as well as the propeller-type species [Ag₂(bptz)₃][AsF₆]₂ (**16**)⁸³ and [Ag₂(bptz)₃][SbF₆]₂ (**17a** and **17b**). Reactions of bppn with AgX produced the grid-type structures [Ag₄(bppn)₄][X]₄ (**18-21**), regardless of the anion present. In **18-21**, π - π stacking interactions were maximized, whereas multiple and shorter (therefore stronger) anion- π interactions between the anions and the tetrazine rings were established in **13-17b**. These differences reflect the more electron-rich character of the bppn pyridazine ring as compared to the bptz tetrazine ring. The evidence gleaned from the solid-state structures was corroborated by density functional theory calculations. In the electrostatic potential maps of the free ligands, a higher positive charge was present in the bptz as compared to the bppn central ring. Furthermore, the electrostatic potential maps of **15**, **16**, and **17b** indicated an electron density transfer from the anions to the π -acidic rings. Conversely, upon addition of the [AsF₆]⁻ ions to the cation of **19**, there was negligible change in the electron density of the central pyridazine ring, which supports the presence of weaker anion- π interactions in the bppn as compared to the bptz complexes. It was concluded that anion- π interactions play an important role in the outcome of self-assembly reactions that involve bptz, while those systems which include bppn rely heavily on π - π interactions, an effect that most likely results from the strong π -acidic character of the central tetrazine ring of bptz in comparison to the central pyridazine ring of bppn.

These studies provide strong evidence that complexes including bptz rely heavily on anion- π interactions during the self-assembly process, but the results could not be reasonably compared to the existing computational results of anion- π interactions in the literature due to the use of large complex anions. A computational study of anion- π interactions involving these multi-atomic anions does not exist for comparison with the studies examined in Chapters II and III. Chapter IV is an excellent start on filling this gap in anion- π research by examining a series of heteroaromatic π -systems of differing π -acidic character in the presence of $[\text{BF}_4]^-$ (as a representative of tetrahedral anions) or $[\text{PF}_6]^-$ (as an octahedral representative). The π -systems examined, pyridazine, *s*-triazine, and *s*-tetrazine, were substituted with bromine, chlorine, fluorine, and cyanide in order to provide several systems with varying degrees of π -acidity without the complications of hydrogen-bond interactions. The results indicate that the rules governing anion- π interactions involving halides are different than those that direct the participation of complex anions, and some of the assumptions made in the Chapter III about anion position and strength based on computational studies of halides participating in anion- π interactions, while viable, were incorrect. The presented results lay out new rules to describe the different nature of anion- π interactions involving multi-atomic anions in the presence of heteroaromatic ring systems and could possibly assist in the design of systems to trap complex anions.

While many results that help explain the importance and nature of anion- π reactions are presented in the literature as well as in this dissertation,¹³⁸ more work clearly needs to be performed. Future work on the chemistry presented will include computational examinations of systems involving one complex anion and two π -

acidic ring systems as well as the opposite (two anions with one ring system). Due to the bond lengthening and shortening trends seen in the results of favorable and unfavorable anion- π interactions from Chapter III, a thorough examination of the orbitals involved in anion- π interactions between complex anions and heteroaromatic ring systems needs to be performed. Furthermore, austere one ring-one anion systems should be studied experimentally (*e.g.*, [(*n*-Bu)₄N][BF₄] crystallized in the presence of C₂N₄(CN)₂) to provide simpler systems for comparison with the computational data.

Recently, the need for more thorough fundamental studies on anion- π interactions was made evident by a new literature communication on the use of anion- π interactions in synthetic transport systems through a trans-membrane lipid bilayer.¹³⁹ This π -acidic “anion- π slide” based on oligo-(*p*-phenylene)-*N,N*-naphthalenediimide molecules was shown to selectively transport [Cl]⁻ anions over other halide anions. Although this is only the first example in which anion- π interactions have been invoked for use, it hints that they could have a large impact on various areas of chemistry.

REFERENCES

1. Steed, J. W.; Atwood, J. L. *Supramolecular Chemistry: A Concise Introduction*; Wiley-VCH: Chichester, UK, 2000.
2. Pedersen, C. J. *J. Am. Chem. Soc.* **1967**, *89*, 7017.
3. Park, H.E.; Simmons, H.E. *J. Am. Chem. Soc.* **1968**, *90*, 2431.
4. Bell, R.A.; Christoph, G.G.; Fronczek, F.R.; Marsh, R.E. *Science* **1975**, *190*, 151.
5. (a) Yang, X.; Knobler, C.B.; Hawthorne, M.F. *Angew. Chem. Int. Ed. Engl.* **1991**, *30*, 1507. (b) Zheng, A.; Knobler, C.B.; Hawthorne, M.F. *J. Am. Chem. Soc.* **1995**, *117*, 5105.
6. Kang, S. O.; Hossain, Md. A.; Bowman-James, K. *Coord. Chem. Rev.* **2006**, *250*, 3038-3052. (b) Bowman-James, K. *Acct. Chem. Res.* **2005**, *38*, 671.
7. (a) Steed, J. W. *Chem. Commun.* **2006**, *25*, 2637. (b) Steed, J. W.; Wallace, K. J. *Adv. in Supramol. Chem.* **2003**, *9*, 219.
8. Vilar, R. *Angew. Chem. Int. Ed.* **2003**, *42*, 1460.
9. Bianchi, A.; Garcia-Espana, E. *Thermodynamics of Anion Complexation*, in *Supramolecular Chemistry of Anions*; Bianchi, A.; Bowman-James, K.; García-Espana, E., Eds.; Wiley-VCH: New York, NY, 1997; 217.
10. (a) Hosseini, M. W. Lehn, J.-M. *J. Am. Chem. Soc.* **1982**, *104*, 3525. (b) Dhaenens, M.; Lehn, J.-M.; Vigneron, J.-P. *J. Chem. Soc., Perkin Trans.* **1993**, *2*, 1379. (c) Schmidtchen, F. P. *J. Am. Chem. Soc.* **1986**, *108*, 8249.
11. Lehn, J.-M. *Supramolecular Chemistry: Concepts and Perspectives*, Wiley-VCH: New York, 1995.
12. (a) Alkorta, I.; Rozas, I.; Elguero, J. *J. Am. Chem. Soc.* **2002**, *124*, 8593. (b) Mascal, M.; Armstrong, A.; Bartberger, M. D. *J. Am. Chem. Soc.* **2002**, *124*, 6274. (c) Quiñero, D.; Garau, C.; Rtooger, C.; Frontera, A.; Ballester, P.; Costa, A.; Deyà, P. M. *Angew. Chem. Int. Ed.* **2002**, *41*, 3389.
13. Schnieder, H.-J.; Schiestel, T.; Zimmeremann, P. *J. Am. Chem. Soc.* **1992**, *114*, 7698.

14. Moller, C; Plesset, M. S. *Phys. Rev.* **1934**, *46*, 618. (b) Head-Gordon, M.; Pople, J. A.; Frisch, M. J. *J. Chem. Phys. Lett.* **1988**, *153*, 503.
15. Hehre, W. J.; Ditchfield R.; Pople, J. A. *J. Chem. Phys.* **1972**, *56*, 2257.
16. Roothan, C. C. J. *Rev. Mod. Phys.*, **1951**, *23*, 69. (b) Pople, J. A.; Nesbet, R. K. *J. Chem. Phys.* **1954**, *22*, 571. (c) MeeWeeny, R; Dierksen, G. *J. Chem. Phys.* **1968**, *49*, 4852.
17. (a) Ditchfield, R.; Hehre, W. J.; Pople, J. A. *J. Chem. Phys.* **1971**, *54*, 724. (b) Hehre, W. J.; Ditchfield, R.; Pople, J. A. *J. Chem. Phys.* **1972**, *56*, 2257. (c) Hariharan P. C.: Pople, J. A. *Mol. Phys.* **1974**, *27*, 209. (d) Gordon, M. S. *Chem. Phys. Lett.* **1980**, *76*, 163. (e) Hariharan P. C.; Pople, J. A. *Theo. Chim. Acta* **1973**, *28*, 213. (f) Blaudeau, J.-P.; McGrath, M. P.; Curtiss, L. A.; Radom, L. *J. Chem. Phys.* **1997**, *107*, 5016. (g) Francl, M. M.; Pietro, W. J.; Hehre, W. J.; Binkley, J. S.; DeFrees, D. J.; Pople, J. A.; Gordon, M. S. *J. Chem. Phys.* **1982**, *77*, 3654-. (h) Binning R. C., Jr.; Curtiss, L. A. *J. Comp. Chem.* **1990**, *11*, 1206. (i) Rassolov, V. A.; Pople, J. A.; Ratner, M. A.; Windus, T. L. *J. Chem. Phys.* **1998**, *109*, 1223. (j) Rassolov, V. A.; Ratner, M. A.; Pople, J. A.; Redfern, P.C.; Curtiss, L. A. *J. Comp. Chem.* **2001**, *22*, 976. (k) Curtiss, L. A.; McGrath, M. P.; Blaudeau, J.-P.; Davis, N. E.; Binning. R. C. Jr.; Radom, L. *J. Chem. Phys.* **1995**, *103*, 6104. (l) McGrath M. P.; Radom, L. *J. Chem. Phys.* **1991**, *94*, 511.
18. (a) Bader, R. F. W. *Atoms in Molecules. A Quantum Theory*; Clarendon: Oxford, U.K., 1994. (b) Bader, R. F. W. *Chem. Rev.* **1985**, *18*, 9.
19. Hernandez, B.; Orozco, M; Luque, F. J. *J. Comput.-Aided Mol. Des.* **1997**, *11*, 153.
20. Luque, F.; Orozco, M J. *J. Comput. Chem.* **1993**, *14*, 587.
21. Garau, C.; Quiñonero, D.; Frontera, A.; Ballester, P.; Costa, A.; Deyà, P. M. *New J. Chem.* **2003**, *27*, 211.
22. Besler, B. H.; Merz, K. M; Kollman, P. A. *J. Comput. Chem.* **1990**, *11*, 431.
23. Garau, C.; Quiñonero, D.; Frontera, A.; Costa, A.; Ballester, P.; Deyà, P. M. *Chem. Phys. Lett.* **2003**, *370*, 7.
24. McLean A. D.; Chandler, G. S. *J. Chem. Phys.* **1980**, *72*, 5639-5648. (b) Krishnan, R.; Binkley, J. S.; Seeger, R.; Pople, J. A. *J. Chem. Phys.* **1980**, *72*, 650.
25. Garau, C.; Frontera, A.; Quiñonero, D.; Ballester, P; Costa, A.; Deyà, P. M. *ChemPhysChem* **2003**, *4*, 1344.

26. Garau, C.; Frontera, A.; Quiñonero, D.; Ballester, P.; Costa, A.; Deyà, P. M. *Chem. Phys. Lett.* **2003**, *382*, 534.
27. Kim, D.; Tarakeshwar, P.; Kim, K. S. *J. Phys. Chem. A* **2004**, *108*, 1250.
28. Jeziorski, B.; Szalewicz, K.; In *Encyclopedia of Computational Chemistry*; Schleyer, P. v. R., Allinger, N. L., Clark, T., Gasteiger, J., Kollman, P. A., Schaefer, H. F., III, Schreiner, P. R., Eds.; Wiley: Chichester, U.K., 1998.
29. Kim, K. S.; Tarakeshwar, P.; Lee, J. Y. *Chem. Rev.* **2000**, *100*, 4145.
30. Garau, C.; Frontera, A.; Quiñonero, D.; Ballester, P.; Costa, A.; Deyà, P. M. *J. Phys. Chem. A* **2004**, *108*, 9423.
31. Schleyer, P. v. R.; Maerker, C.; Dransfeld, A.; Jial, H.; Hommes, N. J. v. E. *J. Am. Chem. Soc.* **1996**, *118*, 6317.
32. Garau, C.; Quiñonero, D.; Frontera, A.; Ballester, P.; Costa, A.; Deyà, P. M. *J. Phys. Chem. A* **2005**, *109*, 9341.
33. (a) Feyereisen, M. W.; Fitzgerald, G.; Komornicki, A. *Chem. Phys. Lett.* **1993**, *208*, 359. (b) Vahtras, O.; Almlöf, J.; Feyereisen, M. W. *Chem. Phys. Lett.* **1993**, *213*, 514.
34. Mulliken, R. S. *J. Chem. Phys.* **1962**, *36*, 3428.
35. Demeshko, S.; Dechert, S.; Meyer, F. *J. Am. Chem. Soc.* **2004**, *126*, 4508.
36. de Hoog, P.; Gamez, P.; Mutikainen, I.; Turpeinen, U.; Reedijk, J. *Angew. Chem. Int. Ed.* **2004**, *43*, 5815.
37. Furkawa, S.; Okubo, T.; Masaoka, S.; Tanaka, D.; Chang, H.; Kitagawa, S. *Angew. Chem. Int. Ed.* **2005**, *44*, 2700.
38. Gamez, P.; van Albada, G. A.; Multikainen, I.; Tupeinen, U.; Reedijk, J. *Inorg. Chem. Acta.* **2005**, *358*, 197.
39. Dorn, T.; Janiak, C.; Abu-Shandi, K. *CrystEngComm* **2005**, *7*, 633.
40. Frontera, A.; Saczewski, F.; Gdaniec, M.; Dziemidowicz, B.; Kurland, A.; Deyà, P. M.; Quiñonero, D.; Garau, C. *Chem. Eur. J.* **2005**, *11*, 6560.
41. Mahewswari, P. U.; Modéc, B.; Pevec, A.; Kozlevčar, B.; Massera, C.; Gamez, P.; Reedijk, J. *Inorg. Chem.* **2006**, *45*, 6637.
42. Casells, H.; Massera, C.; Buda, F.; Gamez, P.; Reedijk, J. *New J. Chem.* **2006**, *30*, 1561.

43. Maeda, H.; Osuka, A.; Furuta, H. *J. Incl. Phenom. Macrocycl. Chem.* **2004**, *49*, 33.
44. Rosokha, Y. S.; Lindeman, S. V.; Rosokha, S. V.; Kochi, J. K. *Angew Chem. Int. Ed.* **2004**, *43*, 4650.
45. Canceill, J.; Cesario, M.; Collet, A.; Guilhe, J.; Lacombe, L.; Lozach, B.; Pascard, C. *Angew. Chem., Int. Ed. Engl.* **1989**, *28*, 1246.
46. Fairchild, R. M.; Holman, K. T. *J. Am. Chem. Soc.* **2005**, *127*, 16364.
47. Berryman, O. B.; Hof, F.; Hynes, M. J.; Johnson, D. W. *Chem. Commun.* **2006**, 506.
48. Campos-Fernández, C. S.; Clérac, R.; Dunbar, K. R. *Angew. Chem., Int. Ed.* **1999**, *38*, 3477.
49. Campos-Fernández, C. S.; Clérac, R.; Koomen, J. M.; Russell, D. H.; Dunbar, K. R. *J. Am. Chem. Soc.* **2001**, *123*, 773.
50. (a) Leininger, S.; Olenyuk, B.; Stang, P. J. *Chem. Rev.* **2000**, *100*, 853. (b) Davis, A. V.; Yeh, R. M.; Raymond, K. N. *Proc. Natl. Acad. Sci. USA* **2002**, *99*, 4793.
51. (a) Mukherjee, P. S.; Min, K. S.; Arif, A. M.; Stang, P. J. *Inorg. Chem.* **2004**, *43*, 6345. (b) Addicott, C.; Das, N.; Stang, P. J. *Inorg. Chem.* **2004**, *43*, 5335. (c) Atwood, J. L.; Barbour, L. J.; Dalgarno, S. J.; Hardie, M. J.; Raston, C. L.; Webb, H. R. *J. Am. Chem. Soc.* **2004**, *126*, 13170. (d) Hanan, G. S.; Volkmer, D.; Lehn, J.-M. *Can. J. Chem.* **2004**, *82*, 1428. (e) Uppadine, L. H.; Lehn, J.-M. *Angew. Chem. Int. Ed.* **2004**, *43*, 240. (f) Kryschenko, Y. K.; Seidel, S. R.; Muddiman, D. C.; Nepomuceno, A. I.; Stang, P. J. *J. Am. Chem. Soc.* **2003**, *125*, 9647. (g) Kryschenko, Y. K.; Seidel, S. R.; Arif, A. M.; Stang, P. J. *J. Am. Chem. Soc.* **2003**, *125*, 5193. (h) Patroniak, V.; Baxter, P. N. W.; Lehn, J.-M.; Kubicki, M.; Nissinen, M.; Rissanen, K. *Eur. J. Inorg. Chem.* **2003**, 4001. (i) Goshe, A. J.; Steele, I. M.; Ceccarelli, C.; Rheingold, A. L.; Bosnich, B. *Proc. Nat. Acad. Sci. USA* **2002**, *99*, 4823. (j) Oxtoby, N. S.; Blake, A. J.; Champness, N. R.; Wilson, C. *Proc. Nat. Acad. Sci. USA*, **2002**, *99* 4905. (k) Kuehl, C. J.; Kryshenko, Y. K.; Radhakrishnan, U.; Seidel, S. R.; Huang, S. D.; Stang, P. J. *Proc. Natl. Acad. Sci. USA* **2002**, *99*, 4932. (l) Holliday, B. J.; Mirkin, C. A. *Angew. Chem. Int. Ed.* **2001**, *40*, 2022. (m) Eddaoudi, M.; Moler, D. B.; Li, H.; Chen, B.; Reineke, T. M.; O'Keeffe, M.; Yaghi, O. M. *Acc. Chem. Res.* **2001**, *34*, 319. (n) Kim, J.; Chen, B.; Reineke, T. M.; Li, H.; Eddaoudi, M.; Moler, D. B.; O'Keeffe, M.; Yaghi, O. M. *J. Am. Chem. Soc.* **2001**, *123*, 8239. (o) Cotton, F. A.; Lin, C.; Murillo, C. A. *Acc. Chem. Res.* **2001**, *34*, 759. (p) Bera, J. K.; Smucker, B. W.; Walton, R. A.; Dunbar, K. R. *Chem. Commun.* **2001**, 2562. (q) Greig, L. M.; Philip, D.

- Chem. Soc. Rev.* **2001**, *30*, 287. (r) Johnson, D. W.; Raymond, K. N. *Supramol. Chem.* **2001**, *13*, 639. (s) Swiegers, G. F.; Malefetse, T. J. *Chem. Rev.* **2000**, *100*, 3483. (t) Caulder, D. L.; Raymond, K. N. *Acc. Chem. Res.* **1999**, *32*, 975. (u) Jones, C. J. *Chem. Soc. Rev.* **1998**, *27*, 289. (v) Linton, B.; Hamilton, A. D. *Chem. Rev.* **1997**, *97*, 1669. (w) Baxter, P. N. W. In *Comprehensive Supramolecular Chemistry*, Atwood, J. L.; Davies, J. E. D.; MacNicol, D. D.; Vogtle, F.; Lehn, J.-M., Eds., Pergamon: Oxford, 1996, Vol. 9, p 165.
52. Olenyuk, B.; Fechtenkötter, A.; Stang, P. J. *J. Chem. Soc. Dalton Trans.* **1998**, 1707.
53. Claderone, C. T.; Williams, D. H. *J. Am. Chem. Soc.* **2001**, *123*, 6262.
54. (a) Kuehl, C. J.; Huang, S. D.; Stang, P. J. *J. Am. Chem. Soc.* **2001**, *123*, 9634. (b) Yamamoto, T.; Arif, A. M.; Stang, P. J. *J. Am. Chem. Soc.* **2003**, *125*, 12309.
55. Müller-Dethlefs, K.; Hobza, P. *Chem. Rev.* **2000**, *100*, 143.
56. Heintz, R. A.; Smith, J. A.; Szalay, P. S.; Weisgerber, A.; Dunbar, K. R.; *Inorg. Synth.* **2002**, *33*, 75.
57. Geldard, J. F.; Lions, F. *J. Org. Chem.* **1965**, *30*, 318.
58. ISOPRO3.0: Senko, M. Sunnyvale, CA; <http://members.aol.com/msmssoft>.
59. SAINT, Program for area detector absorption correction, Siemens Analytical X-Ray Instruments Inc., Madison, WI 53719, USA, 1994-1996.
60. G. M. Sheldrick, SADABS, Program for Siemens area detector absorption correction, University of Göttingen, Göttingen, Germany, 1996.
61. Barbour, L. J. X-Seed, Graphical interface to SHELX-97 and POV-Ray, 1999 (<http://www.x-seed.net>).
62. Sheldrick, G. M. SHELXS-97. *A Program for Crystal Structure Solution*. University of Göttingen, Germany, 1997; Sheldrick, G. M. SHELXL-97. *A Program for Crystal Structure Refinement*. Univ. of Göttingen, Göttingen, Germany, 1997.
63. Spek, A. L. PLATON, University of Utrecht, The Netherlands, 2001.
64. Nardelli, M. PARST, *J. Appl. Crystallogr.* **1995**, *28*, 659.
65. Flack, H. D. *Acta Crystallogr.* **1983**, *A39*, 876.

66. A previous report in the literature describes the synthesis and molecular structure of $[\text{Zn}_4(\text{bptz})_4(\text{H}_2\text{O})_4(\text{CH}_3\text{CN})_4][\text{ClO}_4]_8 \cdot 2\text{CHCl}_3 \cdot 4\text{CH}_3\text{CN}$; Bu, X.-H.; Morishita, H.; Tanaka, K.; Biradha, K.; Furusho, S.; Shionoya, M. *Chem. Commun.* **2000**, 971.
67. Mingos, D. M. P.; Rohl, A. L. *Inorg. Chem.* **1991**, *30*, 3769.
68. (a) Dijt, F. J.; Canters, G. W.; den Hartog, J. H. J.; Marcelis, A. T. M.; Reedijk, J. *J. Am. Chem. Soc.* **1984**, *106*, 3644. (b) Kong, P. C.; Theophanides, T. *Inorg. Chem.* **1974**, *13*, 1981.
69. (a) Ting, Y.; Lai, Y.-H. *J. Am. Chem. Soc.* **2004**, *126*, 909. (b) Burgeson, J. R.; Renner, M. K.; Hardt, I.; Ferrence, G. M.; Standard, J. M.; Hitchcock, S. R. *J. Org. Chem.* **2004**, *69*, 727.
70. Amouri, H.; Rager, M. N.; Cagnol, F.; Vaissermann, J. *Angew. Chem. Int. Ed.* **2001**, *40*, 3636.
71. Fleming, J. S.; Mann, K. L. V.; Carraz, C.-A.; Psillakis, E.; Jeffrey, J. C.; McCleverty, J. A.; Ward, M. D. *Angew. Chem. Int. Ed.* **1998**, *37*, 1279.
72. Gillespie, R. J.; Hartman, J. S.; Parekh, M. *Can. J. Chem.* **1968**, *46*, 1601.
73. Parac, T. N.; Caulder, D. L.; Raymond, K. N. *J. Am. Chem. Soc.* **1998**, *120*, 8003.
74. Mann, S.; Huttner, G.; Zsolnai, L.; Heinze, K. *Angew. Chem. Int. Ed. Engl.* **1996**, *35*, 2808.
75. Nakamoto, K. *Infrared and Raman Spectra of Inorganic and Coordination Compounds*, John Wiley: New York, 1997.
76. Johnson, A.; Taube, H. *J. Indian Chem. Soc.* **1989**, *66*, 503.
77. While performing mass spectrometric studies on inorganic complexes associated with $[\text{BF}_4]^-$ and $[\text{PF}_6]^-$ anions, ion peaks that could be assigned only as fluoride adducts, due to their isotopic patterns and molecular masses, were observed.
78. Su, C.-Y.; Cai, Y.-P.; Chen, C.-L.; Lissner, F.; Kang, B.-S.; Kaim, W. *Angew. Chem. Int. Ed.* **2002**, *41*, 3371.

79. (a) Takeda, N.; Umemoto, K.; Yamaguchi, K.; Fujita, M. *Nature* **1999**, 398, 794. (b) Fujita, M.; Nagao, S.; Ogura, K. *J. Am. Chem. Soc.* **1995**, 117, 1649. (c) Xu, J.; Parac, T. N.; Raymond, K. N. *Angew. Chem. Int. Ed.* **1999**, 38, 2878.
80. Paul, R. L.; Bell, R. Z.; Jeffery, J. C.; McCleverty, J. A.; Ward, M. D. *Proc. Natl. Acad. Sci. USA*, **2002**, 99, 4883.
81. (a) Tabellion, F. M.; Seidel, S. R.; Arif, A. M.; Stang, P. J. *J. Am. Chem. Soc.* **2001**, 123, 11982. (b) Ellis, W. W.; Schmitz, M.; Arif, A. M.; Stang, P. J. *Inorg. Chem.* **2000**, 39, 2547.
82. Steed, J. W.; Juneja, R. K.; Atwood, J. L. *Angew. Chem. Int. Ed.* **1994**, 33, 2456.
83. Schottel, B. L.; Bacsá, J.; Dunbar, K. R. *Chem. Comm.* **2005**, 46.
84. Meyer, E. A.; Castellano, R. K.; Diederich, F. *Angew. Chem. Int. Ed.* **2003**, 42, 1210.
85. Ma, J. C.; Dougherty, D. A. *Chem. Rev.* **1997**, 97, 1303.
86. Schneider, H. J.; Blatter, T.; Palm, B.; Pfingstag, U.; Ruediger, V.; Theis, I. *J. Am. Chem. Soc.* **1992**, 114, 7704.
87. Schneider, H. J. *Angew. Chem.* **1991**, 103, 1419.
88. Maeda, H.; Furuta, H. *J. Porphyrins Phthalocyanines* **2004**, 8, 67.
89. Campos-Ferandez, C. S.; Schottel, B. L.; Chifotides, H. T.; Bera, J. T.; Bacsá, J.; Koomen, J. M.; Russel, D. H.; Dunbar, K. R. *J. Am. Chem. Soc.* **2005**, 127, 12909.
90. Khlobystov, A. N.; Blake, A. J.; Champness, N. R.; Lemenovskii, D. A.; Majouga, A. G.; Zyk, N. V.; Schröder, M. *Coord. Chem. Rev.* **2001**, 222, 155.
91. Cortez, S. M.; Raptis, R. G. *Coord. Chem. Rev.* **1998**, 169, 363.
92. Marquis, A.; Kintzinger, J.-P.; Graff, R.; Baxter, P. N. W.; Lehn, J.-M. *Angew. Chem. Int. Ed.* **2002**, 41, 2760.
93. Weissbuch, I.; Baxter, P. N. W.; Kuzmenko, I.; Cohen, H.; Cohen, S.; Kjaer, K.; Howes, P. B.; Als-Nielsen, J.; Lehn, J.-M.; Leiserowitz, L.; Lahav, M. *Chem. Eur. J.* **2000**, 6, 725.
94. Baxter, P. N. W.; Lehn, J.-M.; Baum, G.; Fenske, D. *Chem. Eur. J.* **2000**, 6, 4510.

95. Baxter, P. N. W.; Lehn, J.-M.; Kneisel, B. O.; Fenske, D. *Angew. Chem. Int. Ed. Engl.* **1997**, *36*, 1978.
96. Oxtoby, N. S.; Blake, A. J.; Champness, N. R.; Wilson, C. *Proc. Natl. Acad. Sci. USA*, **2002**, *99*, 4905.
97. Baxter, P. N. W.; Lehn, J.-M.; Fischer, J.; Youinou, M.-T. *Angew. Chem. Int. Ed. Engl.* **1994**, *33*, 2284.
98. Ruben, M.; Rojo, J.; Romero-Salguero, F. J.; Uppadine, L. H.; Lehn, J.-M. *Angew. Chem. Int. Ed.* **2004**, *43*, 3644.
99. Withersby, M. A.; Blake, A. J.; Champness, N. R.; Cooke, P. A.; Hubberstey, P.; Li, W.-S.; Schröder, M. *Cryst. Eng.* **1999**, *2*, 123.
100. Hannon, M. J.; Painting, C. L.; Plummer, E. A.; Childs, L. J.; Alcock, N. W. *Chem. Eur. J.* **2002**, *8*, 2225.
101. Min, K. S.; Suh, M. P. *J. Am. Chem. Soc.* **2000**, *122*, 6834.
102. Constable, E. C.; Housecroft, C. E.; Kariuki, B. M.; Kelly, N.; Smith, C. B. *C. R. Chimie*, **2002**, *5*, 425.
103. Constable, E. C.; Housecroft, C. E.; Kariuki, B. M.; Kelly, N.; Smith, C. B. *Inorg. Chem. Commun.* **2002**, *5*, 199.
104. Youinou, M.-T.; Rahmouni, J. F.; Fischer, J.; Osborn, J. A. *Angew. Chem. Int. Ed. Engl.* **1992**, *31*, 733.
105. Sung, N.; Yun, K.; Kim, T.; Choi, K.; Suh, M.; Kim, J.; Suh, I.; Chin, J. *Inorg. Chem. Commun.* **2001**, *4*, 377.
106. Constable, E. C.; Housecroft, C. E.; Kariuki, B. M.; Neuburger, M.; Smith, C. B. *Aust. J. Chem.* **2003**, *56*, 653.
107. Case, F. H. *J. Org. Chem.* **1961**, *26*, 4690.
108. SMART, Siemens Analytical X-Ray Instruments Inc., Madison, WI 53719, USA, 1996.
109. GEMINI, Twining solution program suite, Bruker AXS Inc., Madison, WI 53719, USA, 1999.
110. Parr, R. G.; Yang, W. *Density Functional Theory of Atoms and Molecules*; Oxford University Press: New York, 1989.

111. (a) McLean, A. D.; Chandler, G. S. *J. Chem. Phys.* **1980**, *72*, 5639. (b) Krishnan, R.; Binkley, J. S.; Seeger, R.; Pople, J. A. *J. Chem. Phys.* **1980**, *72*, 650.
112. Becke, A. D. *J. Chem. Phys.* **1993**, *98*, 5648.
113. Lee, C.; Yang, W.; Parr, R. G. *Phys. Rev B* **1988**, *37*, 785.
114. Gaussian Gaussian 98, Revision A.11, Gaussian 03, Revision B.05, Frisch, M.J.; Trucks, G.W.; Schlegel, H.B.; Scuseria, G.E.; Robb, M.A.; Cheeseman, J.R.; Montgomery Jr., J.A.; Vreven, T.; Kuden, K.N.; Burant, J.C.; Millam J.M.; Iyengar, S. S.; Tomasi, J.; Barone, V.; Mennucci, B.; Cossi, M.; Scalmani, G.; Rega, N.; Petersson, G.A.; Nakatsuji, H.; Hada, M.; Ehara, M.; Toyota, K.; Fukuda, R.; Hasegawa, J.; Ishida, M.; Nakajima, T.; Honda, Y.; Kitao, O.; Nakai, H.; Klene, M.; Li, X.; Knox, J.E.; Hratchian, H.P.; Cross, J.B.; Adamo, C.; Jaramillo, J.; Gomperts, R.; Stramann, R.E.; Yazyev, O.; Austin, A.J.; Cammi, R.; Pomelli, C.; Ochterski, J. W.; Ayala, P. Y.; Morokuma, K.; Voth, G. A.; Salvador, P.; Dannenberg, J. J.; Zakrzewski, V. G.; Dapprich, S.; Daniels, A.D.; Strain, M.C.; Farkas, O.; Malick, D.K.; Rabuck, A. D.; Raghavachari, K.; Foresman, J. B.; Ortiz, J.V.; Cui, Q.; Baboul, A. G.; Clifford, S.; Cioslowski, J.; Stefanov, B. B.; Liu, G.; Liashenko, A.; Piskorz, P. Komaromi, I.; Maritn, R. L.; Fox, D. J.; Keith, T.; Al-Laham, M. A.; Peng, C. Y.; Nanayakkara, A.; Challacombe, M.; Gill, P. M. W.; Johnson, B.; Chen, W.; Wong, M. W.; Gonzalez, C.; Pople, J. A.; Gaussian, Inc., Pittsburgh, PA, 2003.
115. (a) van Lenthe, E.; Baerends, E. J.; Snijders, J. G. *J. Chem. Phys.* **1993**, *99*, 4597. (b) van Lenthe, E.; Baerends, E. J.; Snijders, J. G. *J. Chem. Phys.* **1994**, *101*, 9783. (c) van Lenthe, E.; Ehlers, A. E.; Baerends, E. J. *J. Chem. Phys.* **1999**, *110*, 8943.
116. Perdew, J. P.; Wang, Y. *Phys. Rev. B*, **1986**, *33*, 8822.
117. (a) ADF2004.01, Baerends, E. J.; Autschbach, J.; Bérces, A.; Bo, C.; Boerrigter, P. M.; Cavallo, L.; Chong, D. P.; Deng, L.; Dickson, R. M.; Ellis, D. E.; Fan, L.; Fischer, T. H.; Fonseca Guerra, C.; van Gisbergen, S. J. A.; Groeneveld, J. A.; Gritsenko, M. Grüning, F. E. Harris, P. van den Hoek, H. Jacobsen, G. van Kessel, F. Kootstra, O. V.; van Lenthe, E.; McCormack, D. A.; Osinga, V. P.; Patchkovskii, S.; Philipsen, P. H. T.; Post, D.; Pye, C. C.; Ravenek, W.; Ros, P.; Schipper, P. R. T.; Schreckenbach, G.; Snijders, J. G.; Sola, M.; Swart, M.; Swerhone, D.; te Velde, G.; Vernooijs, P.; Versluis, L.; Visser, O.; van Wezenbeek, E.; Wiesenekker, G.; Wolff, S. K.; Woo, T. K.; and Ziegler, T., Scientific Computing and Modeling (SCM) <http://www.scm.com/>; Theoretical Chemistry, Vrije Universiteit, Amsterdam, The Netherlands. (b) te Velde, G.; Bickelhaupt, F. M.; van Gisbergen, S. J. A.; Fonseca Guerra, C.; Baerends, E. J.; Snijders, J. G.; Ziegler, T. J. Comput.

- Chem. 2001, 22, 931. (c) Fonseca Guerra, C.; Snijders, J. G.; te Velde, G.; Baerends, E. J. *Theor. Chem. Acc.* **1998**, 99, 391.
118. (a) Dijt, F. J.; Canters, G. W.; den Hartog, J. H. J.; Marcelis, A. T. M.; Reedijk, J. J. *Am. Chem. Soc.* **1984**, 106, 3644. (b) Kong, P. C.; Theophanides, T. *Inorg. Chem.* **1974**, 13, 1981.
119. (a) Dijt, F. J.; Canters, G. W.; den Hartog, J. H. J.; Marcelis, A. T. M.; Reedijk, J. J. *Am. Chem. Soc.* **1984**, 106, 3644. (b) Kong, P. C.; Theophanides, T. *Inorg. Chem.* **1974**, 13, 1981.
120. Hoogenboom, R.; Kickelbick, G.; Schubert, U. S. *Eur. J. Org. Chem.* **2003**, 4887.
121. (a) Komeda, S.; Ohishi, H.; Yamane, H.; Harikawa, M.; Sakaguchi, K.; Chikuma, M. *J. Chem. Soc., Dalton Trans.* **1999**, 17, 2959. (b) Komeda, S.; Lutz, M.; Spek, A. L.; Yamanaka, Y.; Sato, T.; Chikuma, M.; Reedijk, J. J. *Am. Chem. Soc.* **2002**, 124, 4722.
122. Ting, Y.; Lai, Y.-H. *J. Am. Chem. Soc.* **2004**, 126, 909.
123. Burgeson, J. R.; Renner, M. K.; Hardt, I.; Ferrence, G. M.; Standard, J. M.; Hitchcock, S. R. *J. Org. Chem.* **2004**, 69, 727.
124. Reduction potentials $E_{p,c}$ (vs. Ag/AgCl) in CH₃CN (V): -0.81 V (bptz); -1.80 V (bppn).
125. ADFview 2004.01, SCM, Theoretical Chemistry, Vrije Universiteit, Amsterdam, The Netherlands, <http://www.scm.com>.
126. Garau, C.; Frontera, A.; Quinonero, D.; Ballester, P.; Costa, A.; Deyà, P. M. *Chem. Phys. Lett.* **2004**, 392, 85.
127. Mingos, D. M. P.; Rohl, A. L. *Inorg. Chem.* **1991**, 30, 3769.
128. Du, M.; Bu, X.-H.; Biradha, K.; Shionoya, M. *J. Chem. Res.* **2002**, 247.
129. Hunter, C. A.; Sanders, J. K. M. *J. Am. Chem. Soc.* **1990**, 112, 5525.
130. Garau, C.; Frontera, A.; Quiñonero, D.; Ballester, P.; Costa, A.; Deyà, P. M. *Recent Res. Dev. Chem. Phys.* **2004**, 5, 227.
131. Doerksen, R. J.; Thakkar, A. J. *J. Phys. Chem.* **1999**, 103, 10009.
132. Famulari, A.; Specchio, R.; Gianinetti, E.; Raimondi, M. *Theo. and Comput. Chem.* **2002**, 10, 313.

133. (a) Gokel, G. W.; Barbour, L. J.; Ferdani, R.; Hu, J. *Acc. Chem. Res.* **2002**, *35*, 878. (b) Zarić, S. D. *Eur. J. Inorg. Chem.* **2003**, 2197.
134. Schottel, B. L.; Chifotides, H. T.; Shatruk, M.; Chouai, A.; Pérez, L. M.; Bacsá, J.; Dunbar, K. R. *J. Am. Chem. Soc.* **2006**, *128*, 5895.
135. (a) Hay P. J.; Wadt, W. R. *J. Chem. Phys.* **1985**, *82*, 284. (b) Hay P. J.; Wadt, W. R. *J. Chem. Phys.* **1985**, *82*, 299.
136. Berryman, O. B.; Bryantsev, V. S.; Stay, D. P.; Johnson, D. W.; Hay, B. P. *J. Am. Chem. Soc.* **2007**, *129*, 48.
138. See Chapter I and references therein.
139. Gorteau, V.; Bollot, G.; Mareda, J.; Perez-Velasco, A.; Matile, S. *J. Am. Chem. Soc.* **2006**, *128*, 14788.

VITA

BRANDI LEE SCHOTTEL
10810 Shadowbrook Lane
Frisco, Texas 75035
Phone: 979/574-3730

EDUCATION

Texas A&M University, College Station, Texas
Ph.D., *Chemistry*. (May 2007)
Dissertation: The Influence of Anion- π Interactions Between Multi-Atomic
Anions and π -Acidic Ring Systems on the Self-Assembly of Coordination
Compounds
Advisor: Prof. Kim R. Dunbar

University of Missouri, Columbia, Missouri
B.Sc., *Chemistry* (May 2002)
B.Sc., *Biology* (May 2002)

RESEARCH EXPERIENCE

Texas A&M University, College Station, Texas
Research Assistant, Department of Chemistry. (August 2002-present)
Teaching Assistant, Department of Chemistry. (August 2002-May 2003, January
2004-May 2004, January 2005-May 2006)

AFFILIATIONS

American Chemical Society
Alpha Chi Sigma Chemistry Fraternity

HONORS & AWARDS

Sharon Dabney Memorial Fellowship for Research and Service
Excellence in Teaching Award, First Year Program, Texas A&M
University
Two time Martell Travel Award Recipient, Texas A&M University
National Science Foundation representative and travel award recipient for the
55th annual Nobel Laureate Conference in Lindau, Germany
Regent's Graduate Scholar Award, TAMU (Fall, 2002)